Conception intégrée optimale du système propulsif d'un avion régional hybride électrique

Matthieu Pettes-Duler

Matthieu Pettes-Duler. Conception intégrée optimale du système propulsif d'un avion régional hybride électrique. Autre. Institut National Polytechnique de Toulouse - INPT, 2021. Français. NNT : 2021INPT0043 . tel-04170659

THÈSE

En vue de l'obtention du

DOCTORAT DE L'UNIVERSITÉ DE TOULOUSE

Délivré par :

Institut National Polytechnique de Toulouse (Toulouse INP)

Discipline ou spécialité :

Génie Electrique

Présentée et soutenue par :

M. MATTHIEU PETTES-DULER

le vendredi 23 avril 2021

Titre :

Conception intégrée optimale du système propulsif d'un avion régional hybride électrique

---

Ecole doctorale :

Génie Electrique, Electronique, Télécommunications (GEETS)

Unité de recherche :

Laboratoire Plasma et Conversion d'Energie (LAPLACE)

Directeur(s) de Thèse :

M. XAVIER ROBOAM
M. BRUNO SARENI

Rapporteurs :

M. FREDERIC GILLON, ECOLE CENTRALE DE LILLE
M. SALVY BOURGUET, UNIVERSITE DE NANTES

Membre(s) du jury :

MME DELPHINE RIU, INP DE GRENOBLE, Président
M. BRUNO SARENI, TOULOUSE INP, Membre
M. JEAN-FRANCOIS ALLIAS, AIRBUS FRANCE, Invité(e)
M. JEAN-FRANCOIS LLIBRE, TOULOUSE INP, Invité(e)
M. MARC BUDINGER, INSA TOULOUSE, Membre
M. XAVIER ROBOAM, TOULOUSE INP, Membre

RÉSUMÉ

En 2019, le transport était le secteur qui connaissait la croissance la plus rapide au niveau mondial, contribuant du même coup à la dégradation de l'environnement. Trouver des solutions durables moins polluantes est un élément clé pour résoudre ce problème, en particulier pour le secteur aéronautique, qui représente environ 2 % des émissions mondiales de CO2. Avec l’apparition de la Covid-19, le trafic aérien semble assez durablement interrompu, mais cette pandémie renforce la nécessité d’aller vers « un ciel plus propre » et respectueux de l’environnement, ce qui constitue l’objectif du programme Clean Sky2 (H2020 EU), contexte dans lequel le projet ’’HASTECS’’ et notre thèse se situent.

L’objectif principal d’HASTECS (Hybrid Aircraft Academic reSearch on Thermal and Electrical Components and Systems) est de coupler études thermiques et électriques au sein de la chaine de propulsion hybrides électrique d’un avion régional, ceci en intégrant les contraintes d’environnement (en particulier les décharges partielles) spécifiques au secteur aérien. Le but est d’identifier les technologies et ruptures les plus prometteuses et de mettre au point les outils qui permettront d’accroitre de manière significative la compacité et l’efficacité des processus électriques au sein de la chaine de propulsion hybride. Dans notre cas, seule l'architecture électrique hybride série a été étudiée dans ce projet, car elle conduit à une grande puissance de dimensionnement maximisant les contraintes technologiques sur la chaîne.

Les cibles technologiques fixées dans HASTECS, considérées sous deux horizons (2025 puis 2035), sont les suivantes :

	Cible 2025	**Cible 2035**
Moteur électrique + refroidissement		
Densité de Puissance	5 kW/kg	10 kW/kg
Redement en phase de croisière	96%	98.5%
Rendement au point nominal	94.5%	97%
Electronique de puissance + refroidissement		
Densité de puissance	15 kW/kg	25 kW/kg
Rendement en croisière	98%	99.5%
Rendement au point nominal	96.5%	99%

Dans le cadre de ce projet, notre thèse vise la conception par optimisation de la chaîne de propulsion complète intégrant en particulier les modèles issus des développements technologiques des constituants majeurs (électroniques de puissance, câblage et architecture de distribution, actionnement) tout en considérant, à partir d’une gestion d’énergie simplifiée, l’hybridation d’une source principale (thermique) et auxiliaire (électrique).

Un premier objectif de notre thèse a concerné le développement d’un modèle d’environnement. Ces conditions étant fixées, l’intégration système consiste à bâtir une suite de modèles réduits dont la granularité permet l’évaluation globale (systémique) des rendements énergétiques et des masses de chaque composant jusqu’à la chaine de propulsion

complète. Le système propulsif est conçu, via un processus itératif estimant, selon les choix de conception, les variations de masses et leurs conséquences sur la poussée : cette approche de conception intégrée permet entre autre d'évaluer les effets boules de neige dont l'influence est majeure en aéronautique. En effet, l'ajout de masse sur un dispositif entraine des conséquences sur la structure et le carburant embarqué.

Après un état de l'art situant le contexte de l'étude, nous proposons une suite de « modèles réduits » intégrables au sein d'un processus d'optimisation de la chaine complète (avec un temps de calcul raisonnable) : ces modèles sont issus :

- D'études antérieures : turbines à gaz, sources électriques auxiliaires (batteries, piles à combustible), réducteur de vitesse, hélice ;
- Ou d'une adaptation (réduction) des modèles technologiques issus des work packages d'HASTECS : électroniques de puissance et leur refroidissement, moteurs électriques et leur refroidissement, contraintes de décharges partielles.

Avant de progresser vers l'intégration système et l'optimisation du dimensionnement, un chapitre est consacré à l'analyse de sensibilité dont l'objectif est de préciser les degrés de liberté (variables de décision) les plus sensibles vis-à-vis des principaux objectifs (réduction de masse et des pertes) de la conception. Des techniques d'analyse de sensibilité basées sur les indices de Sobol sont en particulier exploitées.

Enfin, la dernière partie et l'objectif final de ce projet concerne la conception optimale de la chaine complète intégrant une gestion d'énergie propre à l'architecture hybride électrique. Cette étude démarre par des études locales sur les constituants majeurs (chaine d'actionnement) pour progresser vers l'intégration système et la chaine complète. De nombreux résultats mettent en évidence l'émergence de couplages systèmes qui n'apparaissent pas dans l'assemblage d'optima locaux.

ABSTRACT

In 2019, transportation was the fastest growing sector, contributing to environmental degradation. Finding sustainable solutions that pollute less is a key element in solving this problem, particularly for the aviation sector, which accounts for around 2% of global CO2 emissions. With the advent of Covid-19, air traffic seems to have come to a fairly permanent halt, but this pandemic reinforces the need to move towards a "cleaner sky" and respect for the environment, which is the objective of the Clean Sky2 program (H2020 EU), the context in which the HASTECS project and our thesis are set.

The main objective of HASTECS (Hybrid Aircraft Academic reSearch on Thermal and Electrical Components and Systems) is to couple thermal and electrical studies within the hybrid electric propulsion chain of a regional aircraft, by integrating the environmental constraints (in particular partial discharges) specific to the aviation sector. The aim is to identify the most promising technologies and breakthroughs and to develop the tools that will significantly increase the compactness and efficiency of the electrical processes within the hybrid propulsion chain. In our case, only series hybrid electric architecture was studied in this project, as it leads to a high dimensioning power maximizing the technological constraints on the chain.

The technological targets set in HASTECS, considered under two horizons (2025 then 2035), are the following:

	2025 target	**2035 target**
Electric motor + cooling system		
Specific power	5 kW/kg	10 kW/kg
Cruise efficiency	96%	98.5%
Maximal design point efficiency	94.5%	97%
Power electronics + cooling system		
Specific power	15 kW/kg	25 kW/kg
Cruise efficiency	98%	99.5%
Maximal design point efficiency	96.5%	99%

In the framework of this project, our thesis aims at the design by optimization of the complete propulsion chain integrating in particular the models resulting from the technological developments of the major components (power electronics, wiring and distribution architecture, actuation) while considering, from a simplified energy management, the hybridization of a main (thermal) and auxiliary (electrical) source.

A first objective of our thesis concerned the development of an environment model. Once these conditions are set, the system integration consists in building a suite of scale models whose granularity allows the global (systemic) evaluation of the energy yields and masses of each component up to the complete propulsion chain. The propulsion system is designed via an iterative process estimating, according to the design choices, the mass

variations and their consequences on thrust: this integrated design approach allows, among other things, to evaluate the snowball effects, which have a major influence in aeronautics. Indeed, the addition of mass on a device has consequences on both the structure and onboard fuel.

After a state of the art and context study, we propose a series of "scale models" that can be integrated into an optimization process of the complete chain (with a reasonable computing time). These models are derived from:

- Previous studies: gas turbines, auxiliary electrical sources (batteries, fuel cells), speed reducer, propeller;
- Or from an adaptation (reduction) of technological models from HASTECS work packages: power electronics and their cooling, electric motors and their cooling, partial discharge constraints.

Before moving on to system integration and design optimization, a chapter is devoted to sensitivity analysis, the objective of which is to specify the most sensitive degrees of freedom (decision variables) with respect to the main objectives (mass and loss reduction) of the design. Sensitivity analysis techniques based on Sobol indices are used in particular.

Finally, the last part and the final objective of this project concerns the optimal design of the complete chain integrating clean energy management in hybrid electric architecture. This study starts with local studies on the major components (drive chain) in order to progress towards system integration and the complete chain. Many results highlight the emergence of system couplings that do not appear in the assembly of local optima.

REMERCIEMENTS

Les travaux de recherche présentés dans ce mémoire ont été effectués à l'Institut National Polytechnique de Toulouse, dans le laboratoire Plasma et Conversion d'Energie LAPLACE, au sein du Groupe de Recherche en Energie Electrique et Systémique.

Je souhaite dans un premier temps remercier les membres du jury. Madame Delphine Riu, pour le grand plaisir qu'elle m'a fait en présidant ce jury. Monsieur Salvy Bourguet et monsieur Frédéric Gillon, pour le temps et l'attention qu'ils ont accordés à la relecture de mon manuscrit, ainsi que pour leurs remarques pertinentes sur mon travail en qualité de rapporteur. Merci à Jean-François Llibre d'avoir suivi mes travaux de thèse. Enfin, merci à AIRBUS et particulièrement Jean-François Allias pour s'être intéressé à mes travaux et m'avoir fait confiance.

J'adresse de chaleureux remerciement à mes directeurs de thèse, Xavier Roboam et Bruno Sareni. Merci à vous de m'avoir fait confiance dès mon projet de fin d'étude, cela m'a permis d'aborder plus sereinement le sujet de thèse. Je vous remercie également pour vos conseils avisés, nos interactions ont été riches et j'ai beaucoup appris à vos côtés. Je n'étais pas le « premier de la classe » mais l'encadrement a été bienveillant et ma motivation sans faille. Merci également pour vos qualités humaines qui ont veillé au bon déroulement de ce projet de recherche. J'espère enfin pouvoir fêter tout cela autour d'un bon petit repas avec vous.

Je tiens également à remercier tous les collègues du projet HASTECS, mes travaux sont également les votres, de beaux résultats découlent de cette thèse et c'est grâce à vous : Flavio, Najoua, Philippe, Sarah, Amal, Maillys et Malik.

Un grand merci aux personnes qui constituent le LAPLACE, au-delà d'un laboratoire à la pointe, cette « famille » est bienveillante et assure la bonne ambiance dans les bureaux. Merci à vous tous pour m'avoir mis la pression dans certains moments, accompagné dans les démarches, ou encore fait rire.

Un immense merci à toutes les « forces contractuelles de recherche » du LAPLACE. Tout d'abord merci à Jérôme, de m'avoir permis d'utiliser tes modèles ; Jo, Théo et Robin pour les parties de baby-foot sans fin, et autres activités ludiques. Merci à Sami, Abdelkader et Khaled pour votre acceuil dans votre bureau. Merci à Yazan, Plinio, Andrea, Quentin, Hugo, Davin et les autres pour tous ces bons moments passés en votre compagnie. Je suis heureux d'avoir fait votre connaissance.

Enfin mes remerciements, s'adressent à ma famille qui a toujours été là pour moi. Je remercie mes parents, David et Cathy, pour leur soutien pendant toute la durée de mes études, je ne pensais pas aller jusque là ! Merci à ma sœur, Aurélie, de m'avoir supporté et encouragé pendant ces années.

Je finirai par remercier ma compagne, Elise. Je remercie le destin d'avoir croisé ton chemin ; tu as su m'écouter et me faire confiance, je t'en suis reconnaissant. Je suis heureux d'être à tes côtés pour commencer cette nouvelle vie qui nous attend.

ACKNOWLEDGMENTS

This project has received funding from the [European Union’s Horizon 2020 (cleansky 2 JTI) research and innovation program, 2014-2024] under grant agreement No 715483.

TABLE OF CONTENTS

LIST OF FIGURES

LIST OF TABLES

LIST OF ACRONYMS

ACARE	Advisory Council for Aeronautical Research in Europe
AE	All-Electric (aircraft)
ANPC	Active Neutral Clamped Point topology
ANOVA	Analyze Of VAriance
BLI	Boundary Layer Ingestion
CORAC	Council of Civil Aeronautical Research
CPU	Central Processing Unit
DPWM	Discontinuous Pulse Width Modulation
EIS	Entry Into Service / Electrical insulation System
FEA	Finite Element Analysis
FC	Flying Capacitor topology
GHG	GreenHouse Gas
GSA	Global Sensitivity Analysis
HASTECS	Hybrid Aircraft reSearch on Thermal and Electric Components and Systems
IATA	International Air Transport Association
ICAO	International Civil Aviation Organization
IM	Induction machine
ISA	International Standard Atmosphere
LEAPTECH	Leading Edge Asynchronous Propeller TECHnology
MDO	Multidisciplinary Design Optimization
MTOW	Max Take-Off Weight
NASA	National Aeronautics and Space Administration
NPC	Neutral Clamped Point topology
OAD	Overall Aircraft Design
OEI	One Engine Inoperative
ONERA	Office National d’Etudes et de Recherche Aérospatiale
PAX	Passengers
PE	Power Electronics
PH	Parallel Hybrid (electric aircraft)
PT	Partial Turboelectric (aircraft)
EHP	Energy Hybridization Potential
PHP	Power Hybridization Potential
RMS	Root Mean Square
SFC	Specific Fuel Consumption
SH	Series Hybrid (electric aircraft)
SMC	Stacked Multicell Converter topology
SM-PMSM	Surface-Mounted Permanent Magnet Synchronous Machine
SPPH	Serie- Parallel Partial Hybrid (electric aircraft)
SRM	Synchronous Reluctance Machine
Starc-ABL	Single-aisle Turbo-electric AiRCraft with an Aft Boundary Layer propulsor
TE	TurboElectric(aircraft)
VTOL	Vertical Take-Off and Landing
WP	Work Package

INTRODUCTION

Since the 1950s, the aviation industry has made incredible progress in increasing both the power and efficiency of its internal combustion engines. However, recent studies suggest that the technology of these engines is approaching the thermodynamic limits of the amount of energy it is capable of extracting from a carbon-based fuel at a lower cost. This means that the more flights and airplanes there are, the more fuel consumption and greenhouse gas emissions will increase, unless a suitable substitute is found for fossil fuels, such as hybrid and electric airplanes. The electrification of propulsion functions expands the aircraft design space by introducing new configurations. Several hybridizations are possible with more or less advanced hybridization ratios in power and energy depending on the chosen topology.

This thesis deals with series hybrid-electric propulsion, all the propulsion is provided by electric motors, only the sources are dimensioned according to the associated missions. The case study is a 70-Pax regional jet capable of covering a 500 nautical mile mission. The complete hybrid electric propulsion chain is designed by optimization, integrating models resulting from technological developments of the major electrical components. The reference point of the design methodology is a conventional aircraft with thermal propulsion (propeller, gearbox, gas turbines). Snowball effects caused by weight gain are taken into account through an internal loop on the aircraft thrust. The initial investment cost of building the aircraft is not taken into account in this study. Only the environmental costs (fuel mass) will be evaluated during the overall optimization of the propulsion system.

The first chapter focuses on the state of the art of electric (hybrid) propulsion configurations. Several design axes for new aircraft architectures are being studied: Optimal turboshaft designes, improvement of aerodynamics and new energy management of the different mission profiles. Subsequently, the HASTECS project is described with all the assumptions and associated input data. The study areas of the work packages are also presented, as well as their objective within the framework of the project. Finally, the coupling between this work and the previous work packages will be specified by explaining the integrated design approach; the internal loop taking the snowball effect into account will also be detailed.

The second chapter will present a series of "scale models" that can be integrated into an optimization process for the global powertrain (with a reasonable calculation time): these models come from previous studies or from an adaptation (reduction) of technological models from the HASTECS work packages. These models have been modified in order to obtain reasonable calculation times and are presented in the rest of the chapter.

An initial study is carried out in Chapter III to explore the design space for a regional aircraft with series hybrid-electric propulsion. The energy missions of each source (electric and thermal) will be modified in order to evaluate the impact of these variations on the aircraft's weight and fuel consumption. Subsequently, a global sensitivity analysis (GSA) is implemented in order to highlight the parameters which have the greatest impact on the previous output variables (aircraft mass/ fuel consumption). This sensitivity analysis is based on the study of

Sobol indices which express the sensitivity of each input variable on the output. First, fixed configurations of hybrid electric aircraft will be studied by varying power densities and efficiency. Then the global sensitivity analysis will be applied to the masses and efficiencies of the components themselves by directly varying the sizing variables. The propeller-gearbox-electric motor assambly will be studied in more detail because it is the most crucial part of the propulsion system to be sized.

Finally, the last part and the final objective of this project concerns the optimal design of the complete powertrain integrating an energy management to the hybrid electric architecture. The same path as the sensitivity analysis will be studied for optimization. A first optimization on the component itself (electric machine) will be performed taking all interactions into account (electromagnetic, thermal and partial discharges) for its sizing. Then the complete propulsion system will be optimized in several ways in order to highlight the difference in "approach level" (local approach / systemic approach). Finally, the hybridization ratios will be added to the optimization variables to obtain the most optimal regional hybrid-electric aircraft from a fuel consumption point of view.

This entire study has highlighted the interest of a multidisciplinary approach to the design of a hybrid electric propulsion aircraft. In reality, the process is even more complex because all the surfaces of the plane must be resized at the same time as the propulsion and the mass. However, one essential thing has been underlined in this study, the hybrid electric propulsion brings even more complexity and this is not free, an additional investment cost for the construction of this aircraft should not be overlooked. Is hybridization of the propulsion system really the solution for this type of single-aisle aircraft? Is a true complete technological breakthrough more interesting?

CHAPTER I. The electric revolution impacts aviation.

CONTENTS

I.1 Why are (hybrid-)electric aircrafts headed for a takeoff?

I.1.1 An air traffic growth that was not ready to stabilize before COVID-19.

Global air traffic grew by 6.5 percent in 2018, according to the International Air Transport Association (IATA [1]). Before the COVID-19, passenger air travel was expected to maintain positive growth rates up to 2030, despite a number of industrial challenges to be faced: airlines around the world are struggling with high jet fuel prices and slow economic growth. After COVID, this growth has been brutally blocked probably for some years: according ti IATA assesments, the air traffic will be decreased by 88% for 2020 (see [2]-[3]). Some economic analysis is currently on going that will assess the time to recover the 2019 air traffic and the new growth perspectives but it seems that major trends (assessed before COVID) would be slown down but maintained (after COVID). In that context the lines below were written before the new pandemic situation but remain relevant at the whole, at least for long term situation.

Through the previous different crises air traffic has proven its robustness by doubling every fifteen years. Moreover, with low-cost airlines such as Ryanair or Easyjet entering the race, airline tickets are increasingly accessible to the world's population and do not make things better for the air sector. In order to avoid doubling carbon emissions at the same time as the growth of air transport, major research and development effort required today must be continuousand synchronized. Innovations and technological breakthroughs in the field of propulsion, materials, aerodynamics, on-board systems, must be coordinated in order to design a new generation of innovating devices. In French aircraft industry this is the whole purpose of the CORAC (Council of Civil Aeronautical Research): a state-industry think tank which acts for the set up of the French research program. This is also the object of ACARE (Advisory Council for Aeronautical Research in Europe), CleanSky [4] and SESAR technological research programs, bringing together thousands or researchers and European engineers mobilized to change the future of aviation.

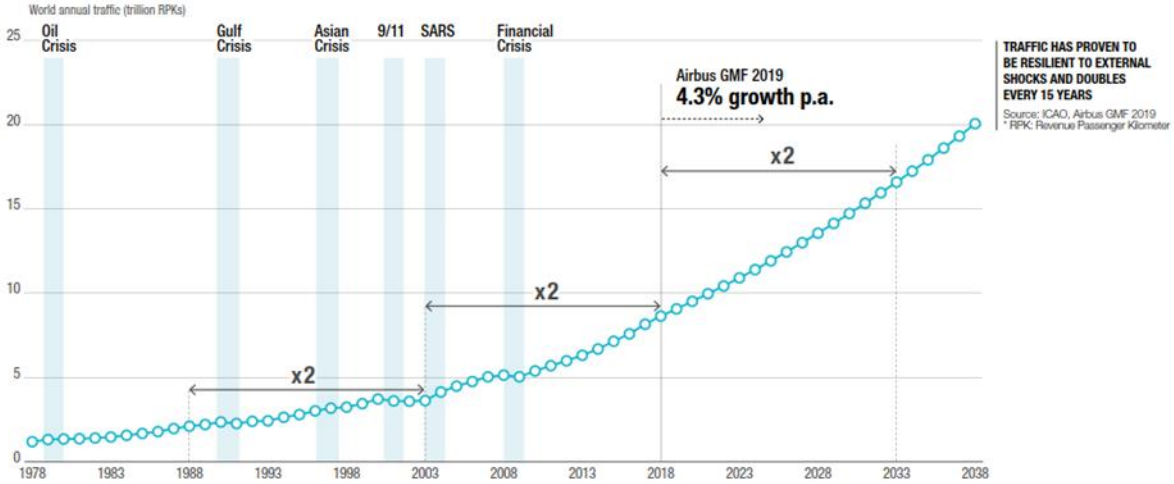

Fig. I-1: Air traffic evolution since 1977 and estimate to 2037 (Source AIRBUS GMF 2019 [5]*).*

In 2000, the ACARE has launched two programs: one for 2020 named VISION 2020 [6] and the second is the FLIGHTPATH 2050 [7]. For the environment, the 2020 target predicted a 50% reduction in CO_2 emissions per passenger kilometer and an 80% Nox emission reduction. In 2050 available technologies and procedures would allow a 75% reduction in CO_2 emissions per passenger kilometer and a 90% reduction in NOx emissions to support the ACARE target. The perceived noise emission of flying aircrafts has to be reduced by 40% for the first target 2020 and 60% for the second one. These are relative to the capabilities of typical new aircraft in 2000 ([7]).

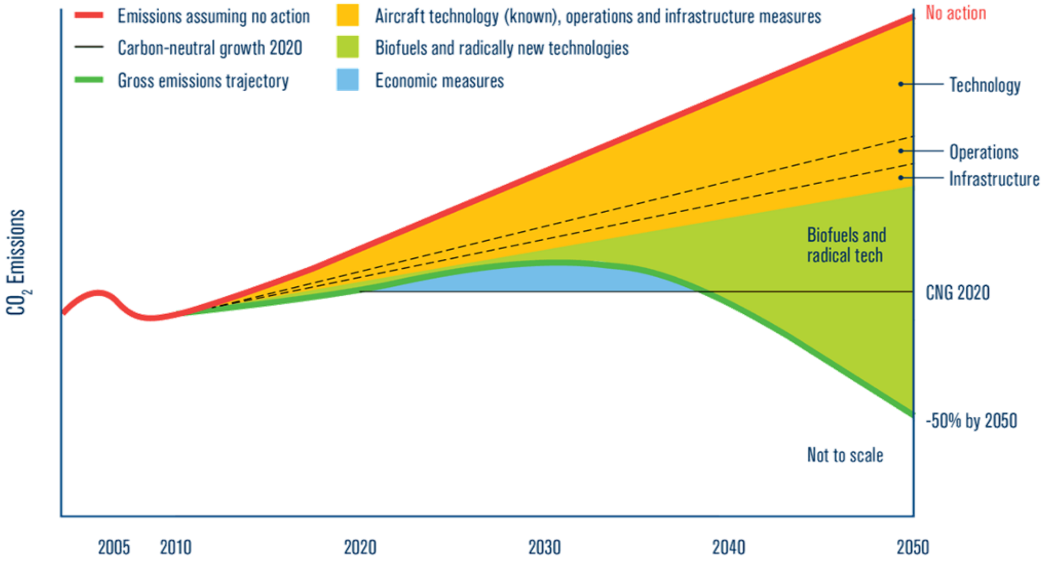

Fig. I-2: Schematic CO_2 emissions reduction roadmap (Source IATA [8]*).*

The International Air Transport Association (IATA) announced three huge level goals for the greenhouse gas emissions roadmap (green line) [8]:

- An average improvement in fuel efficiency of 1.5% per year from 2009 to 2020.
- A cap net emission from 2020 through carbon neutral growth between 2020 and 2040.
- By 2050, net aviation carbon emissions will be half what they were in 2005.

Although if aircrafts appear to be a polluting means of transport the aviation's contribution to global man-made CO_2 emissions currently reaches between 2% and 4% depending on various studies.

Furthermore, a new global movement called "Flygskam" meaning flight shame wants to raise people's awareness about airplane pollution.

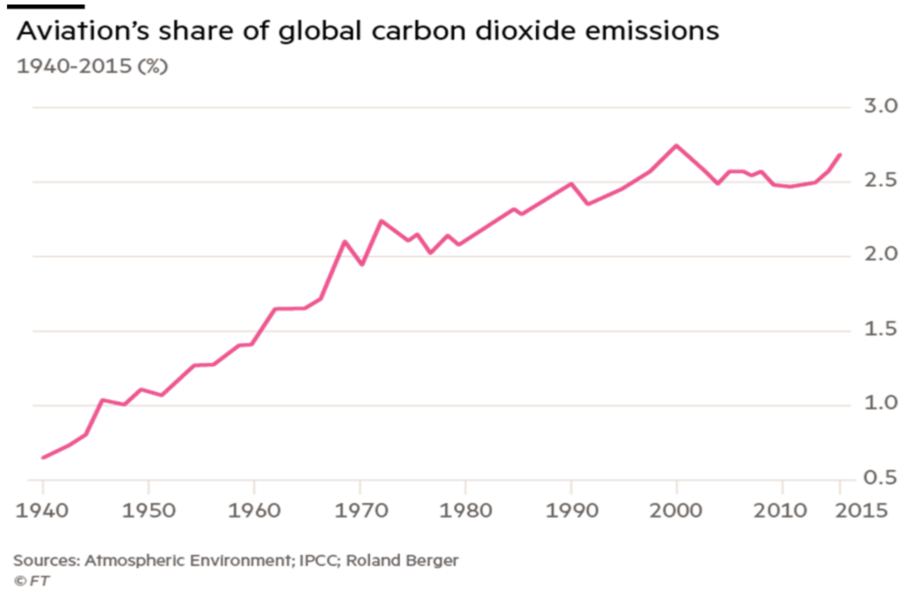

Fig. I-3: CO_2 emissions evolution in % from 1940 to 2015 (Source Roland Berger[9]*).*

I.1.2 Flygskam or flight shame.

"We stay on the ground "said Maja Rosén in 2018 [10] recruiting people in her group of the same name, to pledge to give up flying for one year. So far, more than 8000 people around the world have made the pledge. The length of Sweden, 1570-km-long, explains why its inhabitants use the plane more than the global average (5 times more). The use of regional aircraft releases 14 to 40 times more CO2 gas emissions. Another Swedish, a 16-year-old climate change activist named Greta Thunberg campaigns against air travel. She went on strike from school the same year protesting against the country government's inaction on climate change. She attended the United Nations Climate Change Conference (COP 24) and addressed the summit, explaining the severity of global warming. In other countries, AVINOR (the Norwegian Civil Aviation Administration) works to ensure that Norway takes a leading role at an international level on a development and innovation project for electric aircrafts. According to this administration, by 2040, all short haul and regional aircrafts should be electrically-powered. A good example is that of the consortium Airbus and SAS Scandinivian Airlines which are collaborating to explore the hybrid-electric and electric potential.

More generally, that whole context push aviation sector to innovate towards greener aircraft solutions.

I.1.3 Towards a new revolution in the aviation industry?

Since Frank Whittle (the jet engine inventor) in 1937, aircrafts have been fuel powered. After decades, improvements have been made in the field of materials, battery technology and electric systems. This revolution does not prevent established leaders to maintain their pole position. That is why major aerospace companies are competing to put electrically powered devices on market so as to avoid competition from a new generation of aircraft manufacturers. Since 2009, more than 150 electric aviation projects have been launched worldwide. A third of these come from them (Airbus, Boeing, Roll Royce…), others come from start up or new born companies in aviation industry.

Fig. I-4: Electric propulsion is finally on the map (or hybrid-electric aviation) (Source Roland Berger [11]*): number of electric or hybrid electric aviation projects.*

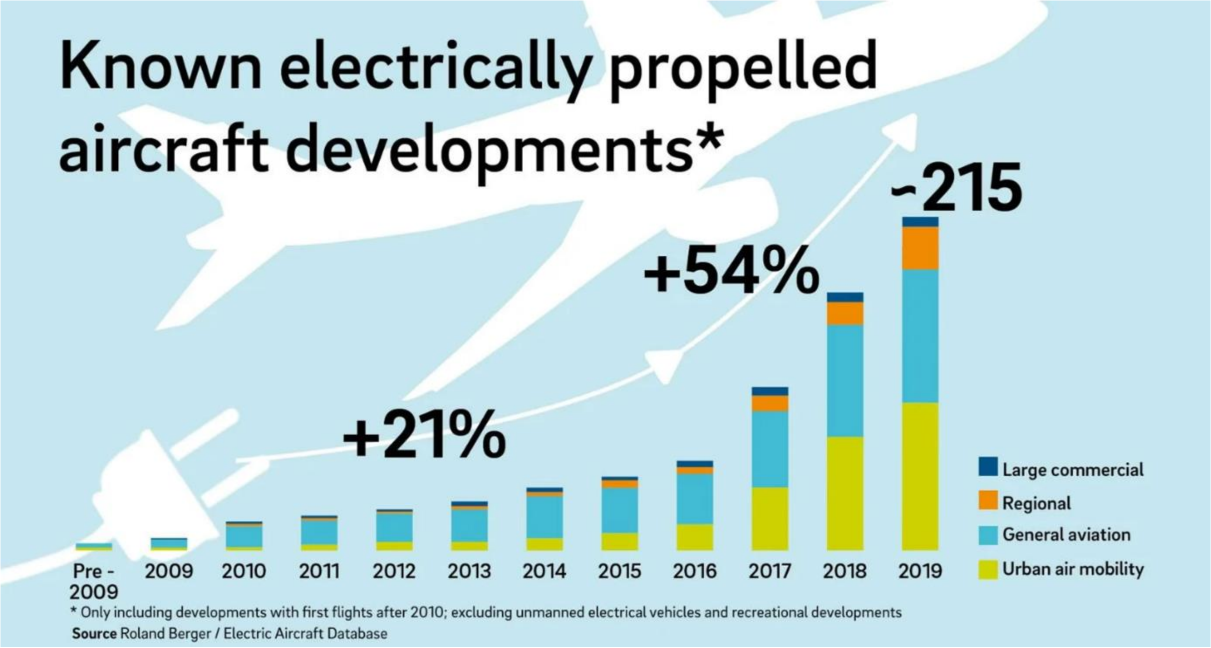

* Only including developments with first flights after 2010; excluding unmanned electrical vehicles and recreational developments

Source Roland Berger / Electric Aircraft Database

Fig. I-5: Evolution of the number of projects aimed at taking off electric planes according to the type of aircraft (Source Roland Berger[11]*).*

The growing trend of electric propulsion is emerging: all over the world, a convergence of factors contributing to electric propulsion is becoming a reality. From technological development to investments by new entrants, including the activity of the main aerospace players, the sector seems ready to undergo a radical change.

I.1.4 Enemy number one in aeronautics: weight!

To make the dream of electric propulsion a reality, aeronautical companies must bridge the technological gap due to the power required for flight: for a 70 Pax regional aircraft the power required for the takeoff is around 4MW. The challenges to be met are mainly technological challenges for the system components of hybrid electric propulsion system. But adding electric components to transform mechanical power into electricity in the propulsive system, adds weight to the hybrid-electric aircraft. A heavier aircraft needs more wing surface and all the more power to fly therefore a more powerful propulsive system this consequently entails overconsumption: this is the snowball effect. In the following study [12], a conventional reference aircraft was taken to show the snowball effects of mass additions on fuel consumption. The Fig. I-6 is a comparison between three conventional aircrafts (thermal propulsion system) with three different payloads (6500/8500/10500 kg).

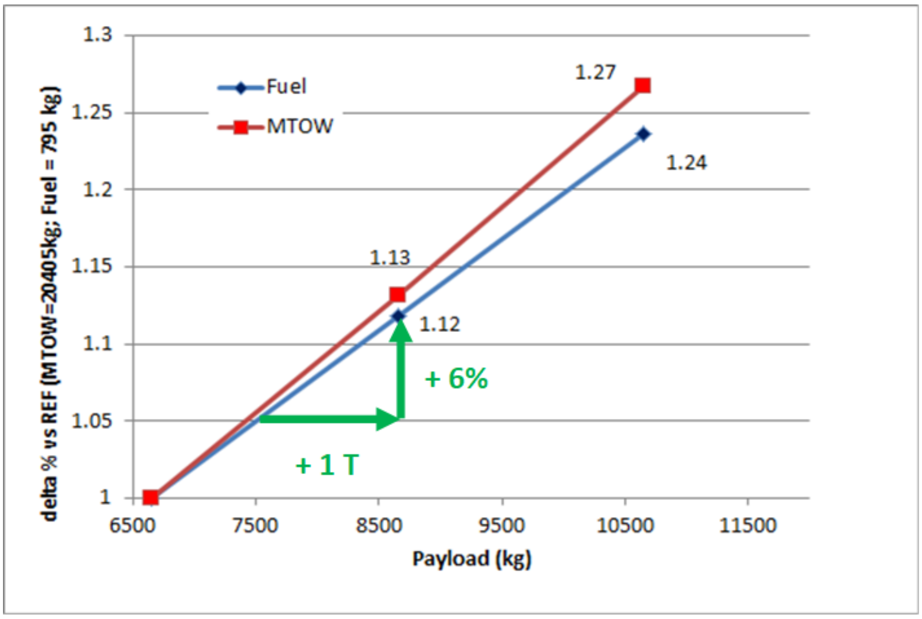

Fig. I-6: "Snowball effect" on conventional architecture fixed aircraft mass additions and fuel consumption effects.

The conclusion is clear: each ton added to the aircraft cause a 6% over consumption of fuel. In this study, the thermal propulsive system has been adapted and resized in order to succeed with a 400 nm flight mission. The red line shows the snowball effect on the Max Take Off Weight (MTOW) caused by the new propulsion system. A prediction can be made concerning the hybrid-electric aircraft: it will be heavier than conventional ones. Heavy electric components like e-motors and e-generators will increase the weight of the propulsive system also involving snowball effects. That is why their design and efficiency are essential to improve hybrid-electric aircraft performance.

An electric aviation roadmap has been made by a French aeronautical equipment manufacturer SAFRAN, it predicts increasing both voltage and power for electric devices. For huge powers increasing the voltage reduces the current and tends consequently to reduce the mass. For example, a cable is sized by its thermal limit directly conditioned by the Joule losses related to the current rating. The same applies to electric motors and generators whigh may requirehigh voltages for high conversion powers.

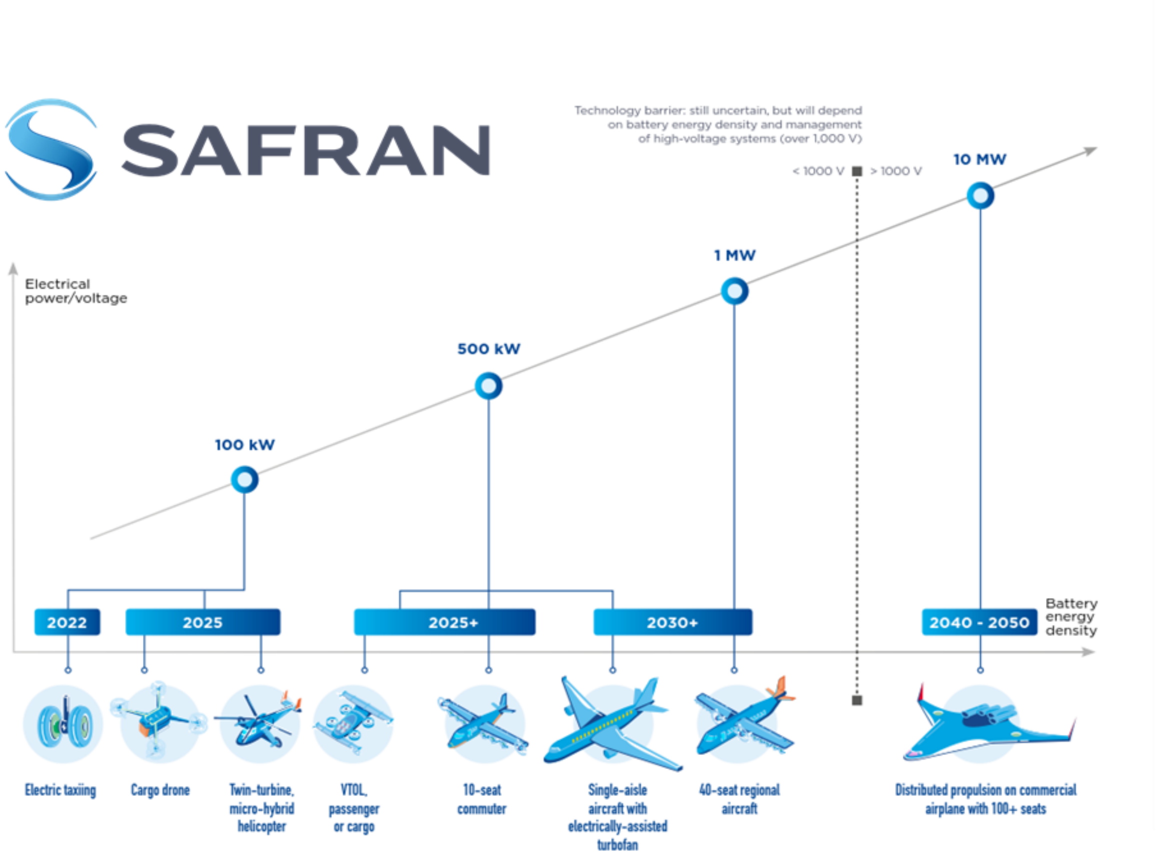

Fig. I-7: Safran aircraft electrification roadmap [13].

Unfortunately, beyond voltage values of ~1000V new phenomena appear: the partial discharges. They are created by a large potential difference between two conductors which could damage their insulation. In electric motors, partial discharges in windings may appear that can affect the lifetime of actuators. This is all more critical than electric machines are supplied by high frequency power electronics with high voltage derivatives.

Success of the electric aircraft does depend on both the power efficiencies and specific powers. These two factors must be enhanced not only on electric powertrain devices but also on electrical sources whatever if hybrid or full electric architectures are considered.
Stephane Cueille (Safran Chief Technical Officer at Safran) has estimated the weight of a full electric Airbus A320: it should carry a 170 tonnes battery-pack while its whole mass is about 60 tonnes today…

In the PhD thesis of Jerome Thauvin [12] in cooperation with airbus, a full electric aircraft prospective study has been made in order to determine the maximum aircraft range with respect to the battery specific energy assessment. Two different entry in service (EIS) were assessed for a 2025 and a 2030+ EIS. The overal aircraft structure are optimized for each value of both design range and specific energy. For both EIS, the assumptions taken into account for the main powertrain devices are the following:

Table I-1: Electrical component assumptions according to EIS (Source: J. Th PhD Thesis).

		EIS2025	EIS2030+
Electric machine	Specific power	7 kW/kg	11 kW/kg
	Efficiency	96 %	98.5 %
Power electronics	Specific power $\overline{P}_{pe}$	15 kW/kg	20 kW/kg
	Efficiency η_{pe}	99 %	99.5 %
Battery	Specific energy $\overline{E}_b$	280 Wh/kg	380 Wh/kg
	Max. ch./disch. C	2/5	2/5
	Efficiency η_b	90%	95 %
Cable	Voltage V_c	540 V	1500 V

In that table, reference figures for the specific energy of batteries are assessed. In the figure below, three different aircraft with MTOW of 25, 30 and 35 tons are compared. By varying the reachable range in nm, the target on battery specifi energy is calculated. For the reference values related to EIS prediction, the acceptable is still very limited:

- for EIS2025 with 280 Wh/kg, the aircraft with a MTOW@25 tons is unable to take off while the MTOW@30 tons is limited to a range of 100nm.
- for EIS2030+ with 380 Wh/kg, the three aircraft ranges are limited below 200nm.

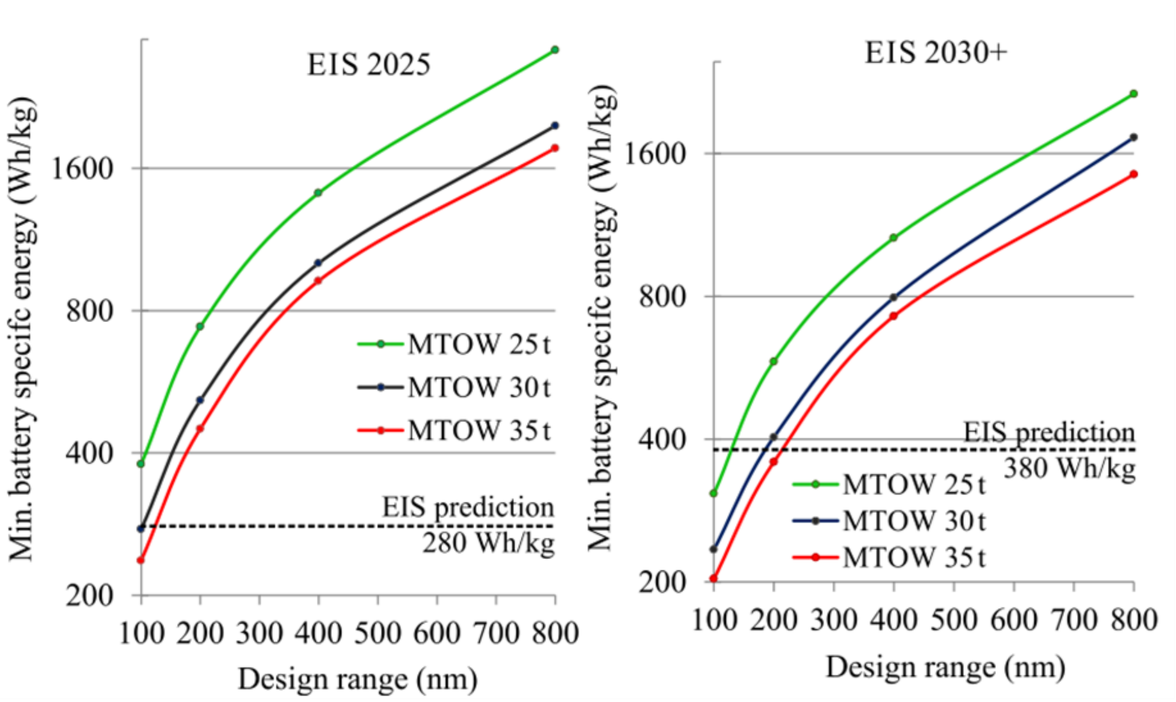

Fig. I-8: Determination of a minimal value of battery specific energy function of the design range according to EIS of three different MTOW aircrafts (Source: J. Th PhD Thesis[12]*).*

The dream of the electric aircraft may become a reality whereas electric source performance strongly progresses in terms of specific energy and/or specific power. In addition, the aircraft structure has to be resized and optimized to reduce weight. As example three studied aircrafts are the results of the previous study for a 400 nm design range and a 2030+ EIS:

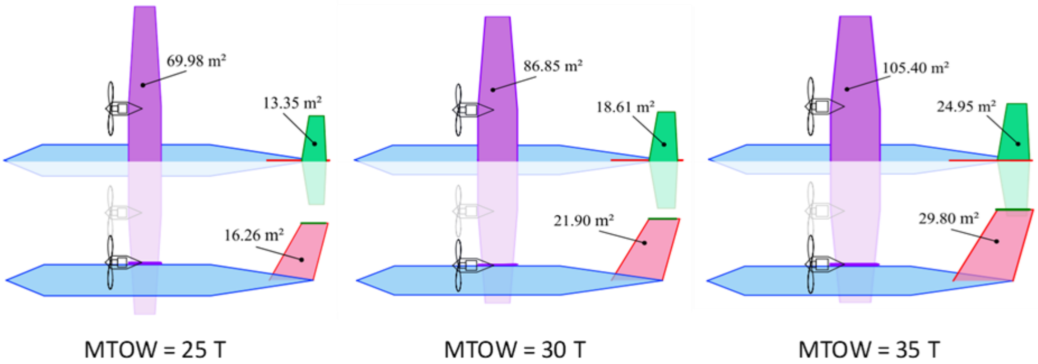

MTOW = 25 T MTOW = 30 T MTOW = 35 T

Fig. I-9: Aircraft geometry comparison for a 400nm design range and a 2030+ EIS (Source: J. Th PhD Thesis [12]*).*

A structural compensation has been found caused by the lack of battery specific energy. These aircrafts need more lift to make the flight mission successful, so the area of wing, horizontal tail and fin are larger. In these cases, the specific energy values will be difficult to reach, that is why the commercial electric flight is not ready to take off. The electric air revolution must learn from hybrid-electric aircraft propulsion to find disruptive technologies in order to create the full electric flight opportunity.

I.2 Potential hybridization gains of the hybrid-electric aircraft propulsive system.

I.2.1 A complicated hybridization of the propulsive sytem…

If in automotive application, or even in railway traction field, hybrid electric propulsion systems exist and are becoming more and more spread hybridization is still a long way off in the aeronautical field. An automotive profile mission is much more intermittent with numerous braking phases with energy recory opportunities contrarily to the aeronautic case. It is interesting to build hybridization indicators to copare these application sectors. In the thesis of Akli [14], two kinds of indicators have been set up:

- The Power Hybridization Potential (PHP) assesses the potential degree of primary energy source undersizing.

$$PHP = 1 - \frac{mean\left(P_{primary_{source}}\right)}{max\left(P_{primary_{source}}\right)} \tag{I-1}$$

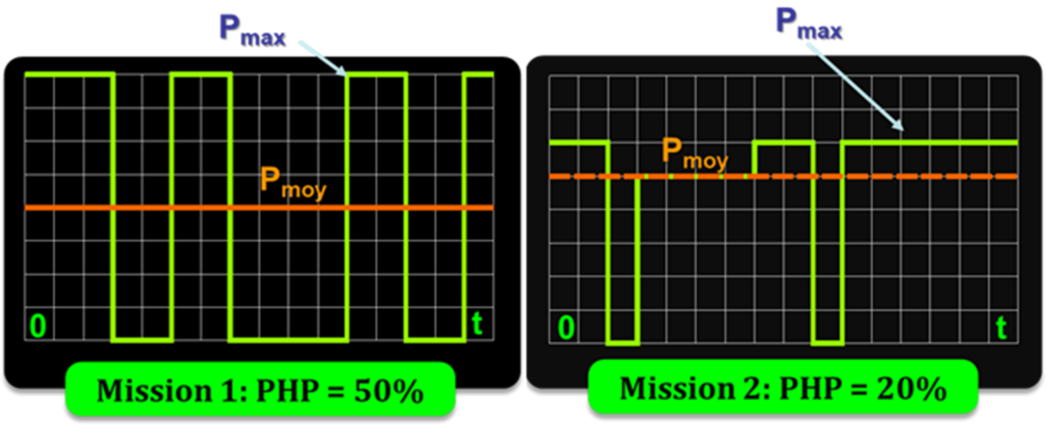

Fig. I-10: Example of different PHP missions.

In this example, P_{mean} and P_{max} are respectively the mean and the maximal power values of the profile missions. In the first case, the PHP value is higher than for the second mission. In deed, the maximal power represents the double of the mean power whereas the maximal power in mission 2 is just slightly higher than the mean one (20% higher): this difference causes the distinct PHP values. The higher the PHP the easier to undersize the primary source power to optimize its integration.

- The Energy Hybridization Potential (EHP) assesses the frequency and the regularity of mission intermittence.

$$EHP = 1 - \frac{max(P_{primary_{source}})}{E_u} \tag{I-2}$$

In the following figure Fig. I-11, the E_u represents the required (useful) energy for each profile mission. The two missions have both the same mean and maximal power. Consequently, they have the same PHP values but with distinct EHP. The required energy for the first mission is more important than the second one, so the energy design (for example in a storage device) will be bigger for the first mission than for the second one. If the source to be designed is a fuel cell, that could be matched by a more important dihydrogen mass (H_2).

The higher the EHP the easier to face the mission in terms of energy.

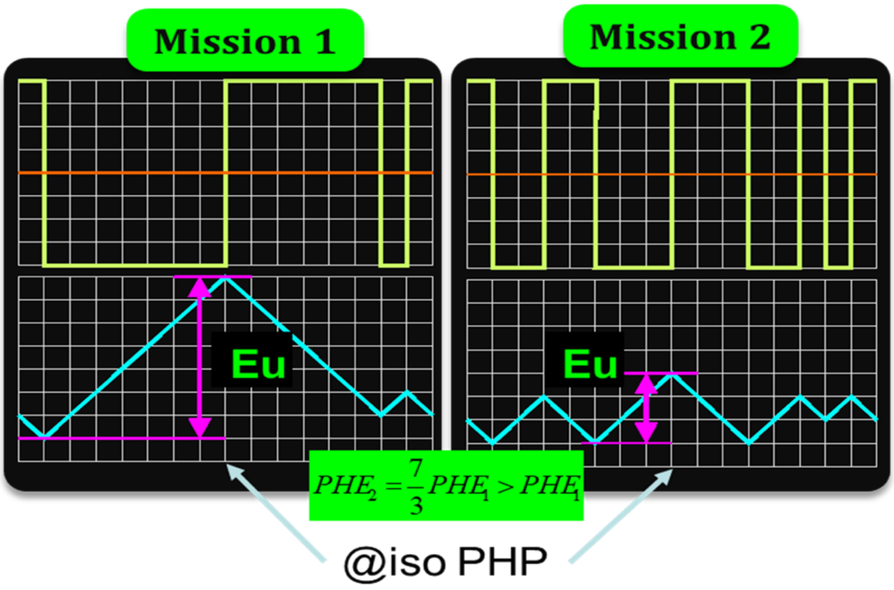

Fig. I-11: Example of two same-PHP value missions with different EHP values.

These indicators permit to evaluate the difficulty of power (PHP) energy (EHP) design. The following figure shows a comparison of different energy storage in the Ragone plan:

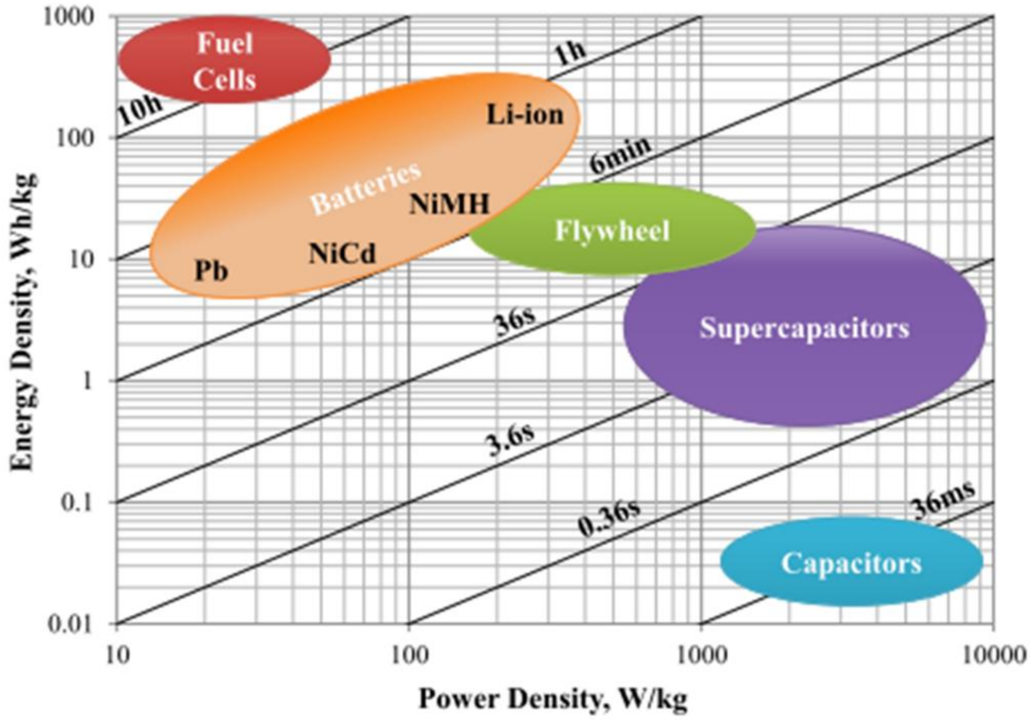

Fig. I-12: Ragone Plan – electric energy storage comparison (specific energy and specific power).

Black lines represent the required discharge/charge time of the different energy storages: low times (high frequencies) are at the bottom right while the low frequencies are on the left top corner. In the aeronautic case, typical profile missions are few intermittent high energy and rather simples, composed of steps of power for the flight phases. It explains that very low PHP and EHP values are assessed compared to other means of transportation (automotive, train, maritime…).

Table I-2: Profile mission comparison (Source: J. Th PhD Thesis[12]*).*

	Car				Train		Ship		Aircraft
	Urban	Rural road	Motorway 150km/h	Local service	Switching	Urban transport	Container	Ro/Ro ferry	Regional 200nm
PHP (%)	94	85	74	65	83	91	43	63	33
EHP (mHz)	66	30	12	3	29	20	n/a	n/a	0.22

The aircraft complexity is partly located in the multitude of interactions between different fields: lift, drag, wing, propulsive system, thrust… as illustrated on the following schematic diagram:

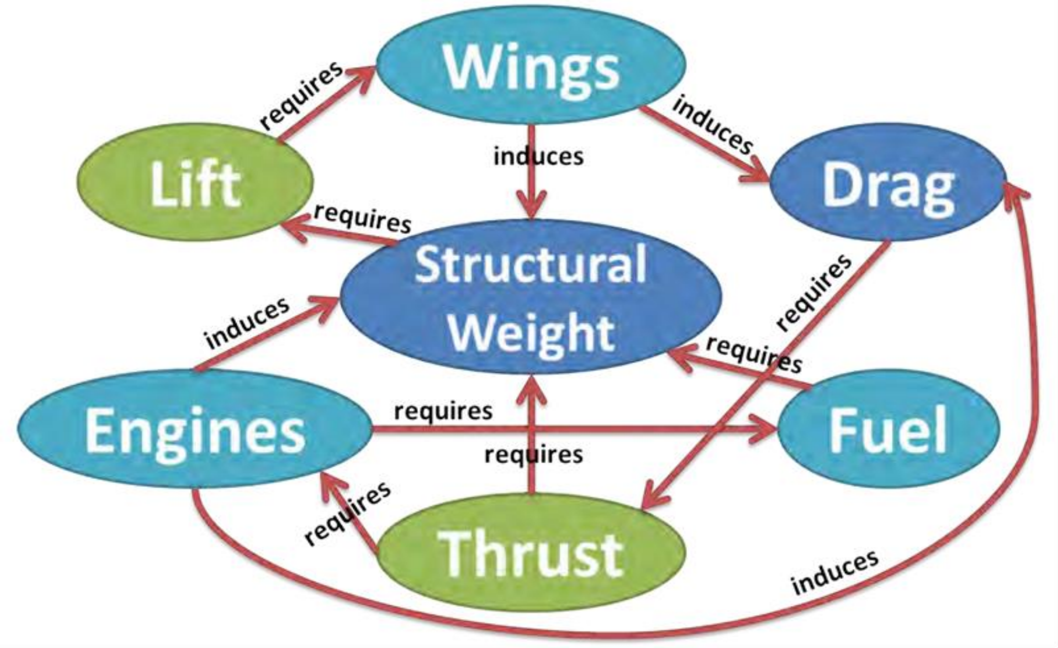

Fig. I-13: Interactions during a complete aircraft design (Source: J. Th PhD Thesis [12]*).*

A complete aircraft design is thus complex because of its high number of decision variables and its high discipline interactions. A systemic study takes into account all (whenever possible) disciplines, and not just components alone. The discrete sum of local optimal solutions rarely leads to the optimal solution of the whole system. It is within this framework that MultiDisciplinary Optimization (MDO) is working because it allows to gather different fields around a single mathematical problem. The complete design of future aircrafts is based on a triptych:

- Optimal turboshaft designs considering good performance and fuel burn.
- Performant aircraft aerodynamics.
- Energy management of different mission profiles.

Using the MultiDisciplinary Optimization (MDO) can determine indicators in order to find optimal solutions for the future (hybrid-) electric aircrafts.

I.2.2 Turboshaft design gains (performance and fuel burn).

I.2.2.1 Optimal design of gas turbines.

Above all engine manufacturers look at the turbomachine design optimization level from a consumption point of view but aiming also at view of changing fuels (biofuels, hydrogen, etc…). This is the work of a small company called TURBOTECH [15] which develops engines using several types of fuel or with relatively low specific fuel consumption.

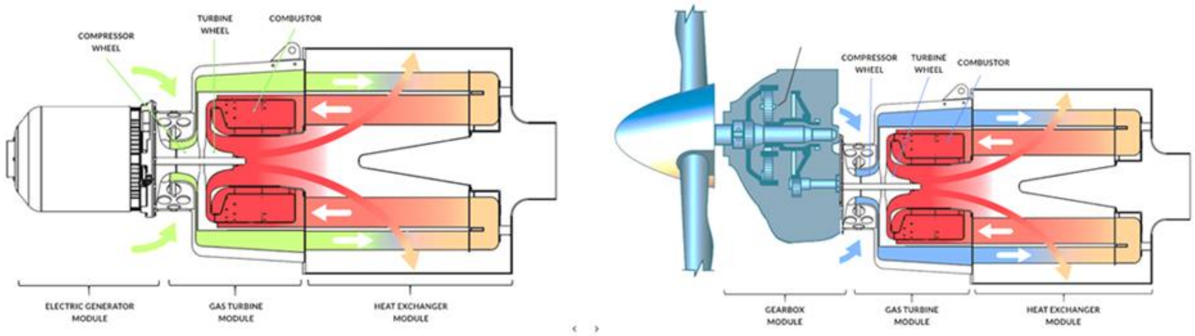

Fig. I-14: Start-up TURBOTECH products: Turbogen and Turboprop.

These products are designed for general aviation and allow important fuel burn gains. Turboprop reduces the noise from the gas turbine, and Turbogen is a module composed of an electric generator and a gas turbine. This product is dedicated to hybrid-electric aircrafts in order to increase their range and their flight time. The principle of the latter is quite simple: the hot exhaust gas is recycled through a heat exchanger and reinjected in the gas turbine. This process is named “regenerative cycle turbine”. This system induces a better efficiency.

I.2.2.2 Intelligent use of gas turbines.

In the Cleansky 2 European project framework a project named RACER [16] deals with hybridization with the aim of optimizing the more electric twin-engine helicopter power. The concept is to develop an economic cruise mode using only one engine at high power to reduce the second engine power (idle mode) for a more efficient mode and consequently save more fuel. An electric motor is used to fast-reactivate the standby turboshaft to meet the needs of high power if required, in the same way as in the automotive sector with the "start and stop" function available in most models.

At this setting, power to one engine is reduced to idle. The other runs at a higher, more efficient setting

Fig. I-15: Racer European project concept and its ecomode presentation.

This project suggests potential fuel consumption gains by hybridizing the propulsive system with an electric motor. Generally, engines are more efficient at a 100% rating power having lower specific fuel consumption (SFC) (Fig. I-16).

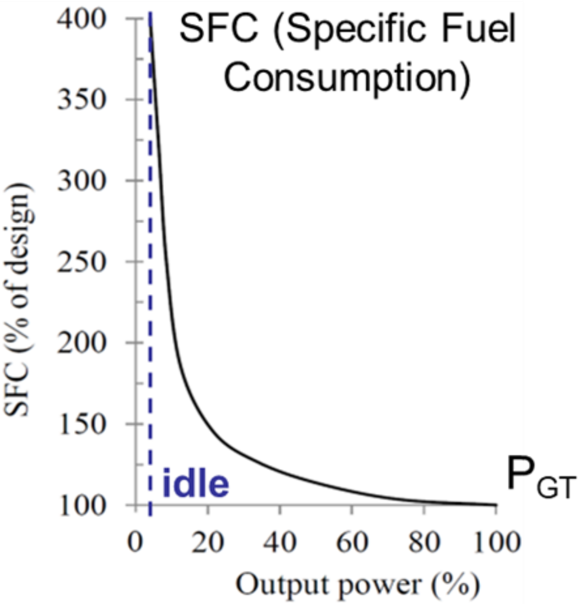

Fig. I-16: Specific fuel consumption of a gas turbine versus the output power rating.

During low power demand flight phases (as for taxiing or descent), the turboshaft fuel consumption strongly increases in a hyperbolic way. That is why hybridization with an electric source can be a solution to save fuel for reduced power ratings. Once the engine is optimally designed, the aircraft structure has to be studied in order to obtain a better aerodynamic performance.

I.2.3 Aerodynamic gains.

I.2.3.1 The distributed propulsion (blown wing).

This configuration has several advantages. The National Aeronautics and Space Administration (NASA) worked on the X-57 concept [17]–[21] since 2014 through the LEAPTECH project (*Leading Edge Asynchronous Propeller TECHnology*). The aim of this study is to improve the aerodynamic performance and the aircraft flight quality with a distributed propulsion thanks to electric motors. The reference aircraft for this study is the TECNAM P2006T, where the wingspan has been changed to incorporate the blown wing concept.

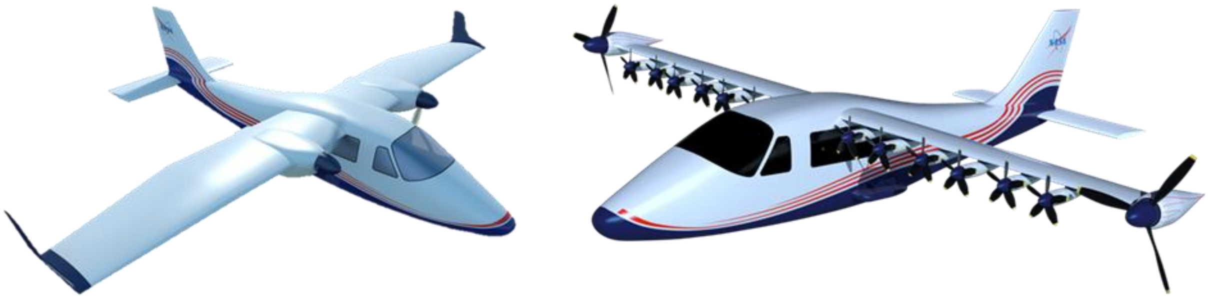

Fig. I-17: Tecnam P2006T (conventional wing) – NASA X-57 Maxwell (distributed powered wing).

- The first benefit of this propulsive system is the blown wing. The aircraft wingspans are sized for an approach speed (low speed performance), so they are oversized for cruise. Dividing the power by using small electric motors at the leading edge of the wing permit to "blow" the latter and consequently to reduce its size. With a reduced wing surface, the wingspan can be designed for cruise improving aerodynamic performance: a benefit of 2.5% in fuel consumption is assessed with only 10% more lift [22].

- In addition to electric motors at the leading edge, electric propellers called "wingtip propellers" are placed at wingtips. These propellers rotate in opposite direction of the vortices created by the wingtips and permit to reduce the drag induced, improving the fuel consumption. The NASA announced a benefit of +18% propulsive efficiency [23] which induces a 13% energy saving [24] thanks to these wingtip propellers. In addition, in this very specific case, distributed propellers along the wing can be retracted in order to let the wingtip propellers propel the plane and to reduce the drag during cruise.

- Another benefit of the distributed propulsion is the differential thrust in failure case: if one electric motor breaks down (among the others), the thrust could be divided on each side to avoid the use of rudder. This is another potential mass gain for future aircrafts.

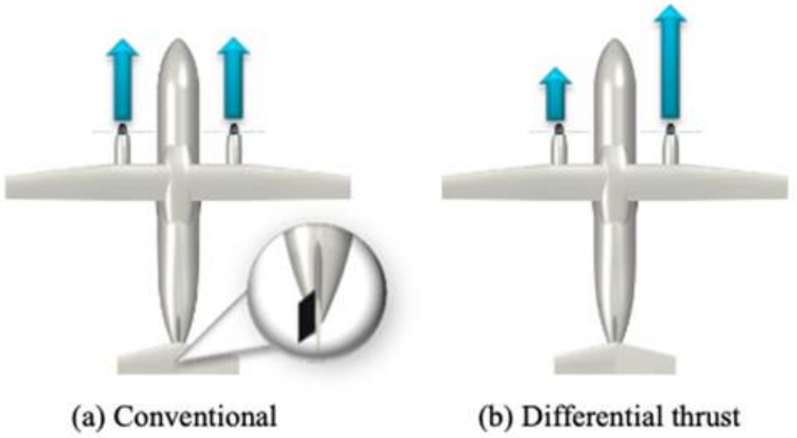

(a) Conventional

(b) Differential thrust

Fig. I-18: Illustration of a yaw control (Source : J. Th PhD Thesis [12]*).*

In the same way, the ONERA (Office National d'Etudes et de Recherche Aérospatiale) works on distributed propulsion with its European project: AMPERE [25], [26]. It is a regional full electric jet able to bring 4 to 6 Pax. This concept plane allows to study the performance of distributed propulsion on aircraft aerodynamics.

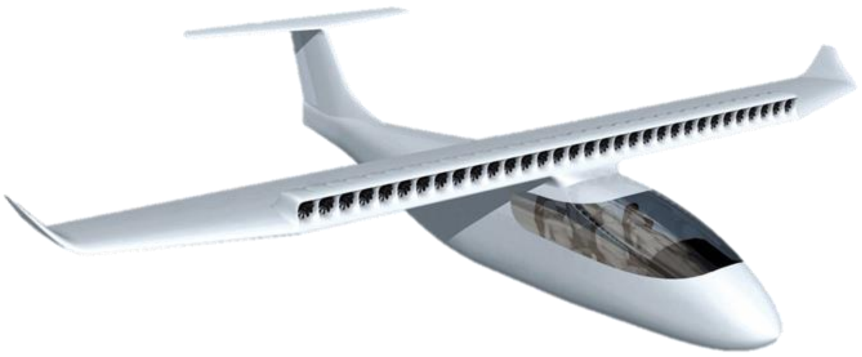

Fig. I-19: AMPERE european project studied by ONERA.

I.2.3.2 The Boundary Layer Ingestion propulsion (BLI).

In the boundary layer the air speed is lower than the aircraft speed. The BLI technique consists in injecting a reduced air flow to correct the output air flow and improve aircraft thrust. This air flow can be injected by a turbofan located at the rear of the fuselage. This principle is used in ship propulsive system. The exact principle is to place the engine downstream of the fuselage to absorb its wake and "reform" it. In Fig. I-20 a lack of air flow is created by the shape of the fuselage marked in blue, while the surplus marked in green is created by the push of the motor. In the case of BLI, the aim is to compensate for the lack of flow by repositioning the motor. The thrust is improved to obtain the same power at the level of the turbofan.

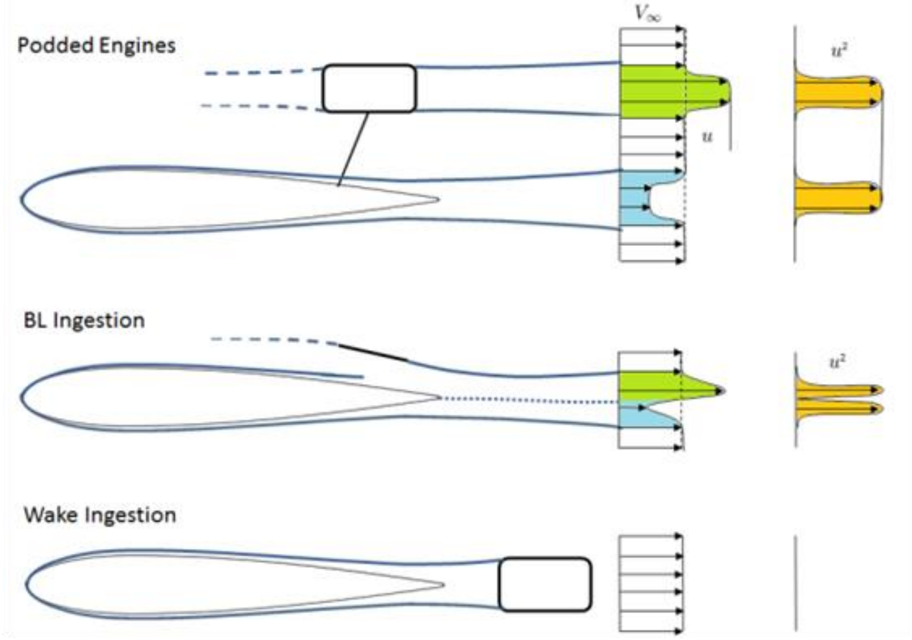

Fig. I-20: Boundary Layer Ingestion Principle (BLI) - Source ONERA [27].

NASA is working on several BLI projects:

- The first one is named Starc-ABL [28]–[32] (Single-aisle Turbo-electric AiRCraft with an Aft Boundary Layer propulsor). The aircraft integrates the BLI concept from a conventional one adding a turbofan at the end of the fuselage. The airplane is a Single aisle with a cruise speed at 0.72 Mach number at 37 000 altitude feet. The propulsion is carried out by a partially turboelectric propulsive system. Conventional turbofans are classically used under wings which are coupled through an electric generator which feeds the BLI electric propulsor at the fuselage rear.

- In the same way, the N3X concept [33]–[36] is another NASA study. The aircraft uses the BLI concept with an optimal fuselage in the wing shape (wing body). This geometric shape helps to reduce the wing length. The difference with the previous one (Starc-ABL) is to anticipate an entry in service of a turbo electric aircraft with optimistic targets in fuel consumption and noise reduction by 2035. There is also another difference in the propulsive system: The N3X concept would use electric supraconductors components to obtain a better and a maximal efficiency.

The fuel saving is between 5% and 12%, it depends of the BLI configuration.

Fig. I-21: Starc-ABL and N3X NASA projects.

On the French side, the ONERA works on the same concept through one European project called DRAGON [37], [38]. This is a partial turboelectric aircraft able to carry 150 Pax with an aircraft speed around 0.8 Mach. The BLI concept is used through gas turbines which supply the distributed electric propulsion under the wings thanks to electric generators. The twin-engines located at the rear of the fuselage help the blown wing generating thrust like turbofans.

Fig. I-22: DRAGON European project studied in ONERA.

I.2.4 Energy gains: how to operate high electric efficiency in a hybrid-electric propulsion?

The electric propulsion holds several benefits:

- Low or null emissions potential during flight.
- Reduced aircraft noise potential.
- New profile mission available for the aircraft.
- Improvement of aerodynamic performance by possible distributed propulsion.

There exist 3 levels of advancement from the more electic aircraft to the full electric one:

1. The turbo electric propulsion (propulsion made by electric motors but with a unique thermal source involving turboshafts which switche on electric generators to produce the whole electrical power).
2. The hybrid-electric propulsion (the system is supplied by two different sources: an electric one involving batteries or fuel cells and a thermal one through gas turbines).
3. The full electric propulsion (aircraft propelled by batteries or fuel cells).

Hybridization ratio in energy and power can be used and permit to locate the propulsive system at these technological advancement levels.

$$H_p = \frac{P_{ELEC}}{P_{TOT}} \ \ and\ H_E \ = \frac{E_{ELEC}}{E_{TOT}} \tag{I-3}$$

In a hybrid electric solution P_{ELEC} represents the maximal value of power during which the propulsive system is supplied by the electric source, while P_{TOT} is the maximal power designed by the total propulsive system. In terms of energy, $\mathrm{E_{ELEC}}$ is the energy profile mission covered by the electric source while E_{TOT} is the total energy mission. It is possible to list the following propulsive systems with these previous indicators.

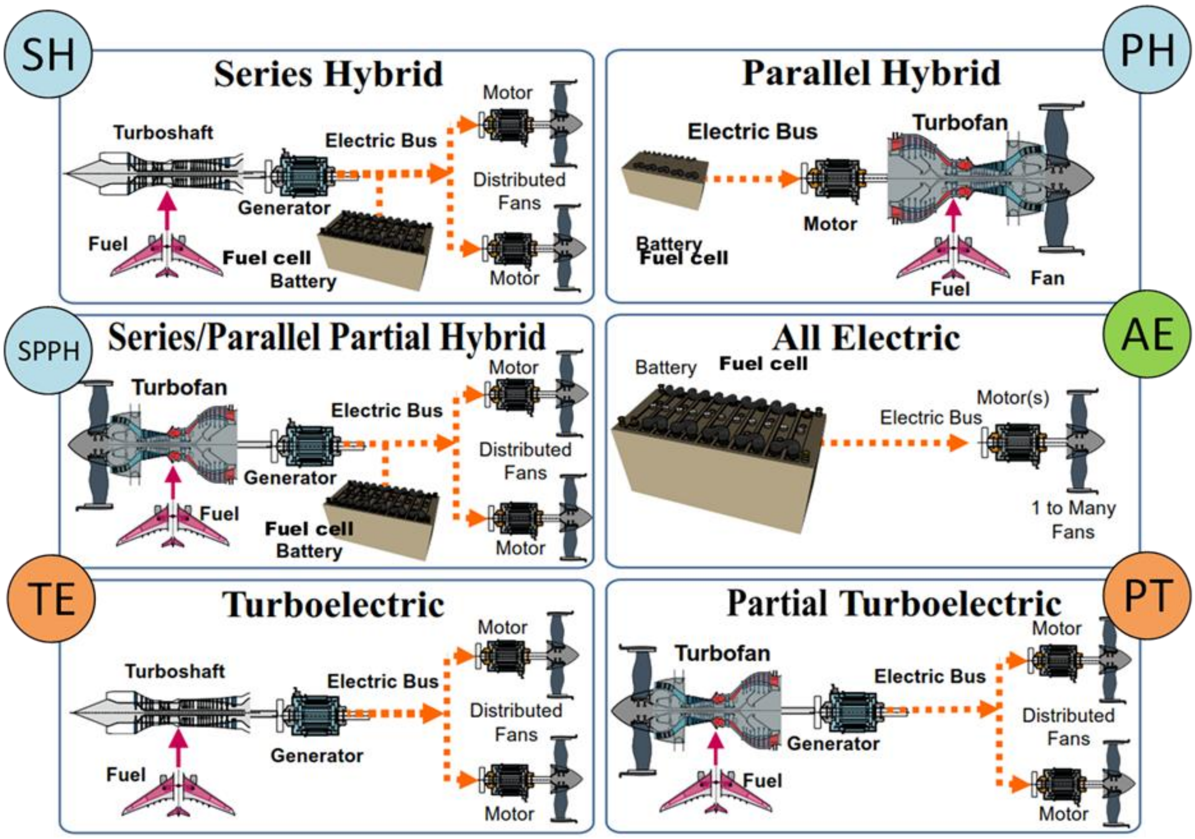

Fig. I-23: Hybrid-electric propulsive system state of the art (NASA [29]).

Table I-3: Listing of hybrid-electric propulsive system thanks to energy and power ratio.

Propulsive system	H_P	H_E
Parallel hybrid (PH)	< 1	< 1
Series/Parallel Partial Hybrid (SPPH)	< 1	< 1
Partial Turboelectric (PT)	< 1	0
Turboelectric (TE)	1	0
Series Hybrid (SH)	1	< 1
All electric (AE)	1	1

I.2.4.1 Parallel hybrid electric propulsive system (PH).

With a parallel hybrid electric propulsion design, the thermal conventional motor is relieved by the electric motor which takes over in high fuel consumption demand phases. This is exactly the same system as in automotive, especially in parallel hybrid electric buses: the electric motor is configured to operate at low speed and high torque. Given these frequency phases and the low power required, the electric motor and its power supply system (battery / power electronics) is light and not very bulky: it is not restrictive. In aeronautics, weights and volumes are problematic with snowball effects: since a more powerful propulsion system is heavier the aircraft’s MTOW is impacted.

I.2.4.1.1 UTC Bombardier Dash 8-100 (hybrid-electric).

United Technologies Advanced Projects (UTAP), a subsidiary of the American leader in aeronautical equipment in 2017 (UTC Aerospace), has embarked on the electrification of aircraft by redeveloping the propulsion system of a 78 Pax aircraft [39]: Bombardier Dash 8-100. The power range of the current propulsive system is about 2 megawatts, the project consists in undersizing the gas turbine by about 1 MW (optimal cruise power) with an additional 1MW-electric propulsion (e-motor and batteries) to complement the 2MW take off power. In this case, the electric source assists the thermal engine during the phases of high-power demand (take-off and climb). According to the Original Equipement Manufacturer (OEM), the fuel economy on a one-hour mission should be around 30%. Both motors (thermal and electric) are mechanically connected by a reduction gearbox (cf Fig. I-24) which is designed to adapt the rotational speed between propellers, eMotors and engines. The advantage of this topology is its simplicity: The electric motor is easy to install in a conventional propulsion system, mechanically coupled to the gas turbine. This is a short-term solution; indeed, the design power of the electric devices is reduced.

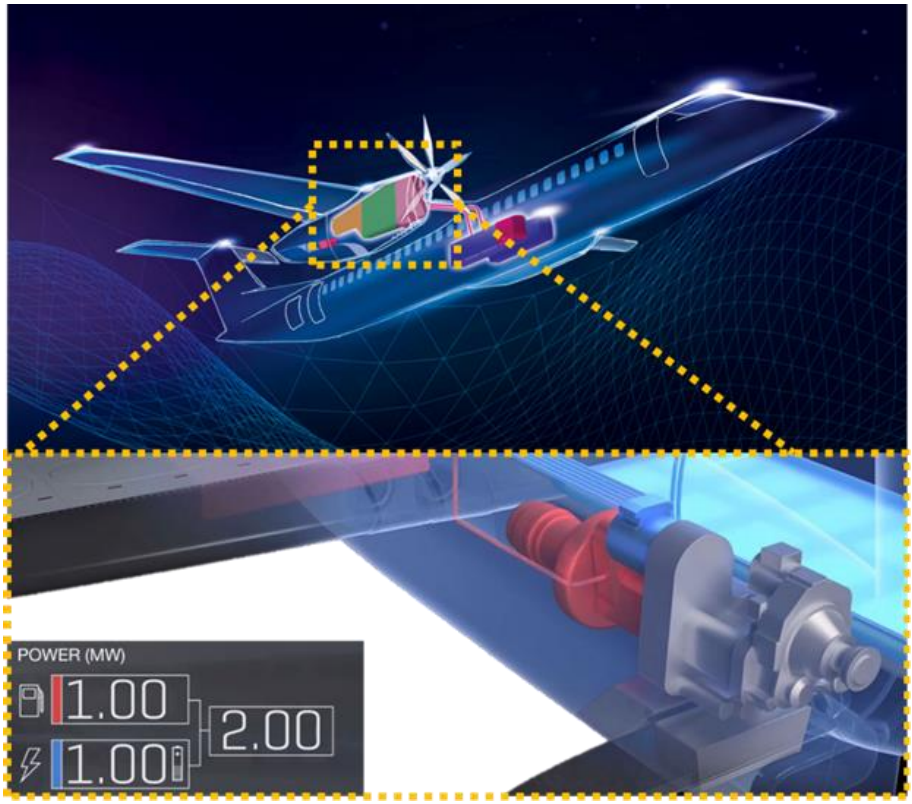

Fig. I-24: 804 Project - UTAP parallel hybrid-electric propulsion system.

I.2.4.1.2 Ampaire Electric EEL.

Still in the USA, a start-up called AMPAIRE has already flown a prototype hybrid-electric parallel aircraft, in June 2019 at the Camarillo airport in California. This was the first flight of a hybrid-electric powered aircraft. The prototype comes from a conventional aircraft (the Cessna 337 Skymaster) [40], whose propulsive system is hybridized with an electric motor and battery system that optimizes fuel consumption in parallel with the conventional combustion engine.

Fig. I-25: Ampaire Electric EEL.

I.2.4.2 Propulsion Series/Parallel Partial Hybrid (SPPH).

Compared to the parallel hybrid system, this partial serial/parallel hybrid electric propulsion system consists of a turboshaft engine that partly drives an electric generator powering electric motors distributed along the wing of the aircraft and coupled to batteries. The thrust of the aircraft is generated by electric and thermal engines.

I.2.4.2.1 Eco-Pulse Project

A collaborative project with SAFRAN, AIRBUS and DAHER named Eco-Pulse project [41] aims to develop an aircraft with this specific propulsive system.

Fig. I-26: Eco-Pulse project (Series/Parallel Partial Hybrid).

Propulsion is divided between the turboprop (single engine in the middle) and the electric motor on the wings. The aircraft can carry 6 Pax with a total power of 600 kW. The main idea of this architecture is to provide take-off and landing in fully electric mode and to use the thermal part for the low fuel consumption phase: cruising. The first flight of this aircraft is planned for 2022.

I.2.4.2.2 Voltaéro – Cassio

A French start-up named VOLTAERO [42] is also in the race for hybrid-electric propulsion and has chosen a partial series/parallel hybrid-electric propulsion system. This small company is the continuity of the AIRBUS E-fan as its founders are the main protagonists responsible for the all-electric two-seater program in 2011. The available power of the aircraft is about 440 kW and the airplane should carry 4 to 9 Pax. As before, the objective of this study is to combine the advantages of electric propulsion with those of conventional propulsion. Two 60-kW electric motors are placed at the front of the plane and will be used during take off and climb, powered by batteries. The 170-kW combustion engine will drive 3 electric generators to recharge the batteries and propel the aircraft during the cruise phase. The original plane is the same as for the start-up AMPAIRE: Cessna 337 Skymaster.

Fig. I-27: VOLTAERO Cassion hybrid-electric aircraft.

I.2.4.3 Partial Turbo electric propulsive system (PT).

The only benefit of this propulsion system is the improved aerodynamics of the aircraft. The partial turbo-electric propulsion combines conventional and electric propulsion: the aim is to use the compactness and additional degrees of freedom offered by electric devices to improve the air flow around the airplane. The Starc-ABL (Fig. I-21) and the DRAGON project (cf Fig. I-22) are good examples of this propulsive system. It is a first step towards the turboelectric aircraft.

I.2.4.4 Turbo Electric propulsive system (TE).

This time, the complete propulsion is electric (not to mention sources). The goal is once again to use electric motors to improve the aircraft aerodynamics. Another example is the Aurora Lightning Strike which is a Vertical Take Off and Landing aircraft (VTOL). This is a new and growing market where hybrid-electric and fully electric propulsion will be used.

Fig. I-28: VTOL Aurora Lightning Strike.

The path to the all- electric aircraft is not easy and a series hybrid-electric architecture will be more interesting to study in order to anticipate the future technologies.

I.2.4.5 Series Hybrid propulsive system (SH).

A series hybrid electric propulsion system (see Fig. I-23) is composed of gas turbines as main energy sources that drive electric generators This architecture is also powered by auxiliary electric sources consisting of batteries or fuel cells.

In such powertrain, generators may be directly coupled to electric propulsion with an AC architecture. Another optionconsists in coupling generators to a DC distribution through voltage rectifiers. Depending on the power range, a ultra-high voltage (uHVDC – beyond the conventional voltage of ± $270V$) standard can be involved in the Electric Power Distribution Unit (EPDU): this option is studied in our thesis involved in the HASTECS project presented latter in this chapter. This power distribution unit supplies electric motors by inverters that drive propellers through a gearbox. Several ambitious projects are being studied all over the world:

I.2.4.5.1 E-Fan X collaborative project

This European project brings together major companies such as AIRBUS, ROLLS-ROYCE and SIEMENS to design a hybrid propulsion system in a regional aircraft the BAE 146. This aircraft is equipped with 4 turbofan engines and the consortium’s project foresees the replacement of one gas turbine by an electric motor. The replaced gas turbine is located in the fuselage and is coupled to a 2 MW electric generator to build a series hybrid propulsion system. A 2 MW battery pack is also installed at the rear of the fuselage to study the hybrid mode.

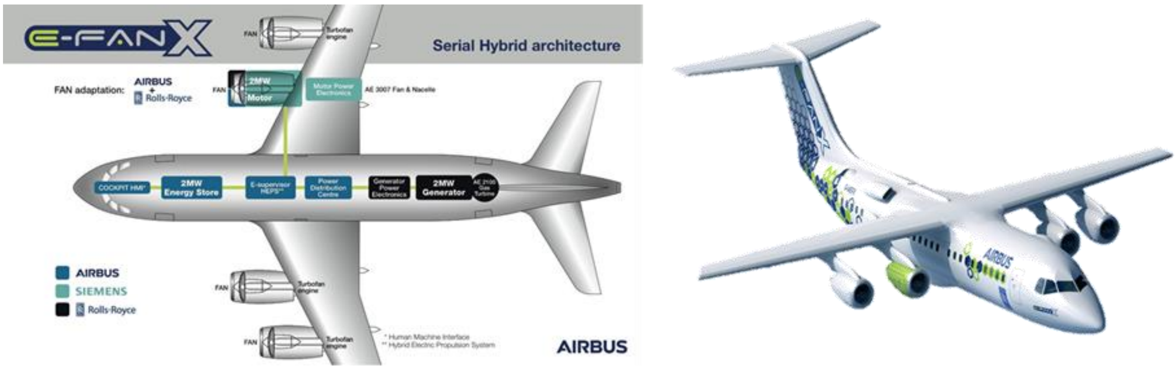

Fig. I-29: E-fan X description and its propulsive system [43].

The objective is to anticipate the arrival of the all-electric aircraft. This “flying laboratory” aims at exploring the challenges of high-power propulsion systems to enable a less polluting commercial flight (thermal effects, electric thrust management, altitude and dynamic effects on electrical systems…).

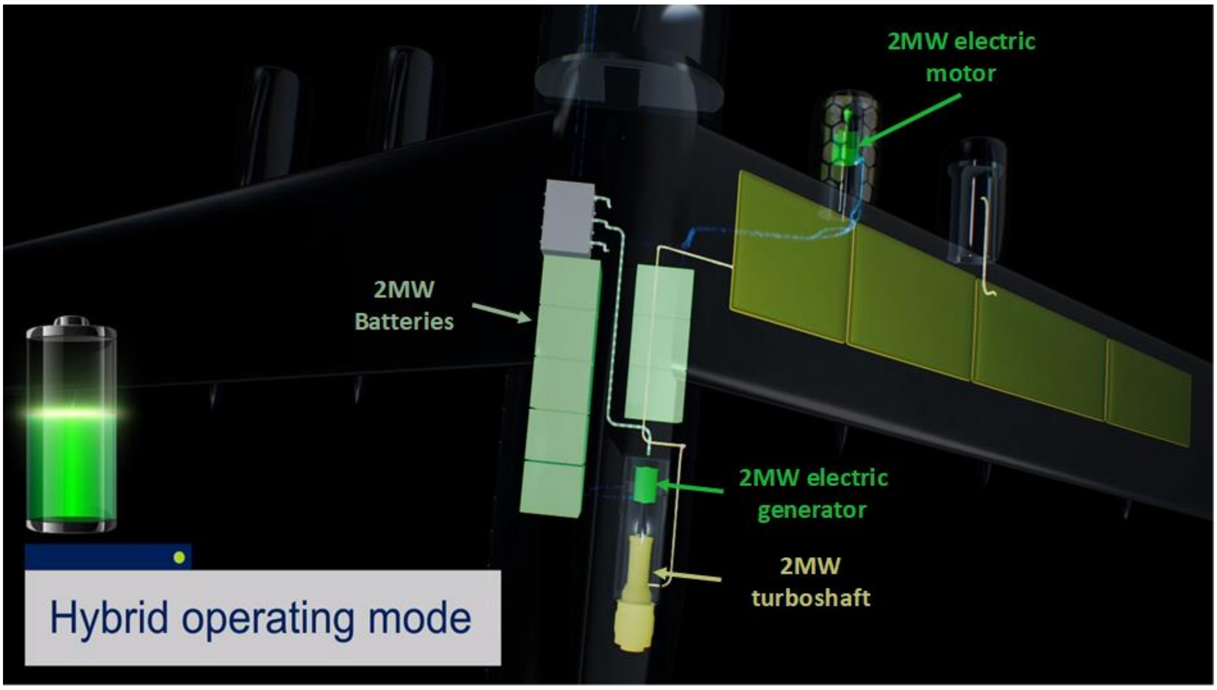

Fig. I-30: E-fan X architecture description.

Despite the great compactness of electric motors (green) compared to turboshafts (yellow), the main challenge of the more electric aircraft remains the electric source and the powertrain. In this case (See Fig. I-30Fig. I-22) the batteries (light green “cabinets”) are sized at 2 MW. The biggest challenge of electric propulsion is the compactness and the weight of the electric devices, especially the energy sources.

I.2.4.5.2 Zunum Aéro.

For this American start-up, the aircraft sizing is more reduced. The company supported by Boeing is considering a family of hybrid-electric regional aircrafts. The first element of this family is the ZA10 able to carry 10 Pax operating over a distance of 600 nm range. The concept of the aircraft is based on the use of an either all-electric or hybrid-electric mode to extend the flight mission. In this case the gas turbine will be used in the cruise phase.

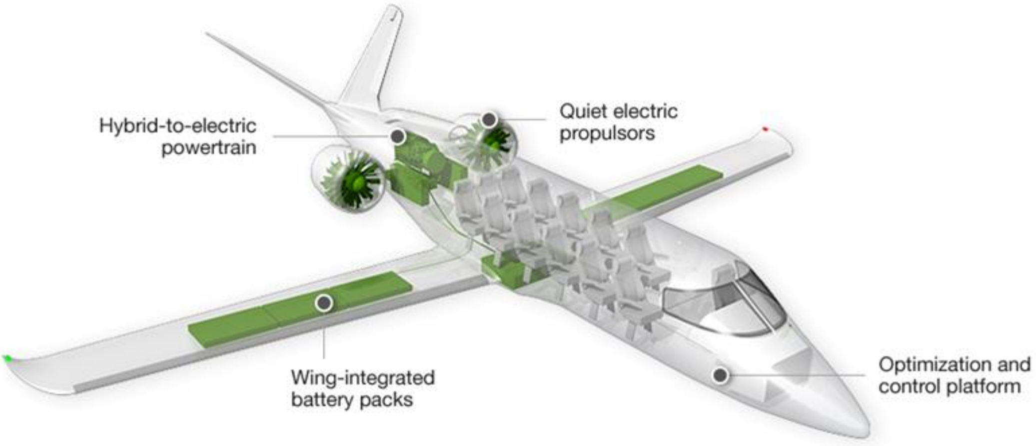

Fig. I-31: ZA10 description concept [44].

In this aircraft a partnership with SAFRAN has been signed and a 500-kW helicopter gas turbine will be the thermal source for hybrid-electric ZA 10.

I.2.4.5.3 Bell NEXUS.

Once again, the hybrid electric propulsion concept can be applied to VTOL and STOL (Vertical & Short Take-Off and Landing aircraft). The Bell NEXUS concept is a hybrid-electric air taxi using a series hybrid-electric propulsion. A thermal source will power a distribution core through electric generators, in the same way as a battery pack. Hybridization is necessary to extend the range of these aircrafts.

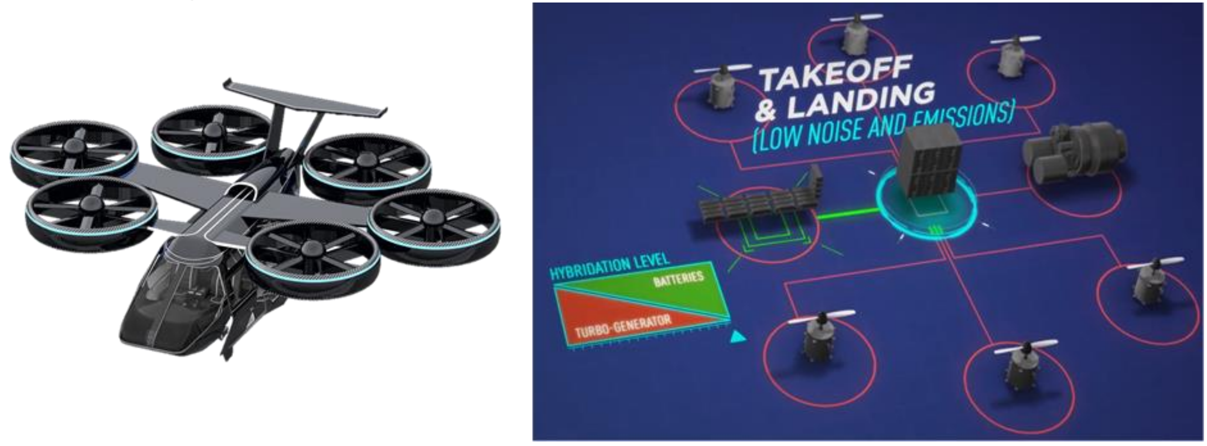

Fig. I-32: VTOL Bell NEXUS propulsive system description from SAFRAN [45].

I.2.4.6 All-electric propulsion (AE).

There is still a long way to go before flying an all-electric drive. The major problem with electrification is energy storage, but the study of small aircrafts is still ongoing. Since 2010, (with the Cricri [46]) commercial aviation has been eager to see electric flights in order to obtain more efficient and lighter propulsion systems to integrate them in heavy / powerful aircraft.

Fig. I-33: Airbus E-fan [46], [47] *and Siemens Extra 330LE all electric aircraft.*

In 2017, the Siemens has propelled the aerobatic plane Extra 330 flying at more than 340 km/h [48], thanks to an electric motor. The specific power of this electric motor exceeds 5 kW/kg. This is a world record for a plane weigthing more than one ton. Beyond these exceptional exploits, a newborn Israeli aviation company, Eviation, is working on another all-electric aircraft. The start-up presented its e-aircraft Alice at the Paris Air Show in 2019. The airplane plans to carry 9 Pax thanks to an all-electric propulsive system of 800 kW. The electric source is composed of Lithium-Ion batteries (Li-Ion) and 95% of the fuselage is made of composite.

Fig. I-34: Eviation Alice (Paris Air Show 2019).

Two electric motors have been chosen by the company: the SP-260D Siemens e-motor [48] and the Magni250 magniX e-motor with a power of about 250 kW each. The first one is a radial electric motor while the other is an axial flux electric motor. The choice of the electric motor is essential in an all-electric drive; it is the most important electrical component to design. A new record has been set by the all-electric hydroplane company powered by the magniX company: HARBOUR AIR which made its first commercial electric flight the 10 December 2019.

Fig. I-35: Successful Flight of World's First Commercial Electric Airplane (Harbour Air – magniX [49]–[51]*).*

Another axial flux electric motor vas chosen by Rolls-Royce with its all-electric aerobatic plane project. The name of the project is: ACCEL [52], [53], the propulsive system is composed of three Yasa 750R e-motors [54] in order to approach the 750-kW maximum required power.

Fig. I-36: ACCEL project (Rolls-Royce).

The aim of the study is clear as Rolls-Royce industry wants to reach a speed of 480 km/h. Owing to this speed the airplane will be the fastest all-electric plane in history. Rolls-Royce is joining the electric race by working on the all-electric propulsion system thanks to electric motor specialists such as Yasa motors.

Fig. I-37: CityAirbus [55].

Alongside these new generations of aircrafts, the VTOL and STOL aircraft are in also the all-electric race. The European aircraft manufacturer is working on the CityAirbus, a four-seater multi-copter vehicle. The prototype is currently undergoing a flight test period. The power of the aircraft is about 800 kW powered by Lithium-Ion batteries. The VTOL and STOL market is growing rapidly: the aircraft manufacturer wants to relieve road traffic congestion and make it more fluid.

I.2.5 Towards greener aircrafts: hydrogen power, a huge challenge that seems reachable

So far, most hybrid electric aircraft are battery-powered, but hydrogen with ICE or fuel cells should not be overlooked. The subsidiary H3 Dynamics (HES Energy systems) announced in 2018 the first regional aircraft powered a 100% by hydrogen: Element One. The evolution is logical: The Singaporean company has been working for 10 years on a hydrogen drone. The aircraft could carry four Pax over distances between 500 and 5,000 km depending on storage (liquid or compressed).

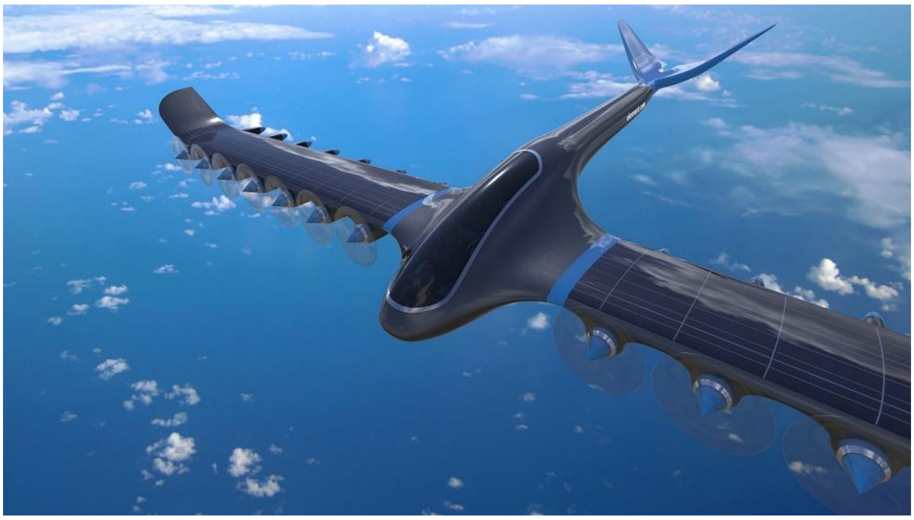

Fig. I-38: Element One (Hydrogen powered aircraft).

A promising American start-up, ZeroAvia, has the same objective: to get a hydrogen-powered plane off the ground. The ambition is greater than the previous one as the plane will carry 6 to 20 passengers on journeys of up to 500 miles. The goal of the Californian company is to change the conventional propulsion system to use a hydrogen-powered plane. Several flight tests are underway on regional aircrafts.

Fig. I-39: Hydrogen aviation vision by ZeroAvia.

Hydrogen seems to be the most promising energy vector in aeronautics thanks to its specific energy. Compared to batteries, the specific energy, recharging time and recycling are better arguments in favour of the fuel cell and its hydrogen storage. But the technological maturity of fuel cells and hydrogen storage is not as developed as that of batteries. This is why batteries are still more used in electrical applications. The American aerospace agency NASA is interested in carbon-free power sources: a project has been launched with the idea of a plane powered by liquid hydrogen. [56].

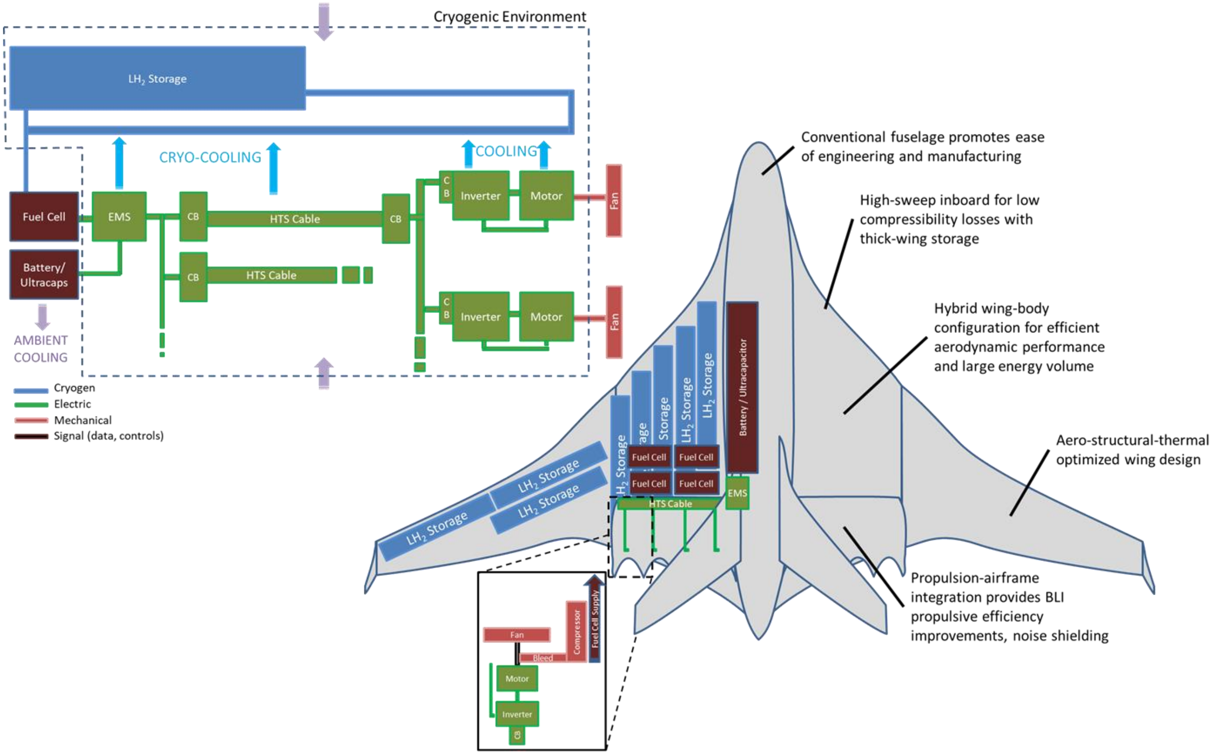

Fig. I-40: Cryogenic hydrogen powered aircraft NASA project.

The liquid hydrogen storage is more efficient than pressured one. The only disadvantage is the very low operating temperature (20 K degrees). The storage of liquid hydrogen is more efficient (15% compacity) than storing hydrogen under pressure (5% compacity). The objective of this study is to use the cryogenic cooling of hydrogen to cool the other electrical components. The cooling of superconducting electrical components allows better performance (low losses) on the electrical conversion chain.

An initial awareness of the climate emergency that has been growing since the end of 2019.With the advent of the Covid19 pandemic, the entire trajectory of global aviation has been called into question. The lockdown measures taken by various governments around the world have caused air traffic drop in particular in Europe the air traffic fell by 88% [2], [3] (see Fig. I-41).

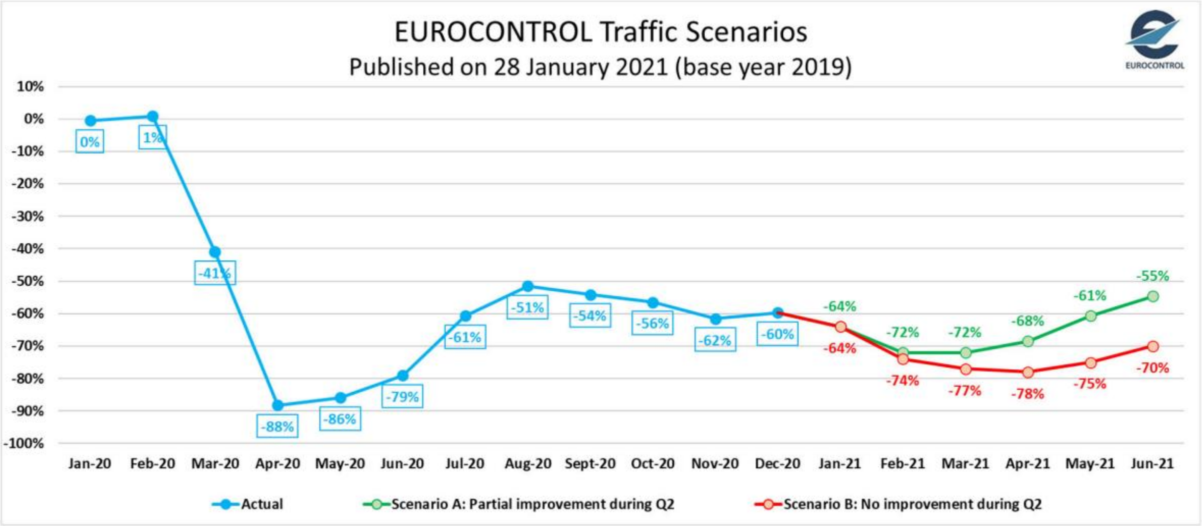

Fig. I-41: EUROCONTROL draft Traffic scenarios (European aviation).

The entire aviation industry is concerned about these numbers. The lack of coordination between states and the lack of confidence on the part of passengers do not help the scenario. The decline in air activity may be a sign of economic crisis, but it is a positive for the planet. This could be an opportunity for the aviation industry to adapt its most polluting practices in order to maintain the reduction in CO2 emissions that is essential to achieve the objectives of the Paris Agreements.

In 2020, the European Union (EU) announced its Clean Hydrogen Plan [57], European Member States put hydrogen at the top of their investment priorities as part of the post-Covid-19 economic recovery. In particular, France and Germany have planned to devote 7 and 9 billion euros respectively of public funds in the hydrogen industry. The systemic approach is the one that has been favoured and which directs consciences towards hydrogen. Electricity networks are not capable of supporting the battery-powered electricity revolution; it is necessary to be able to store the excess energy at sometimes of the year so that it can be reused later on at times when the energy demand is greater than the production.

About aviation, hydrogen feasibility study, made by Clean Sky 2 and Fuel Cells & Hydrogen 2 Joint Undertakings has been realized and presented in June 2020 [58]. "*Hydrogen as an energy source will play a key role in transforming aviation into a zero-carbon / climate-neutral system over the next few decades.*" According to the study if several scenarios are studied, hydrogen seems to be the main actor (burned in turbines, or used through fuel cells). It would be feasible to propel airplanes for regional distances using fuel cells (see Fig. I-42 and Fig. I-43).

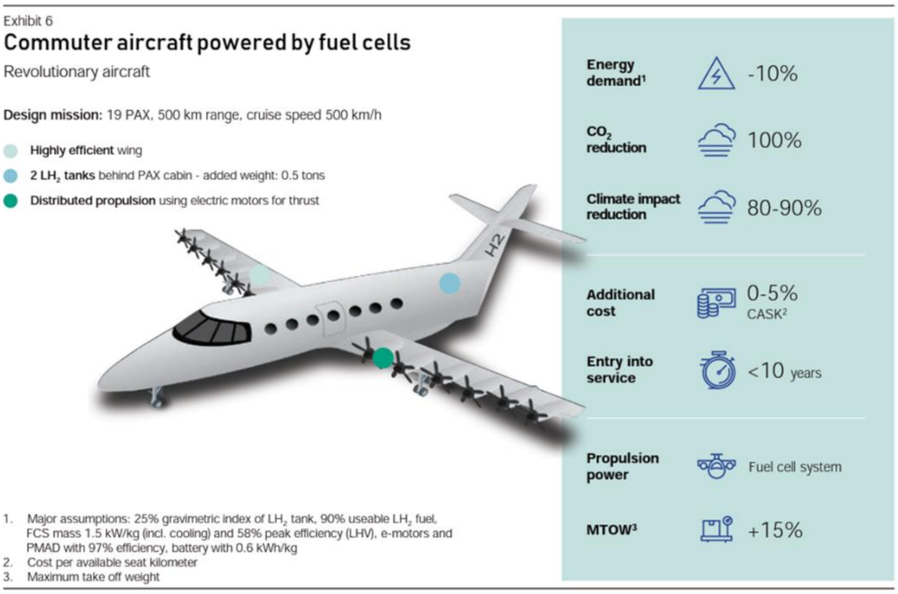

Exhibit 6

Commuter aircraft powered by fuel cells

Revolutionary aircraft

Design mission: 19 PAX, 500 km range, cruise speed 500 km/h

- **Highly efficient** wing
- **2 LH_2 tanks** behind PAX cabin - added weight: 0.5 tons
- **Distributed propulsion** using electric motors for thrust

Energy demand[1]	-10%
CO_2 reduction	100%
Climate impact reduction	80-90%
Additional cost	0-5% CASK[2]
Entry into service	<10 years
Propulsion power	Fuel cell system
MTOW[3]	+15%

1. Major assumptions: 25% gravimetric index of LH_2 tank, 90% useable LH_2 fuel, FCS mass 1.5 kW/kg (incl. cooling) and 58% peak efficiency (LHV), e-motors and PMAD with 97% efficiency, battery with 0.6 kWh/kg
2. Cost per available seat kilometer
3. Maximum take off weight

Fig. I-42: Commuter aircraft powered by fuel cells.

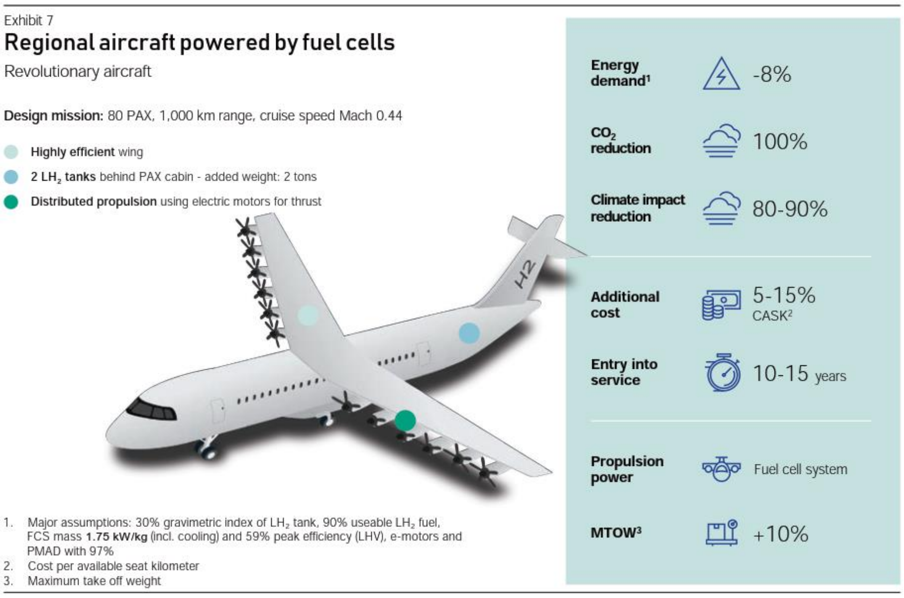
Exhibit 7

Regional aircraft powered by fuel cells

Revolutionary aircraft

Design mission: 80 PAX, 1,000 km range, cruise speed Mach 0.44

- ● **Highly efficient** wing
- ● **2 LH_2 tanks** behind PAX cabin - added weight: 2 tons
- ● **Distributed propulsion** using electric motors for thrust

Energy demand[1]	-8%
CO_2 reduction	100%
Climate impact reduction	80-90%
Additional cost	5-15% CASK[2]
Entry into service	10-15 years
Propulsion power	Fuel cell system
MTOW[3]	+10%

1. Major assumptions: 30% gravimetric index of LH_2 tank, 90% useable LH_2 fuel, FCS mass **1.75 kW/kg** (incl. cooling) and 59% peak efficiency (LHV), e-motors and PMAD with 97%
2. Cost per available seat kilometer
3. Maximum take off weight

Fig. I-43: Regional aircraft powered by fuel cells.

In the regional aircraft case, for a reasonable weight gain (+10%), the gains on the environment are considerable (-100% CO_2). The high specific energy of the hydrogen molecule combined with the efficiency of the all-electric propulsion chain saves the energy required to fly the aircraft (-8%). With the assumptions taken by the McKinsey company, hydrogen seems to be a viable solution to propel small aircraft using fuel cells.

European entities are not alone in believing in the hydrogen revolution in aeronautics, several private industries are also betting on. A general aviation project (see Fig. I-44) in Belfort was also unveiled, promising to carry 6 passengers, have a range of 1,500 km and reach a cruising speed of 370 km/hour.

Fig. I-44: Avion Mauboussin fuel cell powered aircraft concept (AlcyonM3c)[59].

Concerning single-aisle aircrafts, three hydrogen-powered aircraft projects (see Fig. I-45) were recently unveiled by the European aircraft manufacturer Airbus.

Fig. I-45: Airbus ZEROe aircraft concepts[60].

- A turboprop aircraft able to carry about 100 Pax with a maximum range of 1000 nm.
- A turbofan aircraft able to carry about 100 Pax with a maximum range of 2000 nm.
- Finally, the most technologically advanced aircraft a blended-wing body which has the same characteristics as the turbofan.

They all use liquid hydrogen storage as an energy source.

In addition to airplanes, the world of VTOL is also looking for a way into hydrogen. The American company Skai, supported by NASA, imagines to bring five passegers in a new electric vertical take-off landing (VTOL) air taxi using a hydrogen fuel cell powertrain.

Fig. I-46: Alaka'i Skai Hydrogen powered VTOL air taxi[61].

The effervescence around hydrogen is palpable, and with aeronautics, all mobility seems to be turning towards this energy vector.

Let's start with the automobile, only a few companies at the moment, such as Toyota has been developing the hydrogen-powered car model since 2015: The Toyota Mirai. A second edition, released very recently[62], significantly improves the vehicle's performance.

Fig. I-47: Toyota Mirai 1 & 2 (hydrogen powered car).

Hopium, the first 100% hydrogen car manufacturer founded by French driver Olivier Lombard, plans to present the first prototype of its "Hopium Māchina" model in 2021. This innovative vehicle [63] with a neutral carbon footprint will offer an exceptional range of 1000km.

Fig. I-48: Hydrogen Motive Company: the Hopium Machina.

Let's continue in the maritime field, with yachts. In October 2020, Hynova Yachts presented the world's first hydrogen-powered yacht [64].

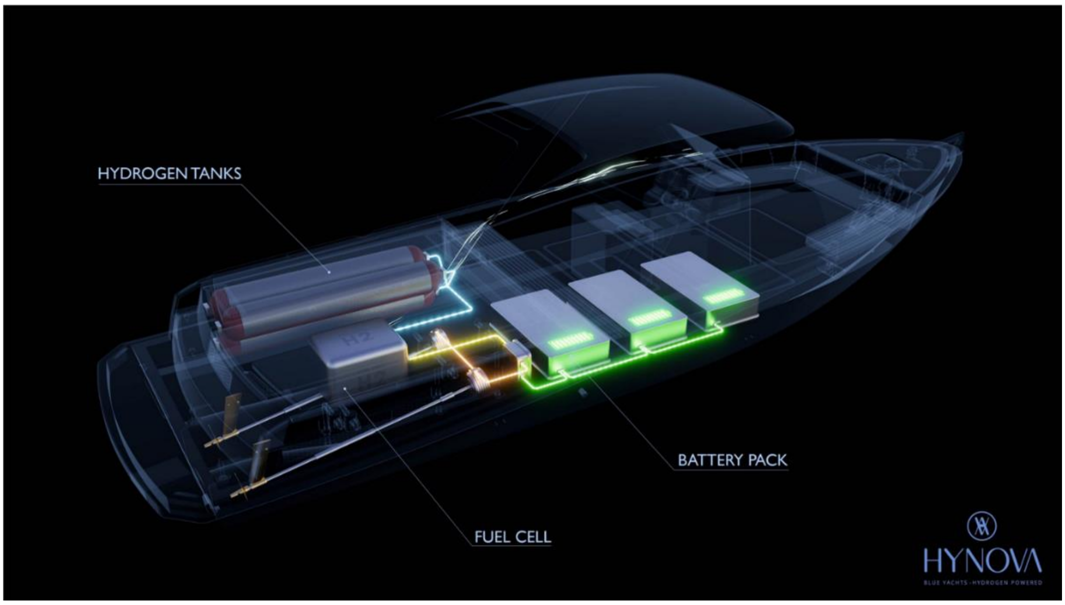

Fig. I-49: Hynova yachts: hydrogen propulsion system

Approximately 12 meters long, the yacht can accommodate up to 12 people and is propelled by an electric motor powered by a fuel cell. There are many other companies that have decided to use hydrogen in their activities.

The difference between these mobilities that require less energy (car, boat, etc...) and aeronautics is the sensitivity to weight, and against this problem fuel cells equipped with a hydrogen tank are much more promising than battery-powered system.

Hybrid-electric aircraft propulsion was beginning to promise us advances on more electric aircraft, but hydrogen brings us the real solution by integrating a real breakthrough technology in our aircraft.

Hydrogen is well on its way to launch the third industrial revolution!

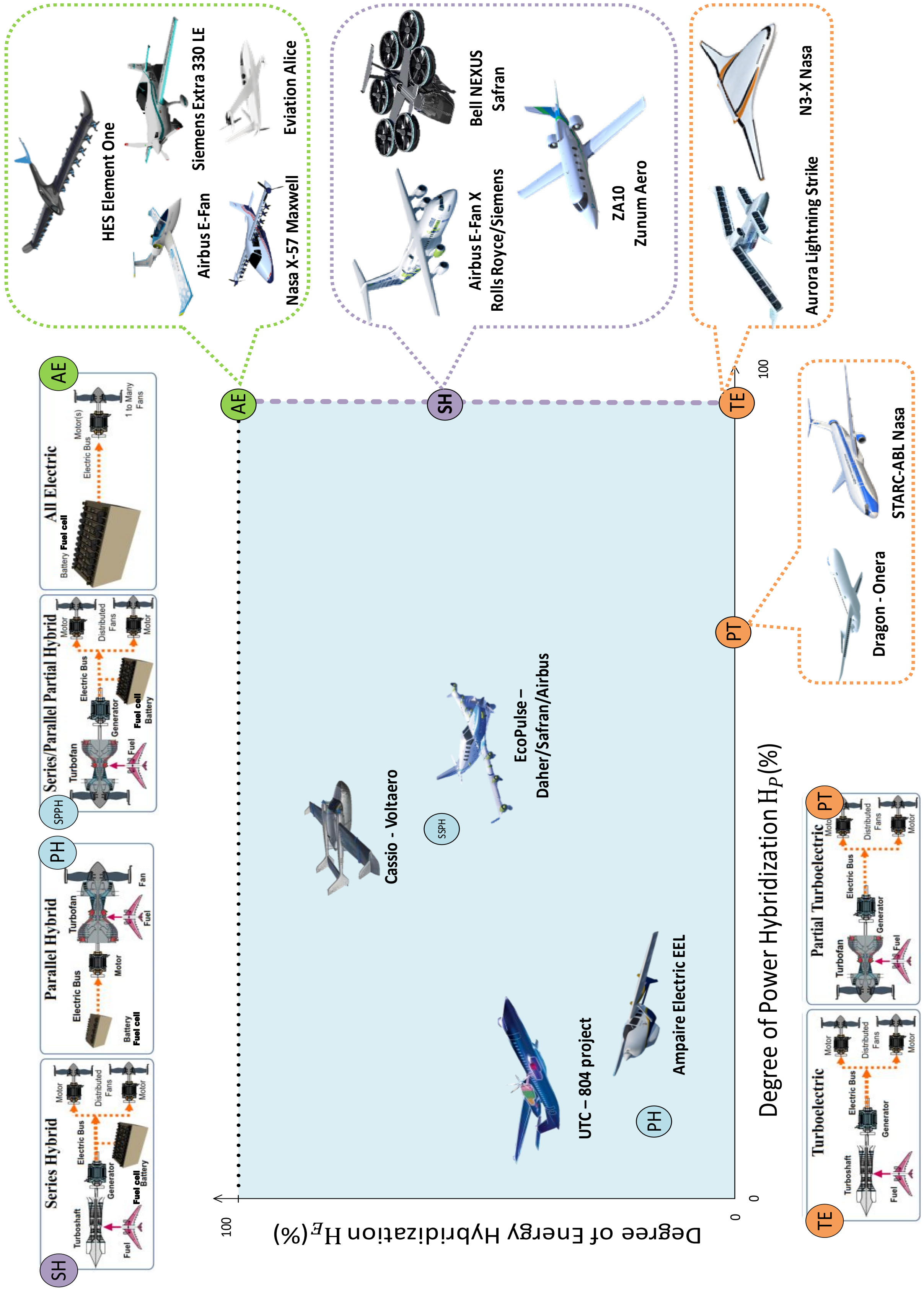

Fig. I-50: Hybrid electric aircraft representation considering hybridization power degree and hybridization energy degree.

I.3 Presentation of the HASTECS Project and thesis objectives.

Some further research is contained in HASTECS, a European project in the framework of CleanSky II HASTECS means: Academic Research on Hybrid Aircraft Thermal and Electrical Components and Systems. The objective of the project is to identify disruptive technologies to significantly improve the specific power and efficiency of electrical components used in hybrid electric aircraft. The stakes are high because, unlike in the automotive, rail or even maritime sectors, the weight of the propulsion system is not the main concern of designers. In aeronautics, weight is the first enemy, which is why objectives have been set within the framework of the project in order to lead the studies with a first level of entry into service in 2025 and a second level of entry into service for 2035. The objectives are as follows:

Table I-4: HASTECS electric component targets.

	2025 target	2035 target
Electric motor + cooling system		
Specific power	5 kW/kg	10 kW/kg
Cruise efficiency	96%	98.5%
Maximal design point efficiency	94.5%	97%
Power electronics + cooling system		
Specific power	15 kW/kg	25 kW/kg
Cruise efficiency	98%	99.5%
Maximal design point efficiency	96.5%	99%

The basic design of the aircraft is a series hybrid-electric architecture, consisting of turboshaft engines as the main source, and batteries and/or fuel cells as auxiliary sources. Each propeller is connected to a gearbox that adjusts the rotation speed between the propeller itself and the electric machine. The electric motors are powered by power inverters, which are themselves electrically connected to an electrical power distribution centre generally known as ultra-high voltage direct current (uHVDC), ultra meaning that the selected bus voltage is beyond the standard voltage network which is ± 270 V.

I.3.1 Input data.

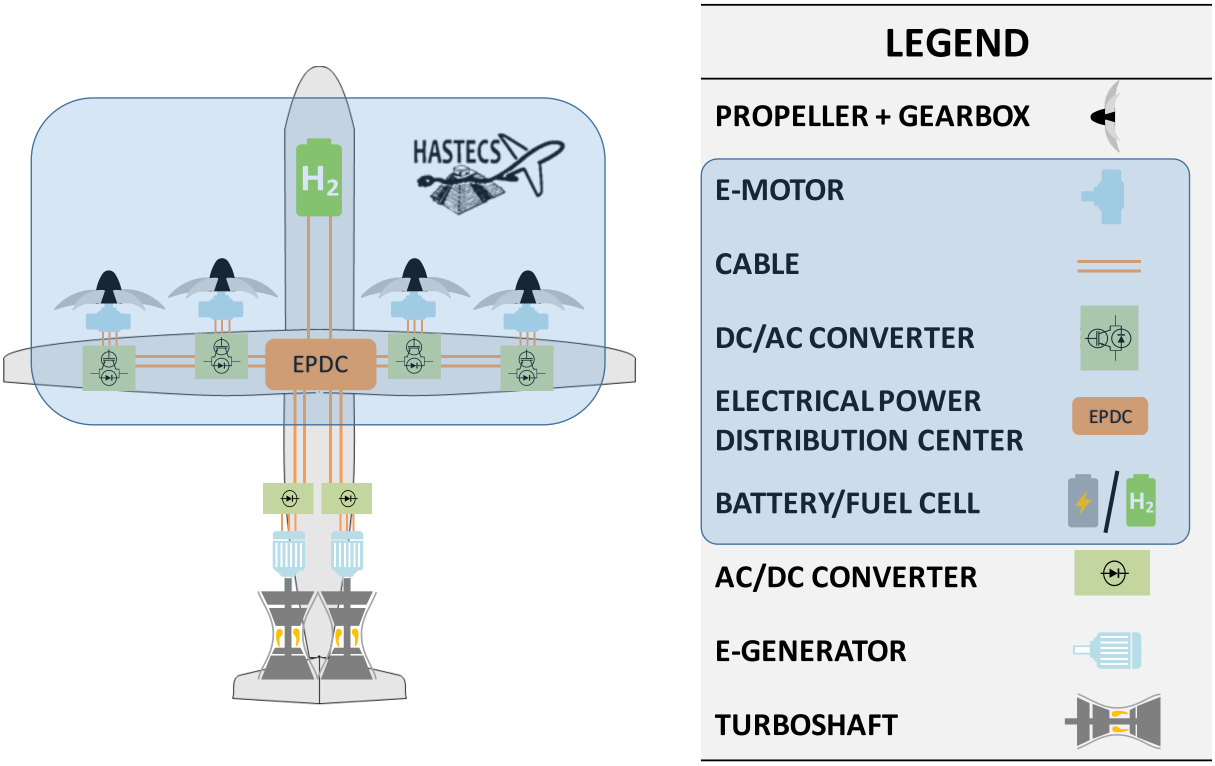

Fig. I-51: HASTECS project reference aircraft.

The aircraft under consideration is based on an ATR-72 which can carry 70 passengers with a reference maximum take-off weight ($MTOW_{ref}$) (without electric propulsion cf [65]). The different mission profiles are given in requirements (see Fig I-42).
This reference aircraft has been defined with Airbus, the HASTECS project leader, setting power, thrust and speed requirements:

- Flies to 25000 feet in a cruise altitude.
- Flies at 0.5 Ma at cruise altitude.
- Takes off with an 80 kN- thrust.
- Takes off with a 4 MW power ($P_{aircraft} = Thrust_{aircraft} \times V_{aircraft}$).

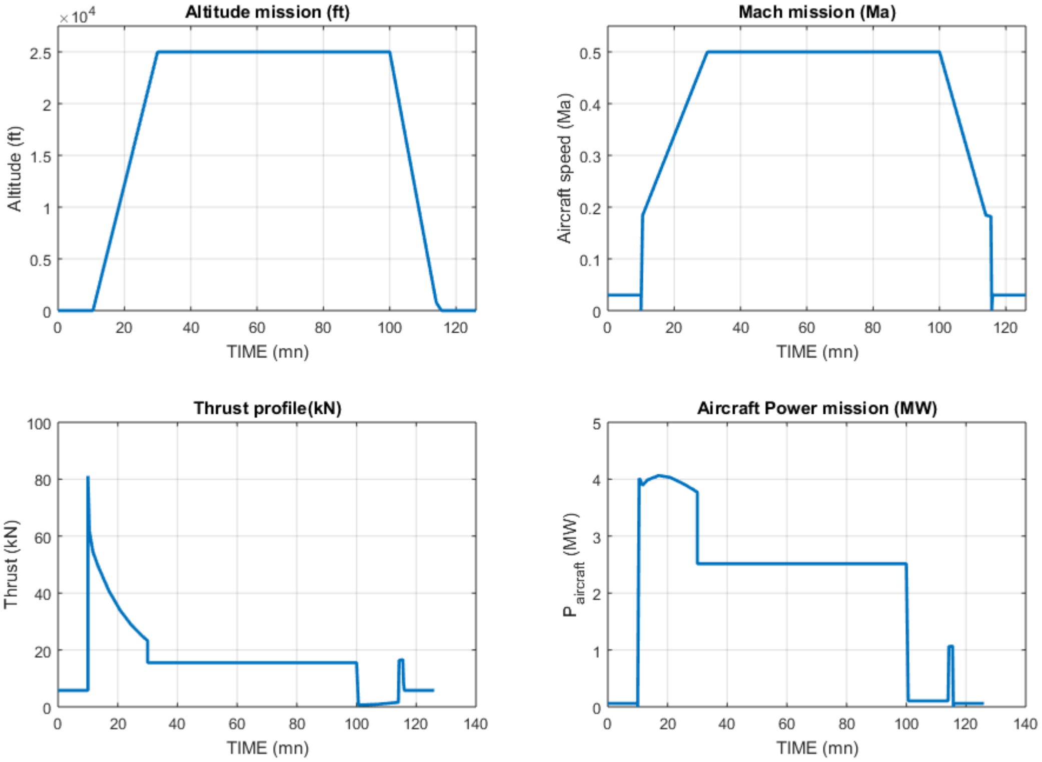

Fig. I-52: Altitude, Mach, Thrust, Aircraft power profile missions.

Table I-5: Flight phase duration.

Flight phase	Taxi (in & out)	Take off & Climb	Cruise	Descent	Approach and landing
Time (min)	5	20	70	14	2

The variation of the speed of sound is taken into account in an environment model. The flight domain of the studied regional aircraft corresponds to the following figure:

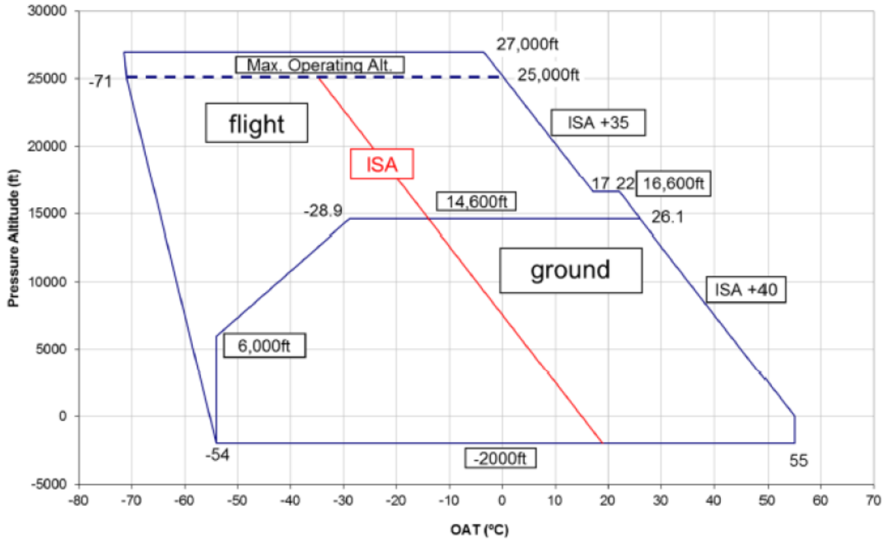

Fig. I-53: Environmental aircraft flight domain conditions (OAT: Outside Air Temperature).

In addition to these design areas, the propeller design must face certain constraints. The main constraint to be checked is the blade tip speed (this latter speed V_b is defined in the scheme below). The maximum blade tip speed must be less than 80% of the speed of sound, as the performance of the propeller is strongly degraded beyond this value. The use of a speed triangle makes it possible to define the blade tip speed versus both the aircraft speed and the tangential rotation speed of the propeller:

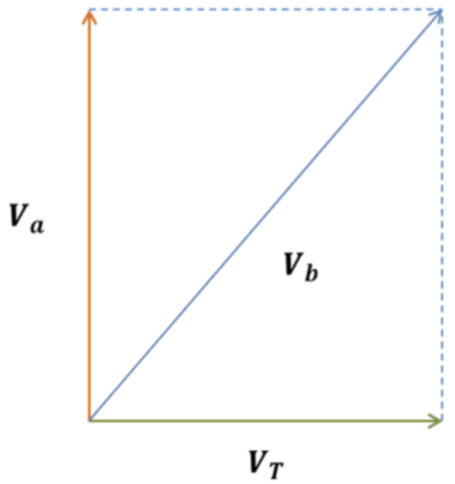

Fig. I-54: Speed triangle ($Aircraft\ speed\ =\ V_a$; $tangential\ rotation\ \ speed\ =\ V_T$; $blade\ tip\ speed\ =\ V_b$)*.*

The diameter of the reference propeller (a four-propelled-drive aircraft) and the dimensions of the nacelle are given in the requirements:

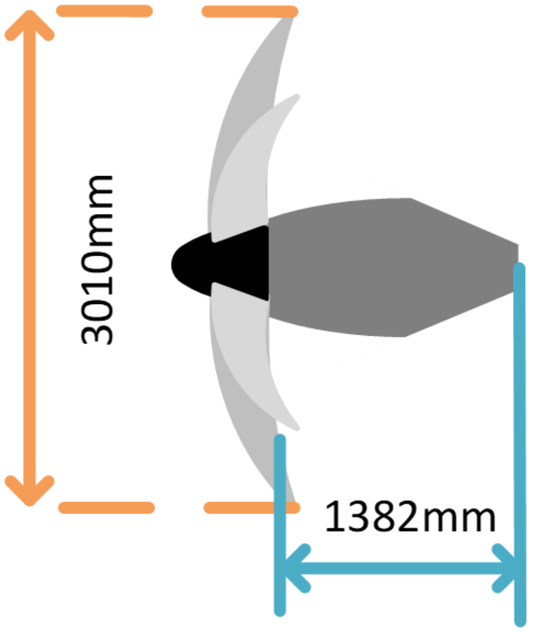

Fig. I-55: Nacelle and propeller sizes.

I.3.2 Project description

From a technical point of view, the project is divided into several work packages (WP), which involve 6 PhD theses and 2 post doc:

1. The WP1 aimed at developing an analytical tool for the design of electric motors. The objective of this work package was to find electric machines with high performance in terms of specific power and efficiencies. This work has been done by the “GREM3” research group in the LAPLACE lab in Toulouse.

2. WP2 done by the LAPLACE “CS” (Static Converter Group) research team was in charge of developing high performance power electronics and design tool. They had to find breakthrough technologies for power converters (inverters and DC DC choppers) in order to highlight the best topology with the best integration performance.

3. WP3 was in charge of developing a tool for the design of high-performance cooling device for electric motors. The objective of the study was to imagine the best technologies and concepts for cooling electric motors. This research has been done in the PPRIME institute in Poitiers.

4. The WP4 mission was quite similar the one dedicated to the WP3 but for power electronic cooling. The aim was to find efficient cooling concepts and technologies to optimize the specific power of the overall power electronic system. This research group is located in the PPRIME institute in Poitiers.

5. The fifth working group has studied partial discharges and their impact on high power electrical devices (power electronics, bus bars and electric motors) by taking account of the aircraft environmental conditions (altitude, pressure, temperature). The partial discharge phenomenon can create temporary short circuits if the insulation is damaged. This LAPLACE “MDCE” research group was in charge of that study.

6. Finally, our thesis is situated in the WP6 which has to integrate all devices in the powertrain and every subsequent fields. A design-oriented model has to be developed based on both state of the art, Airbus data and other work packages in order to optimize the overall hybrid-electric traction chain. A post doctoral study also achieved a review of auxiliary electric sources (batteries and fuel cells) in the typical framework of HASTECS (related to a serie hybrid electric powertrain). Thes studies have been done by the LAPLACE “GENESYS” research group in Toulouse.

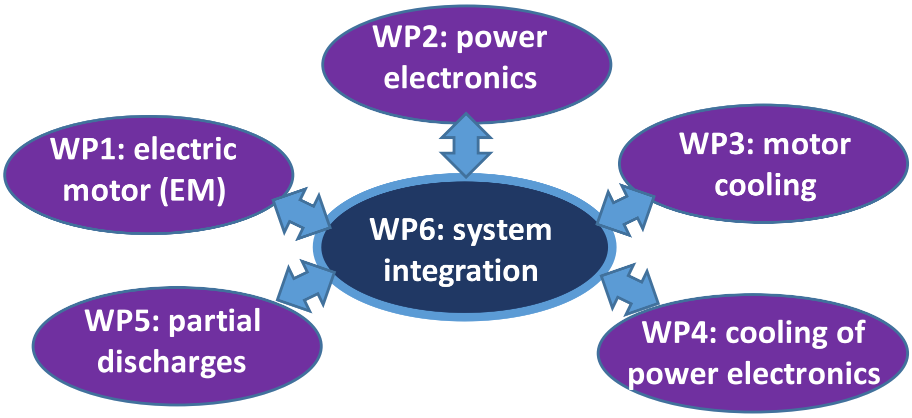

Fig. I-56: Interactions between the system integration work package and the others.

The project leaded by Airbus has been coordinated by the "Toulouse INP" University and includes the following entities:

- Université Toulouse III Paul Sabatier, Toulouse (UPS).
- Institut Supérieur de l'Aéronautique et de l'Espace - Ecole Nationale Supérieure de Mécanique et d'Aérotechnique de Poitiers (ISAE-ENSMA).
- Centre National de la Recherche Scientifique (CNRS).

Three research labs were also involved:
- CIRIMAT Carnot Institute (WP6).
- Laboratoire Plasma et Conversion d'Energie (LAPLACE) (WP1/WP2/WP5/WP6).
- P PRIME Institute (WP3/WP4).

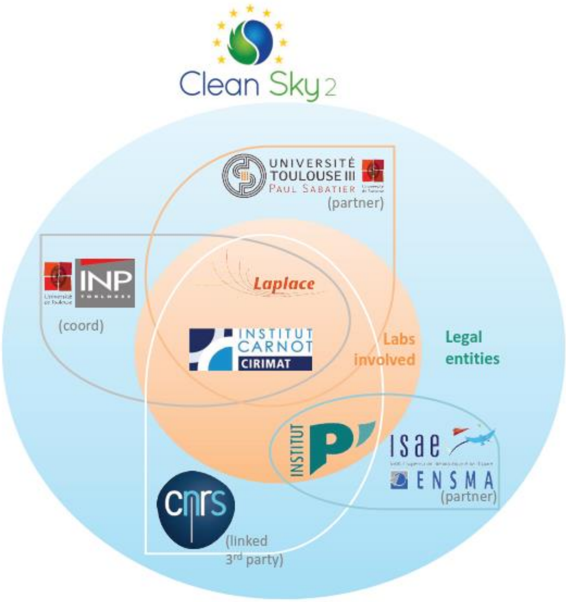

Fig. I-57: Academic HASTECS project perimeter (universities and laboratories).

I.3.3 A major “snowball effect” involving an integrated looped process

The hybridization of a regional aircraft is a complex challengeconsidering that electrical components are added in the hybrid powertrain compared with a full-thermal airplane. Despite the “hopefully” high efficiency power chain, both the powertrain mass and the power to be supplied are significantly increased. This double effect due to the additional mass and the increase of the supplied power leads to an additional fuel mass itself potentially increasing the aircraft structure (wing surface). This successive increase of the embedded mass is wellknown in aircrafts as a “snowball effect” which constitutes a major effect of hybrid aircrafts to be included in the design process. In our case, with regard to the reference value of the MTOW (see the reference aircraft definition in the section III.1), this snowball effect has to be integrated. In order to do that, a looped process has been implemented considering both a reference MTOW ($MTOW_{ref}$) and a reference thrust $Thrust_{ref}$ which correspond to the figure linked with the reference aircraft (defined in III.1). Following the added weights from all designed devices, a “new MTOW” ($MTOW_{new}$) is estimated from which a “new Thrust” is derived. This derivation is based on the linear approximation in Equation (I-4):

$$Thrust_{new} = Thrust_{ref} * \frac{MTOW_{new}}{MTOW_{ref}} \tag{I-4}$$

Both efficiency and weight are assessed from each component model at the end of each iteration of the looped process. After one iteration, based on the new (after redesign) MTOW ($MTOW_{new}$) and its ratio versus the weight reference value ($MTOW_{ref}$) at the initial point of the process, a new thrust must be derived as illustrated in the next figure Fig. I-58:

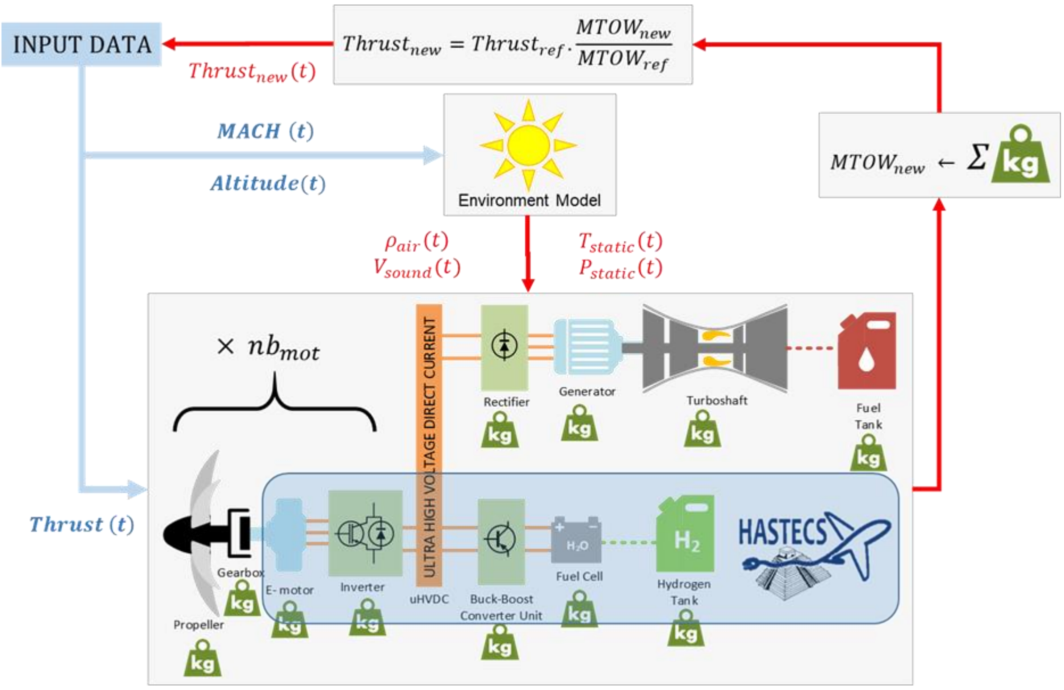

Fig. I-58: Implicit looped integrated process

Thus, by considering the evolution of "new" design variables displayed in equation (I-4) at each iteration, an implicit looped process is achieved which is stopped when the MTOW error between two successive iterations is lower than 50 kg. The process is initialized with a full thermal reference aircraft with a $MTOW_{ref}$. Then, adding the embedded weights corresponding with the electric devices (power electronics, electric motors, auxiliary source, cables), new MTOW and consequently new thrust values are derived. As emphasized on the next figure Fig. I-59, our looped simplified model has been validated with reference to a complete aerodynamic model described in Jerome THAUVIN's PhD thesis [12]. During the flight mission, this comparison shows that thrust shape is quite the same by comparing aerodynamic models with a final MTOW and the previous linear derivation.

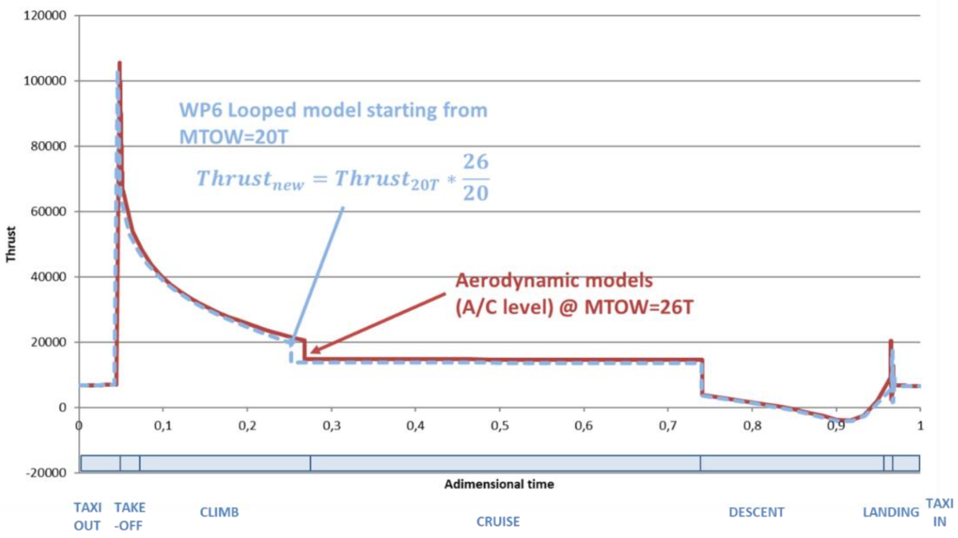

Fig. I-59: Validation of the looped process by comparison of aerodynamic and looped models

The study was carried out on a 20 T aircraft and a 26 T aircraft. Based on the reference aircraft of 20 T weight, the linear extrapolation was used to determine the thrust for a 26 T aircraft: the model used in our case will be the following $MTOW_{end} \leq MTOW_{ref} + 6\mathrm{T}$. Note that this implicit loop converges within 10 iterations which corresponds to an acceptable CPU cost in view of an integrated design by optimization. Aircraft weight and performance can be deduced using the model loop.

I.3.4 About sensitivity of technologies on both max take off weight and fuel burn.

The main target of the European project HASTECS (Hybrid Aircraft Academic reSearch on Thermal and Electrical Components and Systems) is to couple thermal and electrical studies for a regional aircraft. The series hybrid electric architecture has been studied in this project as it leads to huge power constraints on the electric power train, the thrust being fully provided by electric devices. From an input data set and given environment conditions (temperature, pressure, aircraft speed, etc) we will present in this thesis different "surrogate" models to simplify assessments of efficiencies and masses from each device of the whole powertrain. A fixed aircraft structure is considered and only the propulsive system is refined through a looped process linking weight variations and thrust consequences as described in chapter II: this integrated design approach allows assessing energy efficiency and mass benefits.

Technological models with corresponding design have been achieved in every work packages of the HASTECS project and will be discussed latter in that thesis. However, in order to complete this thesis introduction, it is interesting to propose a preliminary analysis at system level in order to emphasize: "how much technologies are sensitive on the integration level (weights, fuel burn)"? This preliminary analysis is simply based on assessments on both efficiencies and specific power/energy defining three successive targets as detailed in [66]. In the HASTECS project, two targets have been challenged for 2025 and for 2035 as displayed in the first (left) column of Table I-6. In the right column of this table, more "aggressive" assessments for a future "20xx target" has been added. In our case, specific powers of both electric motors, (respectively electric generators) and power electronics (rectifiers and inverters) include the cooling devices. Figures corresponding with a liquid hydrogen storage with fuel cell stack are considered with corresponding assessments in Table I-6**.**

Table I-6: Electric component assessments.

	2025 target	**2035 target**	**20xx target**
Emotor/ Egenerator			
$\mathbf{SP}$ +cooling	5 kW/kg	10 kW/kg	15 kW/kg
Efficiency	96%	98.5%	99%
Power Electronics			
$\mathbf{SP}$ +cooling	15 kW/kg	25 kW/kg	35 kW/kg
Efficiency	98%	99.5%	99.8%
Fuel Cell - Liquid H2			
$\mathbf{H_2 + tank\ \ SE}$		3.3 kWh/kg	
Auxiliary $\mathbf{SP}$		1.3 kW/kg	
Stack $\mathbf{SP}$		4 kW/kg	
DC Bus			
Ultra $\mathbf{HVDC}$		2000V	

SP = Specific Power - SE = Specific Energy

Aggressive targets have been chosen, but certain targets are already achieved in other studies. In particular Siemens, with the electric motor SP260D has announced 5.2 kW/kg. The University of Illinois is designing and building a permanent magnet synchronous motor to exceed a specific power of 13 kW/kg and efficiency of 96% showing that these targets may be reached [67]. Concerning inverters, General Electric [68], [69], [70], has reached a specific power greater than 10kW/kg for its product. Other simple models have been developed to assess cable weights and losses, following the transferred power, the voltage level and the cable type (AC or DC). Based on this model set, the mass distribution of the hybrid power train is displayed in Fig. I-60 with the particular assessments dealing with the "2035 Target".

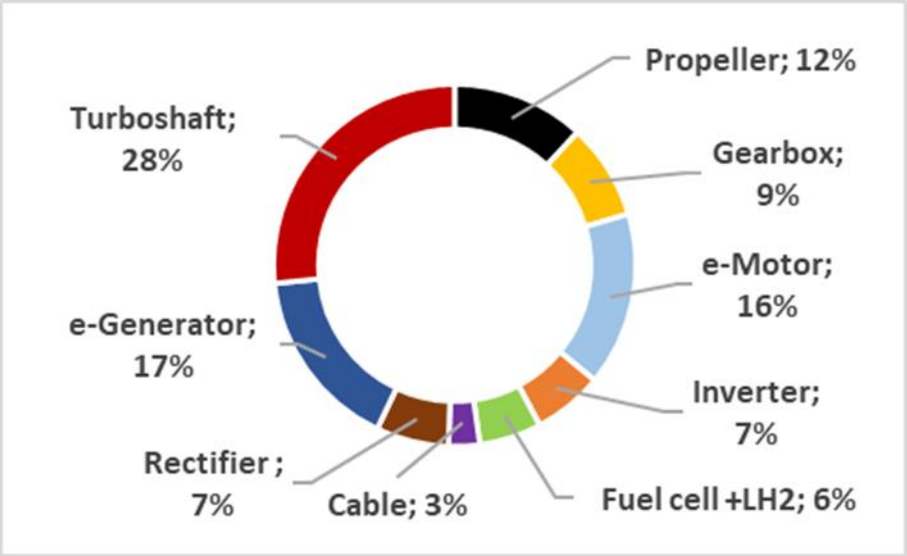

Fig. I-60: Hybrid power train mass sharing.

In this analysis a hybrid-electric aircraft is considered with two similarly sized turboshaft engines which turn generators to supply the electric powertrain. The power distribution over the flight sequences is displayed on Fig. I-61: in this simple but realistic management strategy, electric sources (fuel cells) are used during “full electric” taxi and descent phases which may correspond to a “light hybridization scenario”. For the other sequences, the power is equally shared between both turboshafts.

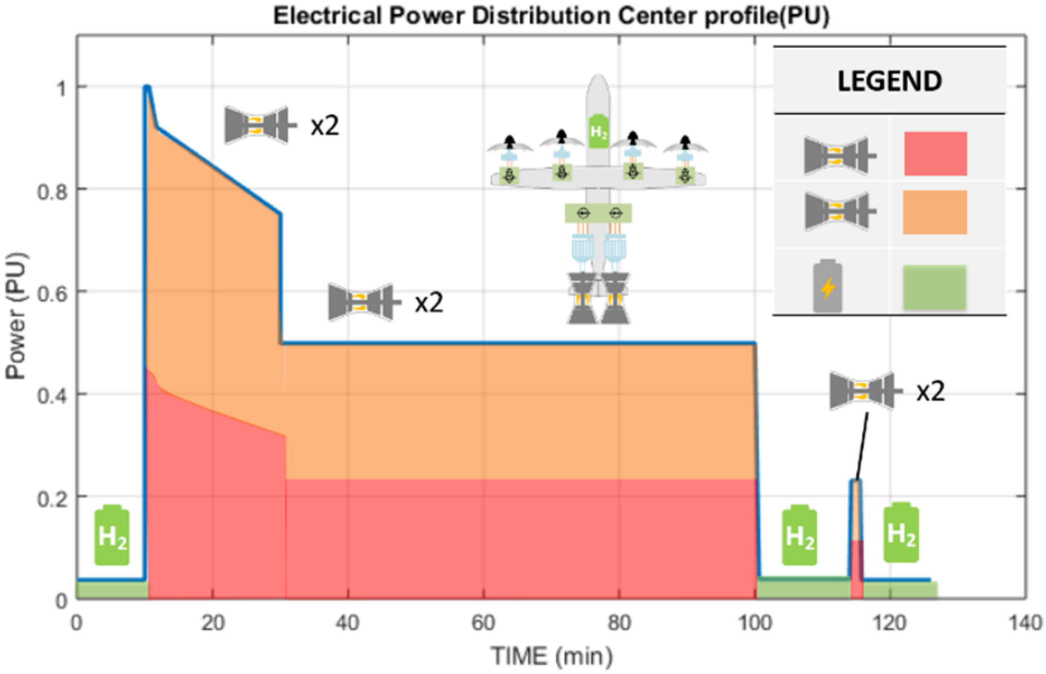

Fig. I-61: Power distribution between sources.

The sensitivity analysis consists in varying two input factors (i.e. the efficiencies and specific powers) on two device classes: the power electronics and electric machines. Taking the 2025 target as the reference and crossing successively towards 2035 (orange bars) and 20XX (grey bars) targets the figure below shows the improvements in terms of fuel burn if the successive steps on the input factors are achieved. The four first set of bars (left of the figure) are related to progress on motors and power electronics considered one by one. The fifth and sixth set of bars gather the influence of these two devices for specific powers and efficiencies. Finally, the set of bars at the right of the figure shows that the overall gain on the fuel burn.

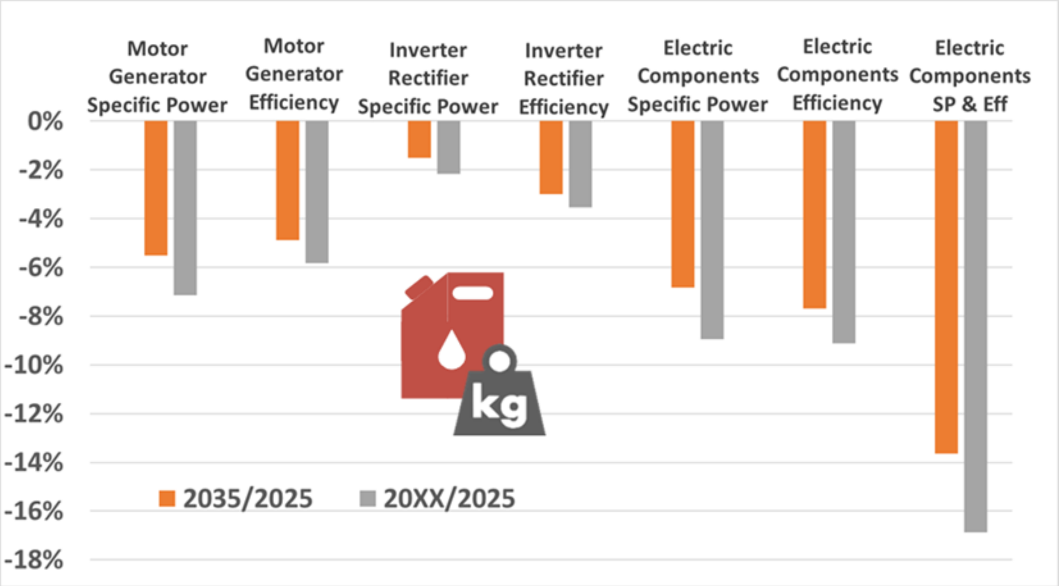

Fig. I-62: Fuel burn variation versus technological improvement of the electric propulsion system from the 2025 target.

It can be noticed that the impact of technological progress both in terms of specific powers and efficiency is significant on the fuel burn even if this impact is slightly lower for power electronics than for electromechanical converters. The figure below shows the results of the same kind of analysis but considering the sensitivity on the overall weight (MTOW) at the aircraft level. The same trends as previously can be observed.

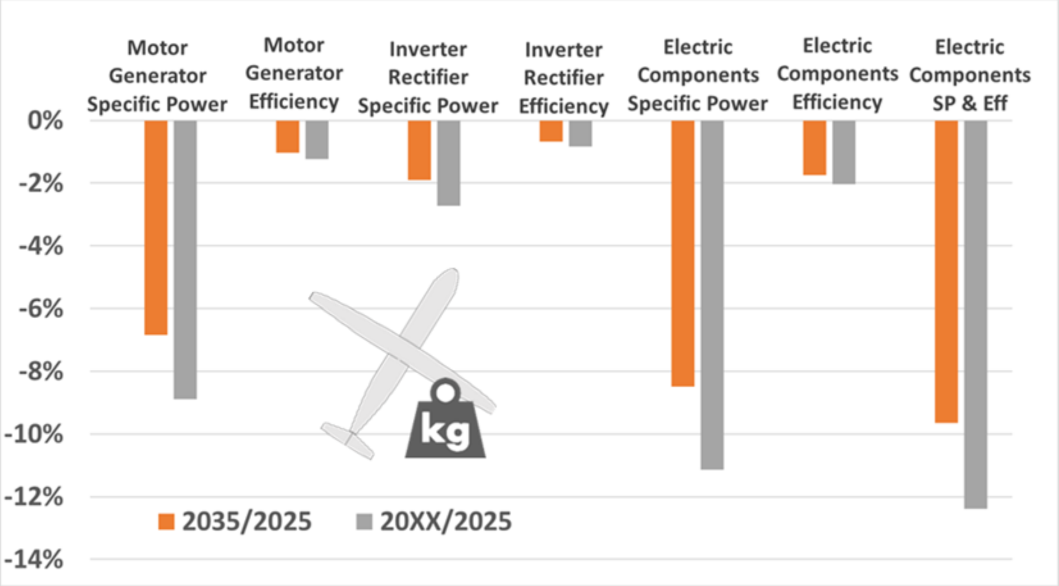

Fig. I-63: MTOW variation versus technological improvement of the electric conversion chain from the 2025 target.

It can also be seen that both progress axis (efficiency and specific power) are really influent on optimization objectives of this study (i.e the fuel burn and weight reduction). With reference to the less aggressive assumptions (target 2025) and regarding the targets 2035 then 20XX assessments, the whole weight (MTOW) would be reduced by more than 12% (Fig. I-63) when the fuel burn would be reduced by 17% (Fig. I-62). Let also notice that specific power is more sensitive to lower the MTOW, but the efficiency effect is not negligible: a trade-off between both specific powers and efficiencies has to be find.

I.3.5 Thesis objectives.

This PhD thesis aims to integrate the technological devices (electrical machines, power electronics, storage components, cooling systems) of the hybrid electric powertrain from new concepts proposed by other work packages (WP1 to 5) and taking into account external information from Airbus data and from the state of the art. In the future context of all-electric aircraft propulsion, this integrated design is a major challenge. The complexity of the optimal design process of the whole powertrain is huge but really relevant.

The first sensivity study on mass variations of both fuel burn and MTOW in the light of technological advances shows that series hybrid electric propulsion system is sensitive to technology. The specific powers and efficiencies must be optimized to lower the mass impact due to the addition of electrical components in the powertrain. The HASTECS project makes it possible to take all the phenomena into account between electrical and thermal components of the hybrid-electric propulsion of the regional aircraft. Meta-models representing different fields of the system integration have to be built but these models need to be simplified (with "acceptable computational time") in order to be able to optimize the complete system in a system integration loop. The second chapter will then focus on the presentation of surrogate models used in the global optimization. These models are based on reference models out of the HASTECS scope, and also on expert models considered in the HASTECS work packages.

Before going towards the overall design optimization and in order to understand couplings between devices, a Global Sensitivity Analysis (GSA) will be proposed highlighting most influent decision variables. Less impacting input variables will be removed from the overall optimization. The Sobol approach has been used for that GSA and will be presented in chapter III. Finally, a Multidisciplinary Design Optimization (MDO) at hybrid aircraft level will be the focus of the last chapter IV. The interest of the MDO will be highlighted. The electric machine and its cooling will be especially focused, being one of the most important (and complex) component to be designed in the powertrain.

CHAPTER II. Modeling for multidisciplinary design optimization of the overall propulsion system

CONTENTS

The main objectives of this thesis, especially the requirements for the modelling process have been introduced in the previous chapter. In order to integrate design models, the system integrator should simplify them and identify trends and trade-offs between the different application fields of the problem. This task can be performed using Multidisciplinary Design Optimization (MDO) which allows a number of phenomena to be taken into account while integrating correlations between the different disciplines. Multidisciplinary integrated design was born from aeronautics; several theses cover the subject [71], [72]. It can be used for the global design of aircraft, for questions of aeroelasticity or industrial problems as in [73].
The success of the MDO has been reflected in other disciplines, notably in the design of electromechanical actuators [74], [75]; in order to minimize the production, maintenance and resistance of a ship [76] or in the design of submarine cables [77].

Beyond the complexity related the multidisciplinarity of our class of systems, several levels of optimization classically exist in engineering systems. As typical example, 5 levels of expertise can be listed in an aircraft design (Fig. II-1). In the HASTECS project the “component” approach is studied to feed the “system” point of view. Several disciplines are coupled in our models: fluid mechanics (environment and propeller models), electromagnetism and electrical engineering (electric machine and power converter models) and thermics (associated cooling and gas turbine). Furthermore, the effects of the aircraft environment must be involved: the partial discharges effects will be studied especially within the electromechanical actuator. Real disruptive technologies will not be found not only in the specialized application areas but also at the interface of the different fields.

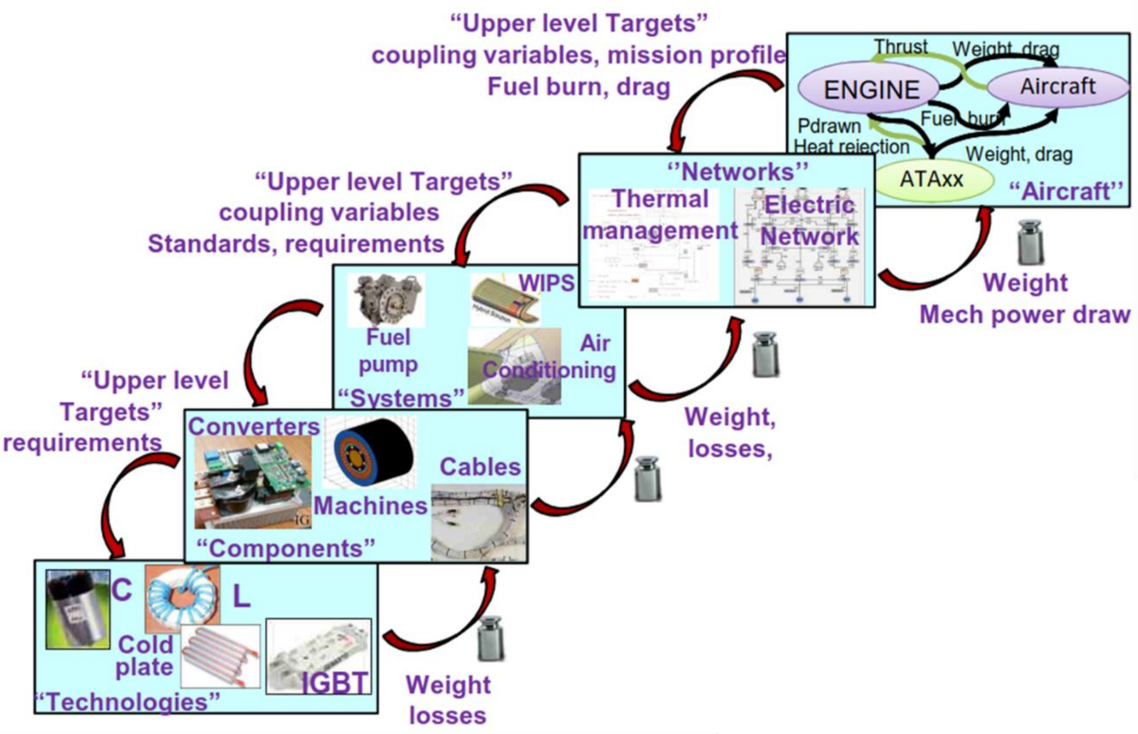

Fig. II-1: Five levels of optimization from "technologies" to "aircraft".

In aeronautics, MDO is popular because of the complexity resulting from the number of components and disciplines which have to be included in the design processs. It should also be noted that the aircraft should be optimized at the lowest technology and component level itself as well as the higher aircraft level which represents an additional difficulty, especially in the case of this 5-level architecture.

The hybrid-electric propulsion system is illustrated in the Fig. II-2. In this study the following components have been studied:

- Propeller
- Gearbox
- Electric motor (with a cooling system model and a partial discharge model)
- AC/DC converter (and its cooling system)
- DC/AC converter
- Electric Generator
- Turboshaft
- Electric source:
    - Fuel cell (stack+ auxiliaries + storage)
    - Battery (Battery Management System and its packaging/cooling)

The components written in orange are part of the HASTECS study framework, for the other models come from previous studies.

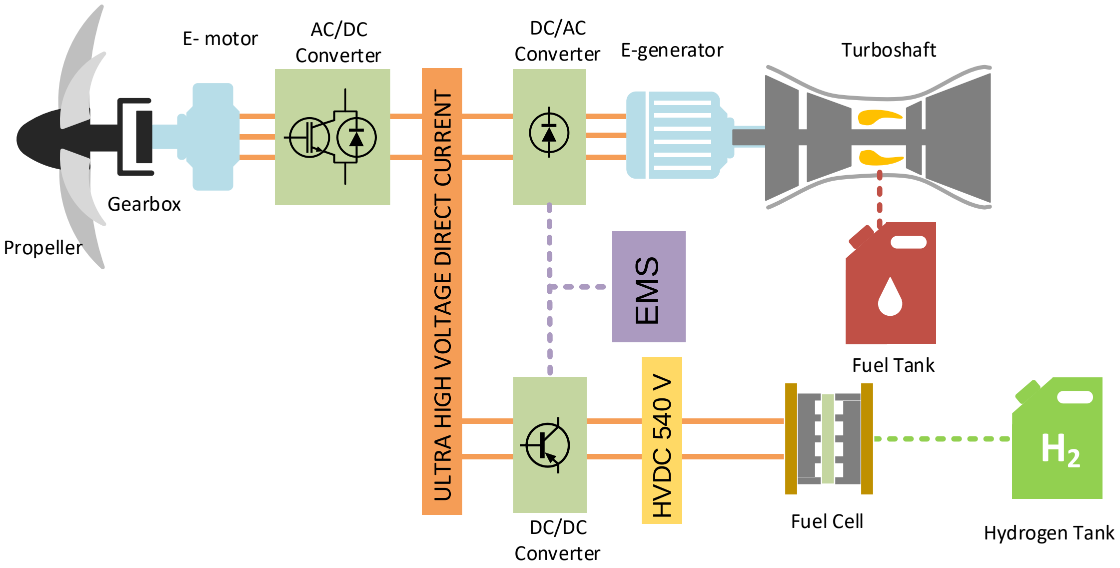

Fig. II-2: Description of the total hybrid-electric powertrain.

II.1 Reference models out of the HASTECS scope.

II.1.1 Propeller model.

The blown wing effect sometimes exploited with distributed electric propulsion (muti propeller) has not been considered in this study.

The propeller model is based on the disk actuator theory [78]. The air flow is steady and it behaves as an incompressible fluid. The schematic model of the disk actuator is illustrated in Fig. II-3 where:

- u_0 is the aircraft velocity,
- u_e is the air flow velocity behind the propeller,
- P_0,P_1,P_2 are respectively the ambient, before and behind the disk (propeller) pressure values. The pressure difference due to the propeller motion is then P1-P2 which creates the thrust:

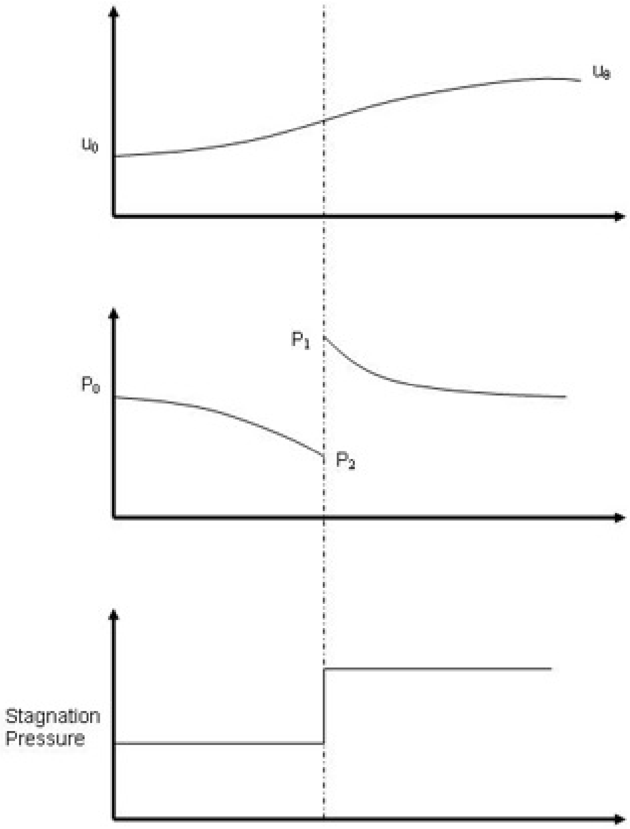

Fig. II-3: Schematic model of disk actuator (dotted line = location of the propeller).

The process consists in determining the propeller shaft power based on flow equations. The thrust $T_{A/C}$ of the disk is:

$$T_{A/C} = \pi.\frac{D_{prop}^2}{4} \times (P_2 - P_1) = A_{disk} \times (P_2 - P_1) \tag{II-1}$$

Where D_{prop} is the propeller diameter, A_{disk} is the disk area. Applying the Bernoulli equation in the regions of the fluid where the pressure and velocity are varying continuously leads to:

$$(P_2 - P_1) = \frac{1}{2}\rho.(u_e^2 - u_0^2) \tag{II-2}$$

The thrust *T* can be rewritten as:

$$T_{A/C} = A_{disk} \times \frac{1}{2}\rho.(u_e^2 - u_0^2) = A_{disk} \times \frac{\rho}{2} \times u_0^2\left(\frac{u_e^2}{u_0^2} - 1\right) \tag{II-3}$$

Then, the following relation can be established:

$$\frac{u_e}{u_0} = \left(\frac{T_{A/C}}{A_{disk} \times \frac{\rho}{2} \times u_0^2} + 1 \right)^{1/2} \tag{II-4}$$

Using the diagram in the Fig. II-3, the disk (medium) velocity u_{disk} is expressed as:

$$u_{disk} = \frac{(u_e + u_0)}{2} \quad <=> u_e = 2.u_{disk} - u_0 \tag{II-5}$$

Combining (4) and (5) leads to;

$$2.u_{disk} - u_0 = u_0 \times \left(\frac{T_{A/C}}{A_{disk} \times \frac{\rho}{2} \times u_0^2} + 1 \right)^{1/2} \tag{II-6}$$

We can finally express the power *P* required from the propeller shaft as a function of the thrust $T_{A/C}$.

$$P = T_{A/C} \times u_{disk} = T_{A/C} \times \frac{u_0}{2} \times \left(\left(\frac{T_{\frac{A}{C}}}{A_{disk} \times \frac{\rho}{2} \times u_0^2} + 1 \right)^{\frac{1}{2}} + 1 \right) \tag{II-7}$$

This model comes from [12] and is referred in APPENDIX B.

II.1.2 Gearbox model.

The gearbox model is based on a surrogate model used by the National Aeronautics and Space Administration in [79]. The maximum torque value and the gearbox ratio are input data for the model.

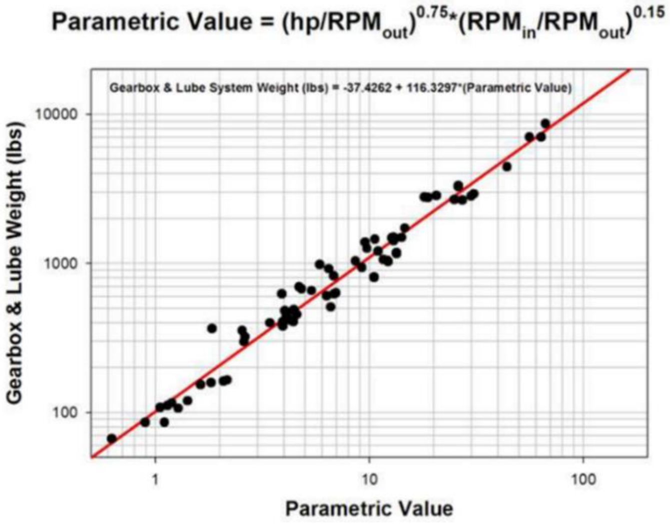

Fig. II-4: Transmission and lubrification system weight correlation [79].

Where:

- hp represents the propeller shaft power in [hp],
- RPM_{out}/RPM_{in} represents the rotation speed ratio with rotation speeds in Round Per Minute (out = proppeller side/ in = e-motor side).

A fixed gearbox efficiency is considered in this model ($\eta_{gbox} = 98{,}5\%$) which is detailed in APPENDIX C.

II.1.3 Turboshaft model.

The same kind of study has been carried out in the thesis of J. THAUVIN [12] to build a model based on data regression for the gas turbine system. The collected data come from turboprop and helicopter engines which have high specific powers. The model is detailed in APPENDIX D.

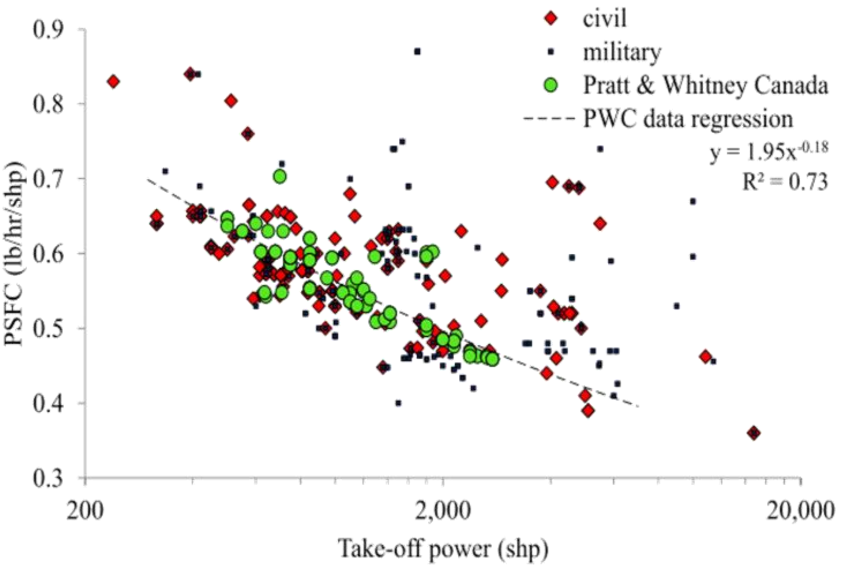

Fig. II-5: Turboshaft data regression.

II.1.4 Cable model.

The cable sizing model is based on an Airbus internal report [80]. Both thermal (based on Joule effect) and voltage drop constraints allows designing cables according to the voltage and the power factor, the cable length and type (AC or DC), the number of phases and wires per phase. Two materials are available in the cable sizing model: Aluminium and copper. The model is explained in details in APPENDIX E.

II.2 "HASTECS" MODELS.

II.2.1 Electric motor design model.

II.2.1.1 Presentation of the electromechanical analytic model, modeling process and results.

II.2.1.1.1 The electric machine topology choice.

The electric motor choice has been driven by efficiency and specific power targets: (cf Table I-6). Indeed, a study of different topologies has been carried out in the automotive field for hybrid (and/or electric) applications [81], [82].

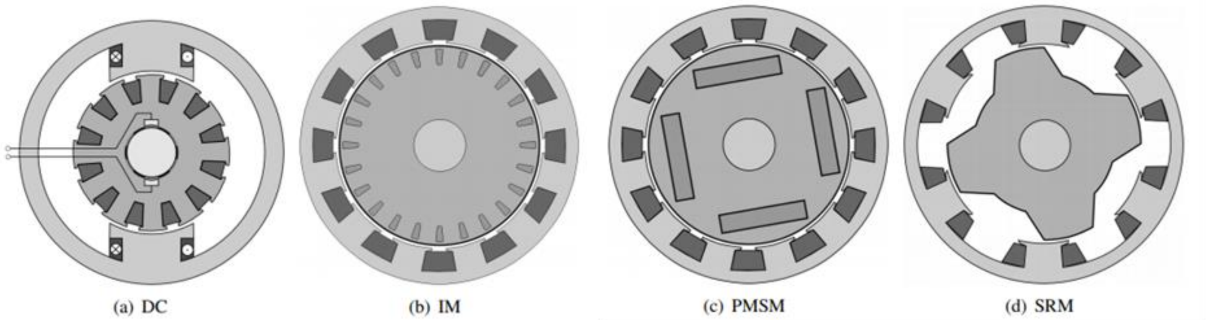

Fig. II-6: Four popular motors in Hybrid Electric Vehicle: direct current machines (DC), Induction machines (IM), permanent magnet synchronous machines (PMSM) and switched reluctance machines (SRM) [82].

Considering both efficiency and specific power the permanent magnet synchronous machine has the best performance. The efficiency is as important as the the specific power in aeronautics because the thermal power for cooling adds drag to the aircraft level. Increasing the power density of the actuator is equivalent to improve each term in the following equation (II-8):

$$\frac{P_{electromagnetic}}{V_{rotor}} = 2\ k_w A_{rms} B_{gap_{rms}} \Omega \tag{II-8}$$

With:

- k_w is the winding coefficient depending on the winding configuration,
- A_{rms} is the root mean square lineic density in A/m depending on the current density,
- $B_{gap_{rms}}$ is the root mean square of the flux density in the airgap,
- Ω is the mechanical rotational speed of the electric actuator,
- V_{rotor} is the rotor volume.

Increasing rotational speed allows decreasing rotor volume and thus its weight. Simultaneously, it leads to increase Iron and mechanical losses. The evacuation of the heat generated due to losses through winding insulation is the main limitation for increasing specific power of electric motors.

II.2.1.1.2 First part of the electromechanical analytic model: Target Setting Tool (TST).

In the following, an analytical model and its evolutions to be in accordance with a MDO process is described. This electromagnetic and electromechanical conversion model has been developed in LAPLACE by the GREM3 team, especially in the PHD thesis of Sarah Touhami [83], [84].This modelling apporch was based on two complementary design tools (TST and SM-PMSM) also developed by this research team.

The following schematic shows the power balance in the PMSM and the associated powers.

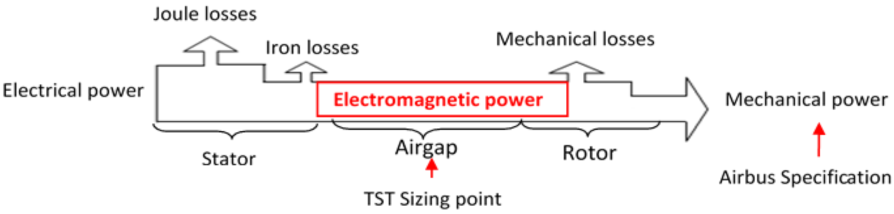

Fig. II-7: Power balance of the permanent magnet synchronous motor (PMSM).

From an input set data, main stator sizes and losses are determined thanks to the TST pre-design model. In a second step a more accurate model is used: The Surface Mounted Permanent Magnet Synchronous Machine model (SM-PMSM). The process is described in the Fig. II-8:

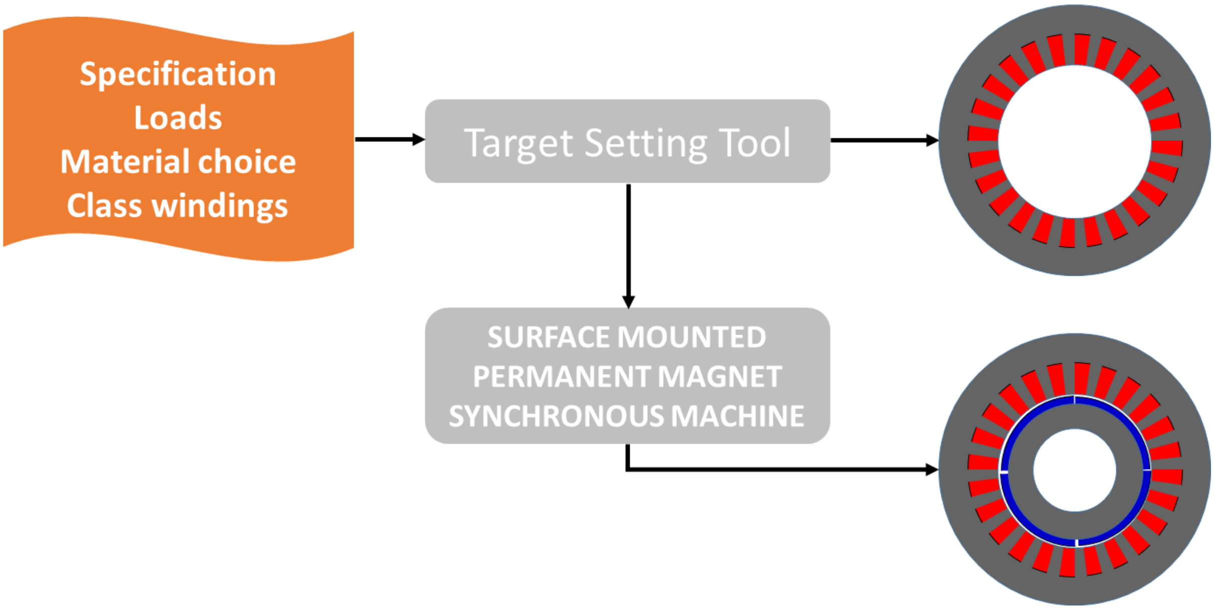

Fig. II-8: Electromagnetic model design process

The second design model SM-PMSM allows determining all sizes of the structure (rotor and stator). The losses are given at the design point. All values have been checked through a Finite Element Analysis (FEA). Fig. II-9) presents the comparison between all models for the air gap flux density.

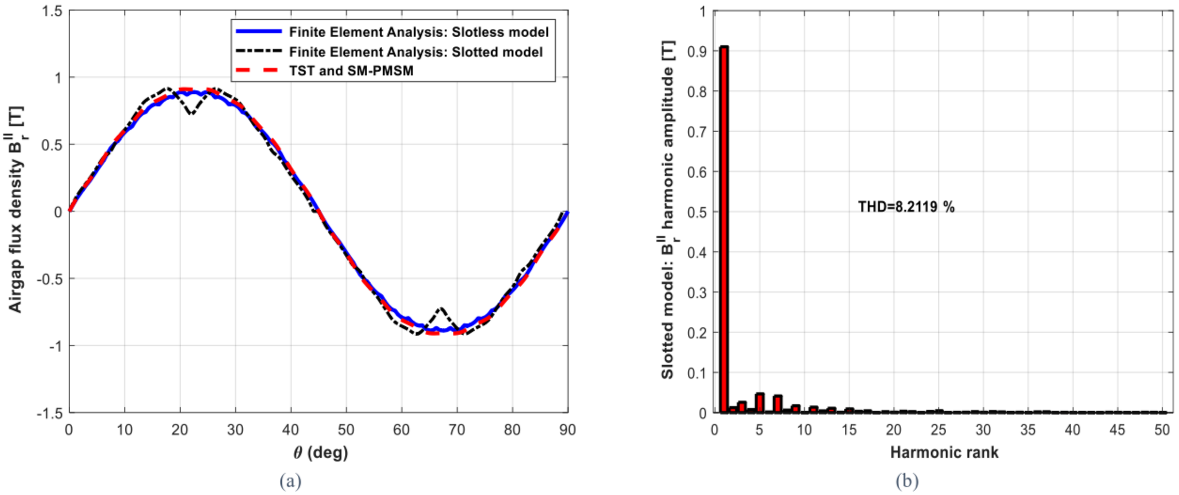

(a) (b)

Fig. II-9: Air gap flux density at no load (a) slotless and slotted models, (b) harmonic analysis [83][83]

In order to optimize the CPU time in the context of a global system optimization, several changes and adaptations have been performed.

II.2.1.2 Adaptation of the PMSM analytical model for system optimization.

II.2.1.2.1 First observation at global system level.

A first overall powertrain optimization was carried out in order to prepare the integration of all models. First results were surprising: the optimizer converged towards several "spread" solutions in the parametric space depending on the initialization conditions. This preliminary analysis forced us to go back to a local study especially at the eMotor level and to review its design model and the choice of the decision variables at the input of the optimization algorithm [85]. While the objective function of the overall system optimization will be the fuel burn, we have reduced in this report the optimization at the local level of the eMotor, the objective function in that case being only the electric machine weight (local objective). The first set of decision variables (input data set) was the following:

- The torque design point $T_{emot_{siz}}$ in Nm,
- The mechanical rotational speed design point $N_{emot_{siz}}$ in RPM,
- The tangential pressure σ_T in Pa,
- The current density design point $J_{rms_{siz}}$ in A/mm²,
- The maximal value of flux density in the airgap $B_{gap_{max}}$ in T,
- The flux density value in the stator yoke B_{yoke} in T,
- The flux density value in the stator teeth B_{teeth} in T,
- The ratio between the inner stator diameter and the active length $R_{Drot_{Lm}}$,
- The number of conductor per slot N_{ce},
- The number of pole pair p,
- The number of slot per pole and per phase n_{epp}.

Regarding the torque speed characteristic, the following preliminary optimization results were obtained using a parameter free version of the CMAES algorithm [86] (100 iterations with 20 same objective function results) :

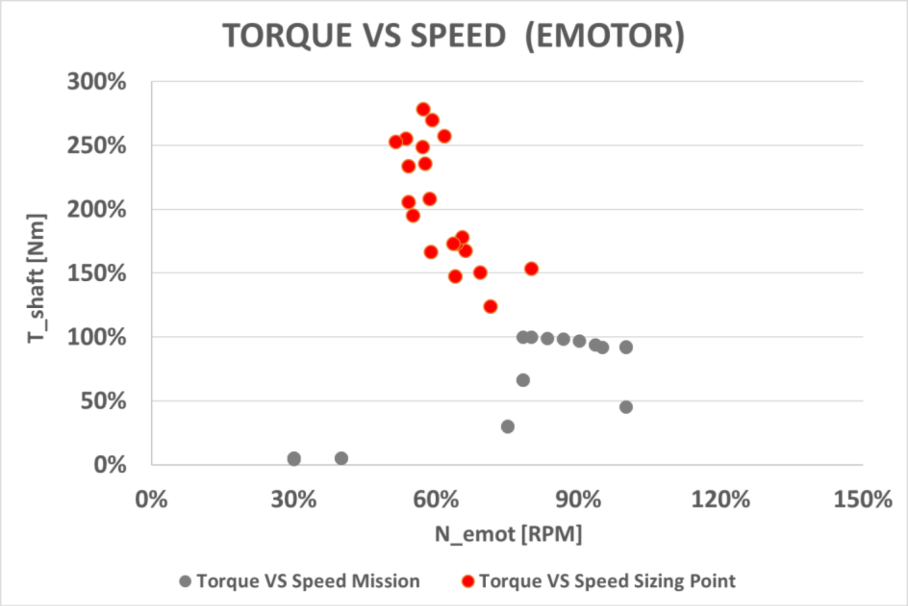

Fig. II-10: First results considering the overall powertrain.

In red color, the results of twenty independent optimization runs are compared with the torque VS speed mission in grey. Several power variables did not seem to converge:

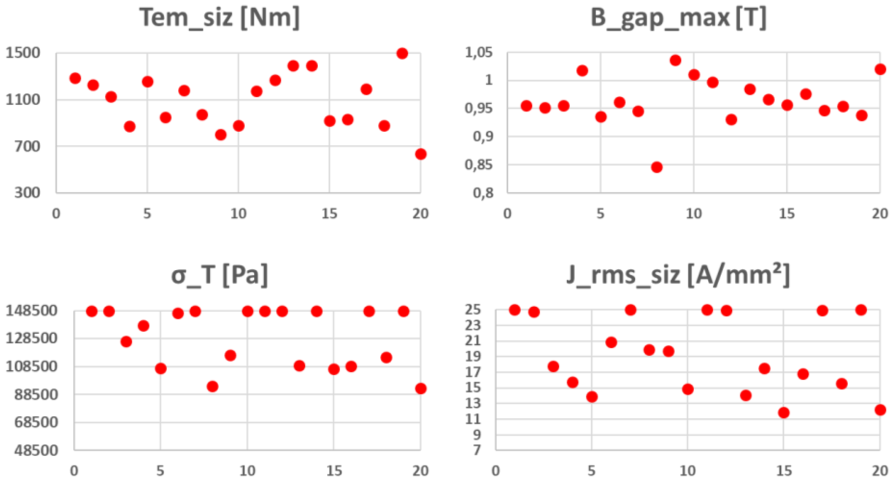

Fig. II-11: 20 independent run solutions.

The optimization seems to find several solutions and to spread decision variables in a wide parameter space. In order to avoid such results, several modifications have been made on the eMotor model.

II.2.1.2.2 A first model modification $\left(B_{gap_{max}} = \boldsymbol{air\ gap\ flux\ density}\right)$.

The flux density in the air gap was initially an input data. But in order to have the correct causality of calculation another decision variable has been chosen to replace the induction value in the air gap. Firstly, to determine the ratio between the magnet thickness and the inner stator radius ($R_{pm_{ral}}$), it is necessary to know the value of the ratio between the air gap and the inner stator radius ($R_{g_{ral}}$). The process of the original model is described in the left part of the Fig. II-12:

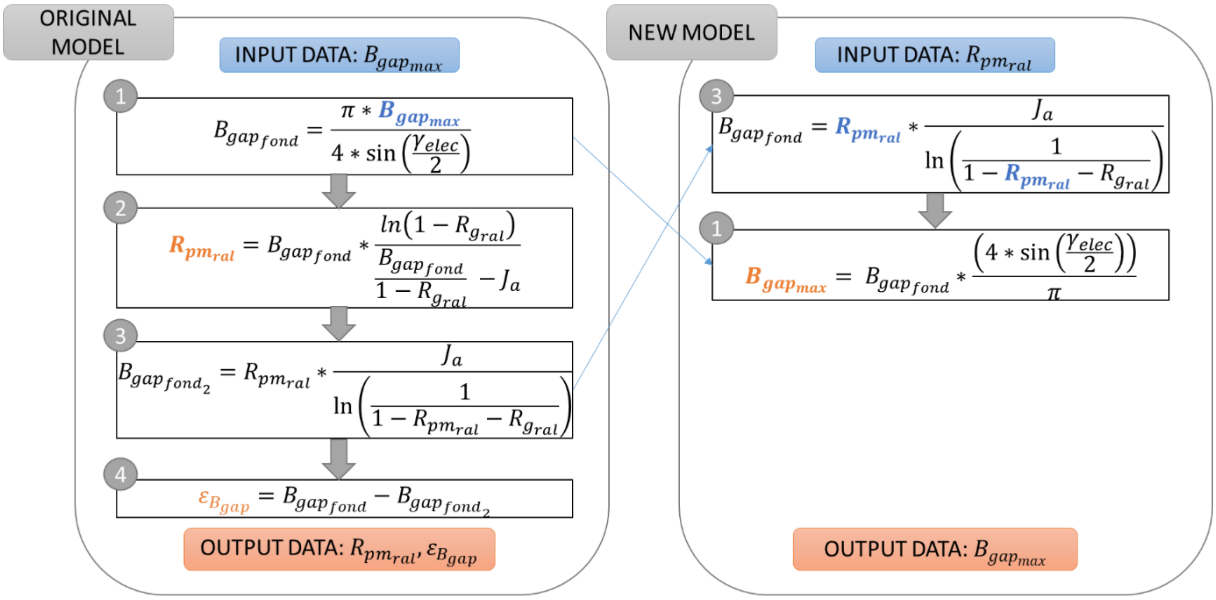

Fig. II-12: Process to determine the real value of flux density in the air gap and magnet thickness (Original model and the new one).

Where:

- J_a is the magnet polarization in T,
- γ_{elec} is the electric pole angle in rad,
- $R_{pm_{ral}}$ the ratio between the magnet thickness and the inner stator radius in %,
- $R_{g_{ral}}$ the ratio between the air gap thickness and the inner stator radius in %,

The original model uses the air gap flux density as an input data. After that, a first equation computes the fundamental value of the flux density in the air gap. From this calculation, an approximation is made for finding the ratio $R_{pm_{ral}}$ (Equation 2 in the Fig. II-12). The direct model of the flux density (Equation 3 in the Fig. II-12) permits to check the real value but an error remains between the approximation and the direct model (Equation 2 and Equation 3 in the Fig. II-12). The new model avoids the approximation by calculating directly the value of flux density in the air gap.

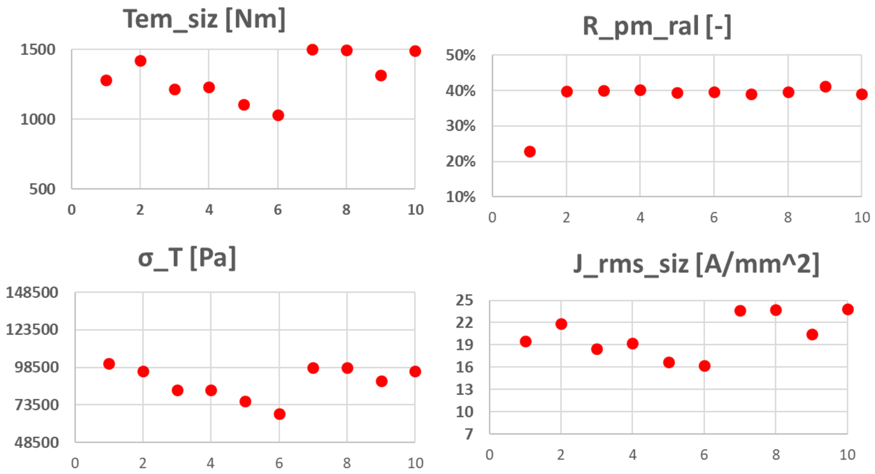

Fig. II-13: 15 independent run solutions after the first model modification.

After this first model adaptation, an apparent coupling is highlighted between three sizing variables $\left(T_{em_{siz}}, \sigma_T, J_{rms_{siz}}\right)$ even for best results at iso weight. The analysis of the code shows that the torque design point ($T_{em_{siz}}$) appears in two equations:

- The equation associated with the rotor volume (Eq. (II-9)).
- The equation associated with slot height (Eq. (II-10)).

$$V_{rotor} = 2.\pi.R_{alesage}^2.L_{motor} = \frac{T_{em_{siz}}}{2\sigma_T} \tag{II-9}$$

$$h_{slot} = \frac{T_{em_{siz}}}{R_{alesage}.L_{motor}.B_{gap_{rms}}.J_{rms_{siz}}.k_{remp}.n_{enc}} \tag{II-10}$$

In order to avoid this effect (spread variables), a second change to the model has been proposed.

II.2.1.2.3 A second model modification $(\boldsymbol{\sigma_T}\ \boldsymbol{tangential\ pressure})$.

Both variables (design point torque and tangential pressure ($T_{em_{siz}}, \sigma_T$)) permit us to determine the stator inner radius through Eq.(9). In order to avoid the problems seen in the previous paragraph, the tangential pressure σ_T has been replaced by the value of the stator inner radius $R_{alesage}$ as a new decision variable. Now the tangential pressure becomes an output of the pre-design model and the torque design point is used for the estimation of the slot height. At this stage, new electric motor optimizations have been carried out and “spread variable” effects are still present when several optimizations are run from various initial situations for the decision variables:

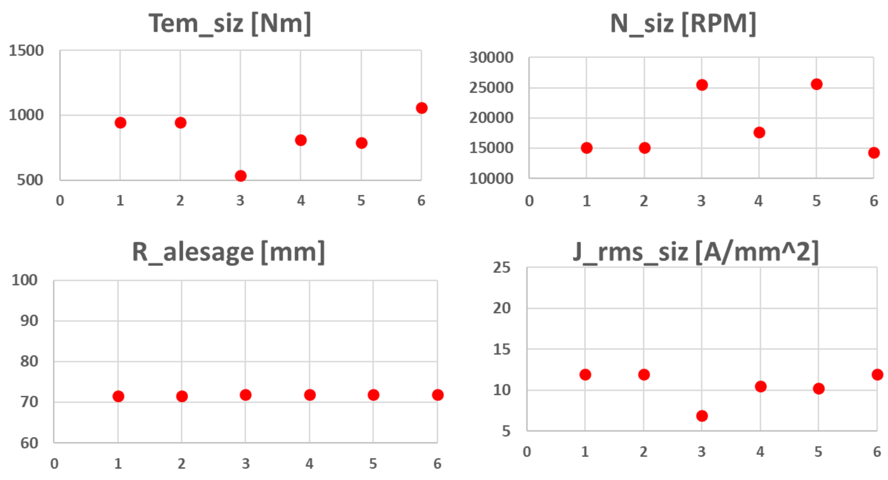

Fig. II-14: 6 independent run solutions after the second model modification.

The corresponding torque/speed characteristic is the following:

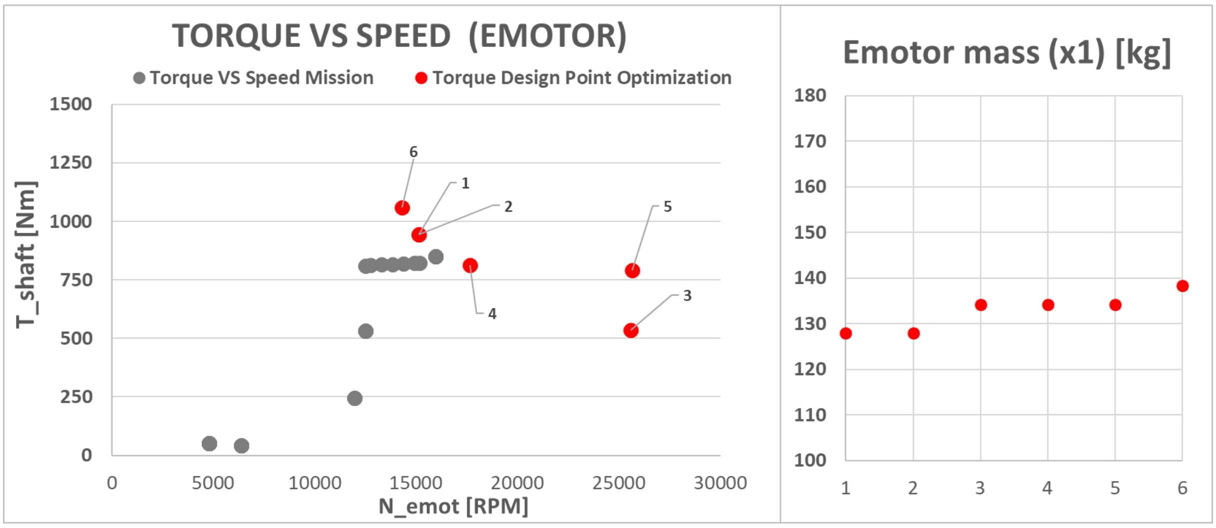

Fig. II-15: Torque/speed characteristic(left) - Emotor mass (objective function)(right).

Once again the obtained results are spread on the parameter space. From an objective function point of view, “optimal results” have the same weight order but the corresponding torque/speed characteristics are totally different. For example, between the sixth and the third solutions, the torque design point is divided by two, while the rotational speed is doubled. Considering both current density and torque design point, their obtained ratio is constant. The Eq. (10) shows the dependency between the slot height and these two latter parameters: if the ratio is constant, the slot height is also fixed. As seen previously with the tangential pressure and the rotor volume, a modification of the decision variable set has to be done.

II.2.1.2.4 A third and final model change (J_{rms} current density and others).

Usually for electric motor design, a base point is used in order to determine the corresponding performances. The current density at design point gives a current at design point, and the supplied voltage is determined through a Behn-Eschenburg diagram without field weakening ($I_d = 0$)(cf Fig. II-16).

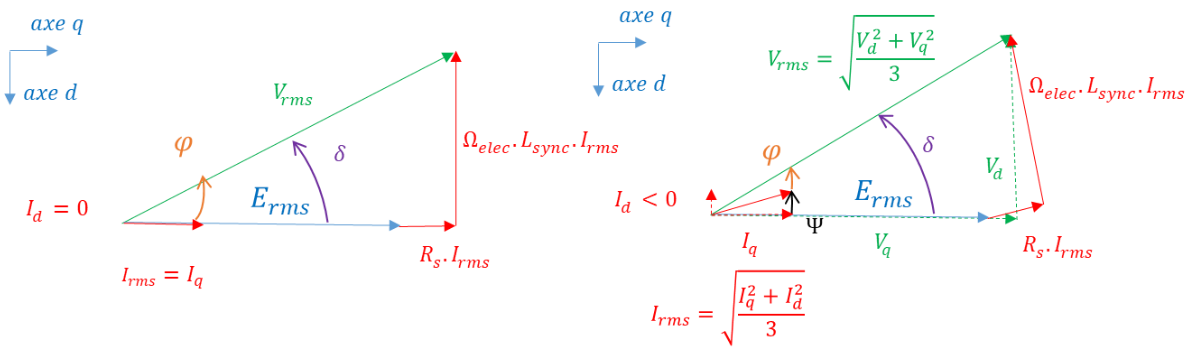

Fig. II-16: Behn-Eschenburg diagrams (without and with field weakening).

- E_{rms} is the root mean square electromotive force in V,
- I_{rms} is the root mean square value of the current in A,
- V_{rms} is the root mean square value of the voltage in V,
- I_d, I_q, V_d, V_q are respectively current and voltage in Park model,
- R_s is the resistor in Ω,
- L_{sync} is the inductor in H,
- Ω_{elec} is the synchronous rotation speed in rad/s,
- φ, δ, ψ are respectively power factor angle, internal angle and the field weakening angle in rad.

The current density appears in the following equation (equation used with a design point):

$$V_{rms_{siz}} = \sqrt{\left(E_{rms_{siz}} + R_s.J_{rms\,siz}.S_{cu_{total}}\right)^2 + \left(L_{sync}.\Omega_{elec_{siz}}.J_{rms\,siz}.S_{cu_{total}}\right)^2}$$ (II-11

Indeed:

$$I_{rms\,siz} = J_{rms_{siz}}.S_{cu_{total}}$$ (II-12

- $J_{rms_{siz}}$ is the root mean square value of current density in A/mm²,
- $S_{cu_{total}}$is the required copper area to perform the mission in mm²,

But based on this equation and given a fixed motor geometry, a set of solutions exist in the torque speed plan for a same V_{rms} : in the next figure, the blue dots represent the set of solutions of the Eq. (5) for a same supplied voltage V_{rms} given an example of electric machine characteristic. The DC bus voltage becomes a sizing parameter, design points in torque and speed are no longer necessary for electric actuator design.

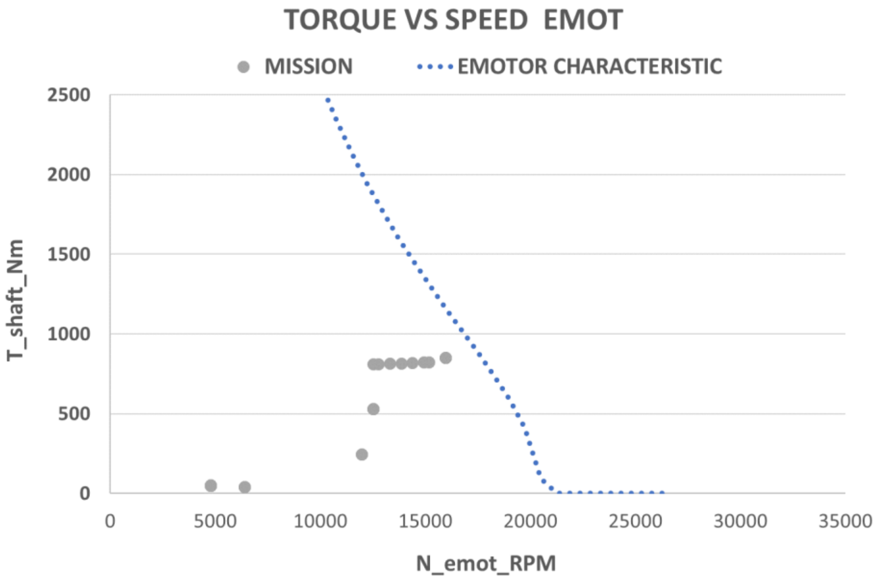

Fig. II-17: Set of solutions of Eq (10) in the torque speed plan for an example of electric motor characteristic and given a sizing voltage

In order to define the voltage value, the following equation is added:

$$V_{emot_{rms_{max}}} = \frac{V_{uHVDC}}{2.\sqrt{2}} . m_{a_{max}} \tag{II-13}$$

With:

- $m_{a_{max}}$ is the maximal value of depth modulation in [%],

Thanks to this modification the following design point input parameters are removed for the optimization:

- The torque design point $T_{emot_{siz}}$ in Nm,
- The mechanical rotational speed design point $N_{emot_{siz}}$ in RPM,
- The root mean square value of current density at design point $J_{rms_{siz}}$ in A/mm²,

Finally, based on this analysis, a review of the electric machine design model is proposed where the initial decision variable ($T_{em_{siz}}$, $N_{emot_{siz}}$) are suppressed. In the same time, the current density at design point $J_{rms_{siz}}$ has been replaced with the ratio between slot height and stator inner radius ($R_{hs_{ral}}$).. Now, the ultra-high direct current voltage V_{uHVDC} is used in order to set the maximal value of e-motor voltage by applying the equation (10).

II.2.1.2.5 Summary of changes and final model checking.

Table II-1 : Summary of changes between the initial sizing model and the integrated model used in optimization.

Initial set of input parameters	1st modification	2nd modification	3rd modification	Final set of input parameters
$T_{em_{siz}}$	-	-	×	×
N_{siz}	-	-	×	×
σ_T	-	$R_{alesage}$	$R_{alesage}$	$R_{alesage}$
$J_{rms_{siz}}$	-	-	$R_{hs_{ral}}$	$R_{hs_{ral}}$
$R_{Drot_{ral}}$	-	-	-	$R_{Drot_{ral}}$
$R_{g_{ral}}$	-	-	-	$R_{g_{ral}}$
$B_{gap_{rms}}$	$R_{pm_{ral}}$	$R_{pm_{ral}}$	$R_{pm_{ral}}$	$R_{pm_{ral}}$
B_{yoke}	-	-	-	B_{yoke}
B_{teeth}	-	-	-	B_{teeth}
N_{ce}	-	-	-	N_{ce}
p	-	-	-	p
n_{epp}	-	-	-	n_{epp}

The original model needed 12 input parameters to design the electric machine. Now thanks to the previous changes resulting from the causality analysis, only 10 decision variables are required. Several optimizations have been perfomed for different values of V_{uHVDC} showing the consistency of this choice. All results are consistent now.

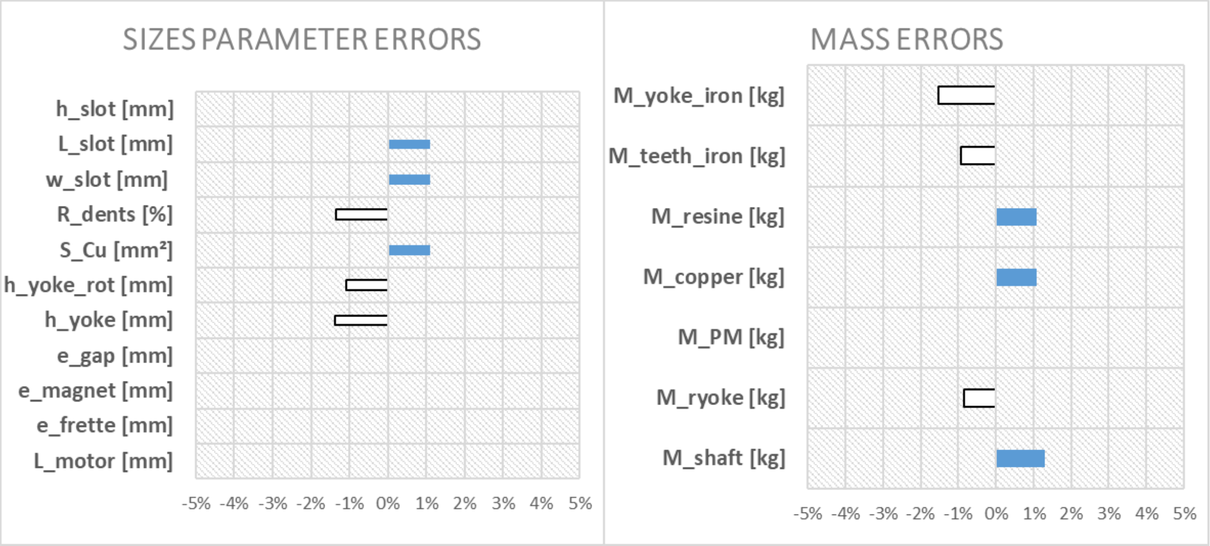

Fig. II-18: Differences between the new model and the original model.

A final checking has been done in order to ensure representativeness between the original model and the integrated. The Fig. II-18 highlights the fact that the new model is well representative, most errors are below 2%, it can be emplemented in the optimization process. The new model equations are described in the Appendix F.

II.2.2 Electric machine cooling system.

II.2.2.1 Presentation of the e-motor cooling research team model.

The cooling system integrated in our MDO integrated process has been developed in the HASTECS framework (Work Package 3) bt the Pprime institute, especially by Amal Zeaiter [87].

In general, a cooling system is used to maintain the temperature controlled on the device to be cooled by evacuating the required thermal load. To accomplish this function, two different methods can be used:

- Cool the device by directly using external air (air cooling also qualified as open loop circuit cooling).
- Cool the device by using an intermediate circuit (liquid cooling also qualified asclosed loop circuit cooling).

In order to have smarter and more efficient solutions, only closed loop circuits will be considered here.

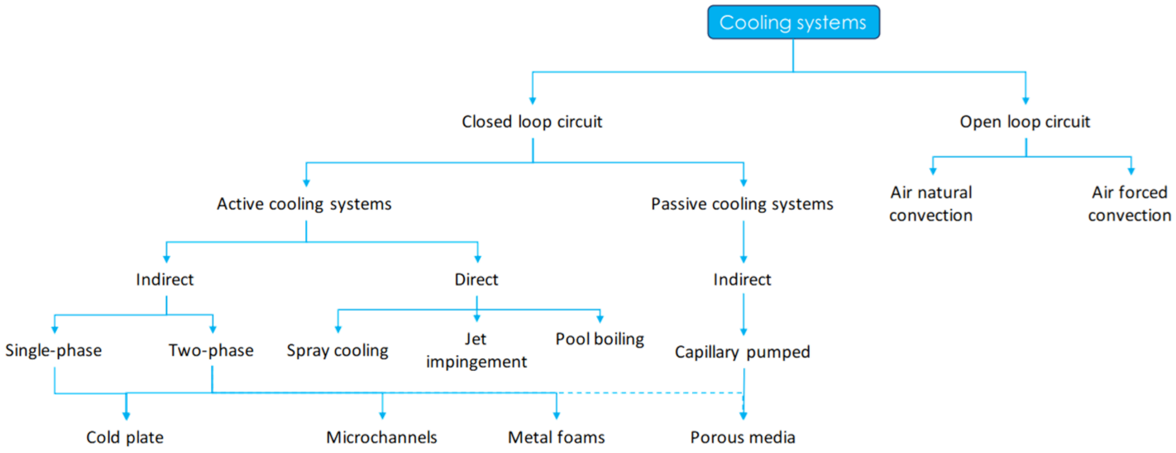

Fig. II-19: Cooling systems classification [88].

According to [88], closed loop circuits cooling systems can be divided into two categories: active and passive cooling. Active cooling systems are characterised by the presence of a pump or a compressor, following the technology, to move the fluid into the circuit. For the electric motor cooling an active cooling system has been considered:

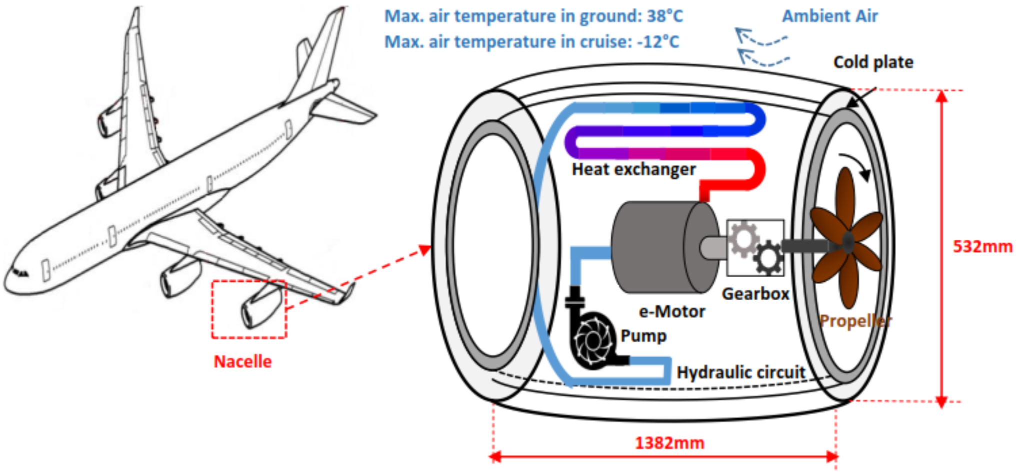

Fig. II-20: Nacelle architecture (electric machine and its cooling system) [83], [87].

The heat exchanger is completely part of the nacelle skin. The cooling primary circuit is composed of a heat exchanger placed near to the cold source, a hydraulic circuit and a pump [87]. Heat exchanger allows the evacuation of heat generated by electric motor to the outside air through plate embedded around the nacelle. It is composed of pipes and a cold plate. Inside the e-motor there is a shaft cooling channel to cool down the rotor part and a water jacket in order to cool the stator part.

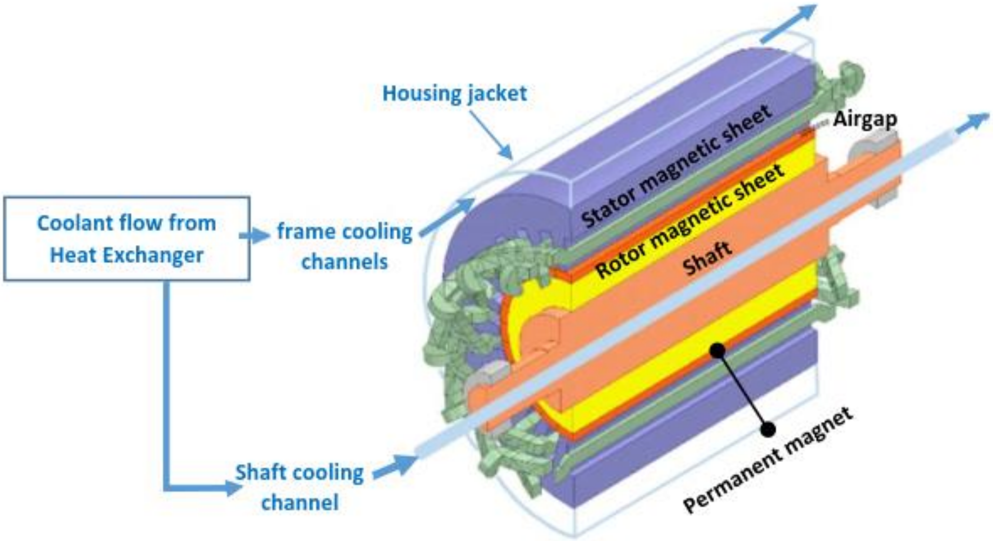

Fig. II-21: Cross section of the electric motor schematic (with its cooling system) [83], [87].

The model will be presented in Appendix G.

II.2.3 Modeling of partial discharges.

II.2.3.1 Presentation of the partial discharges model.

The environement constraint due to high voltage issues and partial discharges phenomenon influencing the insulation system was studied in HASTECS by the LAPLACE/MDCE research team, especially in the PHD thesis of Philippe Collin [89]. The aim of this work package (WP5) is to provide one tool to help designers in order to avoid or to reduce Partial Discharges (PD) that may occur in the Electrical Insulation System (EIS) of motors. If the electric motor voltage is higher than 700 V (2025 target for the WP5 [90]) (i.e.: high voltage value), this tool will reduce both level and amount of PD occurring in the EIS that has been specifically designed to resist to PD. In the literature, the Paschen's criterion [91] is widely used for determining if there partial discharges may occur or not. However, this criterion has been established for metallic plane electrodes.

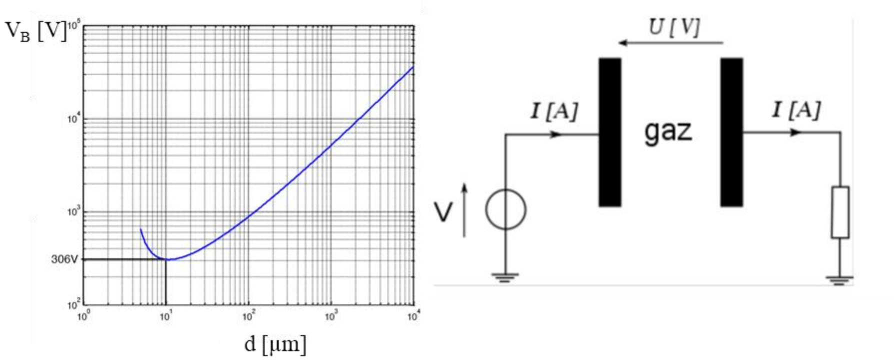

Fig. II-22: Paschen curve in air gap between plane electrodes at normal conditions and at p =760 Torr.

The previous study has been carried out at ambient temperature (20°C) and ambient pressure (1 bar). To be more accurate with the reality, a finite element software is used in order to compute the voltage distributionin the stator slot for the electric motor. Matlab Software is used to process the data. The tools are presented in the following figure:

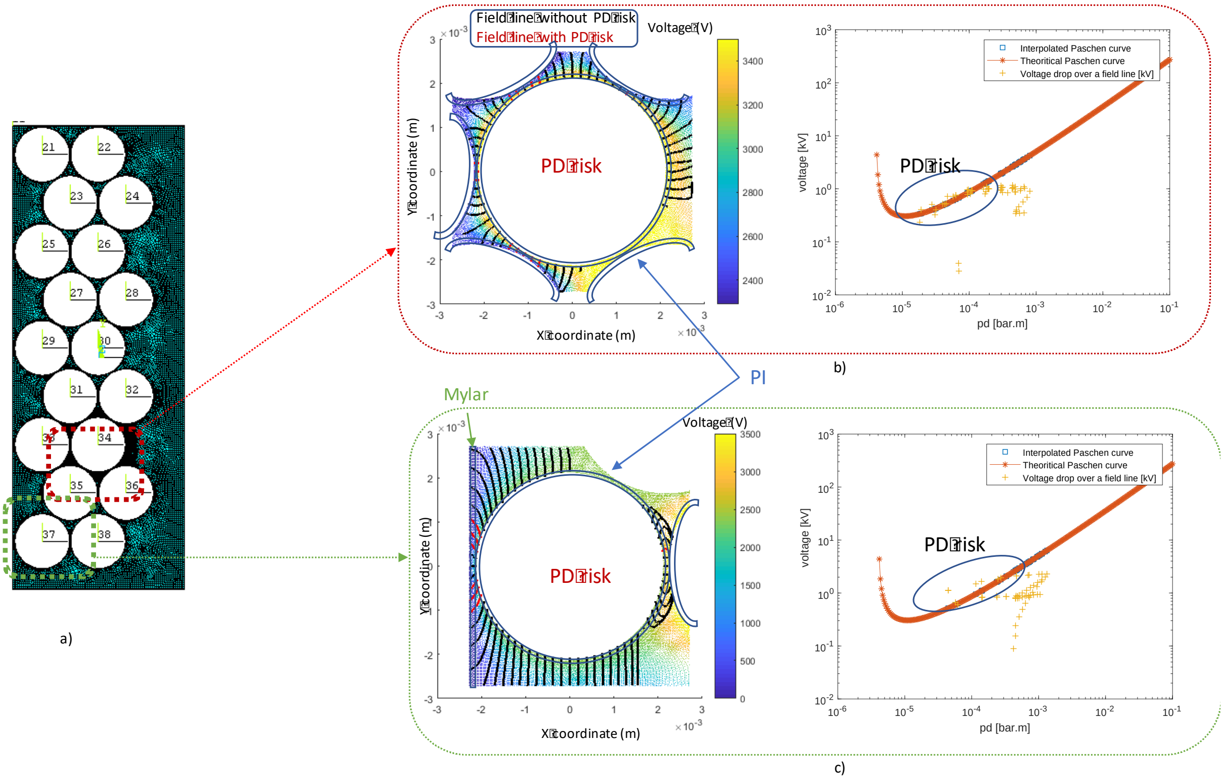

Fig. II-23: WP5 tool outputs: (a) FEA software mesh; (b) & (c) electric field and voltage drops along fields lines (p=1bar).

The figure represents two high-risk areas:

- Between conductors
- Between the stator yoke and the conductor.

Two strategies are developed in order to avoid discharges in these areas: the first is to increase the enamel thickness and the second consists in the integration of a liner in the stator slot. The process is explained in the [92] and [89]:

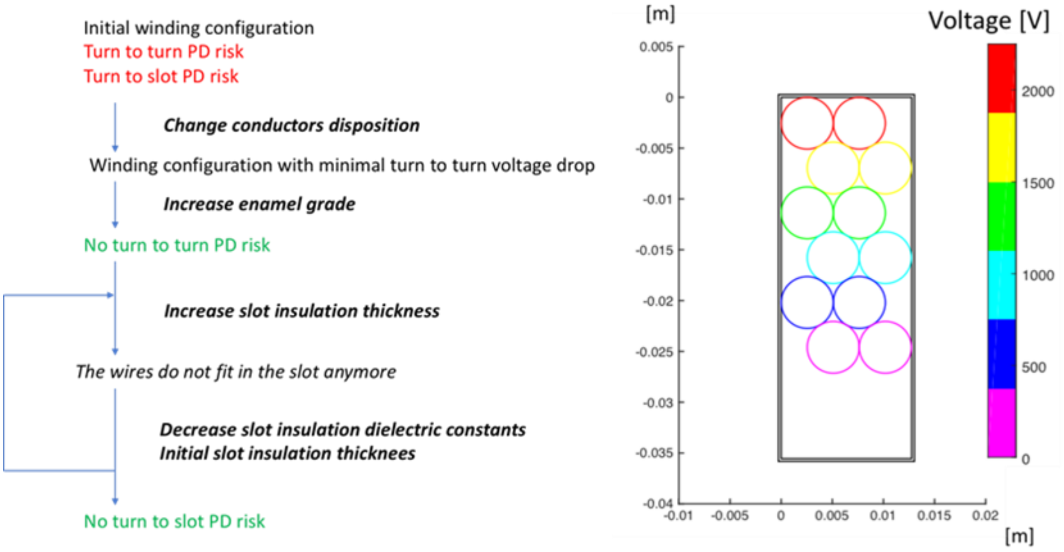

Fig. II-24: WP5 tool process (left), example of a PD free solution with 6 conductors (right) .

The loop between the ANSYS finite element software and Matlab allows determining the high-risk locations for the partial discharges. Considering the computational cost, it was impossible to integrate the whole process in an overall optimization. The next part of the chapter deals with the model adapation.

II.2.3.2 Adaptation for system optimization.

The Paschen curve has been established for normal conditions, but in stator slots, winding temperature can reach 200°C. An abacus taking temperature and pressure conditions into account is integrated into the design process.

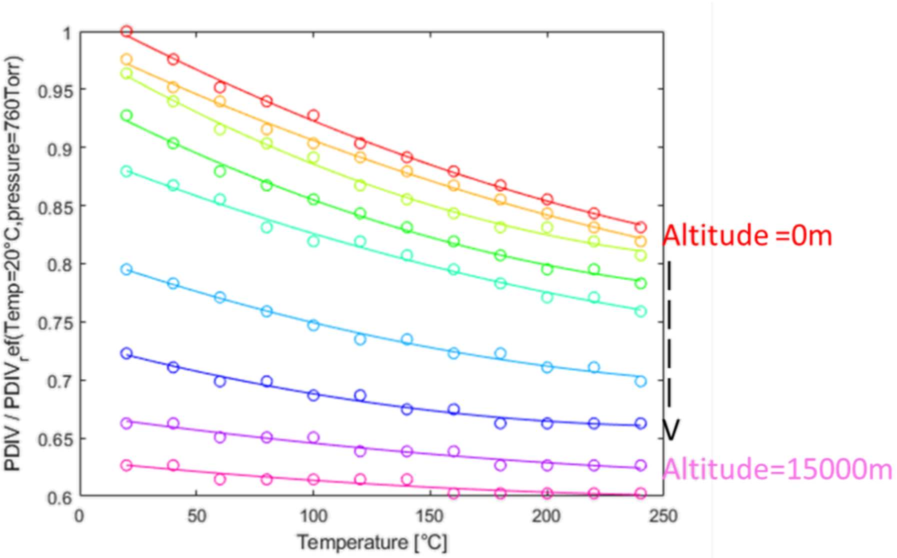

Fig. II-25: Decrease of PDIV for a combined variation of pressure and temperature.

Regarding this figure, a high sensitivity with regard to environmental conditions is highlighted. The PDIV is the maximum withstand voltage value, and it is decreasing with the altitude and the temperature. In order to avoid voltage, overshoot another abacus is considered.

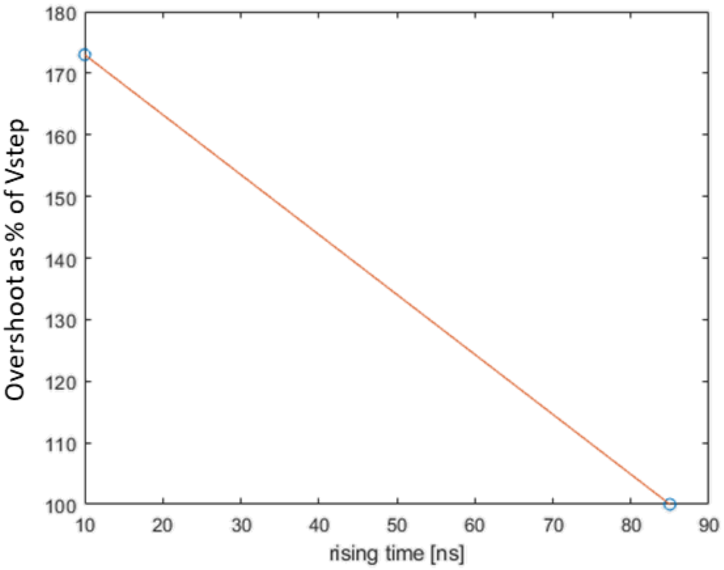

Fig. II-26: Voltage phase overshoot evaluation as a function of the switch rise time.

In the HASTECS case the 7th generation of Mitsubishi IGBT has been considered, with a switch rise time of 200 ns, so there is no overshoot case. Finally, the process presentend Fig. II-24 is used in order to find the right winding configuration. For the complete model, polynomials are created from the FE software in order to reduce the CPU time.

II.2.4 Power Electronics design model.

II.2.4.1 Presentation of the power electronics model and results.

For the power electronics (PE) the work objective is to design a highly integrated inverter with a specific power of 15 kW/kg for 2025 target and 25 kW/kg for 2035 target including its cooling system. The main factor to increase the specific power is finding a trade-off between cooling and electric device masses, the bigger the losses, the heavier the cooling. A study has been realized by the WP2 in the HASTECS project demonstrating that the 2-level power module design was not feasible to achieve the targets. As a consequence, multilevel converters were selected. The Fig. II-27 illustrates the multilevel converter classification. The chosen converter topologies resulting from the WP2 study are underlined in red circles [93].

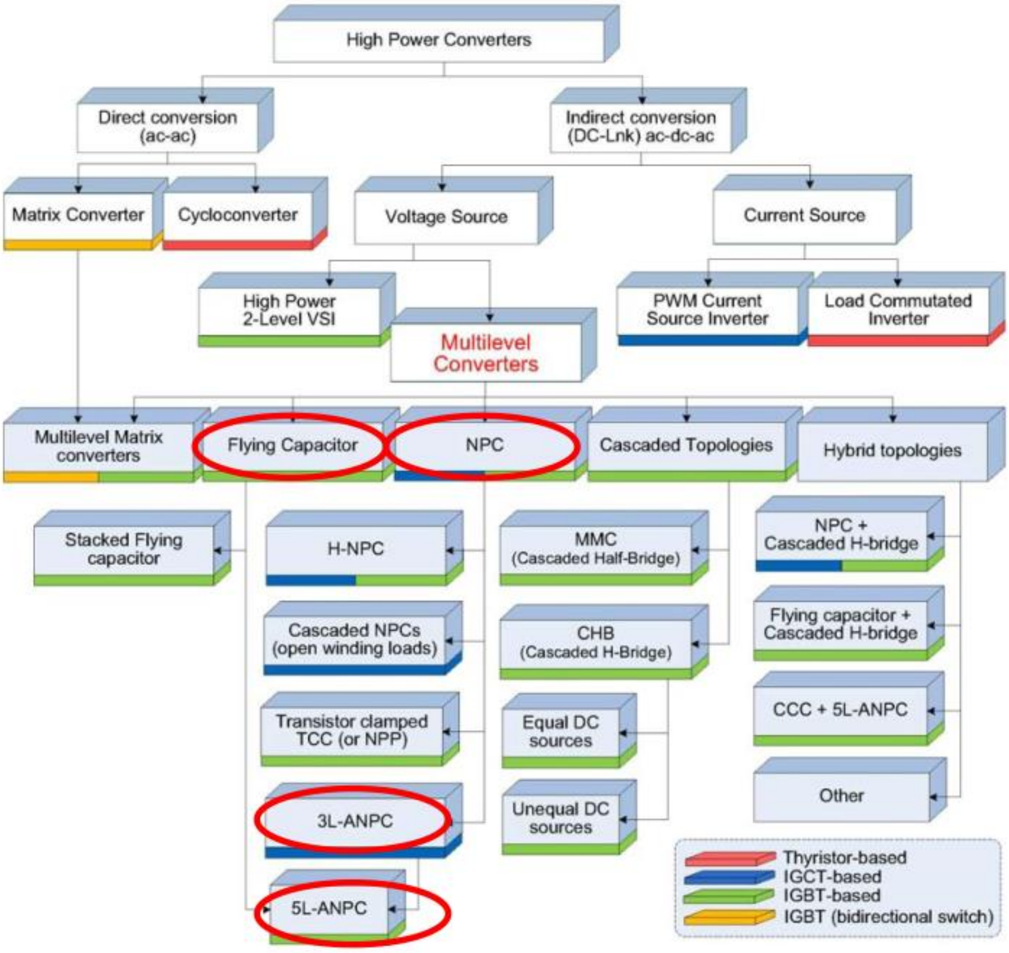

Fig. II-27: Multilevel converter classification.

Where:

- NPC is the Neutral Point Clamped,
- FC is the Flying Capacitor,
- SMC is the Stacked Multicellular Converter.
- ANPC is the Active NPC topology.
- xL denotes the number of levels.

The simulation tool used by WP2 permits us to design these converters with different control strategies. The software organization is described in the following figure [93]:

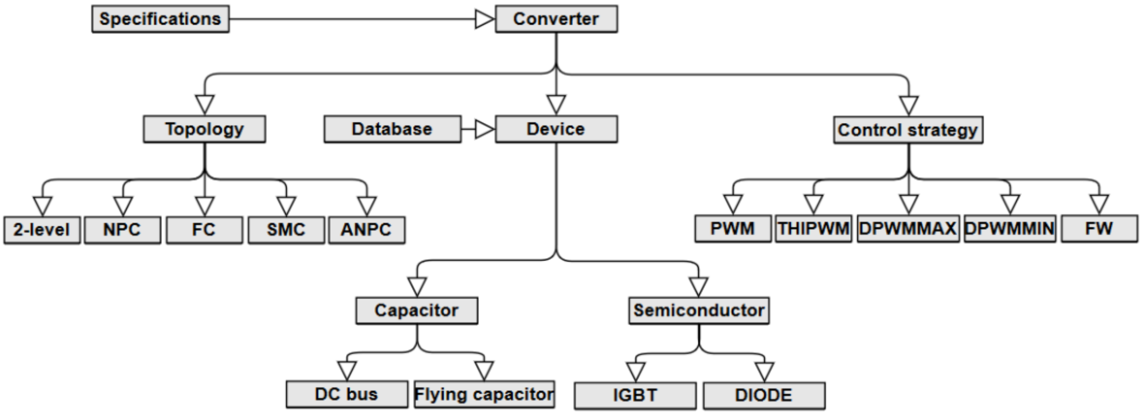

Fig. II-28: Simulation tool organisation.

In order to adapt this simulation tool for system optimization, a performance study has been performed by the power electronics research team to select best topologies.

II.2.4.2 Adaptation for system optimization.

A lot of topologies have been studied and best converters have been selected to adapt this model for system optimization [94]. In fact, DC bus voltage was not established, so the power converter team made a trade-off between best efficiency and maximal specific power at DC bus values.

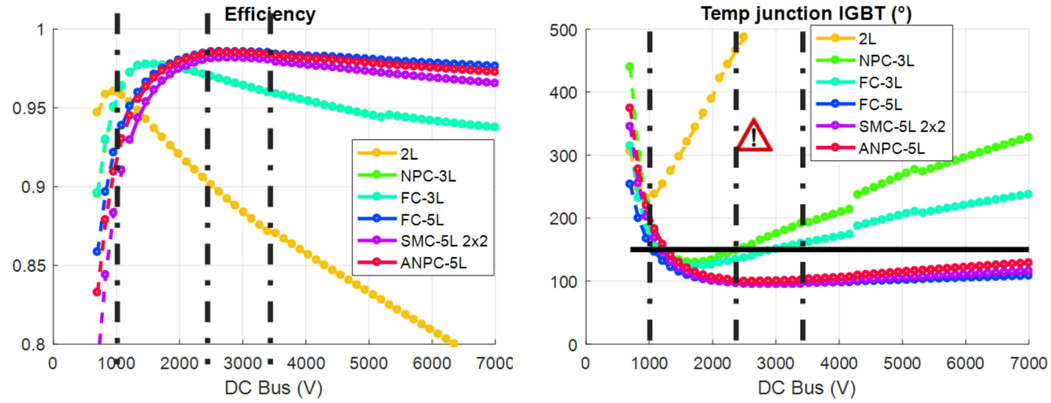

Switching frequency (Hz)	Topology	Maximal specific power (kW/kg)	Corresponding DC bus voltage (V)	Efficiency (%)
5855	2-level	6.73	957	96.04
	3-level NPC	11.39	1600	97.76
	3-level FC	10.42	1730	97.77
	5-level FC	8.43	3143	98.53
	5-level SMC	12.24	3143	98.12
	5-level ANPC	14.05	3143	98.47
879	2-level	14.98	1986	98.19

- 5-level ANPC close to the 15 kW/kg target
- Low frequency switching with the 2-level topology

⇨ Used losses model accuracy

Fig. II-29: Comparison of possible solutions sized [94].

Considering specific power and efficiencies, the best multilevel configurations are:

- 3-Level NPC (Fig. II-30).
- 5-Level ANPC (Fig. II-31).
-

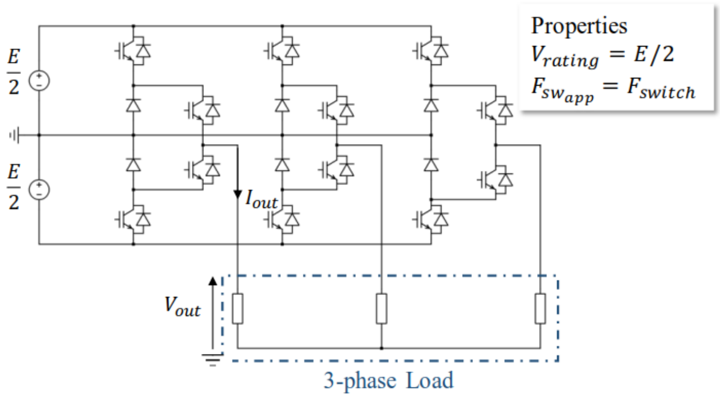

Fig. II-30: 3-level NPC inverter.

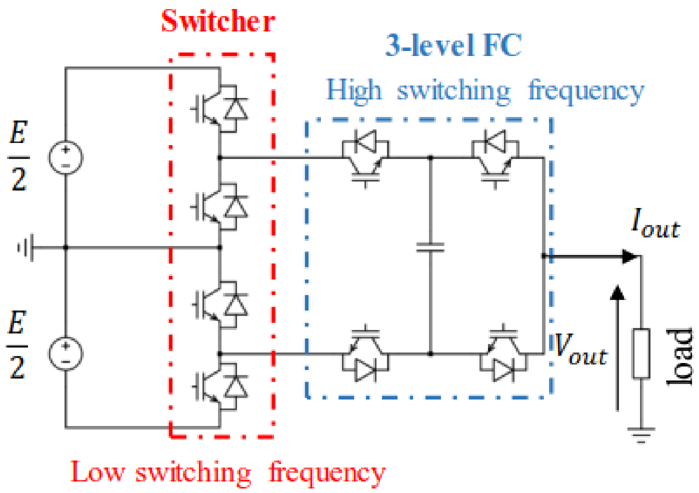

Fig. II-31: 5-level ANPC single phase inverter.

To simplify the use of the simulation tool only two control strategies and two IGBTs have been selected. At the end of the adaptation for system optimization, the following rule related to the bus voltage level has been established.

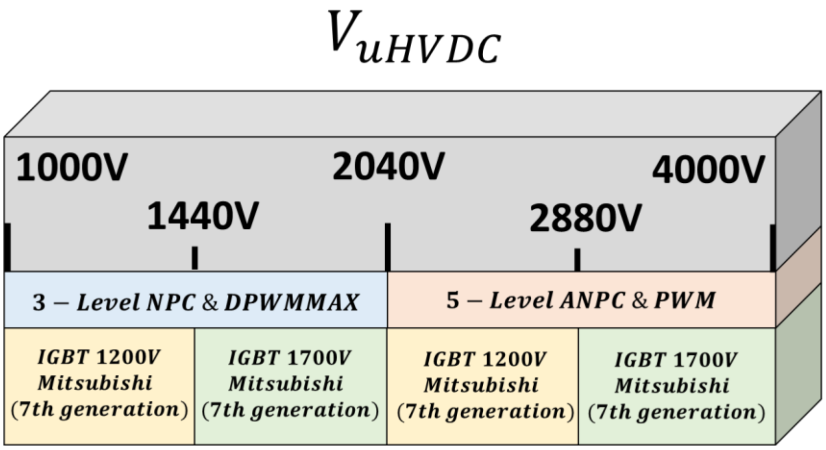

Fig. II-32: Voltage rule for determining the topology and the component to be used.

The first constraint equation permits us to choose the power electronics topology. The summary of topology properties is described in the following table:

Table II-2: Summary of converter topology properties.

Topology	**Number of Levels**	**Voltage rating**	**Output switching frequency**	**Passive components**
2-levels	2	V_{uHVDC}	f_{sw}	-
FC N cells ($N \geq 2$)	$N+1$	$\frac{V_{uHVDC}}{N}$	$f_{sw} \times N$	(*N*-1) Capacitors
3-levels NPC	3	$\frac{V_{uHVDC}}{2}$	f_{sw}	-
(1×2)-levels SMC	3	$\frac{V_{uHVDC}}{2}$	f_{sw}	-
($n \times p$)-levels SMC	$n \times p + 1$	$\frac{V_{uHVDC}}{n \times p}$	$f_{sw} \times n$	*N* Capacitors
5-levels ANPC (FC 2cells)	5	$\frac{V_{uHVDC}}{4}$	FC cells = $f_{sw} \times 2$ Switcher: $f_{low_{frequency}}$	1 Capacitor

The maximal DC bus voltage value for the 3-level NPC topology is determined by the maximal value of the voltage rating. In this case, two IGBTs are used, the first voltage rating is 1200V and the second is 1700V. The DC bus voltage range covered by the 3L – NPC is determined by Eq (II-14)[93]:

$$V_{uHVDC} \leq K_{v_{max}} \times V_{IGBT_{rating_{max}}} \times (N_{level} - 1) = V_{limit_{NLevel_{PE}}} = 2040 \text{ V} \qquad \text{(II-14)}$$

Where:

- $K_{v_{max}}$ is the maximum voltage utilization rate of the component in [%],
- $V_{IGBT_{rating_{max}}}$ the maximum voltage rating given by IGBTs datasheet in [V],
- N_{level} the number of level of the converter topology [-],
- $V_{limit_{NLevel_{PE}}}$ is the voltage limit for the N-Level power electronics topology in [V],

$K_{v_{max}}$ has the value of 60%, and $V_{IGBT_{rating_{max}}}$ has the value of 1700 V:

- The voltage limit value is 2040 V for a 3-level NPC power converter.
- The voltage limit value is 4080 V for a 5-level ANPC power converter.

After choosing the converter topology, The IGBT choice (1200V or 1700V) is determined by the Eq (II-15).

$$V_{IGBT_{rating}} \geq \frac{V_{uHVDC}}{K_{v_{max}} \times (N_{level} - 1)} \qquad \text{(II-15)}$$

II.2.5 Power converter cooling system.

II.2.5.1 Presentation of the power electronics cooling model.

This aspect has been studied into details by the Pprime institute which was in charge of a dedicated Work Package (WP4) in the HASTECS project, especially in the framework of Flavio Accorinti's PHD thesis [88], [95], [96].

In contrast to active cooling systems, passive cooling systems do not require any external source of energy to move the coolant. Neglecting systems using natural convection because of its low heat transfer coefficient, here we will only refer to two-phase passive technologies. Passive cooling systems use gravity or capillary forces to make the fluid flow into the loop. For the power electronic cooling system, the passive method has been studied, in particular the Capillary Pumped Loop for Integrated power (CPLIP). This is a two-phase passive loop which design has been enhanced from classical CPLs. Thanks to gravity and a higher thermo-hydrauliccoupling between the compensation chamber and the evaporator, linked by a vertical tube, problems affecting CPLs were solved in CPLIP. Mass exchanges are so possible: the liquid contained in the reservoir is forced by gravity to come down to the evaporator, and if vapour bubbles are formed in the latter, they can return to the tank.

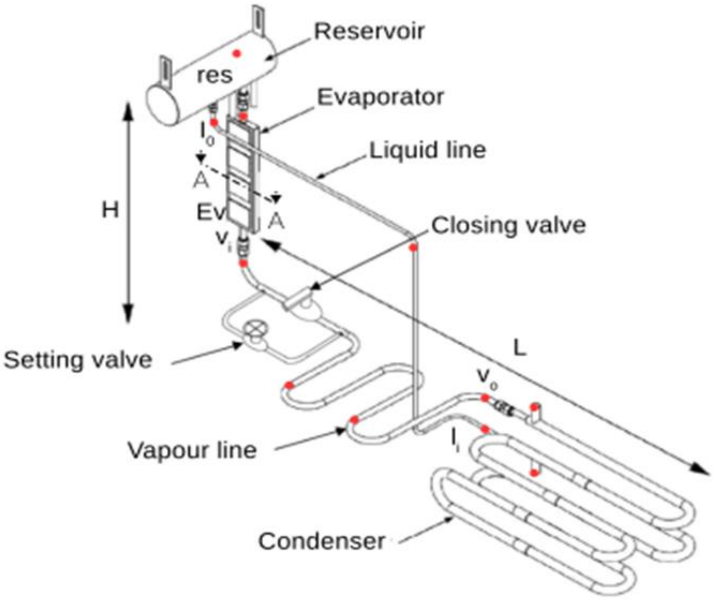

Fig. II-33: CPLIP schematic [88].

The semiconductor modules are placed on both evaporator sides as shown in Fig. II-34. This was recommended by WP4 to take advantage of both the evaporator side in order to evacuate the thermal losses and balance the constraints on both sides. This solution will also help to reduce the volume and weight of the inverter since it creates a more compact inverter and divides by 2 the number evaporators compared to the use of one side of the evaporator. In this case, we end up with 3 evaporators in parallel for the three phases instead of six.

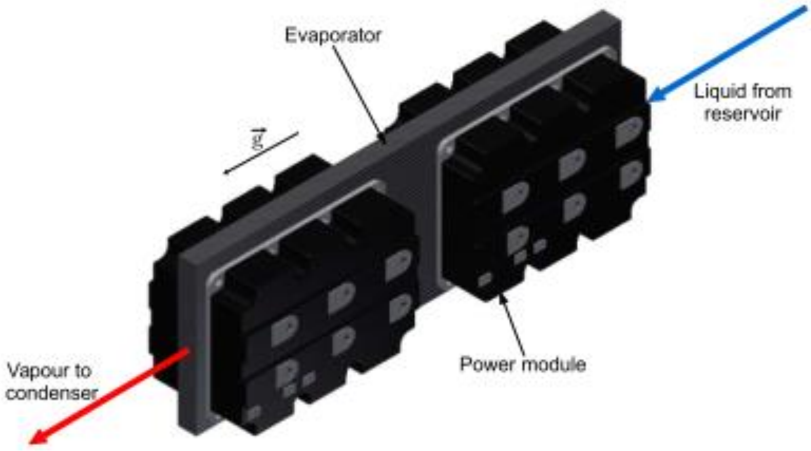

Fig. II-34: Module/evaporator assembly [93].

II.2.5.2 Adaptation for system optimization.

A meta-model totally discouplingthe thermal from the other physical fields has been created for the power electronic module. The calculation of the cooling mass is obtained through a simple surrogate model (seeAPPENDIX I). Converter losses are directly translated into kilograms of cooling system for both targets (2025 and 2035) [88].

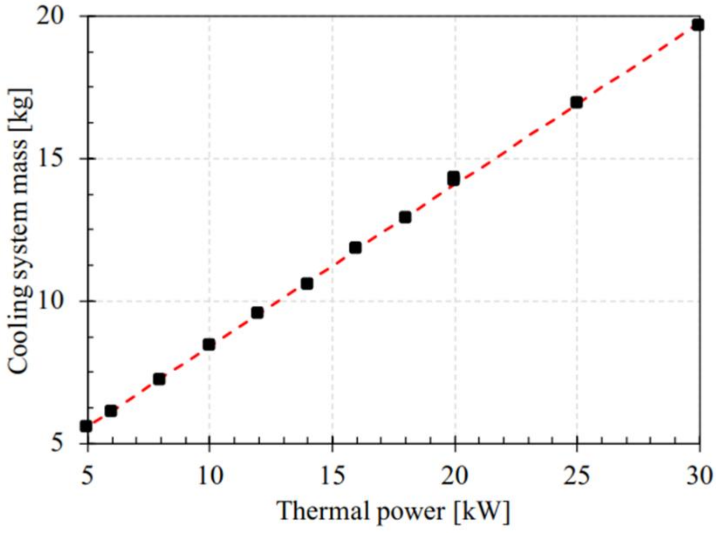

Fig. II-35: CPLIP mass variation as function of the heat power (2025 Target).

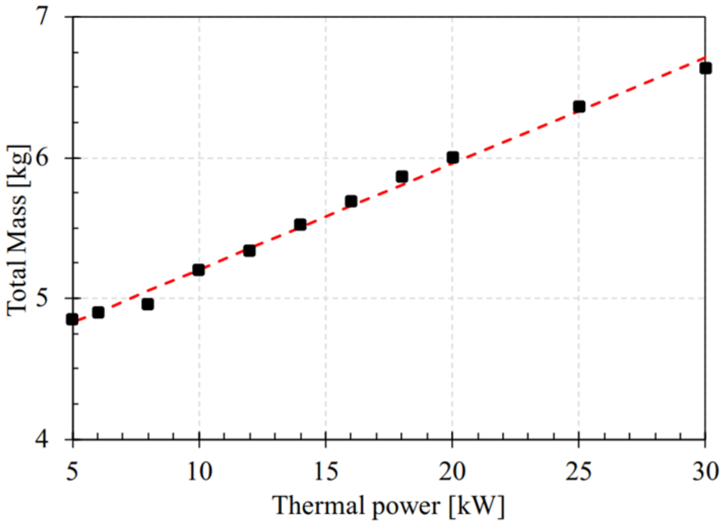

Fig. II-36: CPLIP mass variation as function of the heat power (2035 Target).

II.2.6 Fuel cell and battery model.

This part deals with the auxiliary electric sources hybridizing the main thermal engines, i.e. batteries and/or Fuel Cells (FC) with their associated H_2 storage. A review of the state of the art and a prospective study has been detailed in Laplace by M. Tognan in [97]. In order to limit the study inside reasonable borders, three Lithium-ion battery “families” are pre-considered:

- High Power type: Lithium Titanate Oxide (LTO) anode based Li-ion battery, or their more modern version replacing LTO for a mixed valency Ti-Nb oxide ($TiNb_2O_7$).
- High Energy type: Nickel Manganese Cobalt (NMC) cathode based Li-ion battery (coupled with a graphite anode – cells using Si at the anode are also included here).
- Very High Energy type: Lithium Sulfur (LiS) cathode based battery.

Based on that study, the following assesments in terms of energy density have been proposed at cell level.

Table II-3: Electrochemical source assumptions.

Specific energy e_m (Wh/kg @ cell scale)	Today	2025	2035
High Power: LTO / TNO	~ 140 Wh/kg_{cell}	~ 180 Wh/kg_{cell}	~ 200 Wh/kg_{cell}
High Energy: NMC	~ 250 Wh/kg_{cell}	~ 350 Wh/kg_{cell}	~ 500 Wh/kg_{cell}
Very-high Energy: LiS	~ 500 Wh/kg_{cell}	~ 600 Wh/kg_{cell}	~ 650 Wh/kg_{cell}

In order to jump from the cell to the system (integrating packaging, cooling and BMS), constant integrating factor parameters (f_m and f_v) are considered ($kg_{system} = kg_{cell} * f_m$; $Vol_{system} = Vol_{cell} * f_v$). These values are estimated to be respectively: $\boldsymbol{f_m = 2}$ **and** $\boldsymbol{f_v = 2.5}$.

Based on these assessments batteriy energy densities are strongly limited at system level knowing that most powerful technologies in kWh/kg are often limited in terms of cycling performance and life duration.

For that reasons, hydrogen fuel cells seem more appropriate for our case study.

On Fuel Cell side, three technologies are examined:

- Low Temperature (∼ 70 °C) Proton Exchange Membrane Fuel Cell (LT PEMFC).
- High-Temperature (∼ 170 °C) Proton Exchange Membrane Fuel Cell (HT PEMFC).
- Solid Oxide Fuel Cell (SOFC) working at very high temperatures (∼ 800 °C).

Table II-4: Fuel cell specific power assessments.

FC stack and system specific powers & volumes p_m / p_v (kW/kg and kW/L)	Today	2025	2035
LT PEMFC	∼ 2 kW/kg_{stack} ∼ 0.6 kW/kg_{system} ∼ 3 kW/L_{stack} ∼ 0.3 kW/L_{system}	∼ 4 kW/kg_{stack} ∼ 1 kW/kg_{system} ∼ 5 kW/L_{stack} ∼ 0.8 kW/L_{system}	> 5 kW/kg_{stack} > 1.1 kW/kg_{system} > 6 kW/L_{stack} > 0.9 kW/L_{system}
HT PEMFC	∼ 0.4 kW/kg_{stack}	∼ 1 kW/kg_{stack}	-
SOFC	∼ 0.33 kW/kg_{stack}	-	-

Three H_2 storage possibilities are also considered: compressed H_2 (350 bara or 700 bara) in composite tanks (CH_2), liquid H_2 (T ∼ 20 K) in cryogenic tanks (LH_2), and H_2 storages through metal hydrides.

Table II-5: H2 storage specific energy assessments.

H_2 storage gravimetric efficiencies (-) and specific energy (Wh/kg based on H_2 LHV)	Today	2025	2035
Gazeous (700 bar)	∼ 5 – 7.5 wt. % ∼ 1.67 – 2.5 kWh/kg	∼ 10 wt. % ∼ 3.3 kWh/kg	> 10 wt. % > 3.3 kWh/kg
Liquid (20 K)	∼ 15 wt. % ∼ 5 kWh/kg	∼ 20 wt. % ∼ 6.6 kWh/kg	> 20 wt. % > 6.6 kWh/kg
Solid (metal hydrides)	∼ 2 – 3 wt. % ∼ 0.67 – 1 kWh/kg	∼ 7 wt. % ∼ 2.3 kWh/kg	> 7 wt. % > 2.3 kWh/kg

Due to readiness level and performance, the selected technology for our study will be the Low Temperature Proton Exchange Membrane Fuel Cell. Contrarily to batteries for which power and energy figures are coupled, the fuel stack is sized from power requirements while stored gas volume (i.e energy) is driven by the mission profile. Thus, to compare battery with fuel cell solutions in terms of specific energy (this factor being the most constraining in our requirements), the overall H2 system mass including fuel cell stack, auxiliaries and H2 storage with the gas volume to fulfill the whole fight mission must be estimated. From that estimation, the table below clearly shows that battery technologies are outclassed by fuel cells:

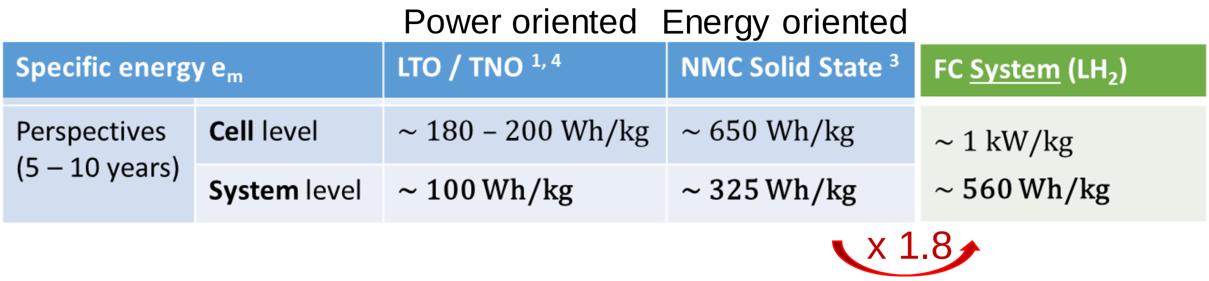

		Power oriented	Energy oriented	
Specific energy e_m		**LTO / TNO [1, 4]**	**NMC Solid State [3]**	**FC System (LH_2)**
Perspectives (5 – 10 years)	**Cell** level	~ 180 – 200 Wh/kg	~ 650 Wh/kg	~ 1 kW/kg
	System level	~ 100 Wh/kg	~ 325 Wh/kg	~ 560 Wh/kg

Fig. II-37: Technological comparison in terms of specific energy given the mission profile.

Looking at all these numbers the fuel cell coupled with liquid hydrogen storage seems to be the best trade-off from a specific power and specific energy point of view. Both models are detailed in Appendix K.

CHAPTER III. Sensitivity analysis on the hybrid-electric aircraft.

CONTENTS

In this chapter, we will focus on the sensitivity analysis of the powertrain, from a global vision at aircraft level to a local one at device level. First, a list of the different aircraft architectures with their associated energy management is presented in order to show the impact of our technological improvements on aircraft performance. A first study taking into account the snowball effects with the target hypotheses will be detailed thereafter. Finally, a global sensitivity analysis of the components will help us to remove the less sensitive variables of the propulsion system and set the decision variables of the optimization process developed in the next chapter.

III.1 New technologies that broaden the scope of possibilities.

III.1.1 Reference aircraft.

Our case study is a regional aircraft which means around 70 pax. For this kind of aircraft, the first reference MTOW is assumed around 23 tons with classical thermal engines without electrical propulsion. The propulsion system is composed of two propellers, two gearboxes directly driven by two turboshafts leading to an embedded mass (“propulsion mass”) of 2880 kg. The fuel mass consumed by this reference aircraft during its reference mission is 1160 kg,

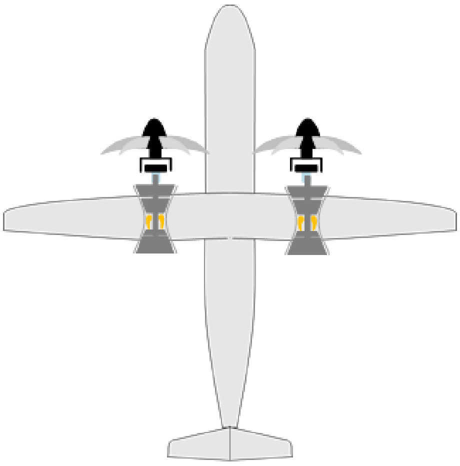

Fig. III-1: Reference aircraft architecture (REF).

III.1.2 Preliminary target results (2025 – 2035).

Several hybrid-electric architectures exist and are reported in the Fig. I-23. The aircraft studied in the next section are all fully powered by electric motors (no direct propulsion generated by gas turbines or turbojets).

III.1.2.1 TEA (TurboElectric aircraft).

In TEA architecture, two turboshafts sized at top of climb are the only power sources and the whole thermal power is converted in electrical power through electric generators (cf Fig. III-2). This architecture is studied with reference to a full thermal aircraft in order to compare the fuel burn saving with electrically driven propellers. This architecture is studied by the NASA with the N3X concept [33]. In this concept the distributed propulsive system permits the improvement of aircraft aerodynamic. But in the HASTECS project, only energy gains are focused and aerodynamic effects are not taken into account.

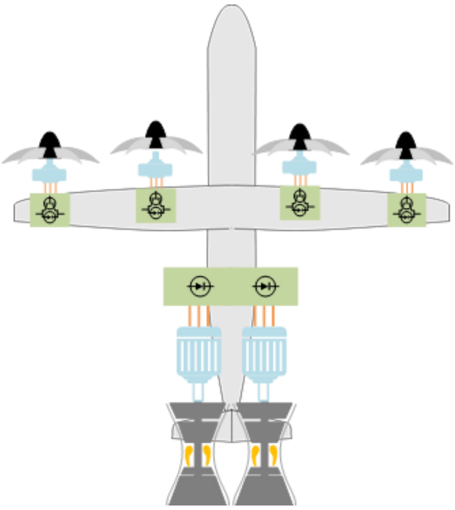

Fig. III-2: Turbo-Electric aircraft architecture (TEA).

III.1.2.2 HEA (Hybrid-electric aircraft).

Unlike the TEA architecture an auxiliary electrical power source is set up in HEA in addition to the main thermal sources. In the following, based on the study proposed in the previous subsection, the considered auxiliary source will be a fuel cell with a liquid hydrogen storage because it seems to be the most adequate candidate (see Fig. II-37) in terms of embedded weight [71]. Thanks to the source hybridization some degrees of freedom are useful to size the main turboshafts by optimizing the energy management. Thus, it results in several candidate architectures linked with several power management strategies.

III.1.2.2.1 Symmetrical HEA (HEASYM)

The first architecture is the “symmetrical hybrid electric aircraft” for which both turboshafts are equally sized: the electric power source (H2 fuel cell) is used for both full electric taxi phases and descent, which corresponds to a “light hybridization scenario” (no hybridization during take off, climb and cruise). These sequences require a low power demand where the turboshafts could be replaced by electric power sources which are really more efficient at low powers. In our case the specific fuel consumption variation of the turboshaft model is taken into account. At low rating the SFC evolution may be referred to a hyperbolic function (Fig. II-5). In that way, using auxiliary energy source in taxi/descent phases and switching off the main thermal source is energy efficient for a hybrid electric aircraft. However, a reliable and fast stop and go system is mandatory in order to be able to restart main engines in case of huge power demand or failures. The architecture schematic is the following:

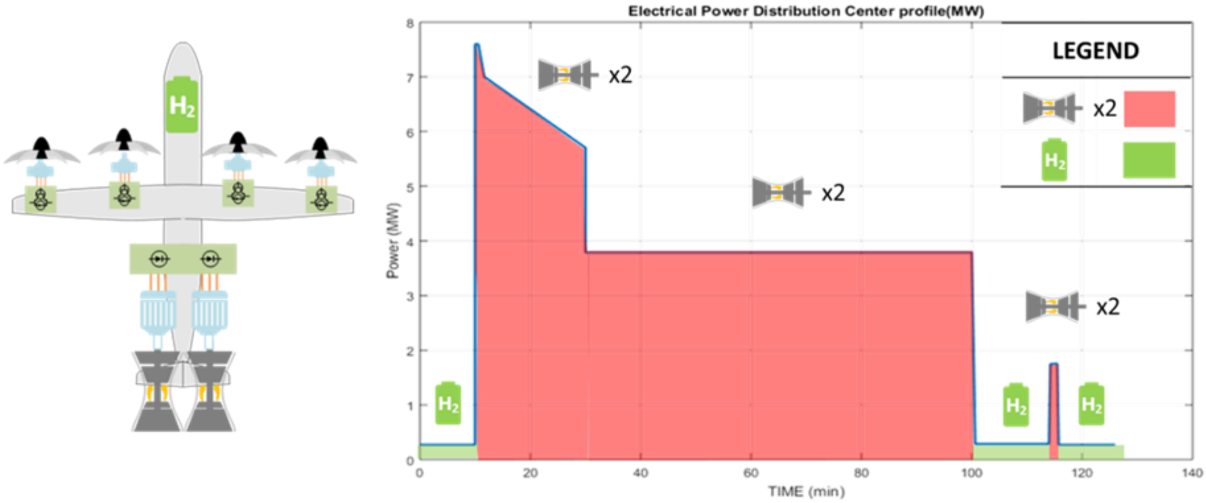

Fig. III-3: Symmetrical Hybrid Electric Aircraft (HEASYM) with the Energy management.

III.1.2.2.2 Asymmetrical architectures

The two next architectures are close to the previous one, except that both turboshaft sizing are not identical in the “Asymmetrical HEA structure” and that only one engine as the main source is considered in the “One engine HEA”. Thus, for these two architectures, particular safety criterion (related to major failure cases) has to be fulfilled: the take-off with one component failure has especially to be carefully studied, especially the One Engine Inoperative (OEI) case. In the OEI case, when the aircraft exceeds the “decision maximum speed” V_1, the take-off is mandatory during the acceleration phase whatever the failure occurrence beyond this speed limit. We have taken this failure case into account based on assessments related to the ATR datasheet (cf Fig. III-4):

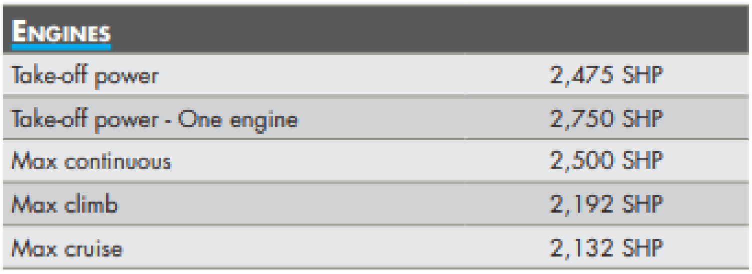

ENGINES	
Take-off power	2,475 SHP
Take-off power - One engine	2,750 SHP
Max continuous	2,500 SHP
Max climb	2,192 SHP
Max cruise	2,132 SHP

Fig. III-4: ATR 72-600 datasheet [65] .

In our case, we consider the same ratio between the “take-off power” versus “take-off power One engine” as in the case of the ATR. The value of this power ratio is then 1.11 (2.75/2.475). Finally, the main engine or/and the auxiliary electric source has to be sized according to this power requirement: in other words, the remaining power, whatever the one device failure case must be enhanced at least by 111% of the normal take-off power.

Asymmetrical HEA (HEA ASYM).

For this architecture, we asymmetrically design both turboshafts: the “main turboshaft” is sized for optimizing the efficiency during cruise while the “auxiliary turboshaft” is switched off. Both turboshafts are used for climb and during take-off at 100% of their rating powers. The auxiliary turboshaft is sized for the take-off phase in the event of an engine failure case; the electric source is required too during this failure case. Subsequently a boost for the top of climb is required, which is ensured by the fuel cell (green part in Fig. III-5).

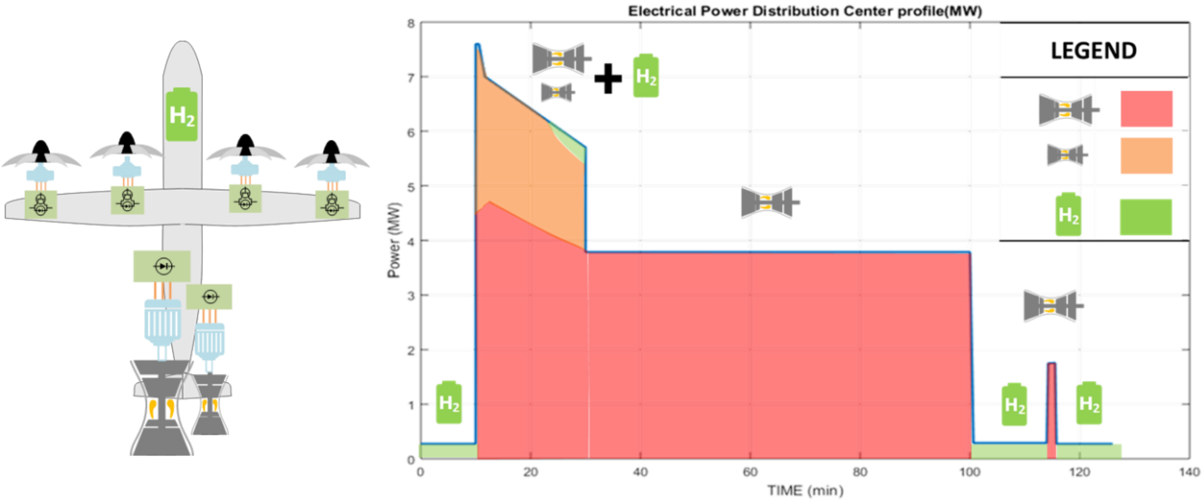

Fig. III-5: Asymmetrical architecture (HEA ASYM) with an energy management.

III.1.2.2.3 One Engine – HEA (HEA -1GT).

Following the same idea and in order to reduce the source rating, one architecture with only one gas turbine may be studied with a "huge hybridization". The remaining power is then supplied by a high power fuel cell: only two power sources are then considered. In such a case, both sources must be sized in order to face alone the take-off while the other source is failed (OEI case) beyond the V_1 limit of speed. Then, the propulsion system weight is reduced with only one turboshaft - electric generator – rectifier association. For this architecture, the MTOW is strongly reduced. This concept is used by Zunum Aero [44], a hybrid electric aircraft manufacturer startup.

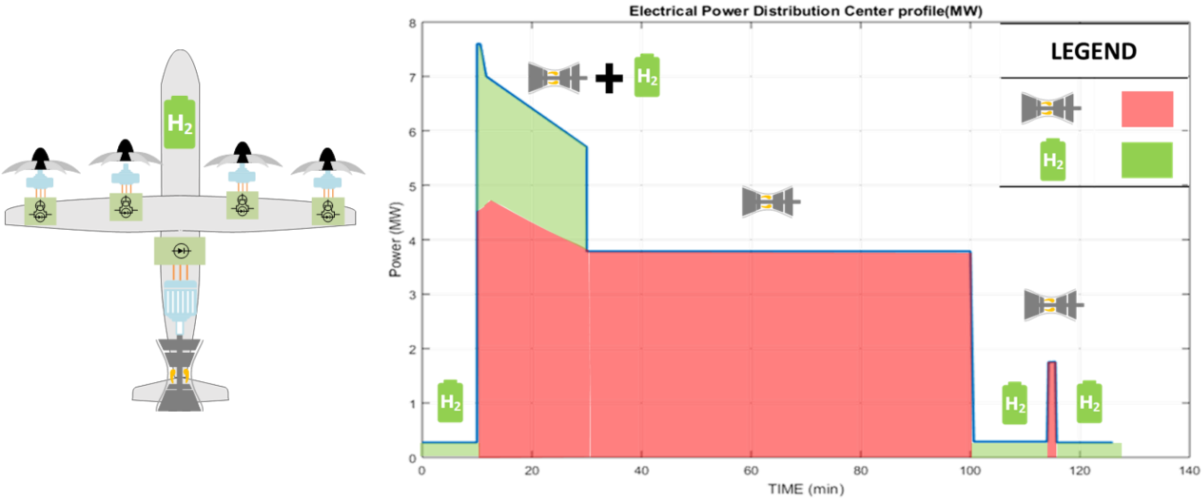

Fig. III-6: One Engine architecture (HEA-1GT) with one energy management.

This sub section has summarized a review of several series hybrid electric architectures. Different energy management scenarios can be guessed as emphasized in the previous examples which consist in an introduction on this topic.

For the rest of the work, the aircraft studied will be based on symmetrical architecture (HEA SYM) because of industrial choices.

III.1.2.3 Global sensitivity analysis of target assessments on global weight and fuel burn.

In this section, a preliminary sensitivity analysis based on target assessments can be done. Both targets (2025, 2035) with respect to the reference aircraft (see Fig. III-1) with full thermal optimized sizing are assessed in order to analyze the sensitivity of technological improvements with regard to the architectures previously presented in this chapter. For the asymmetrical architectures two aircrafts were designed:

- without the failure case of One Engine Inoperative (OEI).
- with the failure case of One Engine Inoperative (OEI).

Let us note that, while variable masses (variable specific powers) are assessed in the sensitivity analysis, snowball effects exist to assess the MTOW as emphasized in the chapter I: the looped process validated in the section I.3.3 is used to adapt the thrust during the flight mission with respect to the MTOW variations.

This global sensitivity analysis shows the effect of technological improvements assuming that 2025 or 2035 targets are reached as defined in the following table. Another "more aggressive" target (named "20xx target") has been guessed for analysis proposed in the next section of this chapter.

Table III-1: Electric component assessments.

	2025 target	**2035 target**	**20xx target**
		Emotor/ Egenerator	
Specific power	5 kW/kg	10 kW/kg	15 kW/kg
Efficiency	96%	98.5%	99%
		Power Electronics	
Efficiency	15 kW/kg	25 kW/kg	35 kW/kg
	98%	99.5%	99.8%
		FC stack + Liquid H2 storage	
H_2 **+ tank specific energy**		3.3 kWh/kg	
Auxiliary specific power		1.3 kW/kg	
Stack specific power		4 kW/kg	
		DC Bus Voltage	
Ultra HVDC		2000V	

Based on these assessments, the following analysis results show the positioning of each architecture in the MTOW vs fuel burn plan with reference to the full thermal optimized aircraft ("reference aircraft").

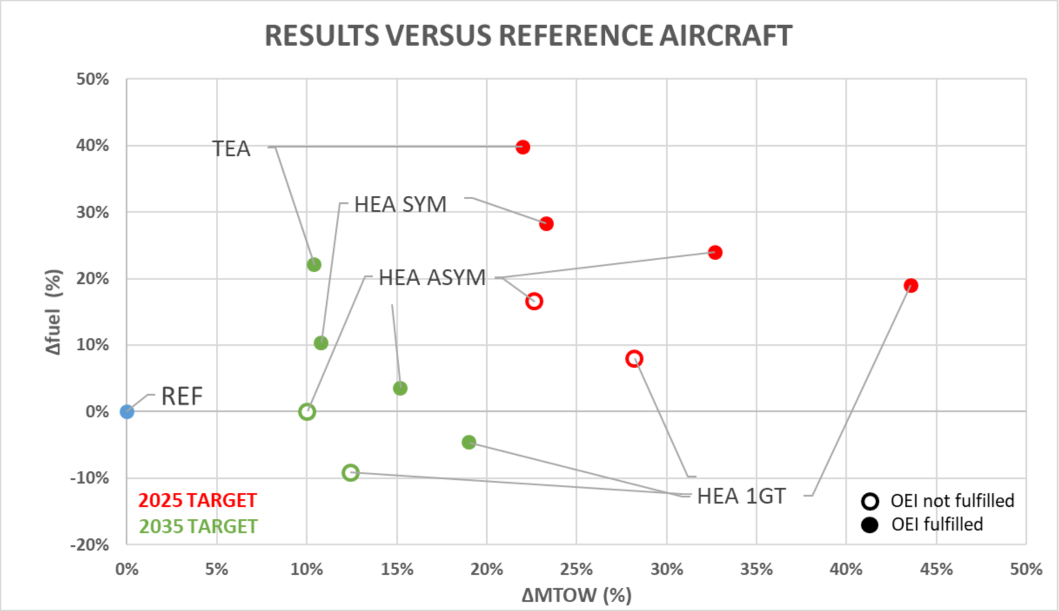

Fig. III-7: Summary of results versus reference aircraft with both targets.

The aircraft performance is really improved crossing from the 2025 to the 2035 target assessments whose specific powers and efficiencies are enhanced. The improvement of electric components is then really sensitive on the design performance of future hybrid-electric aircrafts. The snowball effects due to the weight added to the propulsion system strongly impacts the fuel consumption. Moreover, failure cases, especially the OEI (One Engine Inoperative) must not be neglected. In every case, the MTOW of electrically powered aircrafts are higher than the full thermal reference which seems normal as several devices (power converters, electric generators and motor, etc) are added in the electric powertrain.

In the next section, a further sensitive analysis has been realized using an analysis method based on the Sobol indices. Firstly, studies were carried out at aircraft level in order to retrieve the results previously presented in the chapter I (see Fig. I-62 & Fig. I-63). Then, a local analysis at component level is highlighted. The impact of each design variable on both weight and efficiency of the corresponding device is analyzed.

III.2 Sobol indices-based sensitivity analysis.

In order to prepare the global optimization of the overall hybrid-electric powertrain, a study of each design model of devices has to be assessed with the aim of limiting the number of decision variables. The issue is the selection of the most sensitive variables at the powertrain level.

Among the sensitivity analysis methods, the Sobol indices appeared as one of the most promising. G. Chastaing's, work [98] deals with Sobol indices for global sensitivity analysis.

Such indices were used for dependent variable values in the case study related to an energy efficient building design. Another reference uses these indices to study the most impacting variables of a problem such as the optimization of a cooling system of an electromechanical actuator [99]. In our case, variables are assumed to be independent.

III.2.1 An overview of Sobol indices.

Sobol indices allow identifying particularly sensitive input variables, X_i, with regard to certain output mean values, Y. Such indices are obtained by decomposition of the variance in the case of independent inputs. Model output may be written as follows:

$$f : \mathbb{R}^n \to \mathbb{R}$$
$$[X_1, X_2, X_3, \dots, X_{nb_{var}}] \to Y$$

Following the Hoeffding decomposition [100], the output variable is:

$$Y = f_0 + \sum_{i-1}^{nb_{var}} f_i(X_i) + \sum_{1\leq i\leq j\leq nb_{var}}^{nb_{var}} f_{i,j}(X_i) + \cdots + f_{1,2,\dots,nb_{var}}\left(X_1, X_2, \dots, X_{nb_{var}}\right) \tag{III-1}$$

Where f_0 is constant and calculated by the mean of Y, f_i is a function of X_i, *nbvar* is the number of variables, i and j are the indices. To obtain variance decomposition expression, *f* function is assumed to be square-integral, while the decomposition may be squared and integrated. Dividing Eq.(III-1) by the output variance $Var(Y)$ the following equation is obtained:

$$1 = \sum_{i-1}^{nb_{var}} \frac{V_i}{Var(Y)} + \sum_{1\leq i\leq j\leq nb_{var}}^{nb_{var}} \frac{V_{ij}}{Var(Y)} + \cdots + \frac{V_{1,2,\dots,nb_{var}}}{Var(Y)} \tag{III-2}$$

Where

$$V_i = Var(\mathbb{E}[Y|X_i]) \tag{III-3}$$

$$V_{i,j} = Var\left(\mathbb{E}\left[Y\middle|X_i, X_j\right]\right) - V_i - V_j \tag{III-4}$$

Sobol indices, S_i, $S_{i,j}$,… are defined as follows. They may be of different orders: first order indices express the effects of each variable, X_i with respect to the output Y, but not considering correlation effects between inputs which are considered in the terms $S_{i,j}$:

$$0 \leq S_i = \frac{Var(\mathbb{E}[Y|X_i])}{Var(Y)} \leq 1 \tag{III-5}$$

$$0 \leq S_{i,j} = \frac{Var\left(\mathbb{E}\left[Y\middle|X_i, X_j\right]\right)}{Var(Y)} - S_i - S_j \leq 1 \tag{III-6}$$

Second order indices express correlations between two input variables X_i, X_j.
Finally, total order indices: consider the effects of the X_i variable alone and the correlation effects of all other X_j with $j \neq i$.

III.2.2 Calculation process of the Sobol indices.

Multidisciplinary system studies require the variation of a large number of variables. Most computers are limited by their storage, that is why it is necessary to adopt new calculation methods. In this part two methods have been compared. A choice has been made in order to approximate the indices by limiting the calculation time:

- The ANOVA (Analyze Of VAriance) method based on a regular disposition of the inputs (with nb_{pts} the number of level). In the example of an electric motor model the number of calculated points is: $\boldsymbol{(nb_{pts})^{nb_{var}} = 4^{13} = 67 \times 10^{6}\ pts}$.

- The Pick and Freeze method [101], [102], [103], based on two random samplings of the inputs. In the example of the electric motor model the number of calculated points is:
  $\boldsymbol{2 \times nb_{pts} \times nb_{var} = 13 \times 10^{5}\ pts}$.

The difference in the number of evaluations between the two methods is equivalent to the ratio expressed by Eq. (III-7):

$$\frac{ANOVA_{eval}}{Pick\&Freeze_{eval}} = \frac{\boldsymbol{\left((nb_{pts})^{nb_{var}}\right)}}{\boldsymbol{2 \times nb_{pts} \times nb_{var}}} \sim \boldsymbol{26} \qquad \text{(III-7)}$$

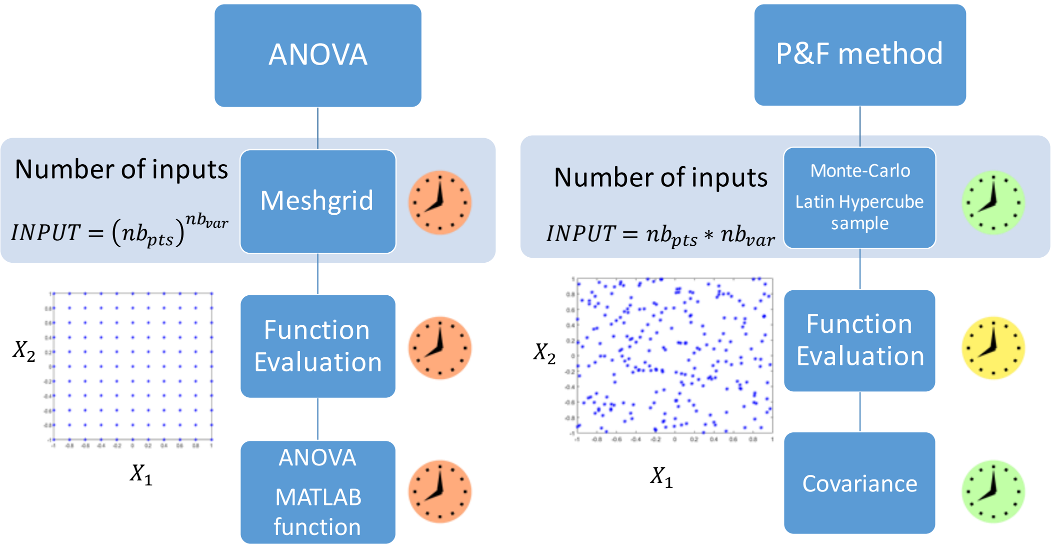

Fig. III-8: Comparison of two Sobol indices estimation methods.

The CPU time cost of ANOVA method is huge due to its input combinatorial explosion when the number of decision variables is also important, the function evaluation being directly amplified by the number of inputs. On the contrary, the Pick&Freeze method complexity manly depends on the number of points used for sensitivity analysis. The random draw for the

Pick&Freeze method has a small CPU cost. In the study case related to the electrical motor model, the comparison in terms of CPU cost gives explicit differences:

1. for ANOVA method, 1.5 days (four levels ($\boldsymbol{nb_{pts}}$) and $\boldsymbol{nb_{var}} = 13$ input variables)
2. for Pick&Freeze method: 20 minutes for 100 000 points (this number of points being sufficient for obtaining the same results as with ANOVA).

III.2.3 Whole sensitivity analysis based on specific power assessments.

In this section, a sensitivity analysis based on the Sobol indices is carried out at a global level for each hybrid electrical architecture previously presented in that chapter. Two outputs are considered: MTOW and fuel burn mass. These outputs are evaluated using the looped process presented in section I-3.3. For each iteration of this looped process, all components of the powertrain are sized by following the flow chart of Fig. III-9 and it is detailed in APPENDIX L.

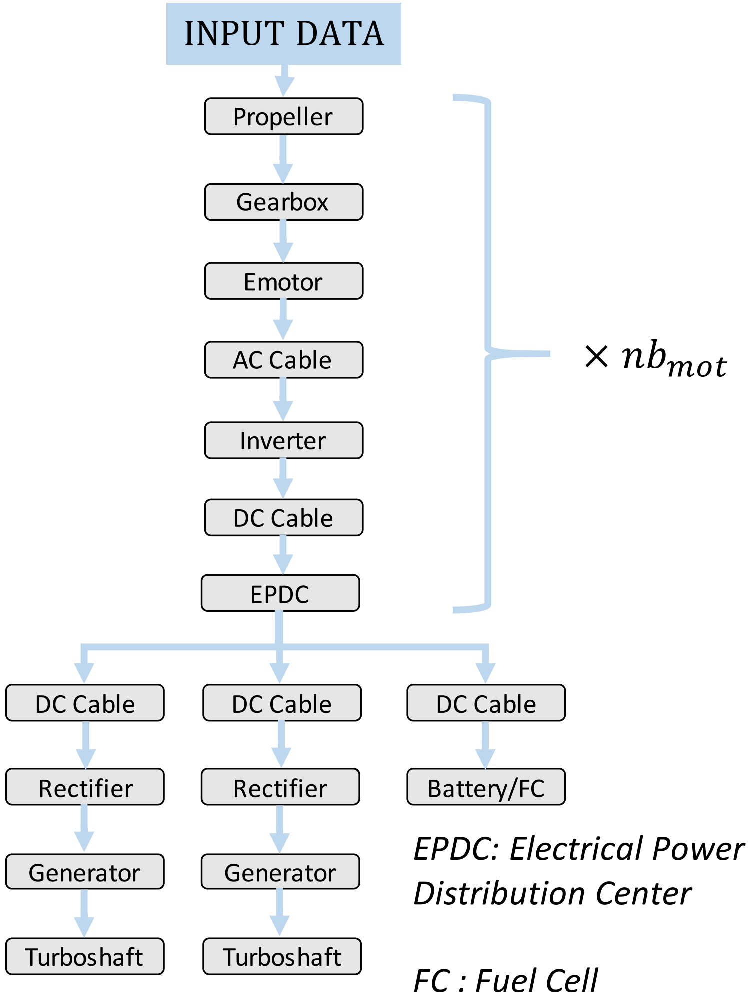

Fig. III-9: Integrated design process flow chart.

The current section aims at confirming the results obtained in the section I.3.4 and presented in [66]. The input variables of sensitivity analysis are related to the assessments of the Table III-1 which correspond to both specific powers and efficiencies for electric motors and power inverters. These assessments are considered to set the upper and lower bounds of the input variables.

Three hybrid-electric architectures are compared: the Turbo electric architecture (TEA), the symmetrical Hybrid-electric architecture (HEASYM called hereafter HEA) and the hybrid-electric architecture with one turboshaft (HEA1GT) corresponding to the previous section (III.1.2.2).

Regarding fuel burn and then the MTOW as the outputs, analysis results are detailed in Fig. III-10 and Fig. III-11 respectively. These analysis confirms the trends previously presented in section I.3.4 (Fig. I.49, I.50) in the particular case of the HEA architecture: based on a simple analysis case with a reduced number of input variables, this comparison allows to prove the ability of Sobol Indices to correctly set the sentitivity effects. In particular, as previously, the electric motor is the most sensitive electrical component so the most important to be optimized with regard to the MTOW. The efficiency (η) also affects the fuel mass. Observing Fig. III-10, efficiencies (η_{emotor} and $\eta_{inverter}$) are sensitive as they directly impact the source sizing so the fuel burn demand. On the other side, the fuel mass is also highly sensitive to the specific power variations confirming the results obtained in section I.3.4 and presented in [66].

Concerning the impact analysis on the MTOW (see Fig. III-11), the specific power ($P_{SPE_{emotor}}$) of the electric motor clearly appears to be the most sensitive variable compared with the effect of efficiencies.

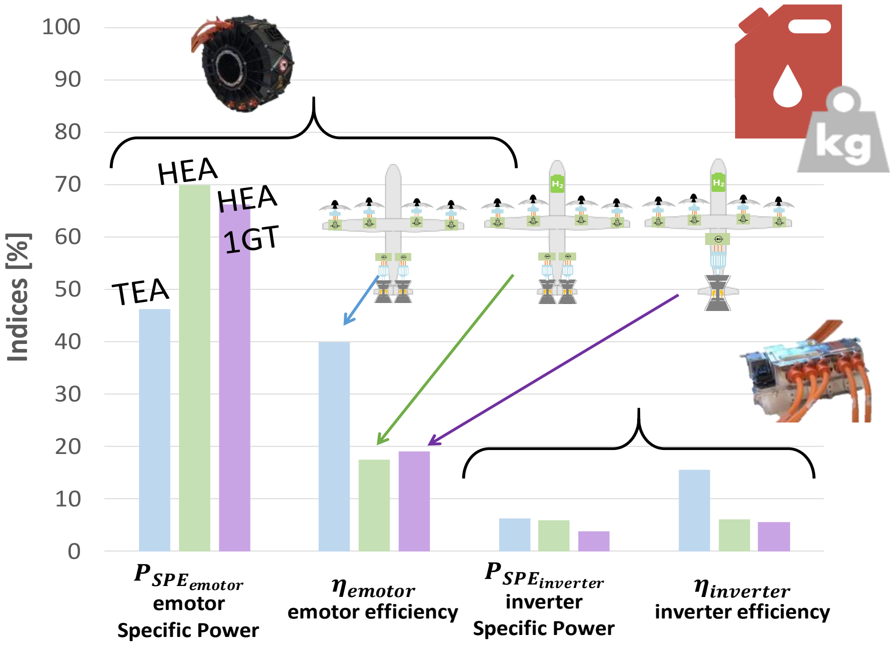

Fig. III-10: First order Sobol indices for three hybrid-electric architectures regarding the fuel mass; bar colors are related to the 3 compared architectures.

In these analyses only the first-order Sobol index is represented (sum of all the first-order indices = 1 therefore no correlation between the variables) because the variables are totally dissociated and have a direct impact on the aircraft's weight or fuel. As stated above, the first-order index represents the sensitivity specific to the parameter (see section III.2.1).

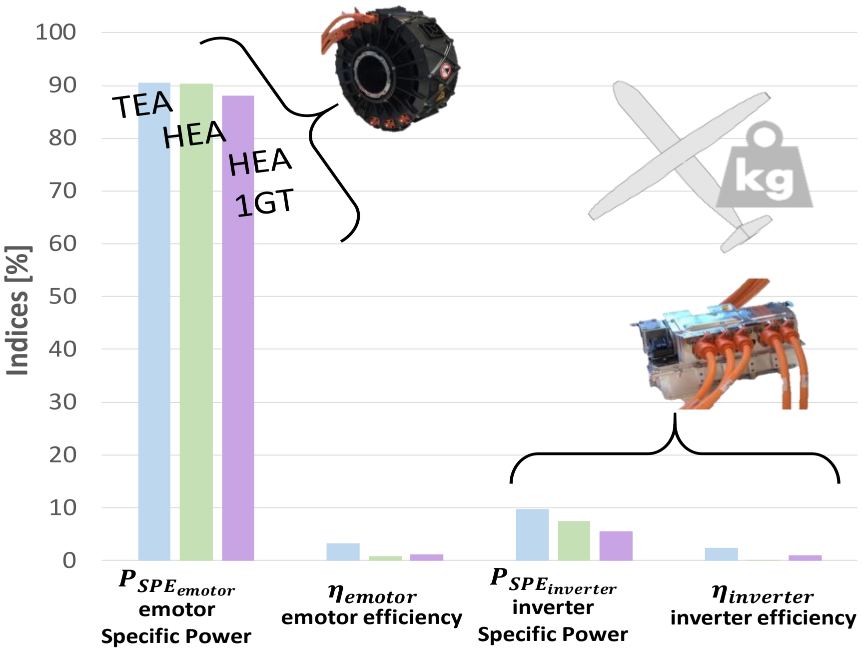

Fig. III-11: First order Sobol indices for three hybrid-electric architectures regarding the MTOW; bar colors are related to the 3 compared architectures.

This analysis was based on very simple models for electronic powers and electric motors which allows validating the sensitivity analysis based on Sobol indices using the Pick&Freeze calculation method which the trends have confirmed previous sensitivity analysis presented in chapter I. The same approach may be used for more complex design models as in the case of the electromechanical actuator models reported in [104]. In order to select the most sensitive design variables in actuators which have been seen to be the most sensitive devices on weight and fuel burn, a local sensitivity analysis based on Sobol indices is investigated in the next section by means of technological design models.

III.3 Sobol indices based sensitivity analysis at component level.

In this section, the attention is focused on the electric motor which has been seen as very sensitive at aircraft level for HEA architectures. The original sizing model developed in [84] for the electric motor design has been considered in order to illustrate the interest of this approach; this model is nearly the same as the one presented in the Chapter II (some adaptations of the original model have been presented in that previous chapter) and used in our thesis for the overall optimal design.

After the choice of the index calculation method, input variables (and subsequent bounds) have to be determined. In our case an input vector including thirteen variables has been chosen for the motor model inputs. A first set of input variables with corresponding lower and upper bounds is presented n the following table:

Table III-2: 1rst sensitivity analysis input variables and their bounds

Input Variables	Name of the variable	Lower bound	Upper bound
Pem_{siz} [%]	% of Power sizing point from the maximum value	80	130
N_{siz} [%]	% of rotational speed sizing point from the maximum value	80	150
$f_T[Pa]$	Tangential stress in the airgap	40000	148500
$J_{rms}[A/mm^2]$	Current density at sizing point	6	25
$B_{gap_{max}}[T]$	Maximum air gap flux density	0.8	1.05
$B_{teeth_{max}}[T]$	Maximum teeth flux density	1	1.53
$B_{yoke_{max}}[T]$	Maximum stator yoke flux density	1	1.53
$B_{yoke-rotor_{max}}[T]$	Maximum rotor yoke flux density	1	1.5
$R_{drot_{lm}}[\%]$	Ratio between the rotor diameter and the rotor active length	0.5	1.25
$V_{uHVDC}[V]$	Ultra-high direct current Voltage	1000	3000
n_{epp} $[-]$	Number of slots per poles and per phases	1	4
N_{ce} $[-]$	Number of conductors per slot	1	4
p $[-]$	Number of pole pairs	2	10

As in the previous section, mass and efficiency have been chosen as the outputs for the model. The process to determine Sobol indices is illustrated in Fig. III-12:

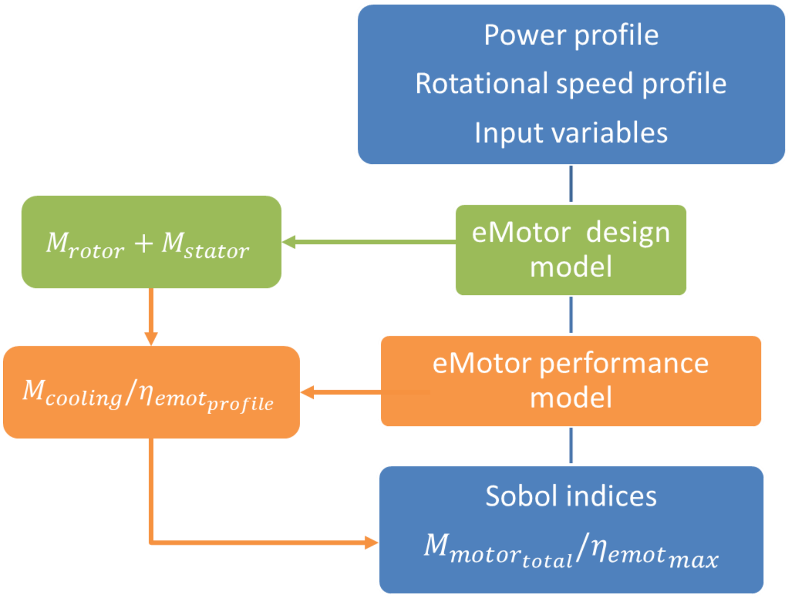

Fig. III-12: Process to determine Sobol Indices for the electric motor sensitivity analysis.

In order to estimate the cooling mass, a specific power of cooling equal to 1 kW (of losses)/kg is assessed. In that way, losses are simply converted into a roughly estimated cooling mass.

III.3.1 Analysis of 1st order Sobol indices on the design-oriented electric motor model.

In the first analysis, both methods (Anova vs Pick&Freeze) for estimating Sobol Indices have been compared. First order Sobol indices comparison is described in Fig. III-13 and Fig. III-14:

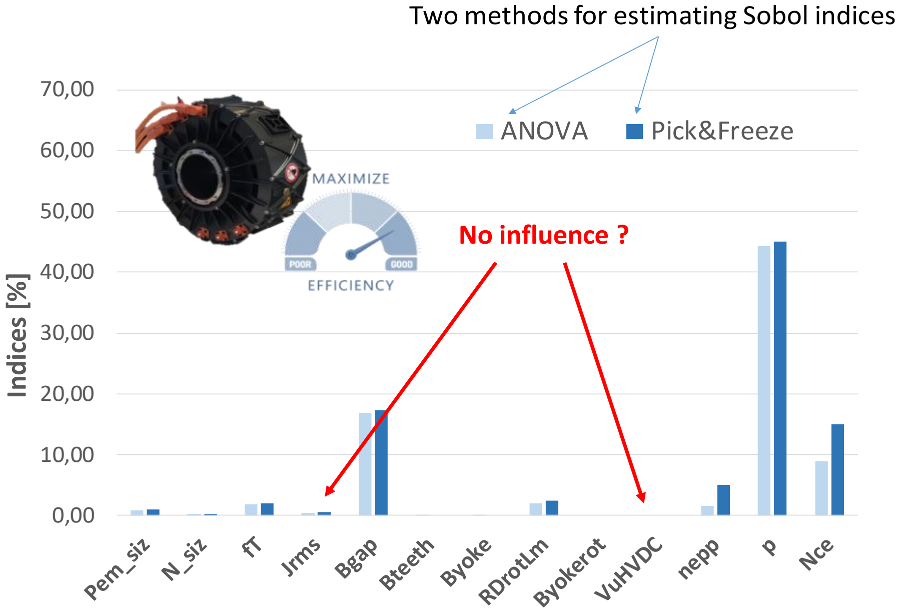

Fig. III-13: First order Sobol indices calculated by the two estimation methods. Output variable: efficiency. Input variables: motor parameters

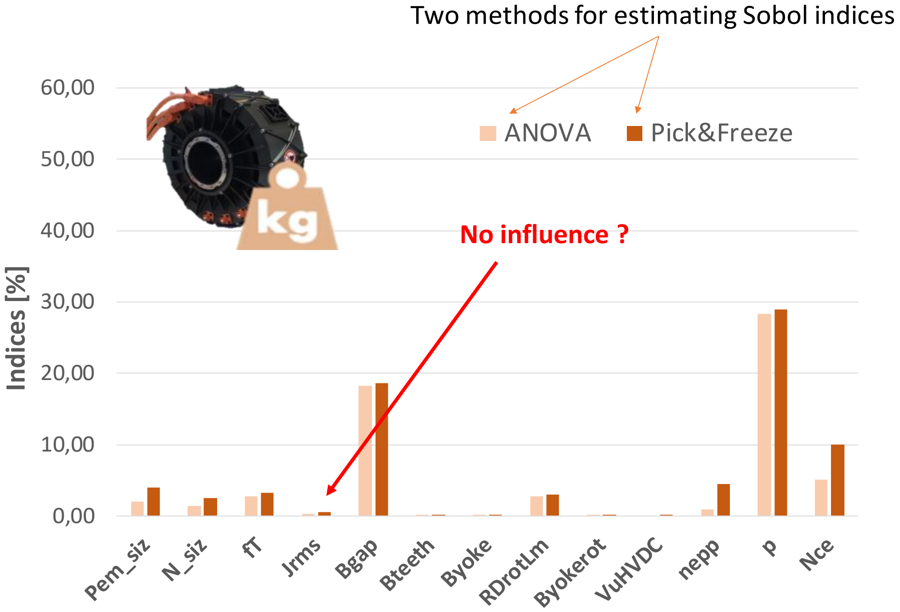

Fig. III-14: First order Sobol indices calculated by the two estimation methods. Output variable: mass. Input variables: motor parameters

At first, this analysis shows that results provided by both estimation methods (Anova vs Pick&Freeze) are quite similar, validating such approaches. In the following the Pick & Freeze method (less consuming in CPU time) is used.

- Regarding the obtained values from this sensitivity analysis, the results are quite surprising. Indeed, some variables which are usually (physically) impacting the electric motor mass for experts as the current density (J_{rms}) are not highlighted by the 1st order Sobol indices. This effect can be explained as follows: the bounds of the corresponding input variable have a clear influence on the Sobol indices; thus, with the help of the electric motor experts, all input variable bounds have been revisited (see the Table III-3).

- The “low influence” of certain input variables is also due to the dependences between input variables: it should be reminded that Sobol’s method assumes the independence of input variables. However, it can be observed from Eq. III-6 that the number of conductors per slot (N_{ce}),is directly linked to other variables of the input data set. :

$$Nce \; = \; floor\left(\frac{ma*V_{uHVDC}}{2*\sqrt{2}*V_{1spire}}\right) \quad with \tag{III-8}$$

$$V_{1spire} = f(p, n_{epp}, R_{DrotLm}, \ldots) \tag{III-9}$$

- V_{1spire} : voltage in one spire [V].
- ma : the modulation depth [-].

Finally, the “dependent variable” (such as Nce) have been be suppressed to the input data set keeping only independent inputs. Furthermore, it has to be underlined that 1st order indices do not take account correlation effects which are rich in information. The total Sobol indices have to be considered for that purpose. Based on those remarks, a second sensitivity analysis study has been carried out by changing the bounds of input variables, suppressing dependent variables and also analyzing the total indices with correlation effects.

III.3.2 Revisited sensitivity analysis with total indices and refined bounds (e-motor level).

As previously mentioned, the total order Sobol index are useful to be exploited (effect of the X_i parameter alone plus correlation effects of all other X_j with $j \neq i$). The new (12) input variables are the following:

Table III-3: 2nd sensitivity analysis input variables and their bounds

Input Variables	Name of the variable	Lower bound	Upper bound
Pem_{siz} [%]	Power sizing point from the maximum value	80	130
N_{siz} [%]	Rotational speed sizing point from the maximum value	80	150
$f_T[Pa]$	Tangential stress in the airgap	40000	148500
$J_{rms}[A/mm^2]$	Current density at the sizing point	6	25
$B_{gap_{max}}[T]$	Maximum air gap flux density	0.8	1.05
$B_{teeth_{max}}[T]$	Maximum teeth flux density	1	1.53
$B_{yoke_{max}}[T]$	Maximum stator yoke flux density	1	1.53
$B_{yoke-rotor_{max}}[T]$	Maximum rotor yoke flux density	1	1.5
$R_{drot_{lm}}[\%]$	Ratio between the rotor diameter and the rotor active length	0.5	1.25
$V_{uHVDC}[V]$	Ultra-high voltage direct current	1000	3000
n_{epp} $[-]$	Number of slots per poles and per phases	1	4
p $[-]$	Number of pole pairs	2	10

Main results of such analysis are reported comparing first order and total Sobol indices with respect of the 12 input variables [105]:

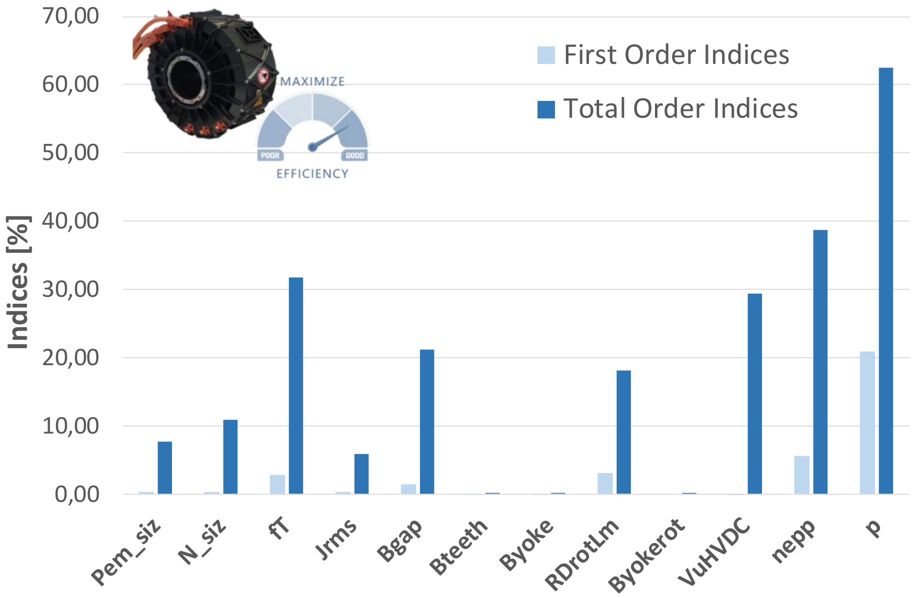

Fig. III-15: First order (pale color) and total order (dark color) Sobol indices and its effects on the e-motor efficiency.

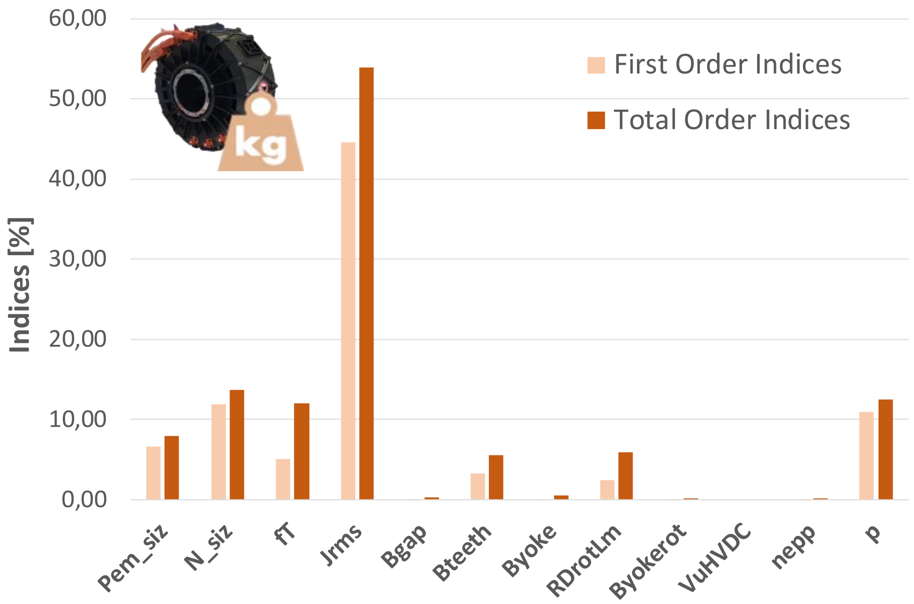

Fig. III-16: First order (pale color) and total order (dark color) Sobol indices and its effects on the e-motor mass.

Analyzing Sobol indices and their effects on electric motor mass, four total order Sobol indices are close to zero. But these variables are impacting the eMotor efficiency (see Fig. III-15). It shows that both outputs (mass and efficiency) need to be considered in order to obtain relevant and complete sensitivity analysis. Finally, only two motor input parameters can be considered as insensitive with regard to both output criteria and whatever if 1st order or total Sobol indices are observed:

- $B_{yoke_{rot}}$ the rotor yoke flux density.
- B_{yoke} the stator yoke flux density.

Thus, in the following, these two variables will be set at a fixed rating value which tends to reduce the number of decision variables for optimization also reducing the computation time and facilitating the convergence of algorithm. For the next sensitivity analysis proposed at electromechanical powertrain level, the number of input variables for the motor is then reduced to 10.

III.3.3 Sensitivity analysis of the electromechanical powertrain (propeller, gearbox, electric-motor).

This section aims to analyze the sensitivity of the electromechanical powertrain coupling gearbox and propeller devices with eMotor.

Previous studies have been performed without considering feasibility constraints: it means that numerous tests in the peak&freeze method do not fulfill feasibility constraints which will be considered in the optimization approach. In the following, two feasibility constraints have been added:

- A thermal constraint (used by research teams in charge of the electric motor design and its cooling) is related to an estimation of the necessary cooling effort and is emphasized by the $A \times J_{eq}$ product. The constraint is: $A \times J_{eq} \leq 2.10^{12}$ with the following parameters:

$$\mathrm{A} \times \mathrm{J_{eq}} = \frac{(\mathrm{P_{Joule}}+\mathrm{P_{Iron}}+\mathrm{P_{windage}}+\mathrm{P_{friction}})}{\mathrm{k_{tb}}*\mathrm{S_{alesage}}*\rho_{\mathrm{CU}}(\mathrm{T_{win}})} \tag{III-10}$$

- P_{Joule} : the Joule losses [W].
- P_{Iron} : the iron losses [W].
- $P_{windage}$: the windage losses [W].
- $P_{friction}$: the friction losses in bearings [W].
- $S_{alesage}$: the bore area of the e-motor [m^2].
- $\rho_{CU}(T_{win})$: the copper resistivity [Ω.m] function of winding temperature T_{win}
- k_{tb} : the end-winding coefficient [-].

This thermal constraint (see Eq (III-10)) allows designing the electromechanical actuator by considering the cooling system. Exceeding this thermal limit prevents the cooling system from cooling the electric motor.

- The 2nd constraint is related to the maximum peripheral speed: $V_{peripheral} \leq 150 m/s$. This is the maximum value reachable without inducing mechanical deformation that can damage the actuator.

Moreover, the variables involved in the propeller and gearbox models have been added in order to complete the sensitivity analysis. The input data are the requirement data (Thrust, Mach, Altitude) and the analysis process is illustrated in Fig. III-17**.**

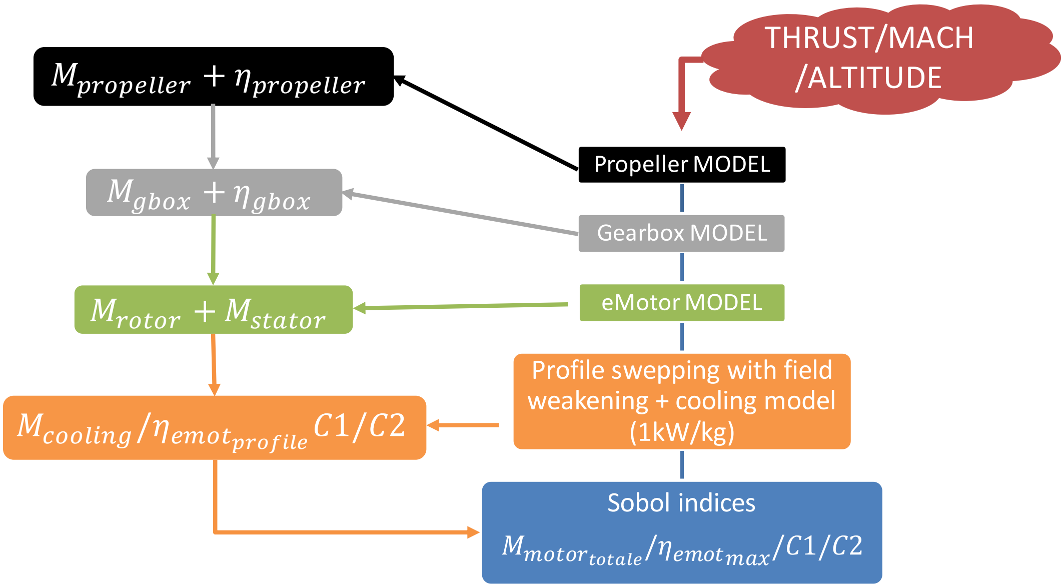

Fig. III-17: Electromechanical powertrain sensitivity analysis process.

The following set of input variables is chosen with their corresponding bounds:

Tab. III-1: 3rd sensitivity analysis input variables and their bounds.

Input Variables	Lower bound	Upper bound
$D_{prop_{siz}}$ [%]	100	150
R_{gbox} [−]	1	15
Pem_{siz} [%]	80	130
N_{siz} [%]	80	150
$f_T[Pa]$	40000	148500
$J_{rms}[A/mm^2]$	6	25
$B_{gap_{max}}[T]$	0.8	1.05
$B_{teeth_{max}}[T]$	1	1.53
$R_{drot_{lm}}[\%]$	0.5	1.25
$V_{uHVDC}[V]$	1000	3000
n_{epp} [−]	1	4
p [−]	2	10

Two inputs parameters have been added in addition to the ten remaining variables for eMotor in order to highlight the interactions between elements.

- $D_{prop_{siz}}$: oversizing of the propeller in %.
- R_{gbox} : gearbox ratio.

III.3.3.1 Sensitivity analysis without feasability constraint fulfilment.

In this section, the sensitivity of the electromechanical powertrain is analyzed during cruise [106]: the efficiency, the mass, and the feasibility constraints are successively displayed as outputs in order to determine the Sobol indices. In addition to the previous outputs (masses and efficiency), the constraint levels are calculated and displayed to emphasize their influence following the values of the input variables. The results are quite similar to those observed in the previous study (see Fig. III-15) except for the tangential pressure and the flux density in the air gap (+10% on the total order Sobol index). This difference arises due to the introduction of the gearbox ratio. Adding this variable allows adapting the rotational speed of the electric motor. Thus, the rotation speed range is higher than in the previous study. Consequently, the tangential stress and the flux density in the air gap are more sensitive on the rotor volume and so on the motor mass. If the constraint fulfilment is not mandatory in the analysis, propeller and gearbox inputs are not too sensitive on outputs.

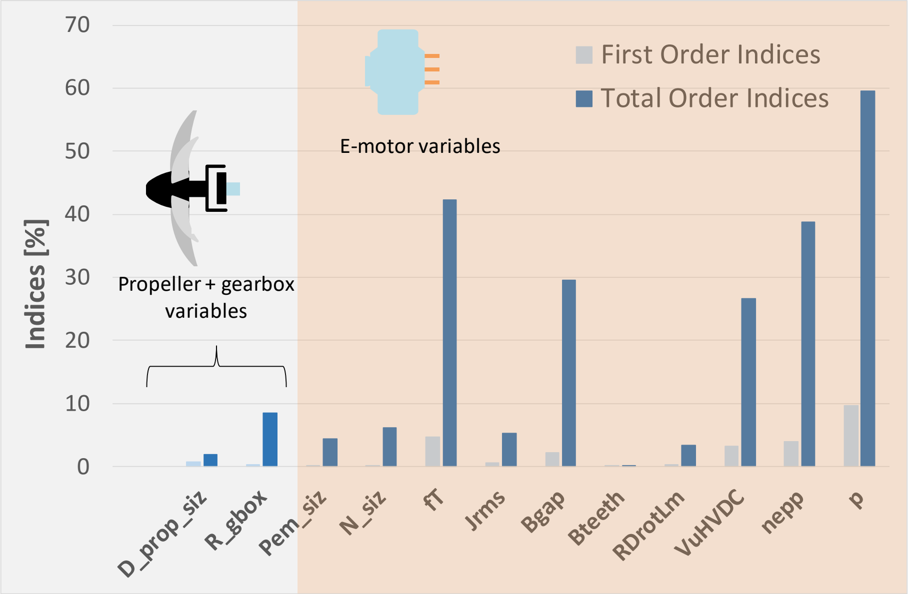

Fig. III-18: First order (pale color) and total order (dark color) Sobol indices with e-motor efficiency as output without considering constraint fulfillment.

Losses of the electrical machine depend on the volume of copper and the volume of magnetic yoke in the stator. The higher the copper and magnetic yoke volume, the larger the amount of losses. Thus, while the stator volume depends on rotor volume, stator yoke and copper volumes are impacted as well, and so the losses. The gearbox ratio directly impacts e-motor rotor volume (consequently the e-motor mass); thus, it becomes the most impacting variable on the overall system mass. This gearbox ratio index highlights an interaction between the electromechanical and propeller devices: this is a key parameter considering the mass of the propulsion system.

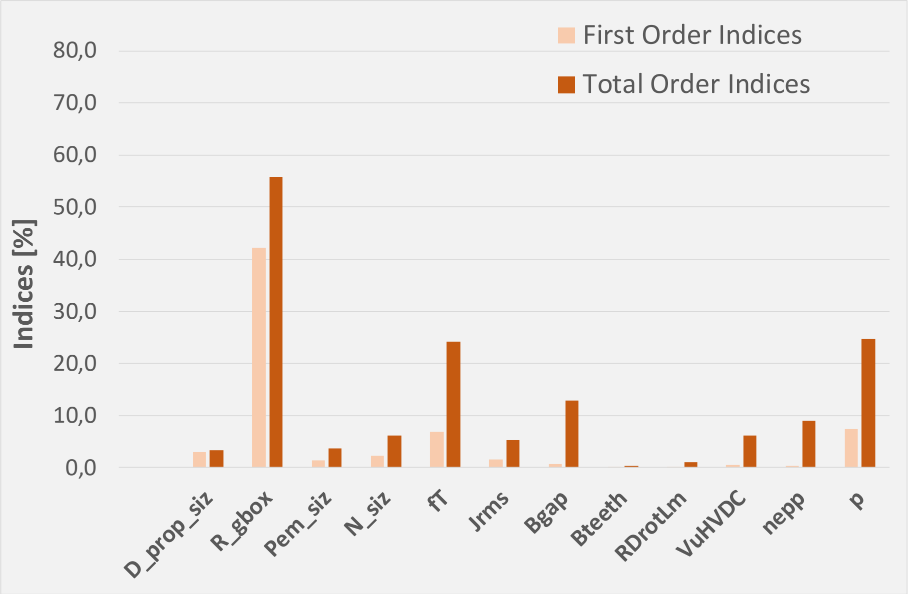

Fig. III-19: First order (pale color) and total order (dark color) Sobol indices with e-motor mass as output without considering constraint fulfillment

The first constraint to be analyzed is the peripheral speed constraint.

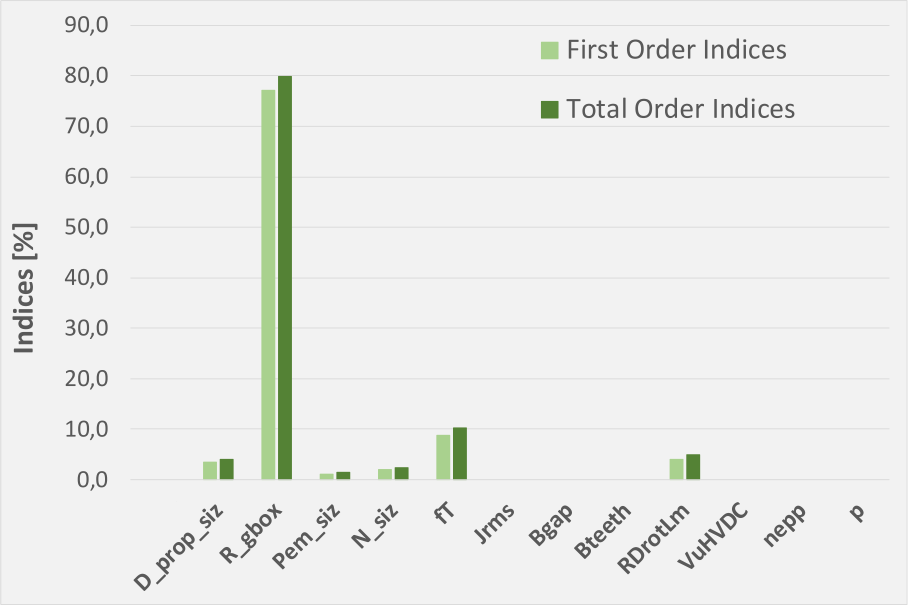

Fig. III-20: First order (pale color) and total order (dark color) Sobol indices with the e-motor peripheral speed as output without considering constraint fulfillment

Several input parameters are directly involved in the maximal peripheral speed equation:

$$\mathrm{V_{peripheral}} = \left(\frac{\mathrm{Pem_{siz}}}{\mathrm{N_{siz}}} * \max\left(\frac{\mathrm{P_{prop}} * \eta_{\mathrm{gbox}}}{\mathrm{N_{prop}} * \mathrm{R_{gbox}}}\right) * \frac{30\pi}{4\mathrm{f_T}} * \mathrm{R_{Drot/Lm}}\right)^{\frac{1}{3}} \frac{\mathrm{R_{gbox}}.\mathrm{N_{prop}}.\mathrm{N_{siz}}}{30} \qquad \text{(III-11)}$$

Where

- η_{gbox} :gearbox efficiency [%]
- N_{prop}: propeller rotation speed [RPM]
- P_{prop}: propeller shaft power [W]

The propeller diameter is indirectly involved through the propeller shaft power, P_{prop}. So, all the sensitive parameters in Eq (III-11) appear in the previous equation. Some sobol indices are null, this can be explained by the absence of the studied parameters in the peripheral velocity equation (for instance, B_{gap} is not necessary to calculate the peripheral speed and therefore its Sobol indices are null) .

The second analysis is related to the thermal limit as reported in Fig. III-21.

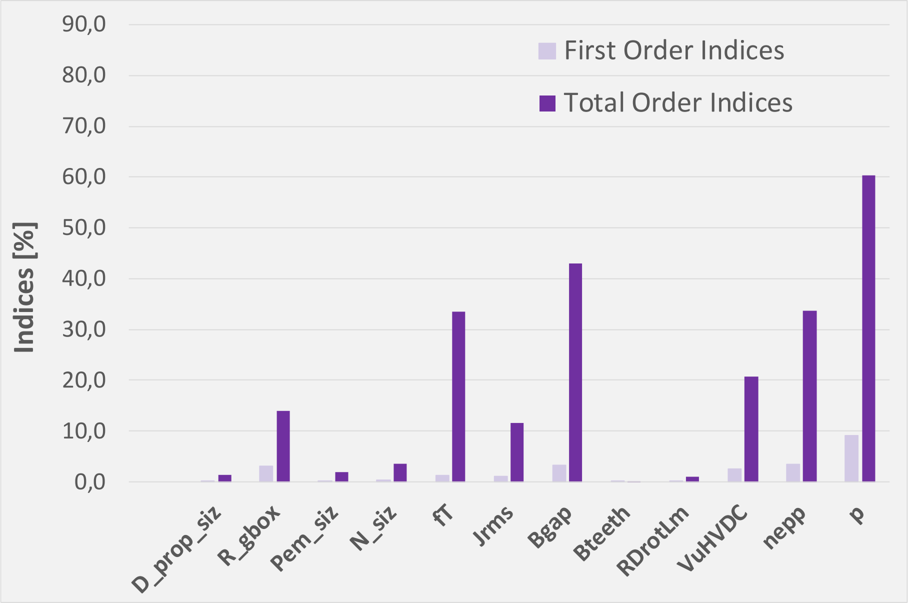

Fig. III-21: First order (pale color) and total order (dark color) Sobol indices on the thermal constraint as output without considering constraint fulfillment

The results are quite similar to those of Fig. III-18 (output: efficiency). Indeed, losses are directly linked to the $A \times J_{eq}$ product which qualitatively represents the thermal constraint. The efficiency is then directly represented in the thermal constraint.

III.3.3.2 Sensitivity analysis with feasability constraint fulfilment

It is interesting to compare results related to the design of the propulsion system following if constraints are fulfilled or not [106]. In that subsection, only tested solutions fulfilling both constraints (peripheral speed and thermal constraints) are considered in the sensitivity analysis (i.e. for the calculation of Sobol indices).

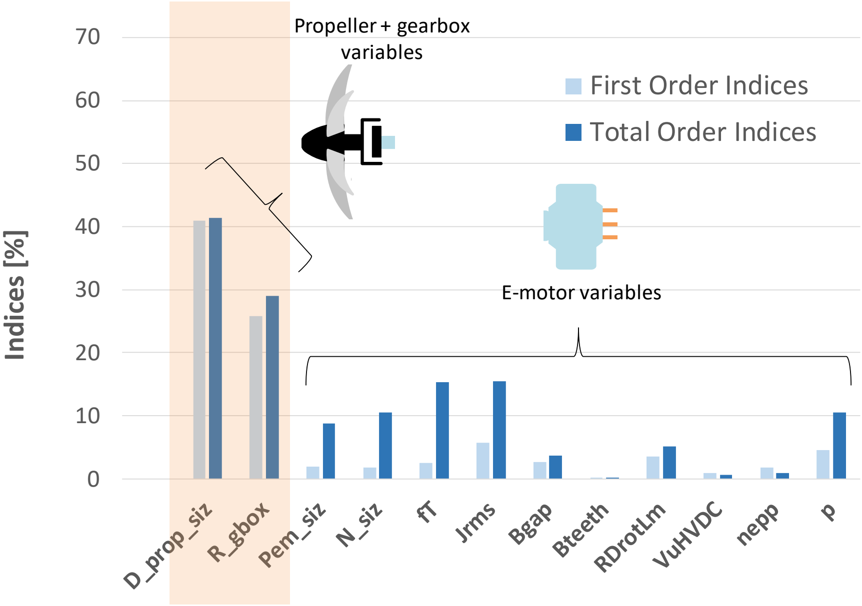

Fig. III-22: First order (pale color) and total order (dark color) Sobol indices with e-motor efficiency as output by considering constraint fulfillment.

If constraint fulfilment is not considered (cf Fig. III-18), electric motor variables are the most sensitive with regard to the efficiency. On the contrary, when constraints are fulfilled, the propeller and gearbox variables become particularly sensitive. This observation shows that constraint fulfilment is essential for a sensitivity analysis process in a technological framework. The propeller is the element of the propulsive system characterized by the broadest efficiency variation range.

The gearbox efficiency is fixed at 98.5%, while the electric motor has an average efficiency of 97%. Considering that the propeller has a maximum efficiency value of 85%, its diameter oversizing significantly impacts the efficiency of the whole electromechanical propulsive system. In the next chapter related to system optimization, this issue will be seen as a major trend of the integrated overall design leading to oversize the propeller diameter to enhance the global efficiency of the powertrain although the mass increase on this device!

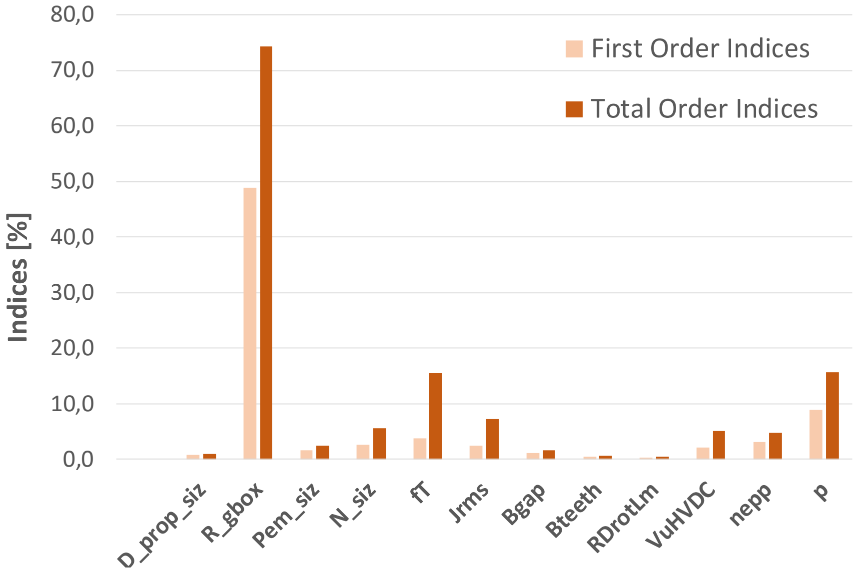

Fig. III-23: First order (pale color) and total order (dark color) Sobol indices with e-motor mass as output by considering constraint fulfillment

Comparing Fig. III-19 and Fig. III-23 for the analysis of motor mass following if constraints are checked or not leads to quite similar trends in both cases even if the gearbox ratio is more sensitive when constraints are fulfilled. In fact, this variable drives the rotor volume and the torque which is directly linked with the thermal constraint. Similarly, the gearbox ratio determines the motor rotational speed and consequently the peripheral speed.

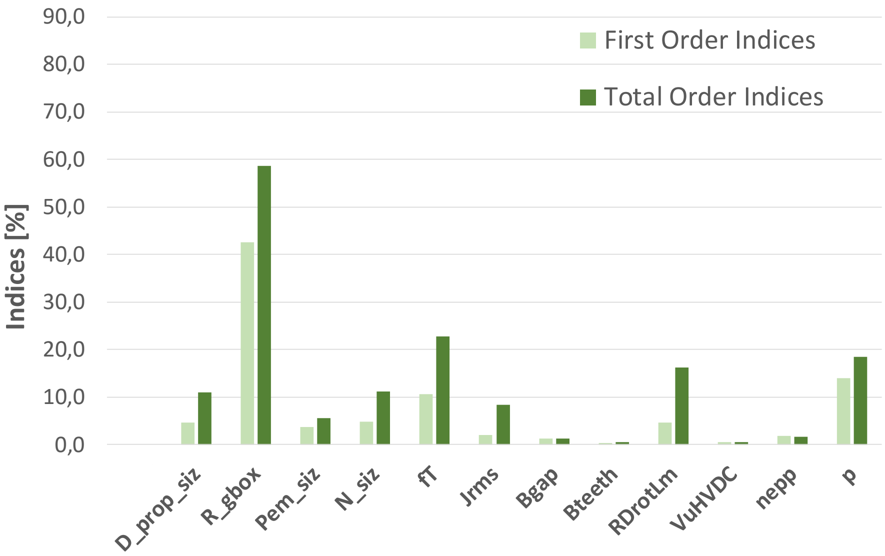

Fig. III-24: First order (pale color) and total order (dark color) Sobol indices with the e-motor peripheral speed as output by considering constraint fulfillment.

By comparing the Fig. III-20 with Fig. III-24 which set influence the peripheral speed seen as output, other input variables are sensitive when both constraints are checked. In other words, in Fig. III-20, the current density J_{rms}, the flux density in the air gap B_{gap}, the flux density in the teeth B_{teeth}, the HVDC bus V_{uHVDC} and the number of slot per poles and per phases n_{epp} were few sensitive (Sobol indices tends to zero while, in Fig. III-24, these indices have a small (but not null) impact on the output.

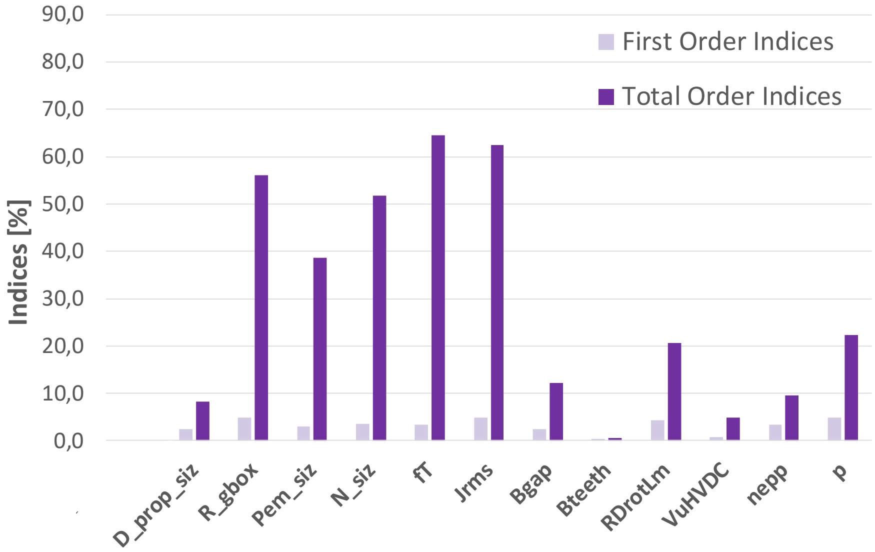

Fig. III-25 : First order (pale color) and total order (dark color) Sobol indices with the e-motor thermal constraint as output by considering constraint fulfillment.

Considering the thermal limit as the analyzed output when both constraints are fulfilled, huge correlation effects appear (see Fig. III-21 and Fig. III-25) and the total Sobol indices are pretty high for most of input variables. It is not surprising that the most impacting variables are the gearbox ratio –which determines the torque–, the power and rotational speed sizing, the tangential stress and the current density which constitutes a direct image of the copper losses.

III.4 Conclusion

These sensitivity analyses based on Sobol indices is useful to drive a convenient sizing the electrical components of the powertrain before to think of optimizing it.
At aircraft level, power densities have a huge impact on the global weight (MTOW). Compared with efficiency sensitivity, embedded masses have a greater impact on the fuel burn.
When the sensitivity analysis is locally carried out on the devices the study allows setting the sensitivy of each sizing variable, providing more accurate results. In particular, three sizing variables on the eMotor device have been suppressed, simplifying the optimization complexity.

At first glance, certain variables were only slightly sensitive with regard to the mass of the system or its performance when the eMotor is analyzed alone. By adding new electromechanical devices (gearbox and propeller) to the system under study (electromechanical powertrain), system couplings were emphised which led to the emergence of new sensitive parameters.

In the framework of technological design, adding the constraint fulfilment in the analysis process (in particular the thermal constraint) is also essential because they the feasibility constraints radically drive the impact of certain variables on mass or efficiency. Parameters that had a small impact at first glance can (through the addition of stresses) be more than essential to the design of the total propulsion chain. Cooling constraints have huge effect in the sizing of electrical components as it will be shown in the next chapter. It is clearly necessary to couple these domains in the sensitivity analysis.

In our case study the propeller is an essential element of the propulsion system, which the efficiency at low speed (during take-off) is a key point for the weight and performance of the aircraft: the sensitivity of its diameter has also been emphasized in this chapter. This point and many others will be clearly confirmed and detailed in the next chapter which deals with the optimization of the overall system.

CHAPTER IV. Multi-disciplinary design optimization of the hybrid-aircraft powertrain.

CONTENTS

From chapter III, we have seen that the heaviest elements of the power chain are the electric motors. It is then necessary to focus on their local optimization before to go further towards the overall optimization of the hybrid powertrain.

Starting with the motor optimization, the prime criterion to be optimized is the weight: it is the unique optimization objective in the next section. At the motor optimization level, only the assessments related the the 2025 targets will be considered to simplify the analysis. A comparison with the 2035 targets is proposed in the second part of that chapter which present the overall optimization at the powertrain level. Several analysis and several formulation of the optimization problem are proposed.

IV.1 Optimal design of the electric motor weight.

In this part, the optimization process of the electric motor is presented taking account of cooling device and partial discharges based on the sizing models presented in chapter 2 and detailed in APPENDIX F (electric motor model) and APPENDIX G (motor cooling model). A relatively large amount of heat may be generated by these motors over operating cycles. To efficiently remove this heat and to maintain the motor temperature within the prescribed range while minimizing energy consumption is the cooling system challenge, certainly the main challenge for this device as we will see in this section. Thus, a smart motor thermal management system with substantial heat transfer capability, compact structure, and low energy consumption is essential for aircrafts. This electro-thermal optimization is all the more important when the specific power of the electromechanical assembly needs to be improved.

IV.1.1 The cooling system: the main challenge.

The model of the motor cooling is described in APPENDIX G. A thermal nodal network is defined in order to calculate main temperatures in the electric motor. In the thermal model equations solving, the transient (capacitive) effects are taken into account: we will see in that section that using thermal capacitance effects during the high power phases (takeoff - climb) is essential for the design.

The qualitative thermal limit defined in the section III.3.3 ($A \times J_{eq} \leq 2.10^{12}$) has been used in [84] to size the electrothermal group. The thermal constraints fulfilment based on a thermal model is verified *a posteriori*. In such process, both electric and thermal model were not coupled inside the motor optimization.

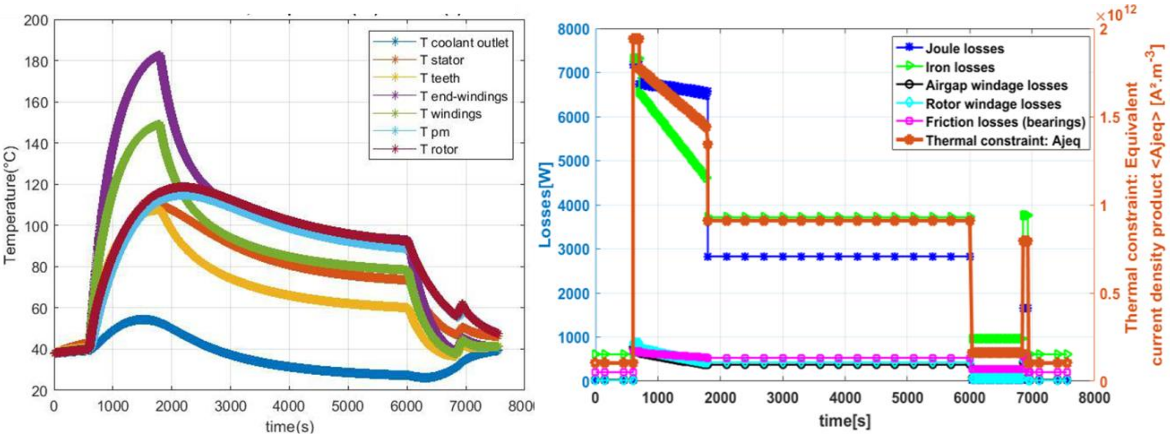

Fig. IV-1: Temperature evolution(left) and losse profile (right) during flight mission [84] .

Regarding the example of the Fig. IV-1, the capacitive effect is more than representative, all maximum temperature values appear at the top of climb: as it can be observed, the temperature transient at that point is far from being completed. The thermal system has been designed in order to reach the limit temperature for the end-windings. The other temperatures are below their limits showing that certain electromagnetic components may be oversized. For example, the stator yoke temperature reaches the value of 120°C which proves that the stator yoke volume can be reduced. In order to face that issue, a multidisciplinary optimization problem can be solved by integrating the cooling model with the electromagnetic design model of the electric motor. The previously used qualitative thermal limit ($A \times J_{eq}$) is then replaced by temperature limits at the most critical points: end-windings, stator yoke and magnets.

For both targets, common limit temperature of 180°C is used for coils and yoke. 150° is the limit for magnets.

IV.1.2 Electric motor optimization results.

In this section, only the electric motor mass is optimized. The main issue is to analyze the performance differences comparing the cooling model at steady state and transient conditions.

The thrust mission (so the aerodynamic power mission) is here fixed and this is the same for both model cases. Thus, the propeller diameter and the gearbox ratio are fixed according to that thrust requirement. The electromechanical MDO process is illustrated in Fig. IV-2. Based on a reference power profile, and after defining the geometry of the machine, the magnetic model allows calculating most of its dimensions. Then, the electrical model specifies the different electrical circuit parameters of the machine which are required for coupling the motor with its power supply. At this stage, the structure of the machine is fully defined, and its mass and volume are determined. The losses in the different parts of the machine are computed for each operating point of the flight mission, enabling the electro-thermal coupling. Finally, the machine design must satisfy specific requirements in terms of thermal resistance of its various parts and the magnetic state of the magnets. Thus, a thermal model has been integrated taking into account the cooling systems.

A more detailed optimization process is illustrated in APPENDIX L in Fig. L-1.

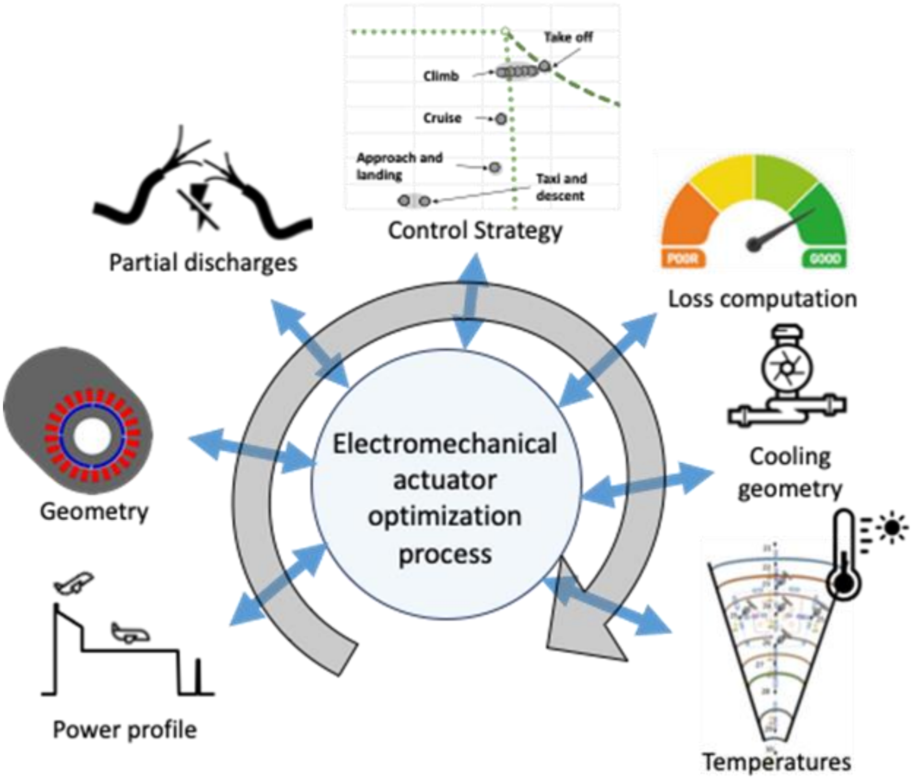

Fig. IV-2: MDO formulation process.

Some electric motor sizing limits are set (detailed in the APPENDIX Fsection F.2):

1. A minimum shaft radius (given by SKF datasheet linear regression [83]);
2. A minimum airgap thickness;
3. A maximum pressure on the sleeve;
4. A maximum rotor peripheral speed.

The partial discharge model (cf APPENDIX H) is implemented in this optimization which involves supplementary constraints:

5. To make sure that the final value of the fill factor (after partial discharge constraint fulfilment) is close to the initial value considered *a priori* in the electric motor sizing (see APPENDIX H, section H4);
6. A flag to check the correct integration of windings in the slot.

Performance constraint: another indicator checks that the mission has been completed (cf APPENDIX F section F.4).

The machine class H is considered in this (target 2025) case, for which the winding temperature must not exceed 220°C. In order to be conservative in the case of the transient model, this limit value is decreased to 180°C for windings and inside the yoke. The temperature of 150°C will be the limit temperature for magnets. For the steady state model, the used values are 220°C and 200°C for coils and magnets respectively (the considered maximum temperature of the yoke is the same as that of the coils).

Three supplementary constraints derive from the thermal model (cf APPENDIX G section G.4):

7. The limit temperature of the end-windings (180°C in transient and 220°C in steady).
8. The limit temperature of the yoke (180°C in transient and 220°C in steady).
9. The limit temperature of the magnet (150°C in transient and 200°C in steady).

The optimization variables and their ranges are summarized in the following table:

Table IV-1: Decision variables (11) for optimization with their respective bounds.

Decision Variables	**Name of the variable**	**Lower bound**	**Upper bound**
$V_{uHVDC}[\mathrm{V}]$	Ultra-high direct current voltage	540	2040
$R_{alesage}[\mathrm{m}]$	Inner radius of the stator	0.05	0.25
$R_{drot_{lm}}[\%]$	Ratio between rotor diameter and active length	50	125
$R_{hs_{ral}}[\%]$	Ratio between stator slot and inner radius	10	150
$R_{g_{ral}}[\%]$	Ratio between the air gap thickness and the inner radius of the stator	1	10
$R_{pm_{ral}}[\%]$	Ratio between the magnet thickness and the inner radius of the stator	5	50
$B_{yoke_{max}}[T]$	Maximum yoke flux density	1	1.53
$B_{teeth_{max}}[T]$	Maximum teeth flux density	1	1.53
$N_{ce}[-]$	Number of conductors per slot	1	4
$n_{epp}\ [-]$	Number of slots per poles and per phases	1	3
$p\,[-]$	Number of pole pairs	1	7

Let us note that the bus voltage (V_{uHVDC}) has been limited here to 2040V which corresponds to the crossing limit between the 3 level NPC and the 5 level ANPC power converter structures (see Fig. II-32 in section II.2.4.2). This choice was made to simplify this local optimization. In the second part of that chapter (section IV.2) this limit will be extended to higher voltage values in order to analyze the system tradeoff in terms of bus voltage regarding its influence on motor, power electronics and cables and including partial discharge constraints.

IV.1.2.1 Electric motor optimization with the steady state thermal model.

All the optimizations were carried out using a niching genetic algorithm (“clearing”) [85]. The clearing procedure was used for optimizing the PMSM mass with regard to the design constraints. Clearing is a niching elitist genetic algorithm which usually out performs standard genetic algorithms on difficult problems with multiple non linear constraints and multimodal features. All constraints were scaled and integrated into the objective function with penalty coefficients. The population size and the number of generations were respectively set to 100 and 200. Classical values for crossover and mutation rates were used (i.e., pc = 1 and pm =

1%). For each optimization case, multiple runs were carried out in order to take the stochastic nature of the algorithm into account and to ensure the reproducibility of results.

In the steady state themal model case only thermal resistances are density of the material are not taken into account. Therefore, the temperatures only depend on the geometrical dimensions. After optimization, the sizes of the electric motor are enlarged and the power density regarding the 2025 target is not reached: $P_{SPE_{steady}} = 2.60\ kW/kg$ (including the cooling device).

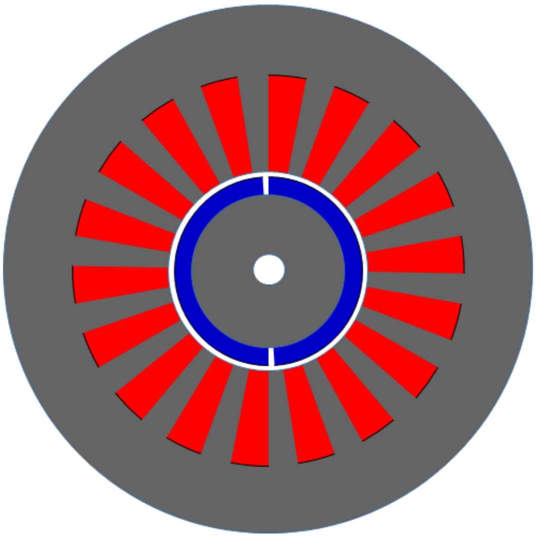

Fig. IV-3: Cross section of the electric motor (optimization with steady thermal model) $P_{SPE_{steady}} = 2.60\ kW/kg$.

The major constraints that drive the so called "optimal" electric motor are clearly the thermal constraints mainly due to end-windings and magnet temperature limits.

A cross section of the obtained machine is presented in the Fig. IV-3 showing the distribution of the different elements (copper, magnet, etc..). This shape clearly illustrates that stator and rotor yokes are prominent. This is mainly due to the stator losses level which involves sufficiently large surface in order to evacuate corresponding heat loads, the outer surface of the motor being the exchange surface with the cooling system.

The number of pole pairs is minimized (1 pole pair) because of the iron losses strong influence: reducing the number of pole pairs also reduces the electrical frequency of the machine and thus the iron losses.

Several constraints (3/9) have been reached:

1. End-windings temperature is maximum at 220°C;
2. Magnet temperature is maximum at 200°C;
3. Shaft radius is minimum (that is why the shaft radius is so small on the figure).

The end-winding temperature has reached its limit because most of the machine losses (70%) are concentrated between the air gap and the stator yoke. The addition of iron losses (in stator teeth) to the Joule losses accelerates the temperature rise in windings and particularly that of the end-windings. The stator yoke temperature has not reached its limit because of its proximity with the cooling system and a reasonable level of losses in relation to the exchange area. The heat dissipation in magnets is all the more complicated because these latter are "blocked" between stator windings and rotor bearings. Moreover, magnets are also heated by aerodynamic losses in the air gap.

Since the diameter of the cooling tube at the rotor depends on the radius of the shaft (10%), it becomes strongly difficult to evacuate losses if the shaft radius is small.

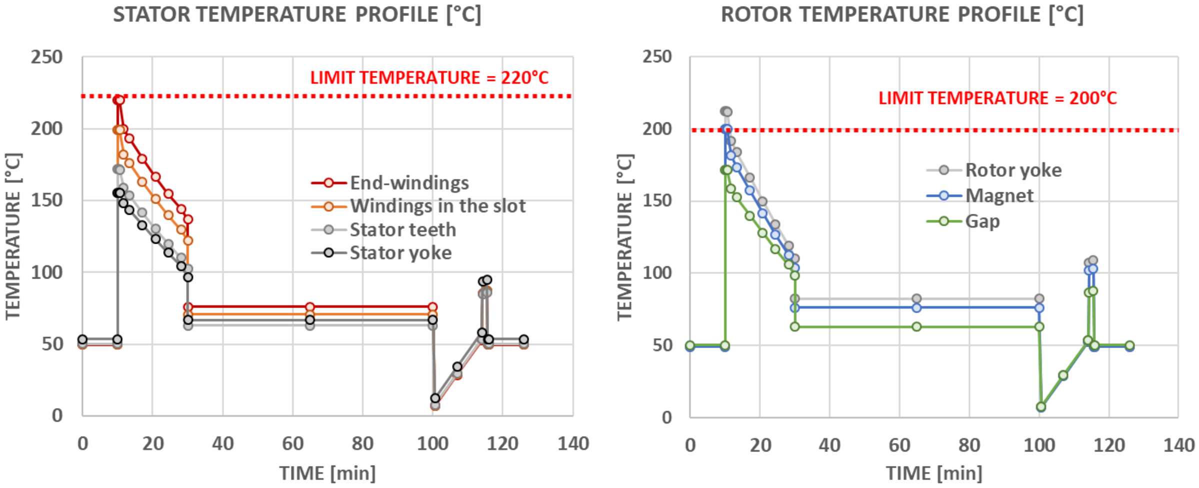

Fig. IV-4: e-Motor temperatures (optimization with steady state thermal) during the flight mission.

Regarding the temperatures of each element on Fig. IV-4 over the flight mission, the sizing (critical) point in the case of the steady state thermal model is during take-off. With that steady state thermal model the maximum of losses is reached at takeoff since this is the phase that consumes the most power even is this flight sequence duration is very short (some seconds). Using thermal capacitance is clearly favourable in order to cross takeoff and climb by reducing thermal constraints which would increase motor power density as it is shown in the next subsection.

IV.1.2.2 Electric motor optimization with the transient state thermal model.

With the transient model, limit temperatures are lower than for the previous study in order to be conservative in sizing. In this optimization two constraints (2/9) have been reached: End-windings temperature and stator yoke temperature are maximum at 180°C. Including the cooling device, the specific power of the electric motor obtained is much better thanks to the use of thermal capacitance, reaching: $P_{SPE} = 7.45\ kW/kg$.

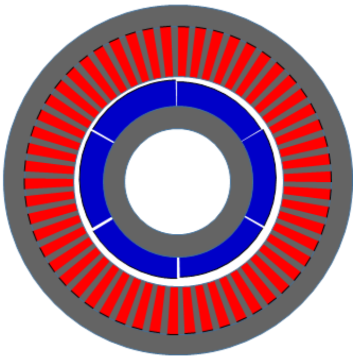

Fig. IV-5: Cross section of the electric motor (optimization with transient state thermal model) $P_{SPE} = 7.45\ kW/kg$.

Numerous slots along the stator yoke "distribute" the losses. The stator yoke is clearly thinner than before. The thermal capacitance depends here on the density of each material; the stator/rotor yokes have a high capacitive effect due to their high volume density. The magnets are larger than previously involving the air gap induction increase. The rotor yoke is directly linked to the stator one: both yokes become thinner due to the induction increase in teeth and yokes.

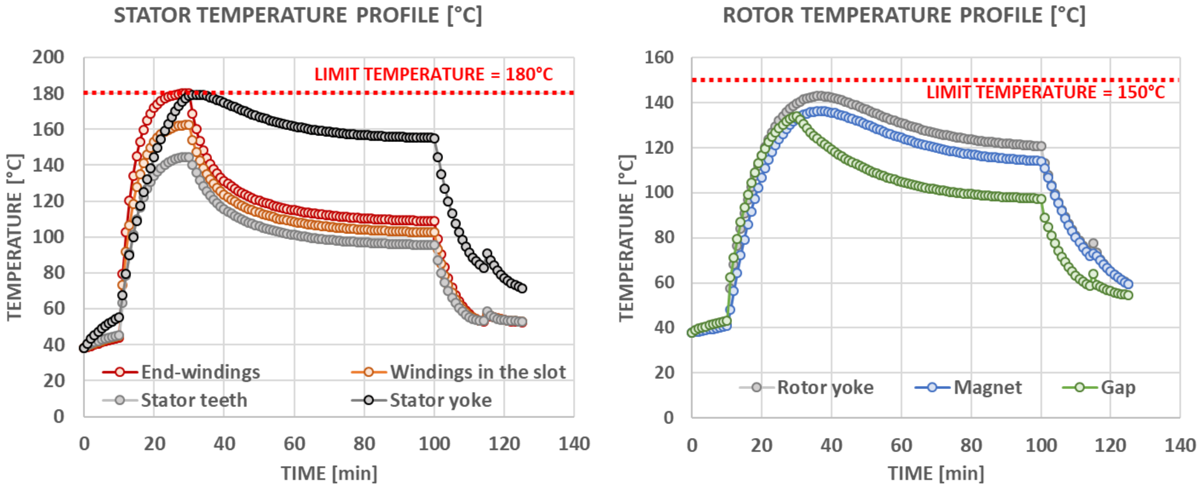

Fig. IV-6: e-Motor temperatures (optimization with transient state thermal model) during the flight mission.

The new temperature profile in Fig. IV-6 highlights the use of thermal capacitances. The temperatures of each part of the electric machine use the capacitive effect of their material. The temperature profile in each figure follows the beginning of the exponential function corresponding to the (R, C) equivalent circuit couplings. It is the same for magnets whose capacitive effect is as important as for the yokes because of their similar densities. The stator teeth are less sensitive to this thermal capacitance because of their small sizes (thin teeth). The thermal capacitanceallows usto significantly push back thermal limits which clearly drives the motor sizing. Thus, optimizing with the transient model allows decreasing the electric machine mass, thus increasing its specific power.

In order to illustrate the influence of these capacitive effects, a simulation of the thermal model at steady state was carried out from the sizing obtained with the previous optimization (based on the transient thermal model): in that case, the maximum temperatures are reached by the machine during take off as for the previous optimization based on the steady state thermal model. The end winding temperature is beyond 320°C compared to the maximum obtained with the transient model (see Fig. IV-7) which stays below the limit of 180°C: a gap of 78% is obtained between both thermal models with the same motor sizing.

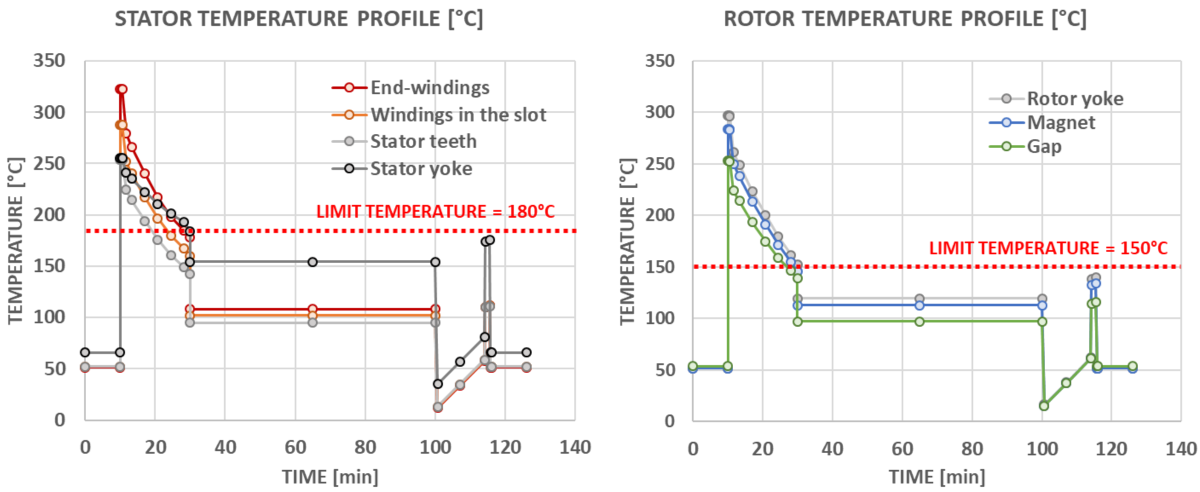

Fig. IV-7: e-Motor temperatures (optimization with transient state thermal model – steady state display) during the flight mission.

In Fig. IV-7, the waveforms are identical to those obtained through optimization in steady state Fig. IV-4:

- The limit temperature of the end-windings and the windings reach respectively 320°C and 288°C.
- The limit temperature of the stator and rotor yoke reach respectively 255°C and 300°C.
- The limit temperature of the magnet reaches 285°C.

The next part focuses on the differences in motor size and in performance (electric actuator torque-speed characteristic).

IV.1.2.3 Comparison of motor optimization between steady state and transient state thermal models with reference to the electric motor sized by the WP1.

In this section, the input variables proposed by the motor design team (in WP1) [83] have been used to optimize the performance of the actuator with the adapted model defined in chapter II. In order to compare sizes, the cross sections of the machines are shown side by side in Fig. IV-8, obviously displaying the main differences.
As presented before, only the thermal model was changed between both optimizations.

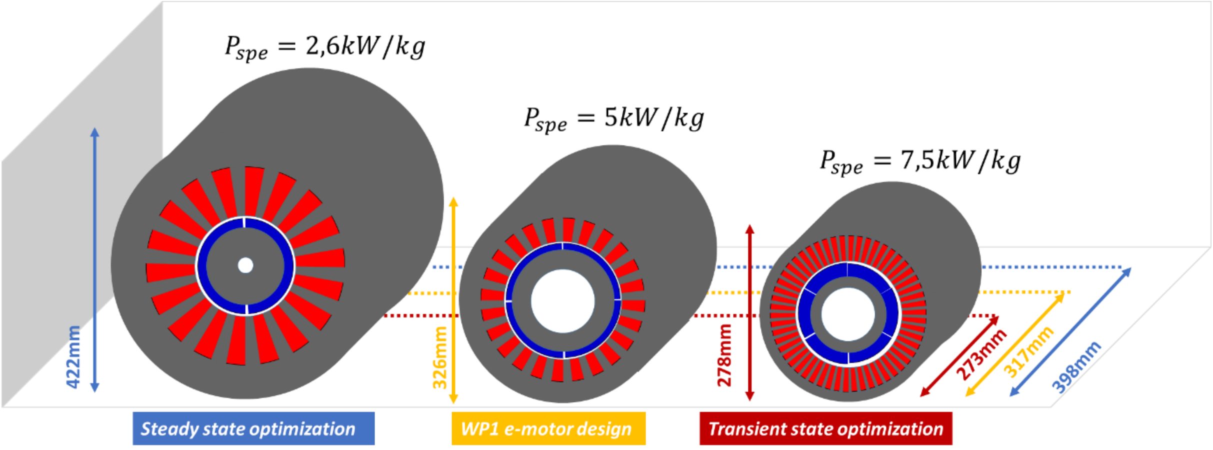

Fig. IV-8: Cross sections of three electric motors (left: steady state optimization, middle: WP1 e-motor design , right: transient state optimization).

In order to be able to make a performance comparison, the torque-speed characteristics of each motor are displayed. The characteristic of the optimized e-motor with a steady state (SS) thermal model is shown in blue; the characteristic of the optimized e-motor with a transient state (TS) thermal model is shown in red and the electric motor designed (without optimization) by the experts of the WP1 is in yellow. An actuator characteristic is limited by a maximum current (maximum torque) while its speed limit is given by a limit voltage which must not be exceeded. When this voltage is reached, the user has 2 possibilities:

- reduce the Iq current of the actuator to allow its to go into a higher speed phase without shifting the current (Id = 0).

- add current in the d-axis of the actuator (Id < 0) to reduce the flux density in the air gap and thus keep a constant power by increasing speed.

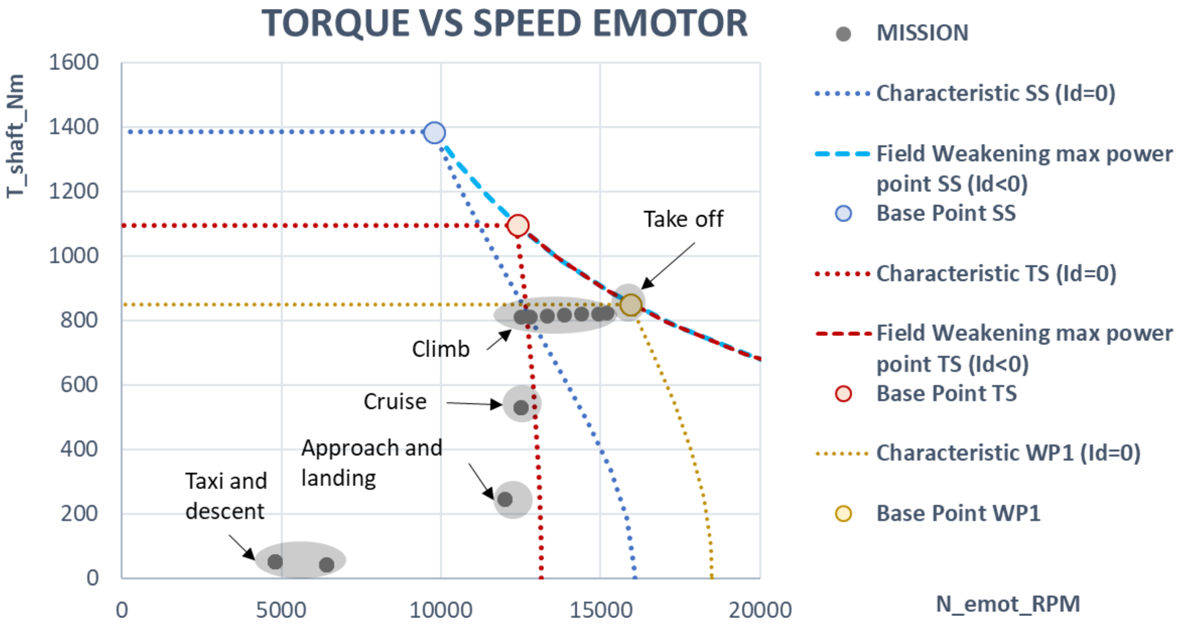

Fig. IV-9: Torque - Speed characteristic (blue steady state (SS) optimization, red transient state (TS) optimization and yellow WP1 electric motor).

Contrarily to the yellow characteristic (WP1 design), both optimized machines (with both thermal models) use field weakening, oversizing the sizing torque compared to maximum torque of the mission profile. Field weakening strategy reduces iron losses when the joule losses are at their maximum. This choice allows shifting the maximum of iron losses with respect to the Joule losses maximum in order to spread out thermal constraints. Field weakening is used by both machines (SS and TS) exactly at the same time during take off and almost during the whole duration of the climb.

Fig. IV-10: Joules and Iron loss profiles.

Looking at loss side, the most preponderant heat sources are Joule losses and iron losses. The use of field weakening is well illustrated by the comparison of the Fig. IV-10. For the machine designed by the WP1 (yellow curve), iron losses rise up to a value of 10 kW during takeoff. Let us note that this design was made only considering a unique (the maximum power during take off) sizing point instaed of the complete missionprofile. Contrarily, the maximum of iron losses is shifted at top of climb for both field weakened machines (blue and red curves) optimized on the whole mission profile. Beyond the loss distribution, another difference between each design is related to the amount of losses that can be dissipated by cooling devices depending if a steady-state thermal model or a transient-state model is coupled with the optimization:

- for the steady state thermal model based optimization, the maximum total level of losses is around 13 kW
- the maximum of total losses is around 20 kW for optimization using thermal capacitance effects.
- Regarding the electric motor designed by WP1, the amount of total losses reaches the value of 19kW, showing that the actuator has not been optimized.

It also means that there are trade-offs between specific power and efficiency because increasing the specific power also means increasing losses thus being less efficient. These results show the importance of system couplings (here electro thermal couplings) in multidisciplinary studies. This will be all the more important on the plane because the added kilos on the powerplant bring snowball effects on the final sizing. Losses are directly linked to the current and voltage levels in the machine.

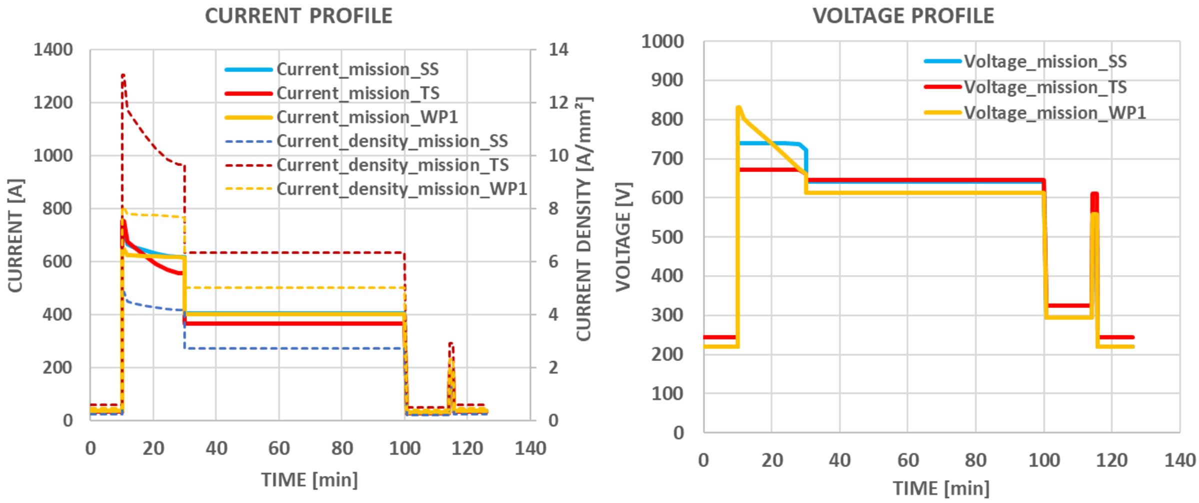

Fig. IV-11: Current, current density and voltage in the three electric motors.

The current shape seems to be similar in steady state thermal model-based optimization (blue curve) and with the transient state thermal model based optimization (red curve). However, looking at the current density, it is clear that there is a huge difference between both optimized machines. The difference in Joule losses is mainly due to the resistance of winding: the copper surface is smaller in the optimal motor in transient thermal regime. This explains the difference in current density between both machines. The voltage profile provides is typical of the use of field weakening during take-off and climb phases (constant voltage operation) for the optimized electric actuators. Contrarily, the field weakening has not been used for the WP1 design based on a unique (maximum) mission point.

The next comparative analysis is related to motor sizes.

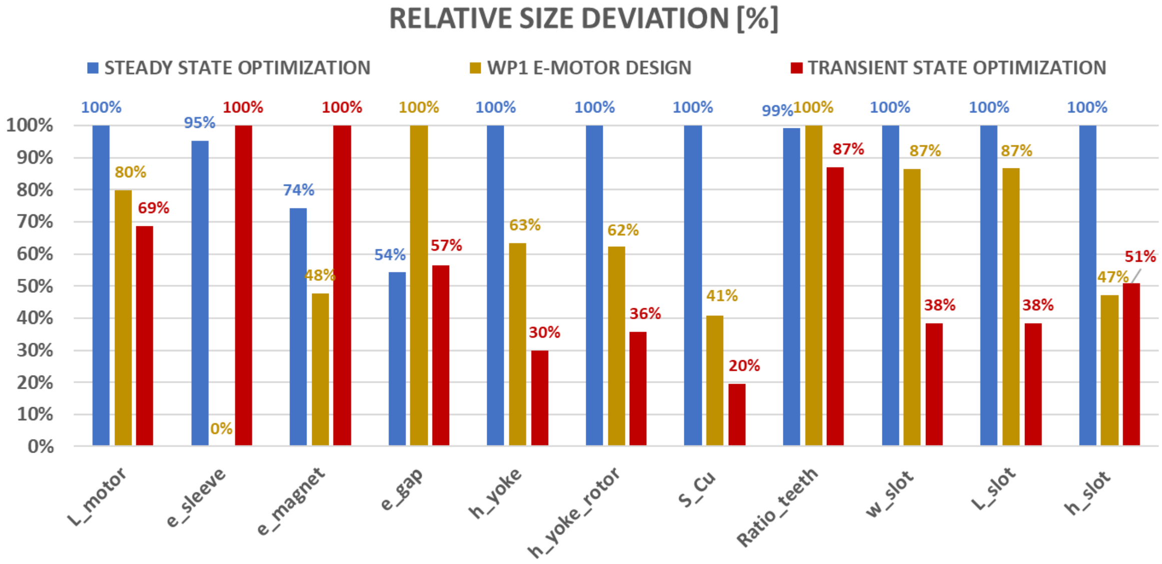

Fig. IV-12: Relative size deviations versus the maximum values.

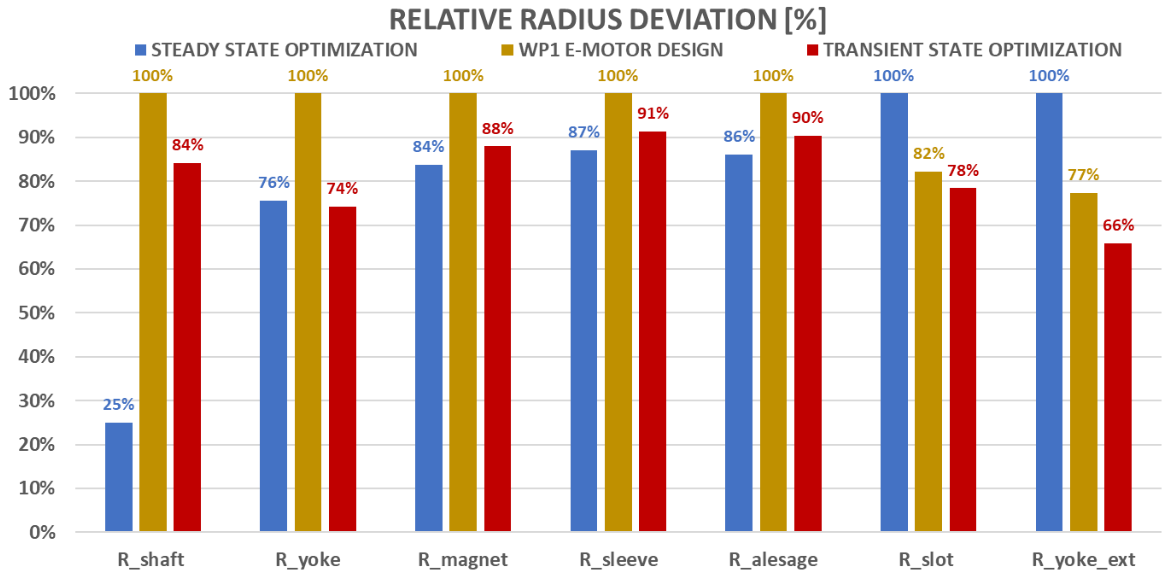

Fig. IV-13: Relative radius deviations versus the maximum values.

In the diagrams of Fig. IV-12 and Fig. IV-13, relative deviations are displayed to better compare the three design: each absolute value has been divided by the maximum value between the three electric machines. This representation shows directly the relative differences between the size of each optimization. For example, the copper surface is at 20% of the maximum in the transient optimization, which means that there is a ratio of 5 between the copper surface of the steady-state optimization and the transient one, moreover there is a ratio of 2 between the WP1 machine and the transient optimization.

In the Fig. IV-12 sleeve thickness has not been considered but the air gap is too small in order to install a sleeve. This is why the air gap thickness is maximum for the WP1 machine. Apart from the absence of sleeve in the WP1 design, the optimized machine coupled with the steady state thermal model has the largest dimension in absolute value, which seems consistent. The copper surface area has been divided by 5 between both optimizations based on both thermal models (the motor height has been divided by 2 and the length by 2,5) leading to the specific power increase as previously mentioned. The yokes have followed the same reduction way (with a ratio of 3 between both optimizations). All these size reductions obviously have an impact on the masses of each component (see Fig. IV-14).

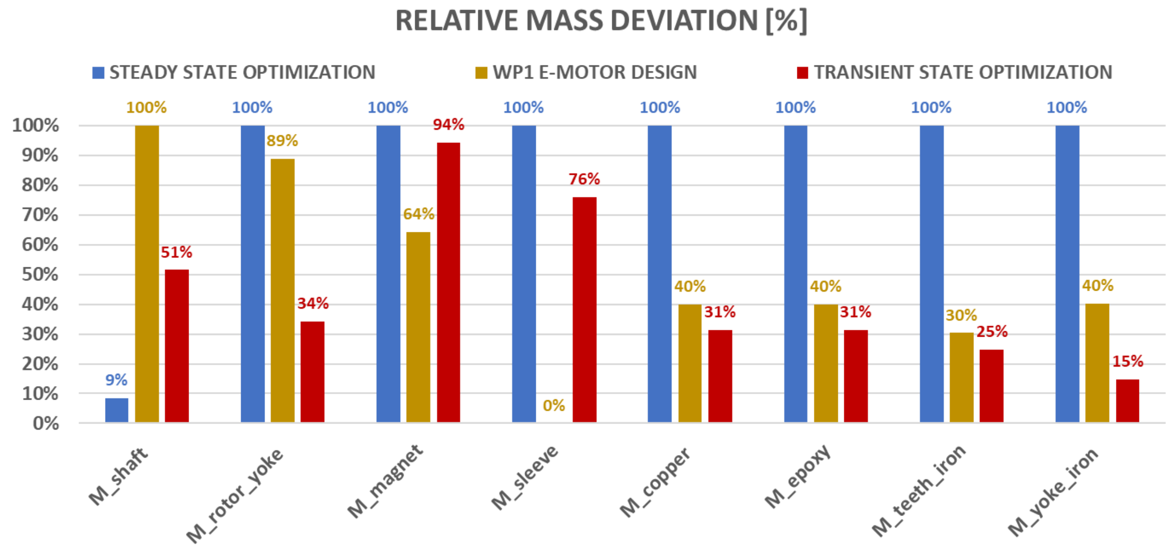

Fig. IV-14: Relative mass deviations to the maximum values.

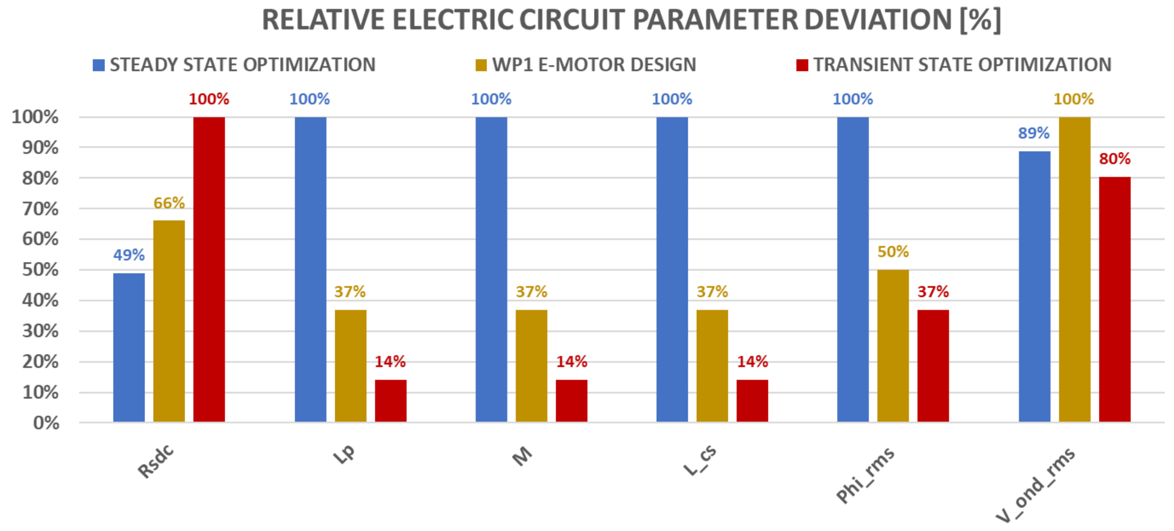

Fig. IV-15: Electric circuit parameter deviations to the maximum values.

Differences on circuit parameters result from different motor sizes. The resistance of the stator windings increases for with the transient thermal model. This comes directly from the equation (see APPENDIX F.1.5 the Eq F-36) because the copper surface area decrease provokes the resistance increase. It can be noticed that the electrical time constant (L/R) of the three machines is strongly different, with a fast-electrical mode for the optimization based on the transient thermal model.

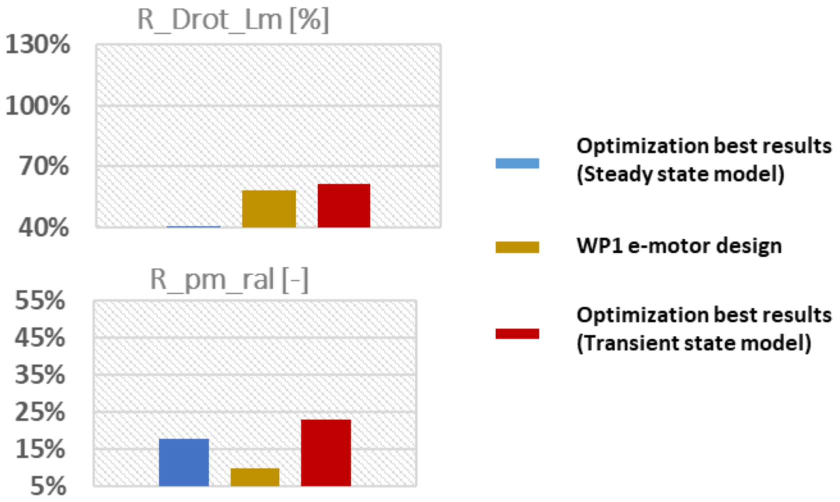

Fig. IV-16: Both values giving the best objective function for both optimizations (blue and red), compared to with the e-motor designed made by the team in charge of WP1.

The model difference on the magnetic flux density of the air gap pushes the optimization to magnify the magnets, during both optimizations (steady state and transient) the value is much larger see Fig. IV-16. The final results of the two optimizations compared with the WP1 design have been summarized in the Fig. IV-17.

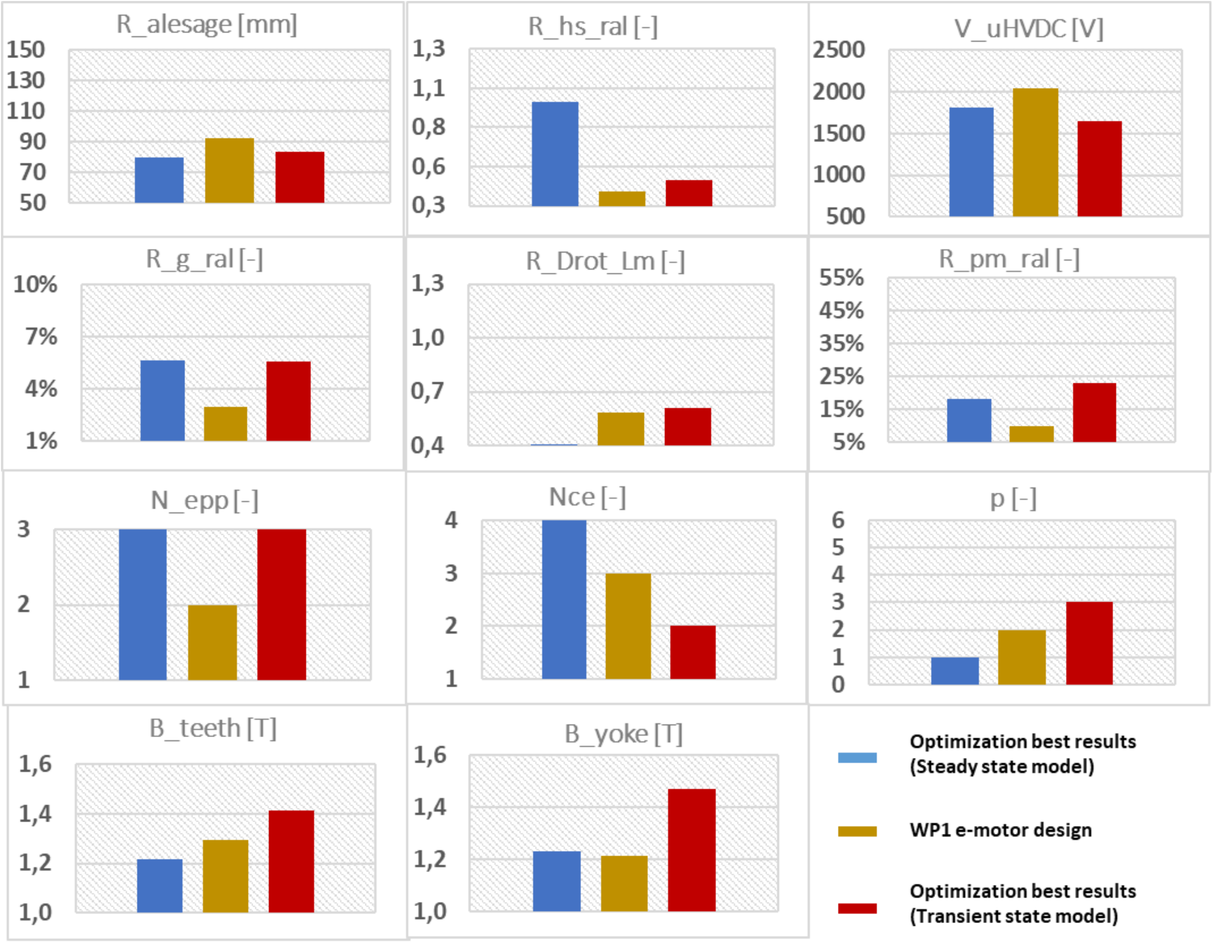

Fig. IV-17: Decision variables giving the best objective function for both optimizations (blue and red), compared with the e-motor designed by the team in charge of WP1.

With lower thermal constraints (as in the case of the transient thermal model), the number of pole pairs can be increased and the actuator sizes are directly reduced. However, the increase in the number of pole pairs increases iron losses in the stator yoke, especially if the flux densities (yoke and teeth) follow the same trend. The field weakening strategy allows counterbalancing this significant increase in iron losses by decreasing them when they are at highest operation during the mission. The electric machine with the best specific power still has to pay for its weight loss by a lower efficiency (even if it remains significantly high 97%>): remember that the motor weight is the unique optimization objective, losses being only limited by thermal constraints.

In the case of a regional aircraft with hybrid electric propulsion, weight plays a first determining role compared with an all-thermal aircraft. However, once the weight is on board the aircraft, efficiency will play an even more essential role in the sizing of the sources as well as consumption. By coming back to the aircraft level, the best trade-off between weight and losses will be found by optimizing the “less consuming aircraft” at system level.

The electric machine optimization has shown the importance of interactions between fields (electric, electromagnetic, thermal, partial discharges constraints, etc). In particular, cooling aspect plays a key role in the sizing of electromechanical components. In the following of that chapter, the overall propulsion system has been integrated with the corresponding set of model. In that case, the fuel burn mass becomes a key objective but this global optimization will also be compared with a mass based optimization by considering the whole powertrain. These two latter optimization problem can also be compared with a local vision based on the optimization of the motor mass alone. Another issue is relative to the energy management strategy of the hybrid electric architecture. Two cases will be successively considered:

- A “light hybridization scenario” (see section IV.2) for which the hybrid ratio (power ratio between electric vs thermal sources) are *a priori* fixed (with a 100% electric taxi and descent);
- A “variable hybridization scenario” for which the optimization is in charge of setting the hybrid ratio along the flight mission (see section IV.3).

IV.2 Hybrid-electric aircraft design with a “light hybridization scenario”.

Several studies focus on the aerodynamic gains possible with electric motor propulsion (distributed electric propulsion) [107], [108]. The scalability of the electrical components makes it possible to intelligently position the various actuators at strategic locations on the aircraft. This thesis focuses on the energy aspects and in particular on the system variables of electric propulsion. The use of electrical component sizing models allows the study of several problems:

- the increase of the power density thanks to an optimal electro-thermal coupling.
- the increase of the DC bus voltage of components to reduce their volume without causing partial discharge problems.
- the impact of ideal component sizing on the propulsion system of a hybrid electric aircraft.

In that subsection, the energy management of the hybrid electric structure is *a priori* fixed as displayed on Fig. IV-18: a full electric taxi and descent (HR[1]=1) is considered while a full thermal operation has been set for climb and cruise flight sequences (HR=0).

The looped process presented in chapter I section I.3.3 was previously conceived to take account of the snowball effects between embedded masses and consequences of the whole mass (MTOW) including the fuel burn. In the context of the integrated optimal design, this looped process has been revised. Indeed, in order to obtain a stable result in terms of MTOW, the process needed to be looped 5 times given one system sizing. Thus, in the optimal design context, two imbricated loops would have to be considered:

- an outer loop dedicated to sizing optrimization;
- an inner loop to take account of snowball effects (Equation (I-4)).

In order to avoid multiple loops but keeping snowball effects into consideration, the equation linking thrust and MTOW is conserved but only by adding a new optimization constraint (Eq.(IV-2)). A new optimization variable also appears: the thrust ratio $RThrust$ (Eq.(IV-1)). This new optimization parameter makes possible to anticipate (and to face) the new max take-off weight $MTOW_{new}$ of the hybrid-electric aircraft obtained after the sizing choice set by the optimizer. It should be reminded that the starting point (ref point) of the optimization is a conventional thermally propelled aircraft with a reference max takeoff weight: $MTOW_{ref} = 23\text{ T}$.

$$RThrust = \frac{Thrust_{new}}{Thrust_{ref}} \tag{IV-1}$$

Thus the following constraint is implemented in the optimization model in order to find the thrust needed to take off the hybrid-electric aircraft:

$$RThrust.MTOW_{ref} \geq MTOW_{new} \tag{IV-2}$$

The new optimization problem has then a new constraint to satisfy but it has been necessary to make this change to drastically improve the computational time and to break the multiple loops approach.

Taking the fuel burn weight as the objective function, this constraint will behave nearly as an equality because an oversized thrust would lead to increase the power demand consequently rising consumption at the aircraft level. In other words, the fuel burn based optimization will set the “just necessary thrust” to fly the optimized aircraft.

A mass limit has also been introduced in the optimization problem. Indeed, the powertrain sizing process is based on a reference aircraft with a given wingspan, this latter being considered as conserved during the optimization convergence: only the propulsion system is reconsidered in this process. Consequently, a gap limit of 6T has been introduced in terms of MTOW: $MTOW_{max} = MTOW_{ref} + 6\text{T}$.

$$MTOW_{new} \leq MTOW_{max} \tag{IV-3}$$

---

[1] HR is the Hybrid Ratio between powers form both thermal (Gas turbine) and electric (fuel cell) sources: HR=0 means that only the gas turbine is powered; contrarily, HR=1 means that a full electric operation is considered.

It is already possible to anticipate the maximum value of the new optimization variable $RThrust$. By respecting these two new constraints, the thrust ratio will not be able to exceed a maximum value.

IV.2.1 Optimization of aircraft fuel burn with a "light hybridization scenario".

In this section, the topic is focused on the symmetrical hybrid electric aircraft (HEASYM) shown in Fig. III-3 reminded in the figure Fig. IV-18.

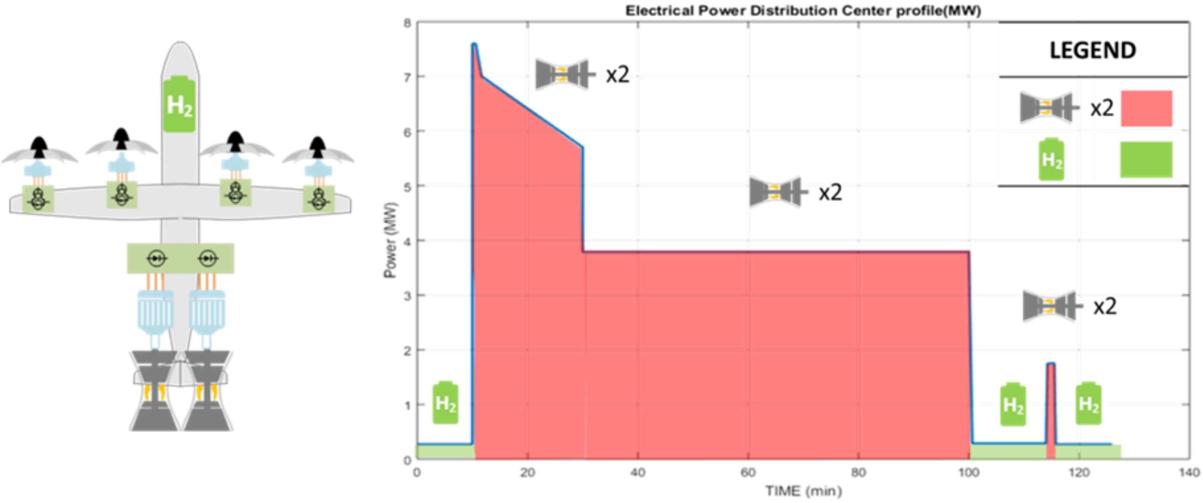

Fig. IV-18: Symmetrical Hybrid Electric Aircraft (HEASYM) with the Energy management..

The hybridization scenario is considered as "light", while the fuel cell is only sized to power the aircraft alone during the taxi and descent phases. All the rest of the mission is supported by the 2 gas turbines: thus the hybrid ratio (HR) are a priori fixed for the whole flight. Three different optimizations have been carried out in order to highlight the systemic approach compared with other, "more local", approaches:

- "Fuel mass optimization": the first optimization has the fuel mass as objective function;
- "propulsion system mass optimization": the second one has the mass of the complete propulsion system as objective function without counting the mass of the fuel burn in the gas turbines;
- "Emotor mass optimization": the last optimization consists in optimizing the electric machine mass alone (as for the previous subsection) with a propeller and a gearbox with fixed performance. This is equivalent to a local approach for the sizing of an electric machine. In that local approach, the machine and its performance will be simulated together with other devices at the aircraft level in order to compute the fuel burn of the gas turbines.

IV.2.2 Adaptation of sizing models to formulate a system optimization problem

In this case study, the level of precision and uncertainty of the models will not allow to draw quantitative conclusions on the absolute values obtained after optimization, but rather to observe trends and correlations.

With these system oriented formulation, 2 propeller and gear box sizing variables are added to the previous decision variables considered for the motor optimization alone.

Except the bus voltage, no additional decision variables are necessary to formulate the optimization problem, neither for the power electronics nor for the hybrid sources (remember in that case that hybrid ratio are *a priori* set).

Let us also note that the bus variable V_{uHVDC} becomes a system coupling variable having influence on cables, power electronics and machine.

Based on the cable sizing model, the gauge, number and material (Cu, Al) of cables are automatically derived knowing the maximum cable voltage (directly linked with V_{uHVDC}), the maximum transferred power and the power factor for AC cables between inverters and Emotors. Thus, no additional decision variables are added for cable optimization.

A frequency ratio (between switching and electric motor frequency) of 7 has been fixed here as proposed in [109] and this is justified in this reference [110] . This ratio is set to limit harmonics due to the inverter – motor coupling. With that ratio choice, the inverter switching losses are strongly limited. Furthermore, in order to simplify the inverter system design, the bar bus mass is assessed by considering a simple percentage of the inverter mass (see APPENDIX I).

The adaptation of power electronics model for system optimization was previously explained in the section II.2.4.2. We remind that:

- two particular structures are selected depending on bus voltage level: 3 level NPC converter is selected if V_{uHVDC} < 2040V else a 5 level ANPC is preffered. For each of these structures, both voltage and current ratings are fixed according to input data from the power electronic experts [93].
- The switching frequency is directly derived from the maximum electrical frequency of the eMotor [110] : $f_{switch} = 7 \times \max(f_{elec_{emot}})$.

Then the IGBT ratings are deducted without additional decision variables. The conducting and switching are then derived with a PWM strategy.

Based on these adaptations, 14 decision variables are sufficient to drive the optimization which are described in the Table IV-1 with their bounds.

Finally, this multidisciplinary design optimization includes (see Fig. IV-19):

- a specification (flight mission data: velocity, altitude, thrust requirement)
- an environment model to take pressure and temperature variations into account over the flight mission
- an integrated powertrain design identifying masses and efficiencies of each component (from the propeller to the power sources)
- the snowball effect at aircraft level into account: the reference mission is adjusted from the reference aircraft

Tab. IV-1: optimization input variables and their bounds.

Decision Variables	Lower bound	Upper bound
$RThrust$	1	1.26
$D_{prop_{siz}}$ [m]	2	5
R_{gbox} [−]	1	20
$R_{alesage}$ [m]	0.05	0.20
$R_{Drot_{Lm}}$ [%]	40	125
$R_{hs_{ral}}$ [%]	10	130
$R_{g_{ral}}$ [%]	1	10
$R_{pm_{ral}}$ [%]	5	50
$Nce[-]$	2	4
n_{epp} [−]	1	3
p [−]	1	7
$V_{uHVDC}[V]$	540	5000
$B_{teeth_{max}}[T]$	0.7	1.53
$B_{yoke_{max}}[T]$	0.7	1.53

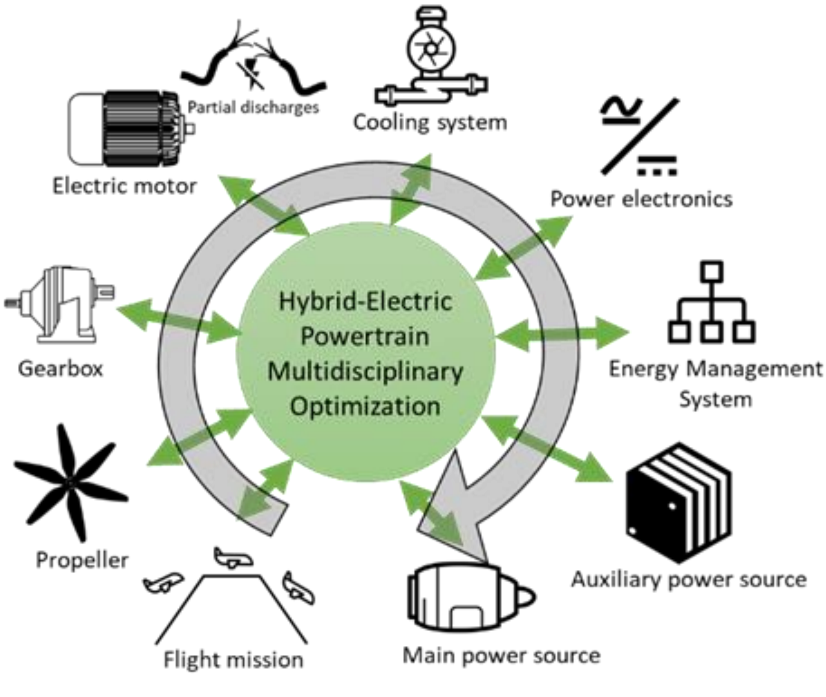

Fig. IV-19: Presentation of the multifields loop approached by the MDO of the hybrid-electric powertrain.

At the end of the process a hybrid-electric aircraft with its own powertrain is designed , the optimization process is illustrated in APPENDIX L - Fig. L-2.

IV.2.3 Optimization results and analysis

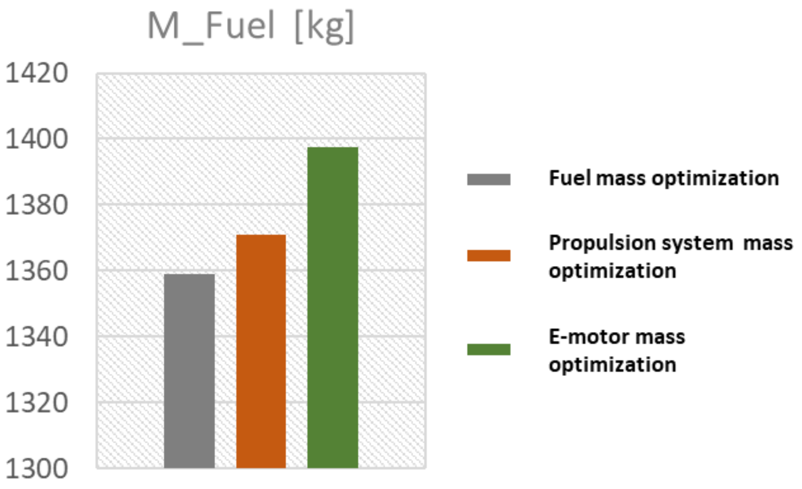

Fig. IV-20: Three optimization results on the fuel burn.

The first optimization (fuel mass) shows the advantages of taking all system couplings into account on the sizing of the propulsion system. The previous figure shows the consequences on the fuel consumption. Compared with others, the second optimization shows that a lightweight propulsion system does not necessarily mean an efficient system with a decreased fuel consumption. The last optimization is based on a local approach as an electric motor designer could have done: “the sum of the local optimum of each element is not the global optimum” from a system of view. This last point is also seen through the results on the specific power of the electric motor.

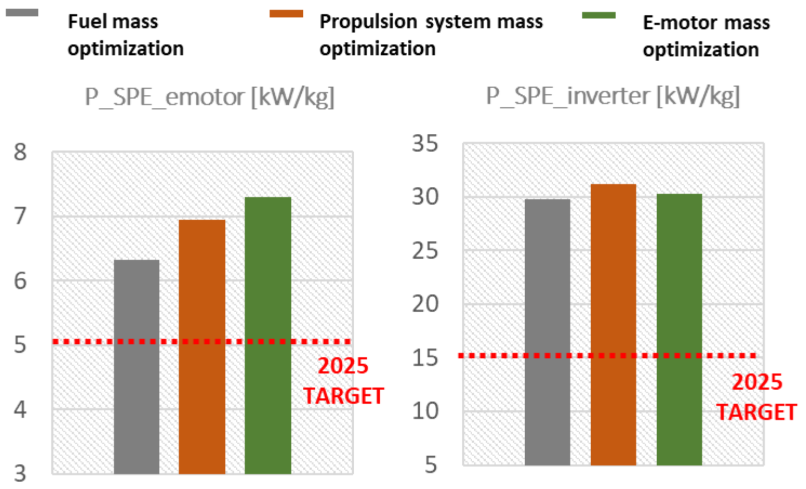

Fig. IV-21: Three optimization results on the specific power of the electric motor and the inverter (including cooling.)

The specific power increase of one component does not guarantee the reduction of fuel consumption, best fuel consumption results being obtained in that study with the lowest electric motor power density.

In the previous figures it can be observed that both specific powers (for inverter as for e-motor) are beyond the 2025 targets for the 3 different optimizations. In particular, the specific power of voltage source inverters is close to 30kW/kg for the three optimizations. This very good ratio is firstly due to the strong limitation of switching losses with a ratio of 7 between switching and electrical frequencies [110]. Secondly, the 3 level NPC structure offers a good tradeoff in terms of losses and structure mass. Finally, with that case study at low switching losses, the 7th generation IGBT power switches combined with the high performance of the cooling system are really convenient for optimization.

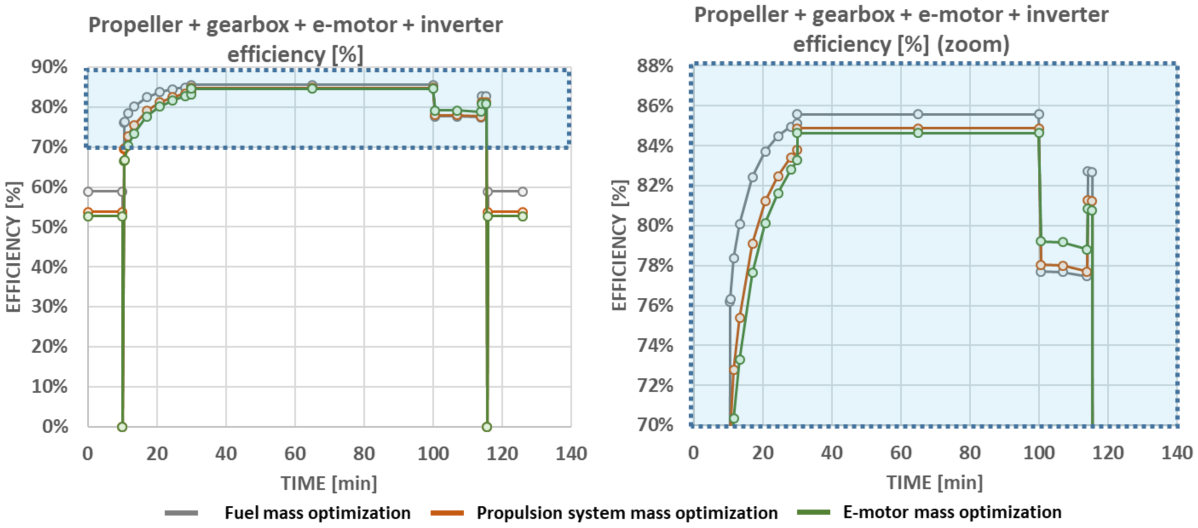

Fig. IV-22: Efficiency of the electro-propulsion chain during the flight mission (propeller -> inverter).

The powertrain efficiencies during the flight mission are displayed in the previous Fig. IV-22. It is important to note that the power density evolves in the opposite direction of the efficiency improvement: the best powertrain efficiency is obtained for the optimization of the fuel mass which drives the lowest specific powers at component (power electronics and Emotors) level. The optimization of the fuel mass highlights the importance of the propulsion system efficiency with regard to the final fuel consumption (see Fig. IV-20 & Fig. IV-22): these efficiency gains finally save 40 kg of fuel burn with respect to a local optimization.

Several parameters are at the origin of the improvement in the whole chain performance especially the propeller sizing.

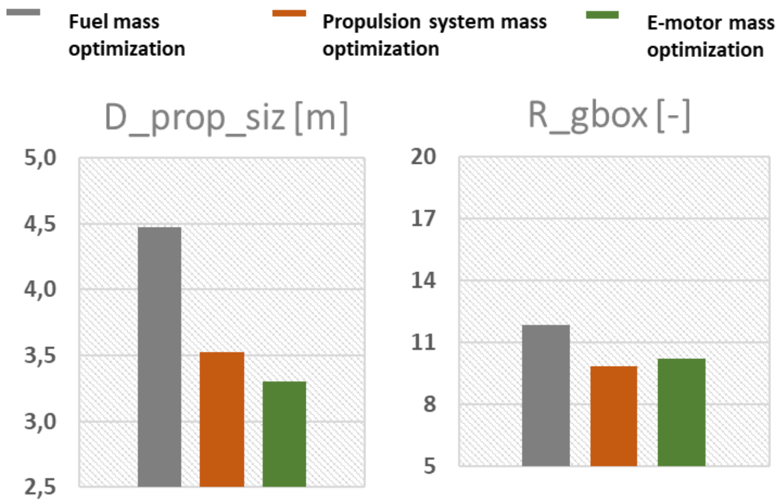

Fig. IV-23: Optimization result on propeller and gearbox input variables.

Indeed, the global sensitivity analysis studied in the previous chapter has shown the importance of the propeller design on the power chain efficiency (Fig. III-22). One point (1%) of efficiency was gained during cruise by oversizing the propeller, between both optimizations on the fuel mass and on the e-motor mass. The efficiency gain is also observed during takeoff and climb involving snowball effects: less power required to get the aircraft off the ground. The ratio of the gearbox is also important for the optimisation of the electromechanical actuator as it adapts the right sizing of the motor rotational speed given a propeller diameter. The gearbox model involving a constant efficiency, the mechanical efficiency improvement comes only from the propeller oversizing.

Differences on system efficiency are directly visible on the masses of both electric generators and rectifiers. Indeed, constant specific powers and efficiencies have been assumed for these devices. So the generator and rectifier masses are a "direct image" of the maximum power to be supplied for each optimization. The same trand can be observed for the Gast Turbine (GT) given a fixed (a priori) energy management. The figure below highlights the mass distribution for all powertrain devices and power sources.

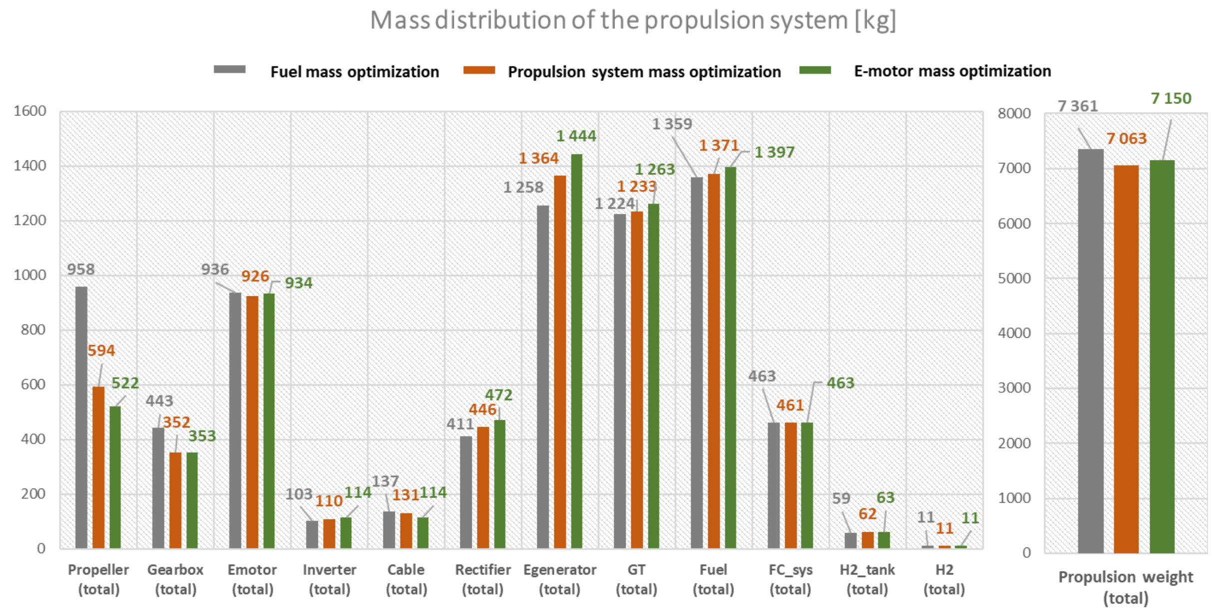

Fig. IV-24: Propulsion system mass distribution

Regarding the mass distribution:
- on propulsion side the motor-gearbox-propeller assembly is the most significant component;
- on source side, the electric generators and gas turbines involve highest masses;
- with a high DC bus voltage around 2 kV, the cable masses are negligible compared with the other components. The cables are thermally designed based on the current they conduct, which explains their low masses at high voltage;
- with this "light" hybridization strategy, the fuel mass saved by hybridization is quite reduced, being mainly due to the whole chain efficiency increase.

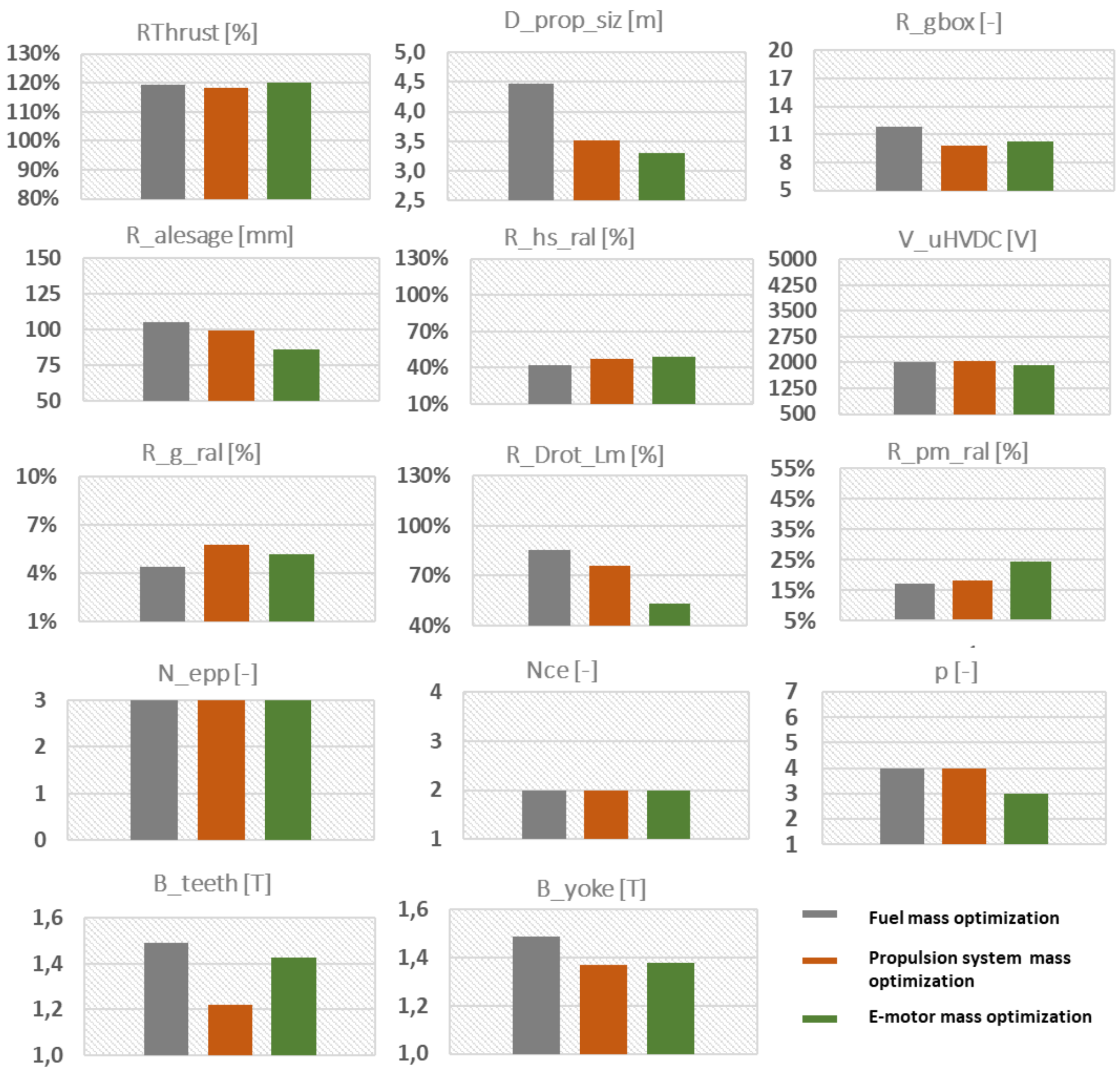

Fig. IV-25: Final decision variables giving the best objective function for the three optimizations.

The previous figure (see Fig. IV-25) shows the decision variables obtained for the best results of the three optimizations.

First of all, the V_{uHVDC} converges towards a value close to 2000 V. Remember that bus voltages lower than 2040 V involve the choice of a NPC 3L topology whereas the ANPC 5L converter structure is used for higher bus values. The 5L topology is more complex, heavier (presence of a flying capacitor). Thus, the bus voltage is close to the maximum permissible voltage provided by the 3L-topology. Based on the simplified model of winding insulation, the partial discharge issue is processed preserving the motor lifetime.

Regarding the electric motor, the improvement of its efficiency is mainly based on the aspect ratio $R_{Drot_{Lm}}$ between diameter and length, and on the increase of the inner stator radius $R_{alesage}$. All parameters related to iron losses (number of pole pairs p and inductions in the teeth and the yoke B_{teeth}/B_{yoke}) have been increased by the system optimization with respect to the local one.

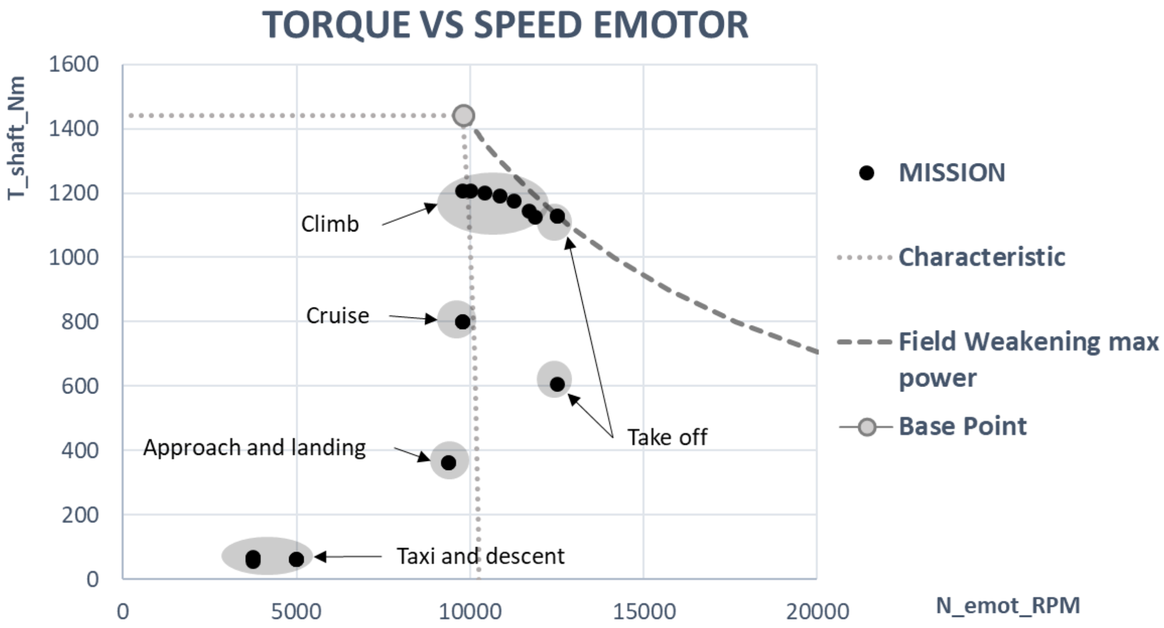

Fig. IV-26: Electric motor torque-speed characteristic for the fuel mass optimization.

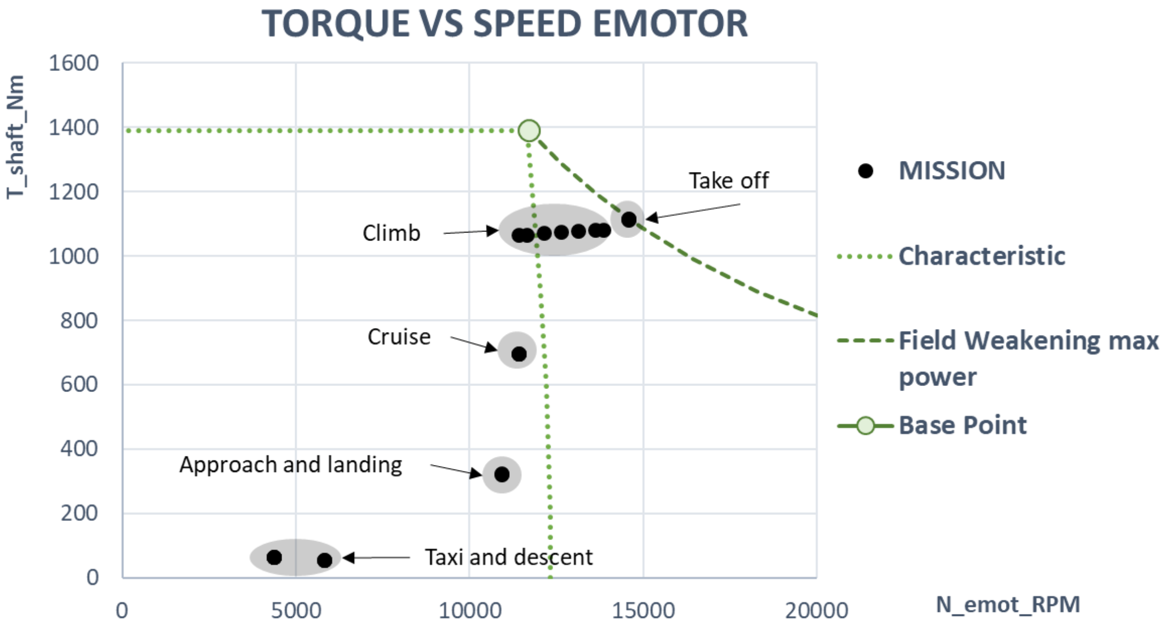

Fig. IV-27: Electric motor torque-speed characteristic for the e-motor mass optimization.

The two previous figures highlight the coupling between sizing choices and the flight mission by displaying the torque-speed plan of the electromechanical actuators for:

- optimization on the fuel mass (Fig. IV-26),
- optimization on the electric machine mass alone (local approach see Fig. IV-27).

In the system optimization, the oversizing of the propeller (involving system efficiency improvement) leads to a reduced the power required during takeoff and climb with respect to the operation of the system based on the local optimzation. In the case where the propeller has not been oversized (local optimization), the maximum torque is requested during takeoff, contrarily to the system optimization case where the whole efficiency is improved and for which the maximum torque is reached at top of climb. The fuel burn optimization case is the most favorable for a field weakening strategy: compared to the local optimization case, the maximum power is reached with a lower value of rotational speed. The torque base point is not as oversized as in the case where the maximum torque is reached at maximum speed.

At the end of these two optimizations, the MTOWs are quite the same, which means that the masses gained by the improved efficiency compensate the increase on propeller mass oversized for system optimization to obtain an efficiency gain (see Fig. IV-24 propeller mass). The propeller is an essential parameter in the propulsion of an aircraft, especially when coupled to an electric motor. The analysis made in the chapter III had predicted this sensitivity to propeller and gearbox design parameters. Last results (see Fig. IV-24) strongly highlight that issue.

While the energy management strategy was *a priori* established for each flight sequence, the next section will be devoted to couple the optimization of the same propulsion system with management strategy. This can be acheived by implementing variable hybridization ratios during the mission, these latter being included as new decision variables of the optimization.

IV.3 Integrated design of a hybrid-electric aircraft coupled with its energy management system.

The objective of this new optimization integrating system sizing and energy management aims at reducing fuel consumption beyond the results obtained in the previous section with the *a priori* fixed management strategy.

The Fig. III-3, Fig. III-5 and the Fig. III-6 in chapter III summarized different ideas of possible EMS for a hybrid-electric aircraft, following if the source power demand is the same for both gas turbines (HEA SYM) or not (HEA ASYM) or also if only 1 GT is embedded (HEA 1GT). In this section the EMS strategy will be determined via hybridization ratios (HR) variable during the mission. When these ratio equals 1, the electrical source provides all the mission power whereas only the gas turbine ensures the propulsion when the HR equals 0.

By adding hybridization ratios in the decision variable set, the optimization problem complexity is increased: 12 variables (HR values spread during the flight mission) are added into the previous set of parameters. Obviously, moving from 14 to 26 decision variables is not without consequence in terms of convergence with such optimization solved under huge constraints. In particular, the calculation time has been strongly increased. The optimization results “after 14 days of computation” are as follows:

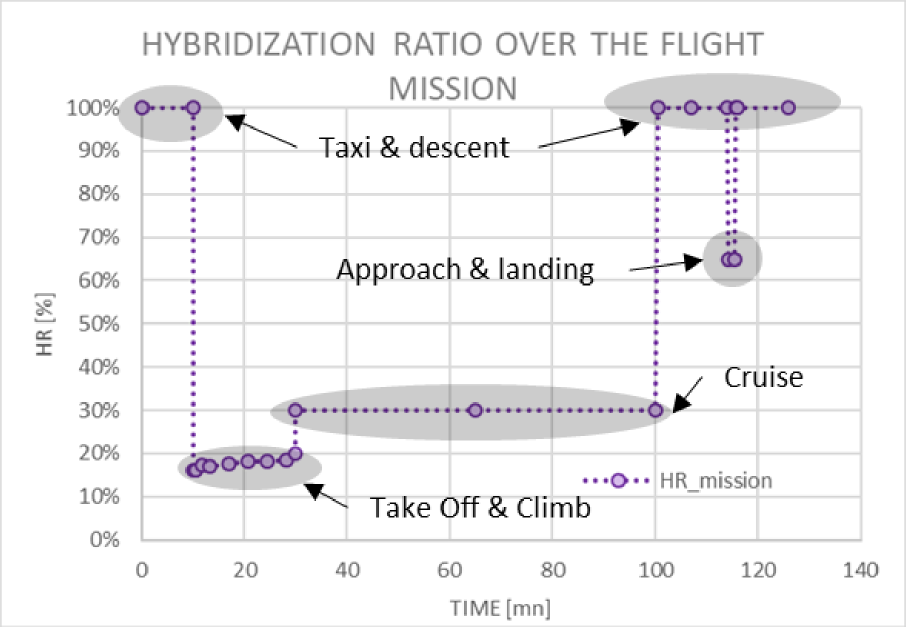

Fig. IV-28: Hybridization ratio over the flight mission.

First, the hybridization ratios (see Fig. IV-28) seems to be quite constant for each flight phases, except for the take-off/climb phases where the HR increases as the airplane climbs (15% -> 20%).

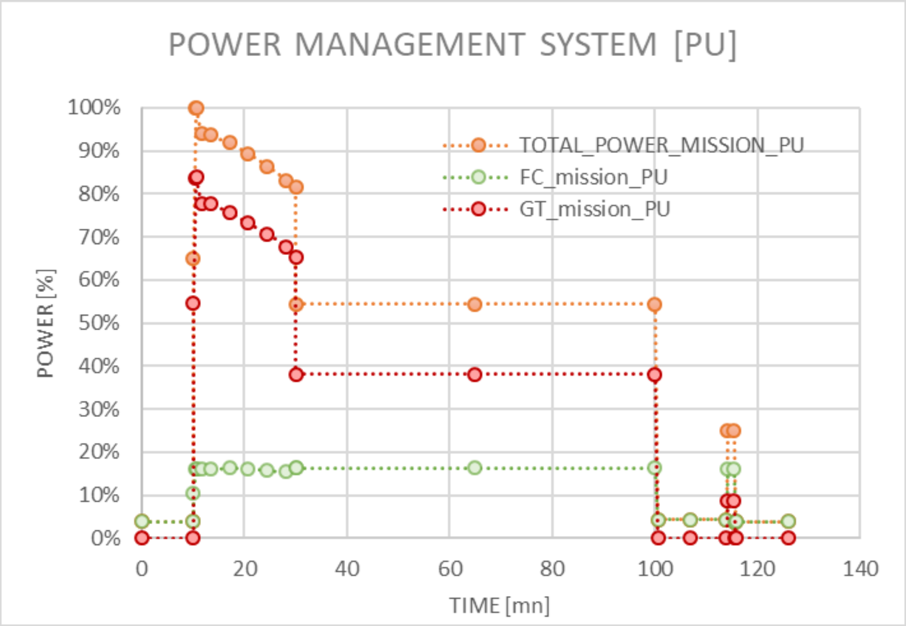

Fig. IV-29: Power management system over the flight mission per unit.

But regarding the total power drawn during the mission (see Fig. IV-29), the power drawn from the fuel cell stack seems to be constant (especially during climb and cruise) when the total requested power is higher than its sizing power. When a fuel cell is integrated to the hybrid propulsion system, the optimizer choices to use it at its design point (optimizing its efficiency) over the flight mission. The main benefit of the fuel cells (with respect to battery technologies) is the dissociation of energy and power. The fuel cell stack is designed according to the power to be supplied, while the storage volume is sized according to the energy needs. This last result will allow us to reduce the number of decision variables to be optimized in the following. Indeed, by using only the fuel cell design power as an optimization parameter, the hybridization ratio profile is simply derived from a division of the sizing fuel cell power with the power profile. This new rule Eq.(IV-4) is now implemented in the optimization problem reducing the number of decision variables from 26 to 15 !

$$HR = \begin{cases} \dfrac{P_{siz_{fuelcell}}}{P_{mission}} & if \ \dfrac{P_{siz_{fuelcell}}}{P_{mission}} \leq 1 \\ 1 & otherwise \end{cases} \tag{IV-4}$$

We also point out that the aircraft weight has reached the sizing limit $MTOW_{ref} + 6T$ by releasing the fuel cell sizing. Indeed, the additional cost in terms of Hydrogen consumption is not counted in the optimization of the fuel burn only focused on kerosen consumption. The propulsion system is then heavier, especially increasing the fuel cell stack and the hydrogen volume of storage but snowball effects in terms of mass are not compensated by the fuel saving induced by an icreased use of the auxiliary electric source. Thus, it should be noted that a heavier propulsion system does not necessarily lead to an increase of the fuel consumption.

NB: it is important to point out that one limit among our model assumptions is certainly reached in that case, due to the linearization of the MTOW variations versus the thrust ones. Indeed, this assumption is considered as valid only if the reached values of MTOW are not to far (here less than 6T) from the "reference aircraft sizing". Here, the MTOW limit is reached with this optimization showing that this (more electric) hybrid aircraft is not completely optimized. In order to explore design solutions with higher MTOW figures, it would become necessary to couple our powertrain sizing model with more complete and accurate aerodynamic design involving flight mechanic equations as it was done in the thesis of Jerome Thauvin [12]. *This research direction seems clearly to be a major prospect of our work "on the road of more electric and of course zero emission future aircrafts".*

A new optimization has been performed with the new energy management rule Eq. (IV-4) only considering the fuel cell sizing as supplementary decision variable. The hybridization ratio obtained during climb and cruise is close to 20% (close to values observed for the Fig. IV-29). The fuel (kerosen) mass saved is around 200 kg (-15%) with respect to the "light hybridization scenario" but the objective function of this optimization still consider the kerosen burn only, without taking account of hydrogen burn during climb and cruise (remember that fuel cell is off in the previous "light hybridization strategy" during these high power flying sequences.

Fuel economy has an impact on the allowable take-off weight: as in the latest optimization result, the weight of the aircraft has reached (as anticipated) the allowable take-off weight limit $MTOW_{ref} + 6T$. Compared to the light hybridization scenario optimization, the snowball effect variable $Thrust_{siz}$ has reached its maximum value allowed during the optimization.

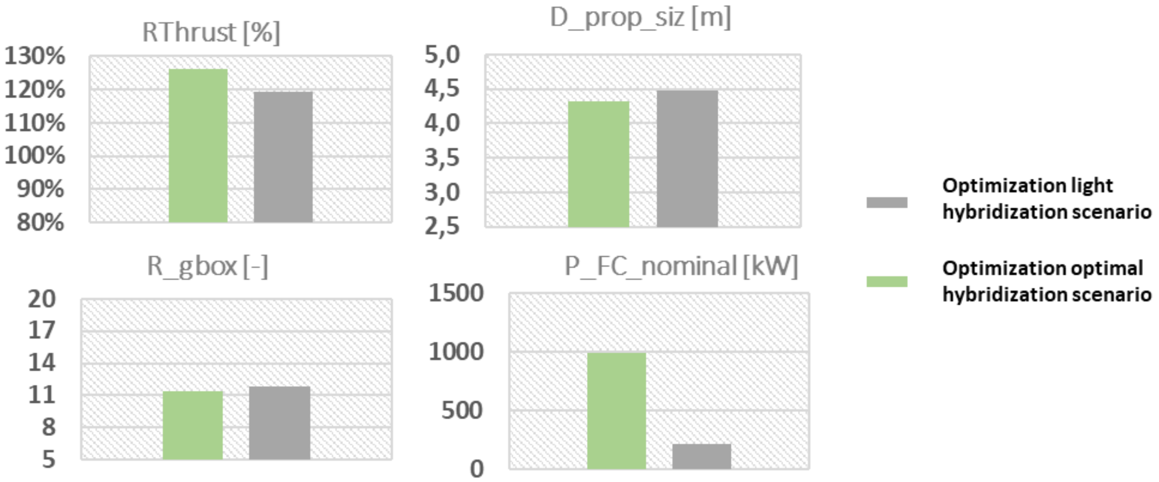

Fig. IV-30: Design variables for the snowball effect, the propeller, the gearbox and the fuel cell stack nominal power for both scenario (green: optimization including fuel cell stak power in the decision variable set – grey: "light hybridization").

The propeller diameter is slightly smaller than for the previous optimization with a light hybridization scenario because the take-off weight value has reached its limit. Therefore, a trade-off was found between improving performance (oversizing the propeller and its weight) and fuel economy by adding a more powerful auxiliary source (more powerful fuel cell and its associated storage). Same conclusions apply for the gearbox ratio between the propeller and the electric actuator which is slightly decreased, consequently reducing its mass in order to allow supplementary mass for the electrochemical source. The hybridization ratios cannot be compared because the light hybridization scenario does not use the fuel cell during the whole mission (HR =0 during the cruise) see Fig. IV-30.

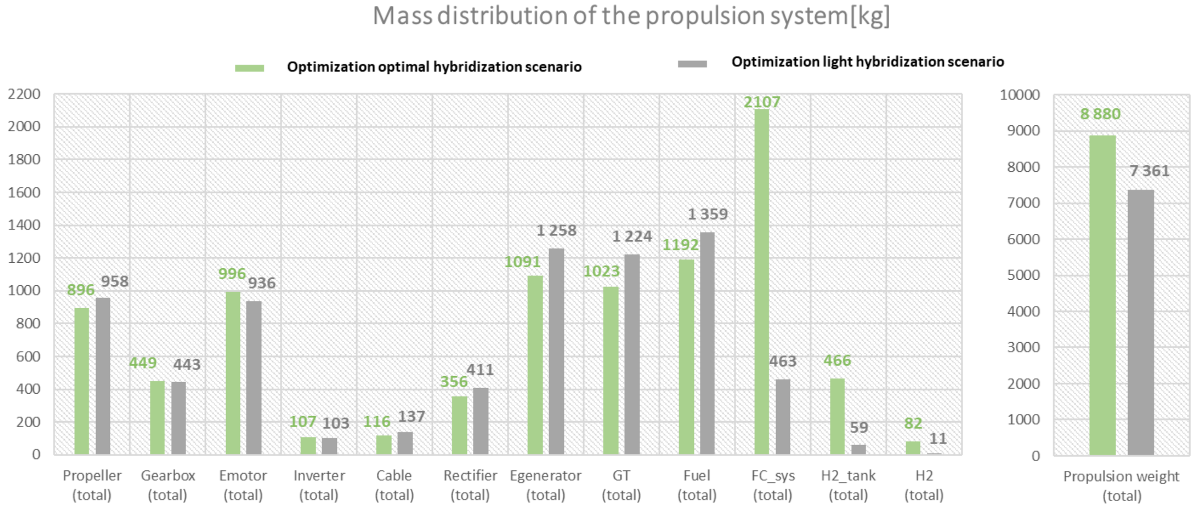

Fig. IV-31: Propulsion system mass distribution for the 2025 HASTECS target.

The fuel cell nominal power was multiplied by five between the light hybridization scenario and the optimal energy management scenario. This difference in sizing has a direct effect on the masses of the electrochemical source. Thanks to the sizing point (~20%), the fuel cell allows to save a large part of the aircraft fuel (around 150kg saved see Fig. IV-31).

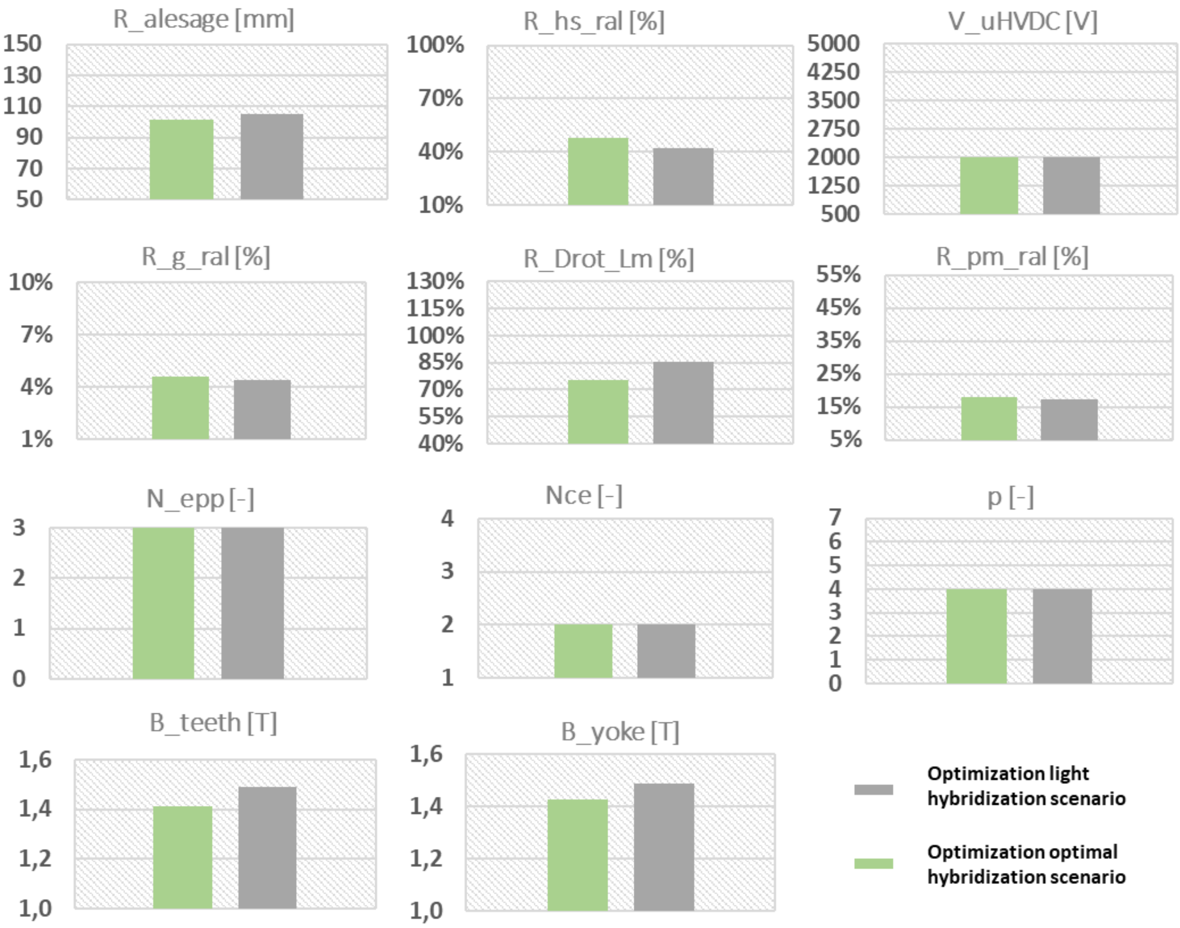

Fig. IV-32: Optimisation comparison (green: optimal hybridization ratio – grey: light hybridization scenario).

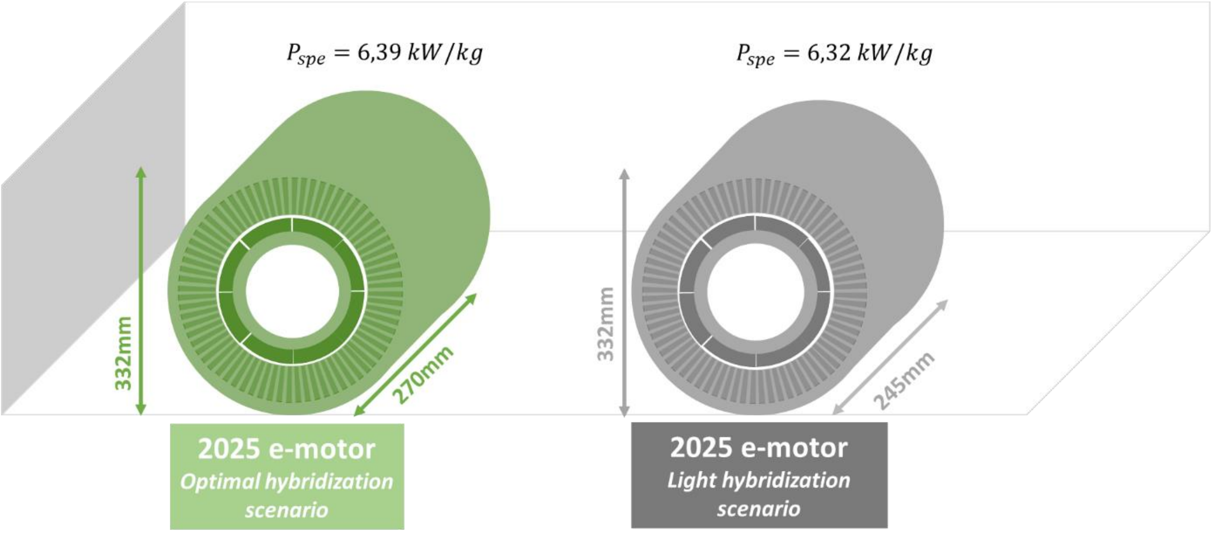

Fig. IV-33: Geometrical comparison (green: optimal hybridization ratio – grey: light hybridization scenario).

In spite of a different hybridization strategy, electric machines have almost the same decision variables and are therefore geometrically very similar. But the use of these machines differs during the mission.

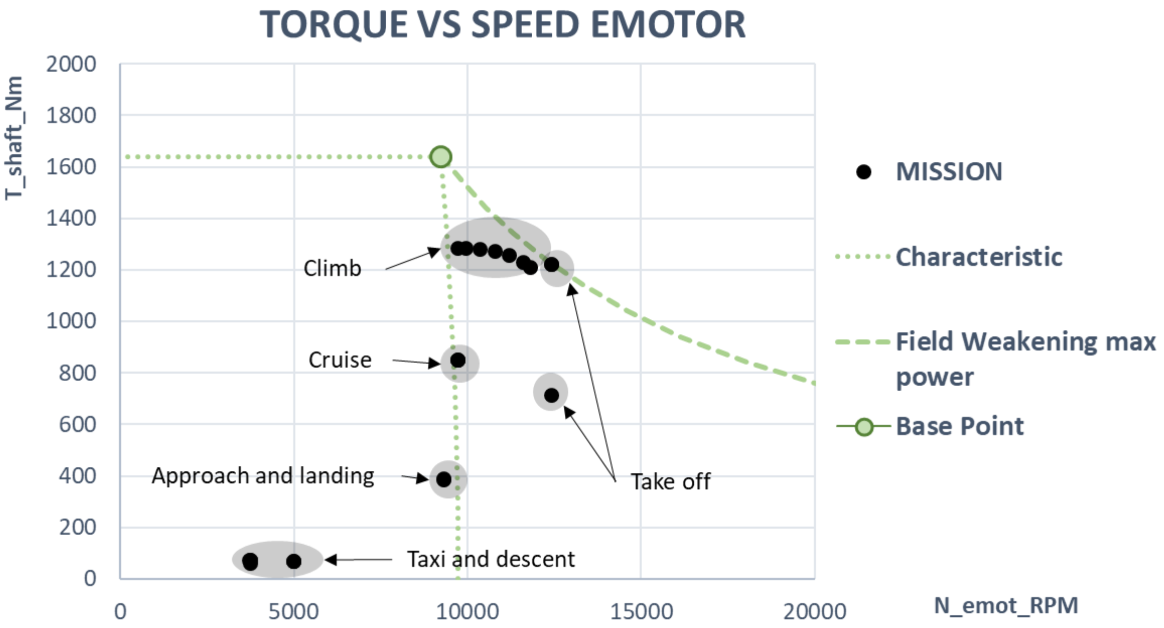

Fig. IV-34: Torque-Speed characteristic for the 2025 optimum results (including FC stack sizing).

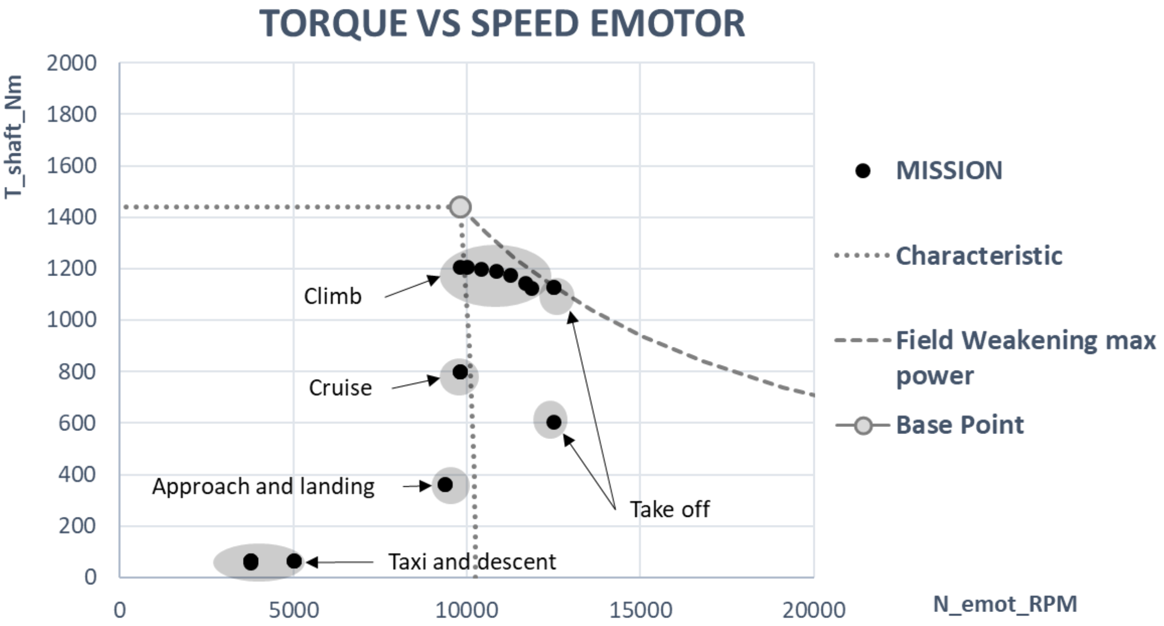

Fig. IV-35: Torque-Speed characteristic for the 2025 light hybridization scenario results.

Both actuators slightly differ in performance during the flight mission (see Fig. IV-34 & Fig. IV-35):

- the base point in the torque-speed plane changes during the mission, with a torque sizing point increased for this new optimization;
- the actuator device exploites the magnetic field weakening operation during cruise (the green dotted characteristic is on the left of the cruise mission point), contrarily to the previous optimization case (the grey dotted characteristic is on the right of the cruise mission point). This field reduction also reduces iron losses improving therefore the actuator efficiency during the cruise phase (the longest in time during the flight

mission). By improving the performance during the cruise, the electromechanical actuator improves the efficiency of the chain, especially when the fuel cell is in operation.

The power densities of the electrical components studied has reached the same values as before (see Fig. IV-21).

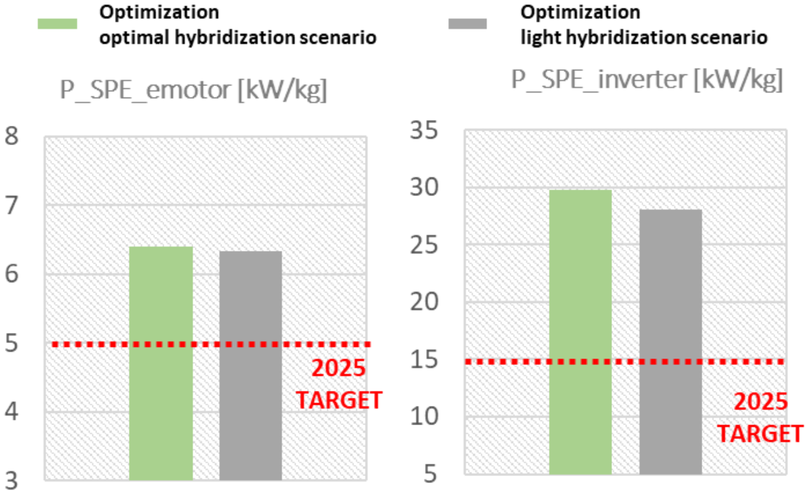

Fig. IV-36: Specific power of the electrical components.

The power densities for both optimizations, the difference in fuel consumption is mainly due to the missions of both sources: with 20% of the power supplied by the fuel cell, the fuel economy is remarkable, at around 150 kg (see Fig. IV-37).

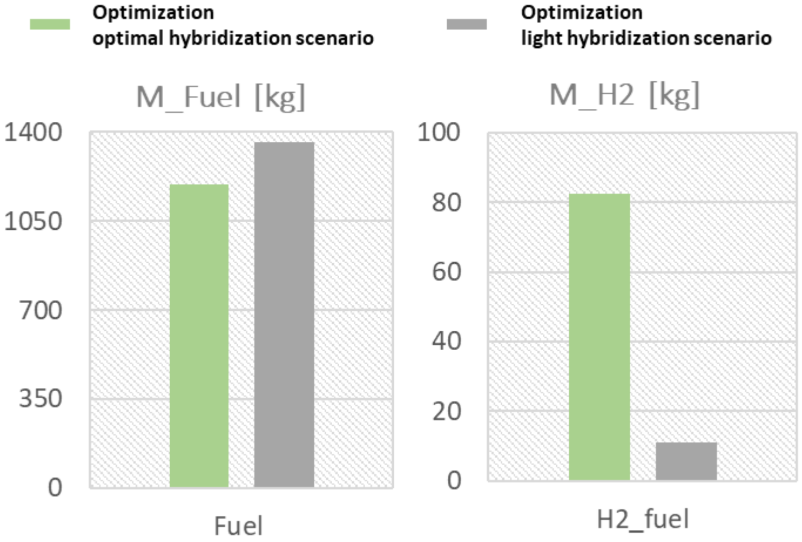

Fig. IV-37: Comparison of the fuels required for the mission.

Looking at the power distribution, the fuel cell element provides up to 20% of the total power required during high power phases (Fig. IV-38). As mentioned before, a MTOW limit has been incorporated into the optimization to avoid reaching too large masses. Without this limit, and with an objective function only dealing with kerosen burn, the optimization would have probably converged towards an all-hydrogen aircraft.

The 150 kg of fossil fuel have been replaced with 80 kg of hydrogen. This difference highlights the difference in energy density between the 2 molecules as well as the difference in efficiency: the efficiency of the gas turbine is lower than the efficiency of the fuel cell.

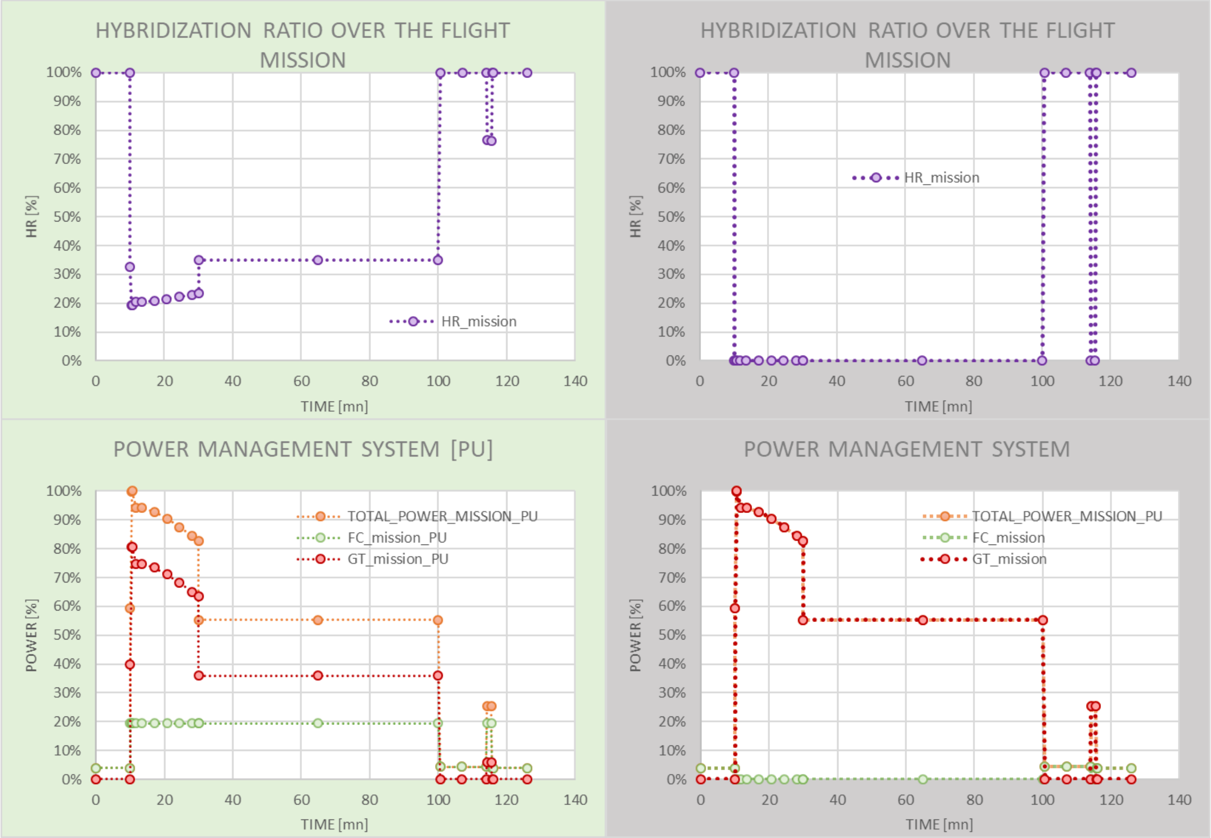

Fig. IV-38: Hybridization ratio and consequence on the power management of the propulsion system (green background: optimal hybridization scenario – grey background: light hybridization scenario).

Regarding the reference (optimized full thermal) aircraft, the optimized "HASTECS 2025 hybrid-electric aircraft" is much heavier (+26%). From a fuel consumption point of view, the "HASTECS aircraft" consumes only 3% more fuel meaning that efficiency improvements do not compensate the aircraft wright increase with the assesments set in the "HASTECS 2025 requirements".

To conclude to this section:

- Taking partial discharges into account and looping back to the sum of all the component masses during the optimization, a system trade-off has been highlighted on the DC bus voltage of the electrical network. This was confirmed during both optimizations. Without taking account of partial discharges in the Emotor insulation, the DC bus voltage would go to its maximum limit in order to relieve the sizing of the electrical components (cables). Considering the insulation issues, the value of 2000 V seems to be the correct system tradeoff, noting that it was also the local optimum obtained by the power electronics research team for the 2025 requirements applied on the inverter itself.
- The coupling of thermal and electromagnetic issues has highlighted the importance of the field weakening strategy for the actuator sizing. The energy-optimized aircraft uses

this strategy during cruise in order to always reduce losses during the most significant phases in terms of energy demand.

- Finally, the change of energy mission allows the saving of kerosene over the whole mission. Once the sizing power is installed in the propulsion system, the fuel cell is used at its rated power in order to save the maximum amount of fossil fuel drawn from gas turbines. The last optimization has shown that the fuel cell was used throughout the mission. Compared to the conventional all-thermal aircraft, the results obtained are more promising than those obtained using constant power density and efficiency (called "target aircraft") as it was previously presented in the chapter III. The Fig. IV-39 illustrates the relative deviations in MTOW and weight of on-board fuel with respect to the reference aircraft.

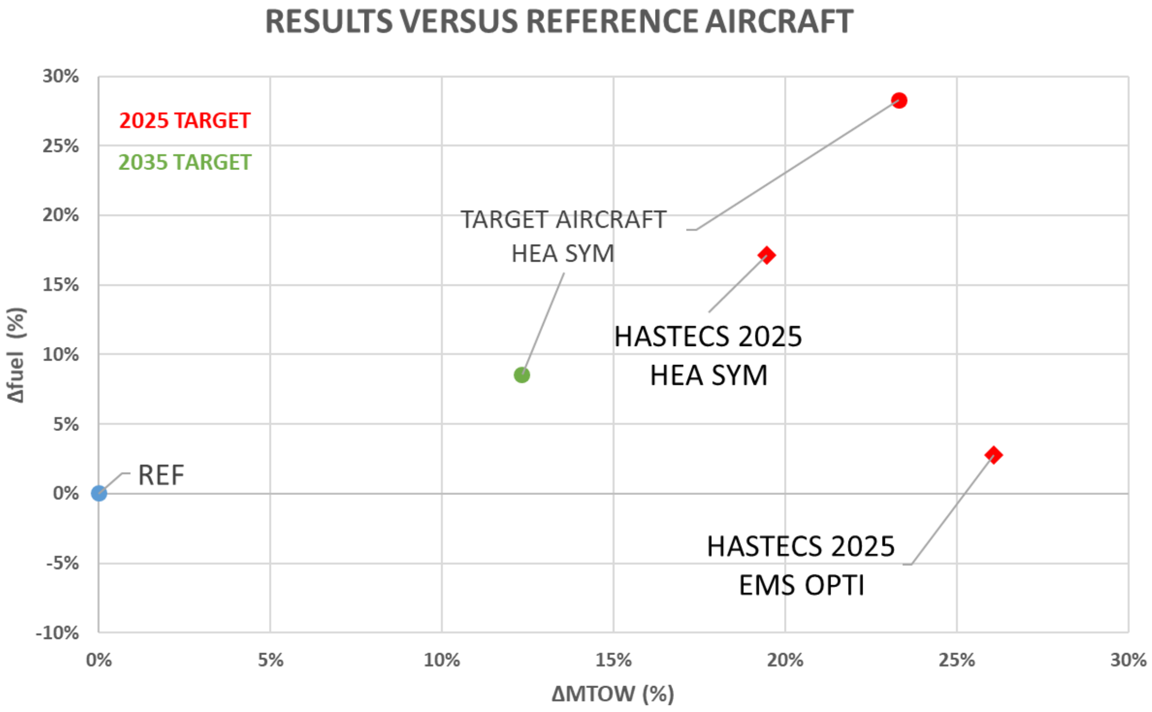

Fig. IV-39: Relative deviations in MTOW and fuel mass with respect to the reference aircraft

Compared to the 2025 "target aircraft" results, "HASTECS optimization" provides better solutions. When hybridization is used during flight ("HASTECS 2025 EMS OPTI"), the aircraft takes off a lot of weight in order to save fuel thanks to an increased fuel cell and hydrogen sizing. These results show here the interest of a multidisciplinary system approach for designing the propulsion chain.

The HASTECS study has focused on two targets: one entry into service for 2025 and another for 2035, these two targets dealing with different technological assessments. Crossing from 2025 to 2035 ssessments, the next section will examine the influence of technological improvements on the performance of future aircrafts.

IV.4 Exploration of the performance of a hybrid-electric aircraft taking account of technological advances in electrical components (target 2035).

The major changes between both 2025 and 2035 targets concern the cooling systems, especially for the electric machine, where spaces in stator slots are reserved for adding an internal cooling channel [87]. For the voltage source inverter, a new condenser technology has been studied in order to improve the power density of the converter [88]. All the details are explained in APPENDIX G (Electric motor cooling model), APPENDIX I (Power electronics and its cooling system.

IV.4.1 Optimization of the eMotor weight (2025 vs 2035 assessments)

In the first part of the chapter IV section IV.1, several optimizations have been carried out in order to observe the sizing differences between steady state and transient models. The power profile was identical for all these optimizations considered for the machine alone. Strongly better specific power has been obtained by the optimization with a transient thermal model allowing the machine to perform the mission with lower temperature rise during the phases of very high power demands (takeoff, climb). The following part is related to the same "exercice" with the new internal cooling model ('target 2035') (APPENDIX G). The power mission is still identical to the study carried out previously (chapter IV section IV.1), only the cooling model was changed.

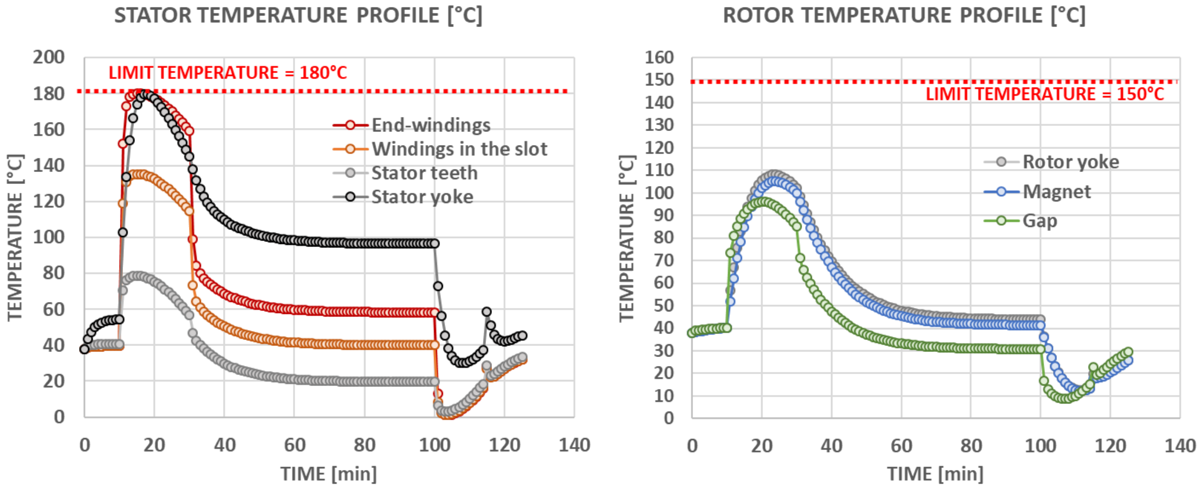

Fig. IV-40: e-Motor temperature (2035 target) over time.

The new 2035 optimization in Fig. IV-40 shows a different dynamic of the thermal behaviour. Indeed, the machine has become so small that the transient is no longer marked to avoid overheating the electric motor during very high power demand phases. The sizing constraints remain once again the temperatures in the stator (yoke and end-windings). The magnet temperature is well reduced. In fact the rotational speed of the actuator is not too high and the stator losses are sufficiently evacuated that they do not disturb the rotor temperatures.

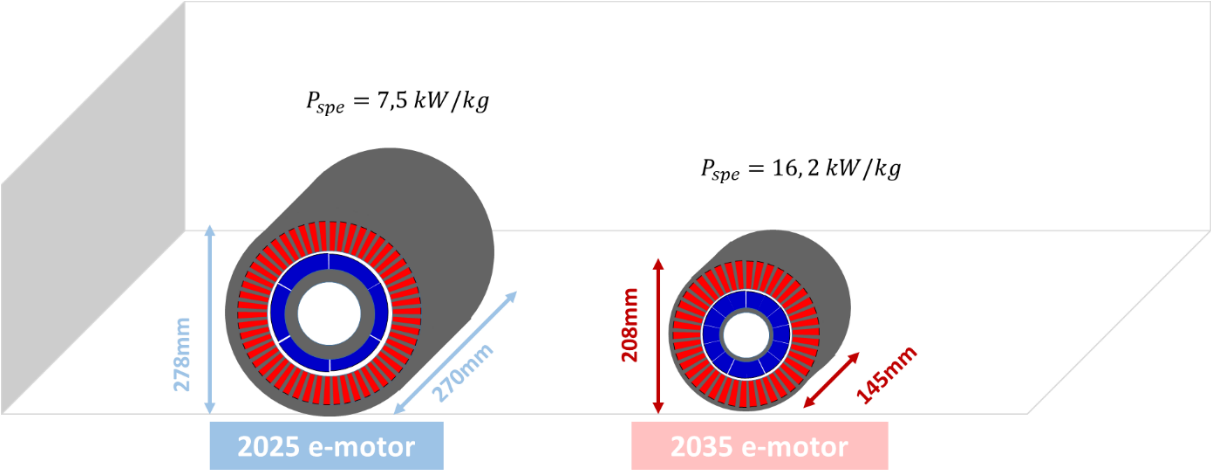

Fig. IV-41: Geometrical comparison (blue: optimal 2025 emotor – red: optimal 2035 emotor).

The difference between the volumes of both actuators illustrated in Fig. IV-41 makes it possible to double the specific power between 2025 and 2035.

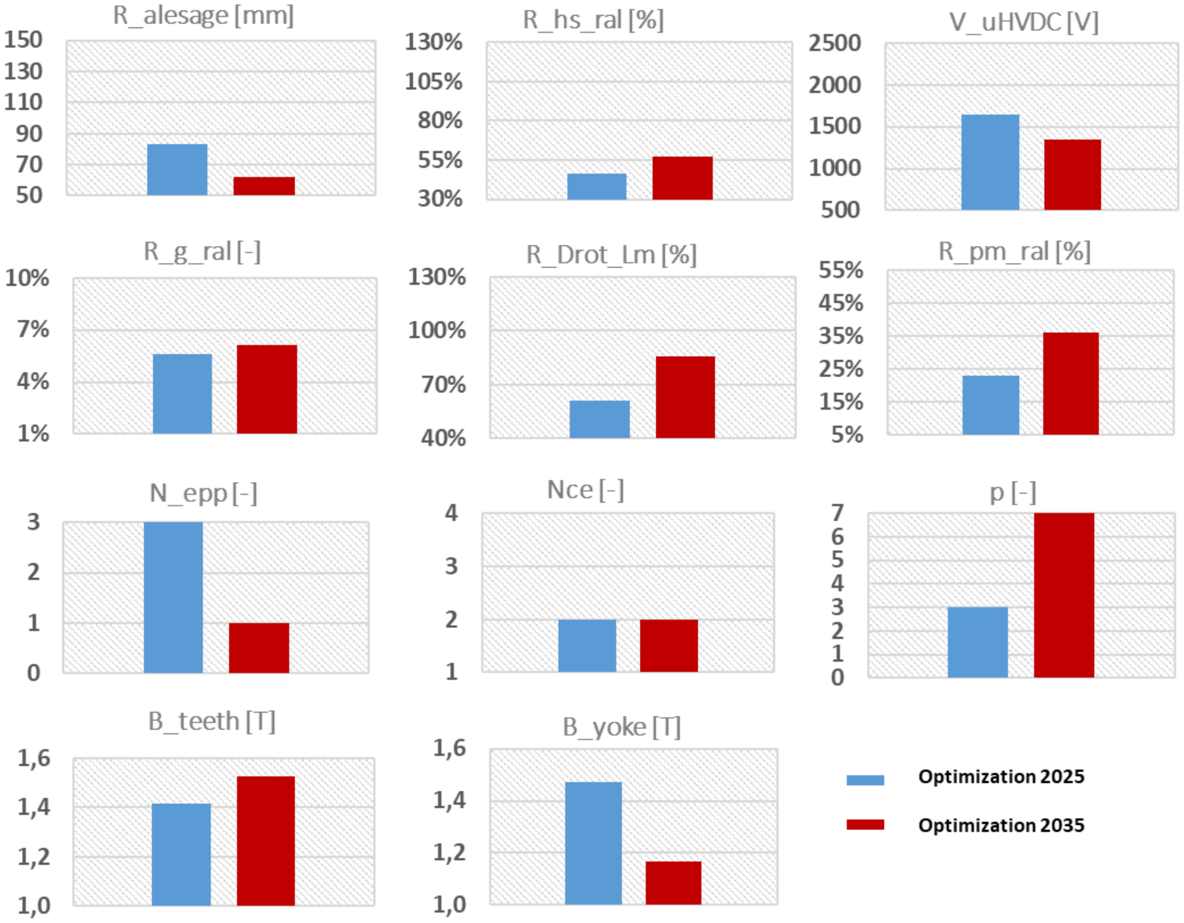

Fig. IV-42: Optimisation comparison (blue: optimal 2025 emotor – red: optimal 2035 emotor).

- The DC bus voltage is reduced for 'optimzation 2035' according to the insulation constraint: the slot is here smaller than for 2025 target because cooling channels are integrated inside the slot. The insulation is directly linked with the DC bus voltage. The lower the DC bus voltage the thinner the wire insulation inside the slots. To continue on the same idea, the number of slots per pole and phase is reduced to 1 to best integrate the cooling channels.
- The ratio between the inner stator radius and the magnet thickness is higher for the 2035 target, the volume of the electric motorbeing reduced, the air gap flux density needs bigger magnets.
- The cooling system is so efficient that it is possible to increase the number of poles pairs till 7. Increasing the number of pole pairs considerably reduces the thickness of yokes and other sizes of the actuator, however greater iron losses are to be expected which is managed by the highly performant cooling. The same explanation can be used for the flux densities in the teeth and in the yoke. The cooling channels are in touch with the windings and the stator teeth, so the flux density in the teeth can be maximized.

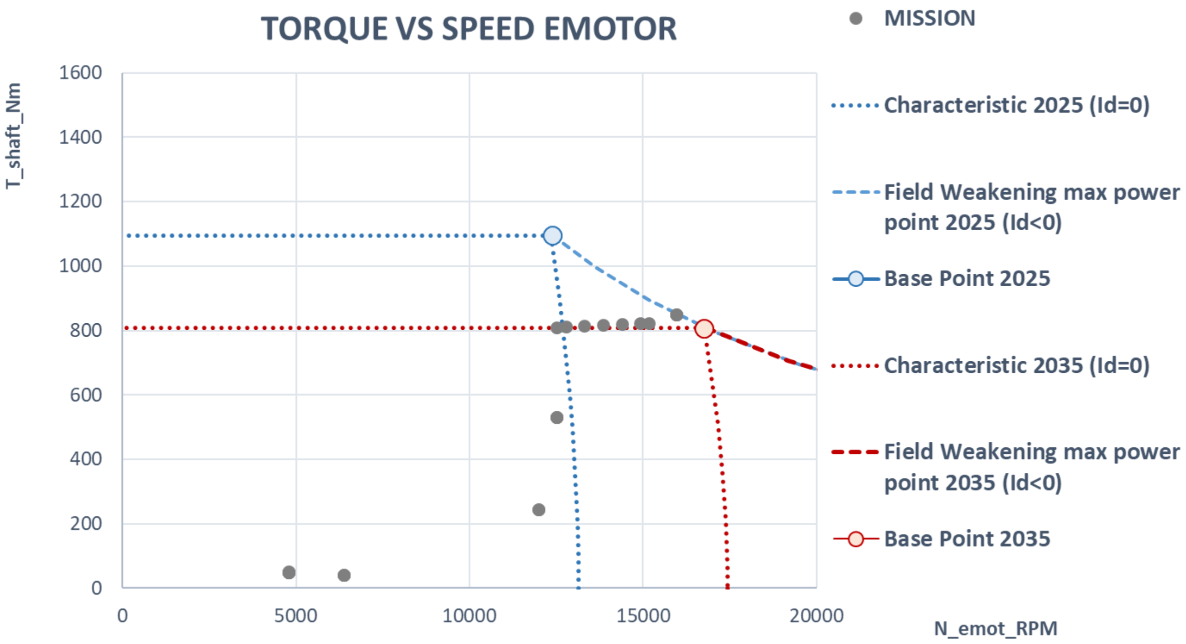

Fig. IV-43: Torque-Speed characteristic for the 2025/ 2035 optimum results.

Compared to the 2025 target (see Fig. IV-43), the mass-optimized 2035 actuator does not use field weakening strategy. The characteristic 2035 is below the maximum torque point: this cooling system is so efficient that it is possible for the actuator to explore an over-torque zone. This is possible because the actuator has become really small and the torque design point has gone down along the iso power curve (maximum power).

This new technological performance of the cooling system for the 2035 target will strongly reduce the mass of the actuator thus increasing its power density. As the machine is one of the heaviest elements in the propulsion system, this will allow the aircraft to lighten the mass of the propulsion system and thus consume less fuel.

IV.4.2 System optimization including energy management strategies

Compared with the previous study (target 2025), the same ecological objective function is considered (reduction of fuel mass) and the same hybridization strategies are used:

- A “light hybridization scenario” for which taxi and descent phases are full electric, the other sequences being full thermal
- An “optimal energy sharing scenario” for which the fuel cell tack can provide 20% of the maximum power demanded over the duration of the mission (see the previous sub section).

An improvement in aircraft performance in terms of weight and fuel consumption is expected with new assessments (“Target 2035”), as a lighter aircraft would consume less fuel because of higher specific powers installed on board.

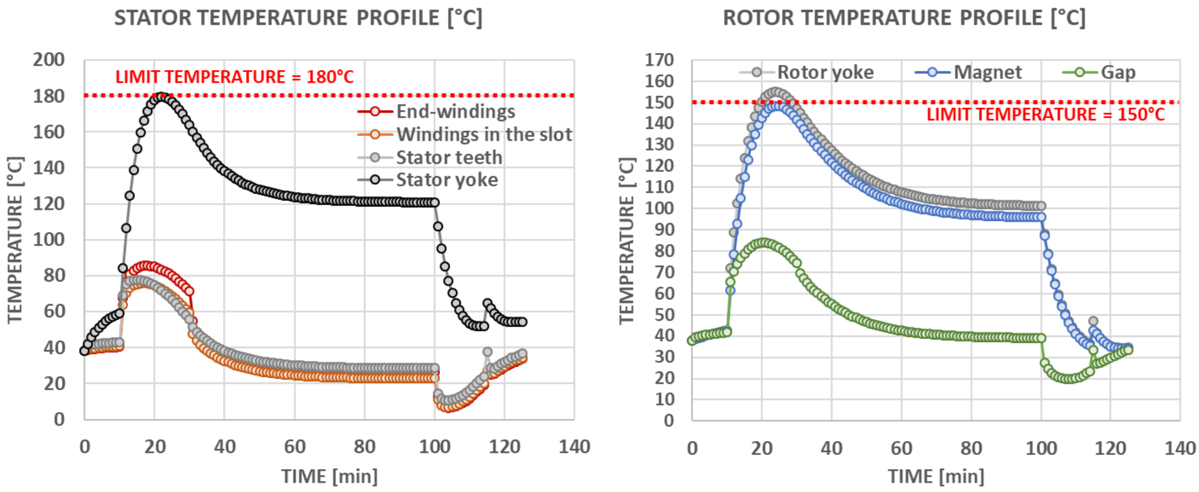

Fig. IV-44: e-Motor temperature (2035 target for both optimisations) over time.

Targets 2035 bring new perspectives from an electromechanical actuator sizing point of view as Joule losses are no longer a thermal limit contrarily to the previous case study (“target 2025”). Indeed, the stator internal cooling channel in the slots allows a direct cooling at the core of the winding. As previously announced the temperatures in the slots of the electric machine (see Fig. IV-44) are lower due to the direct cooling in the windings. Consequently, a new constraint appears on the actuator stator yoke. The current density increases due to the internal cooling of the slots leading to the increase of the magnetic flux density in the stator yoke. Critical constraints are now located at the stator yoke level compared with the “target 2025” case where they were situated at the windings level. These constraints are all the more important considering the reduced volume of the actuator. In addition to the thermal design limits, a new constraint reaches its limit: the centrifugal pressure on the carbon sleeve. The rotational speed of the actuator has been increased, making more difficult to hold the magnets. This constraint also becomes a dimensioning constraint for the 2035 target optimizations.

During the previous optimization of the HASTECS 2025 propulsion system, two energy strategies were presented (“light hybridization scenario” – grey color and the “optimal” one-green color). Furthermore, in order to present the improvements between 2025 and 2035, the same strategies were represented with fuel consumption as the optimization objective function.

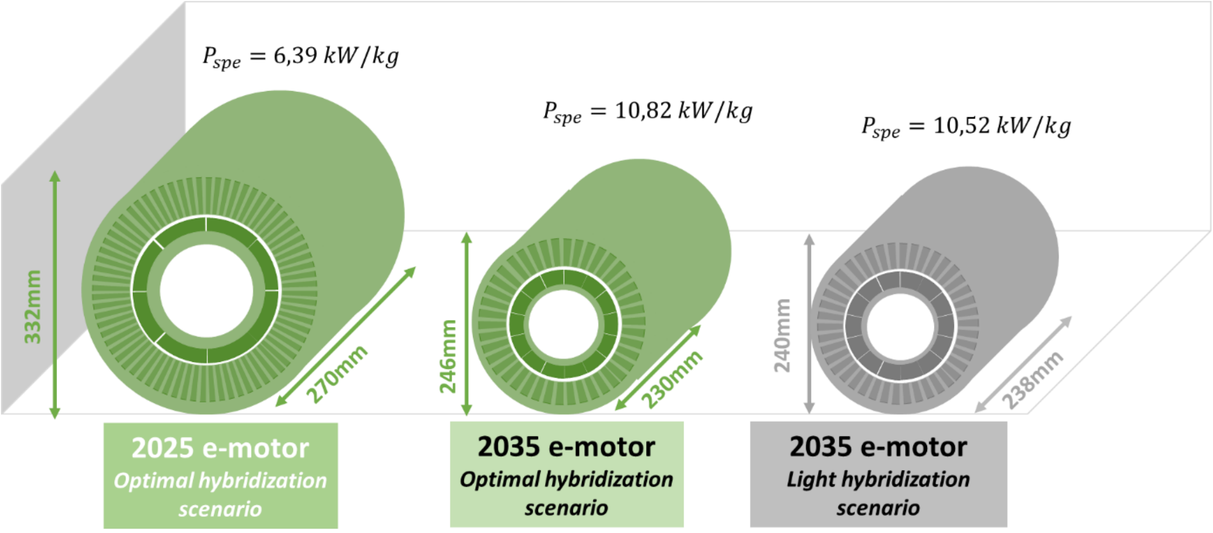

Fig. IV-45: Geometrical comparisons of three electric motors.

From a geometrical point of view (see Fig. IV-45), both machines optimized with “2035 target” are much smaller than their predecessors obtained with “2025 target”. The first machine (“2025 e-motor”) on the left in this figure is the optimal actuator for the 2025 target with an “optimal hybridization scenario”: it reaches 6.39 kW/kg of power density. Both “2035 machines” are the optimal sizing trade-off with the addition of the stator internal cooling system:

- the second actuator obtained with the “optimal hybridization scenario” is much smaller than the previous one. Indeed, its power density reaches 10.8 kW/kg based on the “target 2035” assessments.
- The third actuator obtained with the “light hybridization scenario” involves a specific power of 10.52 kW/kg.

As for the 2025 target, the results between the two hybridization strategies are quite similar (iso geometry for the energy optimal scenario - machine 2 and the light hybridization scenario - machine 3). In order to simplify the comparison, only the energy optimal scenario will be compared between the targets 2025 - machine 1 and 2035 - machine 2.

Fig. IV-46: Comparison between 2025 target and 2035 target.

Comparing results obtained with both “2035 motors” with respect to the “2025 Motor”, several changes can also be noted on the decision variables after the three optimizations (see Fig. IV-46):

- The gain in power density avoids a significant oversizing of the aircraft thrust which can be explained by the variation of the $RThrust$ variable, this latter being decreased with both .
- This thrust variation also involves evolutions of several devices: the propeller diameter is slightly smaller, but with oversizing values which remains high compared to the necessary diameter ($D_{prop} > 4$ m).
- A drastic change has appeared for the gearbox ratio: by increasing the transmission ratio between the propeller and the actuator, this decreases the torque mission while it increases the speed of the actuator. This evolution is not without consequences since the increase in the actuator speed combined with the increase of the number of pole

pairs will considerably increase the electrical frequency and consequently the iron losses of the electric motor.

- As previously announced, the reduction of the torque mission reduces the inner stator radius of the actuator. The ratio between the inner stator radius and the slot height seems to be constant but by comparing these values with the inner stator radius itself, the slot height varies in the same way.
- The DC bus voltage has been indirectly reduced after the evolution of the stator cooling system: the current density through the 2035 machines is higher than that of the 2025 machines. Indeed, the integration of the cooling channels inside the slots leads to additional constraints on the actuator windings. The DC voltage value to be held determines the required insulation thickness, the thickness of the slot layer as well as the copper radius and its reduction makes it easier to integrate the windings into the slot. The “2035 motor” optimization converge towards a DC voltage of 1300 V compared to the 2000 V obtained for the “2025 motor”, given the same energy management scenario. This voltage reduction is directly related to the thickness of the insulation. The presence of the cooling channels in the slot of the actuator causes the optimizer to optimize the available space in the slot. In addition to the thickness of the insulation, the voltage also affects the thickness of the slot insulation paper. The voltage reduction is also due to the reduction of required power, the 2035 aircraft is lighter than the previous one and consequently the amount of power is reduced for the mission profile, thus the required voltage can be reduced. This argument is also supported by the number of slots per pole and per phase which is reduced to 1. The slots are therefore wider than for the 2025 targets.
- The radius-to-length ratio $R_{drot_{Lm}}$decreases and the actuator operates at higher speeds than before.
- Stator inner radius and magnet thickness ratio are set to compensate the change in inner stator radius to have the same magnet height (~18mm).
- The number of pole pairs increases from 4 to 7 to reduce the main dimensions of the electromechanical actuator especially the yokes. However, as mentioned before, this increase contributes to increase the iron losses: there seems to be a tradeoff between size reduction and losses which moves regarding the cooling efficiency.
- The results of the magnetic flux densities in teeth and in the stator yoke are directly related to the cooling mode of the actuator: the flux density in the tooth is higher due to the fact that the cooling is closer to the teeth than to the yoke itself. This means that more iron losses can be evacuate through the stator teeth than through the stator yoke.
- Regarding the Fuel cell nominal power, the same difference is highlighted between light hybridization scenario (grey figure) and optimal scenario (green figures). The improvement from 2025 to 2035 is illustrated by the difference of nominal power between green figures.

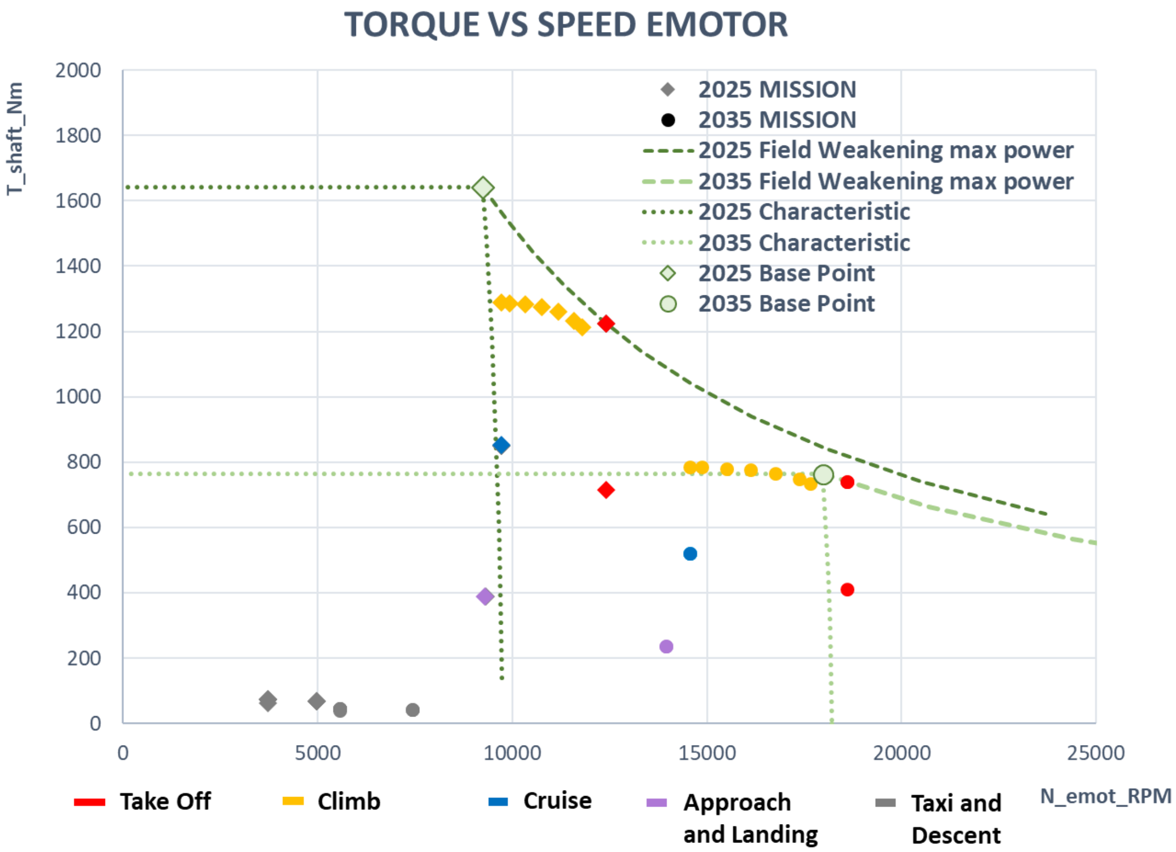

Fig. IV-47 : Torque-speed plan of the electromechanical actuators obtained by optimization of 2025 and 2035 (optimal hybridization scenario).

The previous figure Fig. IV-47 illustrates the characteristics of the 2 electric machines for 2025 and 2035 targets including the field weakening strategies proposed by each optimization. This display corresponds to the less fuel consuming hybridization scenarios ("optimal hybridization scenario") for both motor targets. The actuator mission is completely changed with differences in terms of field weakening strategy: in the "2035 case", the field weakening strategy is not necessary.

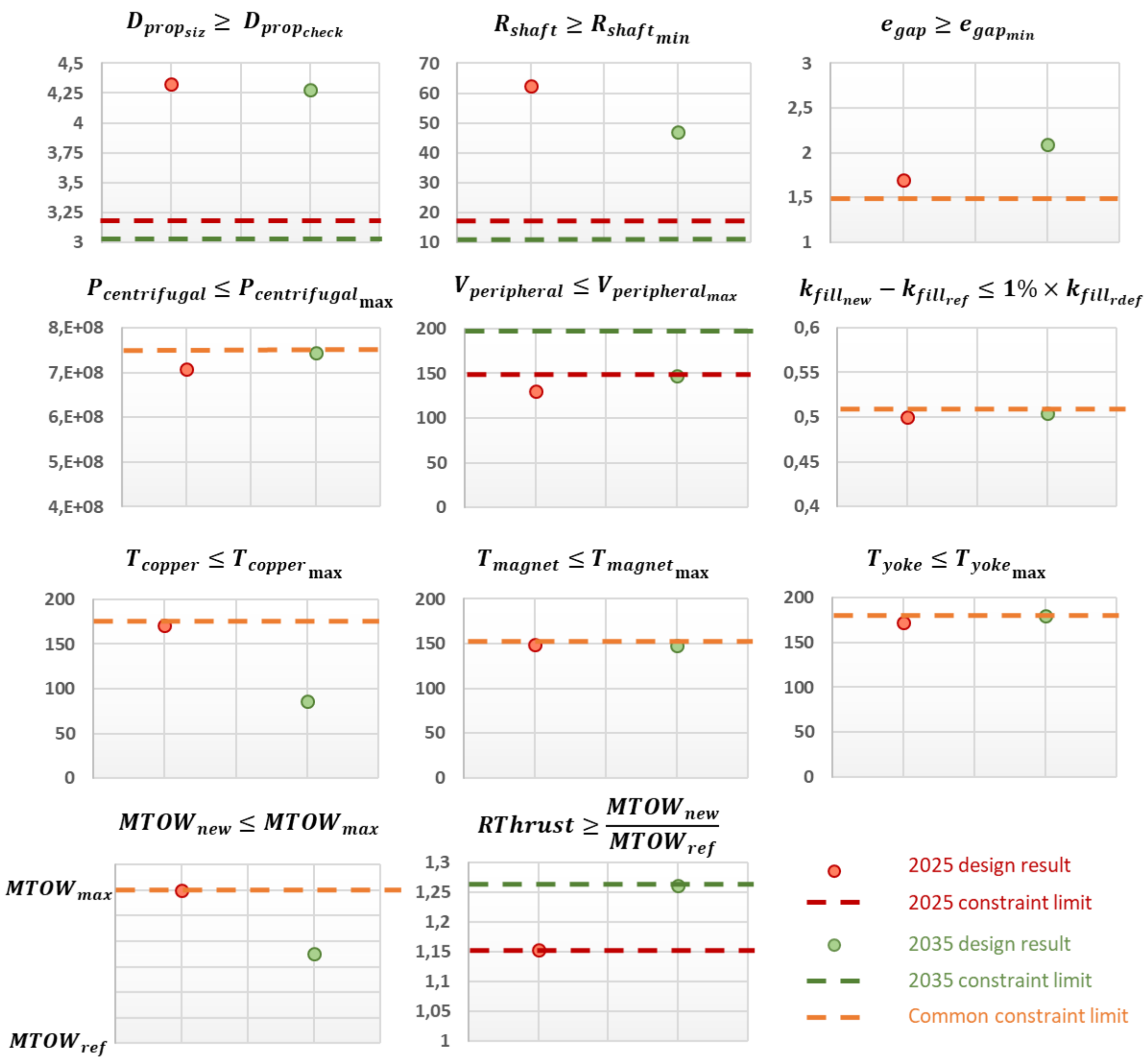

Fig. IV-48 : 2025 and 2035 dashboard of optimization constraints (optimal hybridization scenario).

Regarding the constraints (see Fig. IV-48):

- The oversize of the propeller is once again seen, the required values for the propulsion are around 3m while the design values are above 4m.
- The shaft radius is not a main constraint; the design value is higher than the limit (the minimum value is given by the bearing datasheets).
- The mechanical air gap thickness limit has been reached during the 2025 optimal integrated design in order to maintain an interesting specific power at aircraft level. With the winding cooling system, the mechanical air gap thickness is less restrictive.
- Two constraints have been set for the limitation of rotationnal speed of the actuator, a centrifugal pressure constraint and a peripheral speed limit. The most important constraint is the centrifugal pressure because the peripheral speed limit has not been reached for both optimizations. The design of the electric motor is so compact for the 2035 target that the centrifugal pressure on the carbon sleeve has reached the limit.
- The fill factor has remained close to the reference design value (0,5) in order to avoid undersizing at the actuator level.

- The Joule and Iron losses in the teeth are no longer constraining for the sizing of the actuator with a more efficient cooling system (2035 design results) in contact with copper windings and close to the stator teeth ($T_{copper} \leq T_{copper_{max}}$).
- Furthermore, the temperature in the stator yoke has reached the thermal limit, caused by the increased iron losses in the yoke ($T_{yoke} \leq T_{yoke_{max}}$). This is again a strong sizing constraint because of its connection with the stator yoke thickness and consequently the specific power of the electric actuator.
- The magnet temperature is a strong limitation too, this temperature is directly linked to the magnet thickness, thus the performance of the electric machine.
- At aircraft level, the limit MTOW has been reached for the 2025 optimization, this constraint allows the optimizer to lead the design to a hybrid-electric aircraft, without this constraint the optimizer would converge to full-electric one: the design has reached the limit of the validity domain. The 2035 optimization has lead to a lighter aircraft taking the same EMS strategy as 2025 into account.
- Finally, the snowball effect constraint ($Rthrust \geq \frac{MTOW_{new}}{MTOW_{max}}$) is the limit of convergence for our MDO process. The process of designing the hybrid-electric aircraft from a conventional aircraft stops when the required thrust of the aircraft corresponds to the weight ratios (assumption of constant glide in cruise). It is thus normal to see the 2 optimizations converging towards these 2 own limits.

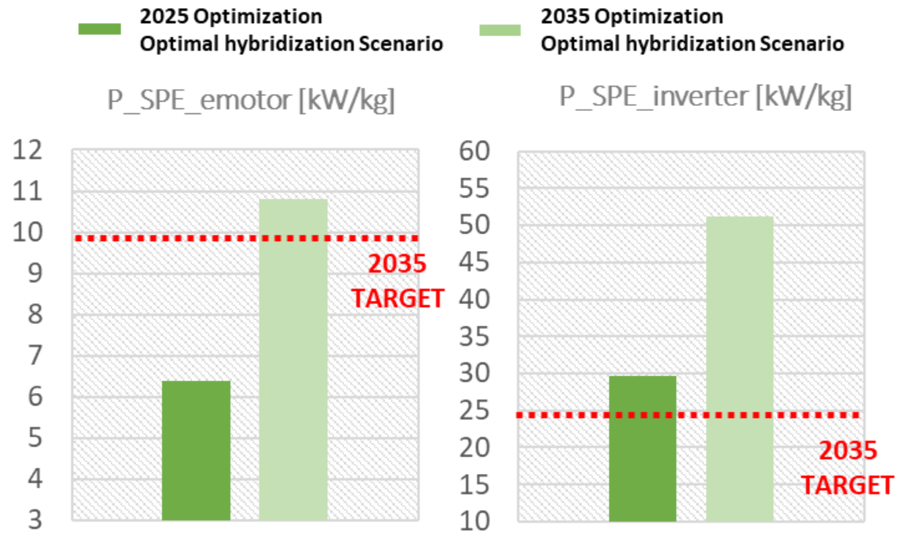

Fig. IV-49: Specific power of the electrical components found by optimization of 2025 and 2035 (optimal hybridization scenario).

The previous figure displays the strong increase in terms of specific powers for both power electronic and eMotors. The results obtained for 2035 assessments are beyond the 2035 targets (i.e. 25kW/kg for power electronics and 10kW/kg for eMotors). This result shows, one more time, the prime importance of the electro thermal coupling.

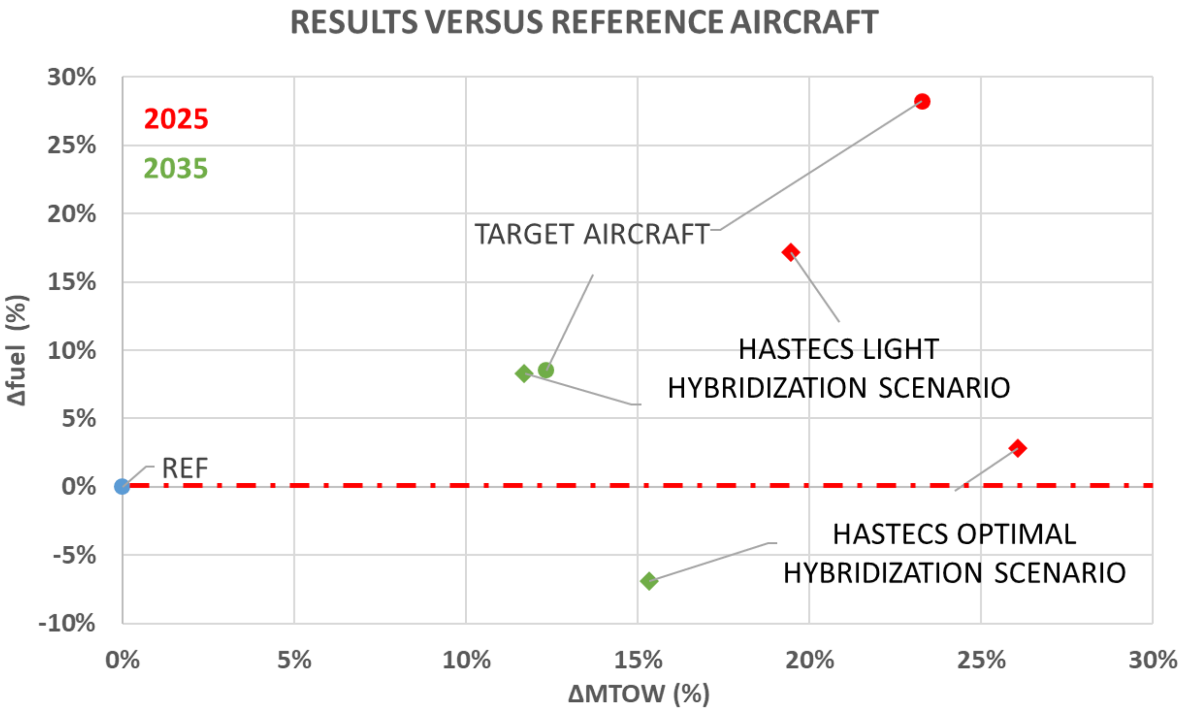

Fig. IV-50: Relative deviations in MTOW and fuel mass with respect to the reference thermal aircraft

"Target Aircraft" means that devices are simply modelled through specific power coefficients

"HASTECS XXX" means that sizing models (see chapter II) are used in optimization

Finally, by completing the relative deviations in the fuel vs MTOW plan with reference to a conventional full thermal-propulsion aircraft, the green diamonds display a less fuel-consuming solution for "target 2035".

The "HASTECS 2035" results coincide with the "target" results of the 2035 aircraft with a light hybridization scenario (8% ΔM_{fuel} and 12% $\Delta MTOW$). This particular case shows the coherence between rough assumptions on power densities and the results obtained with a multi-disciplinary design optimzation approach based on sizing models.

A more fuel-efficient solution has emerged for the "2035 target" (-7% ΔM_{fuel}), resulting from the optimized overall performance of the chain as well as the fuel savings made by the use of a fuel cell. Note the weight of the aircraft is still 15% higher due to the addition of the electrical components of the powertrain.

IV.5 Conclusion.

Through the trends emphasized after several optimizations conducted at component (Emotor) and system level, this chapter has allowed us to reinforced the understanding of main couplings in that complex and multidisciplinary powertrain. The multiple analysis completes the trends shown off from the sensistivity analysis proposed in chapter 3. Among these trends, it is clear that sizing of electromechanical components is strongly constrained by the electro thermal coupling: the integration performance of actuators is directly driven by the thermal cooling performance. Is is then important to include thermal sizing models which allow the estimation of temperature profiles over the whole flight mission. In our case study where the high power demand phases correspond to relatively short duration sequences (take off, climb), the involvement of thermal capacitances and transient thermal phenomena has been proved t be essential in terms of sizing. With reference to actuator model sized with quasi static (“R only”) thermal models, transient thermal model based optimization has allowed to multiply the power density by 3!

The multidisciplinary optimization of the electro-propulsion unit (propeller + gearbox + electric motor + inverter), taking thermal and partial discharges studies into account, has highlighted the importance of certain system parameters:

- the DC bus voltage remains an important parameter strongly coupling these devices (cable, inverter and motor).
- Geometrical parameters of actuators are of course also important as they constrain the winding sizing of the electric motor, this latter being coupled with insulation (partial discharges) constraints and also with the field weakening strategy which is applied along the flight mission: many results have shown that the field weakening is clearly adapted according to the geometry of the actuator.
- The propeller size (diameter) has been strongly oversized in system oriented optimization. Event if such oversizing increases the device (propeller) weight, it also increases significantly its efficiency lowering the power demand of all devices situated upstream in the powertrain. This latter aspect is a clear example of “property emergence” that only occur at system level: a typical systemic issue”.

The complete looped process at aircraft level makes possible to integrate interactions between fields. A complete MDO process has then allowed find the best trade-offs between weight and efficiency of electrical, thermal and mechanical components in order to obtain the optimum solution in terms of fuel mass consumption. However, the complexity of this MDO process pushes designers towards limits in terms of computation cost: indeed, optimizations solved with an “up to date” personal computer have lasted between 8 and 15 days for the whole powertrain optimization involving the management strategy while optimization of motor weight lasted only 1 day of computation!

Two successive management strategy have been proposed: a first (“light hybridization scenario”) setting a priori the hybrid ratio to use the electric source (fuel cell) only during taxi and descent. These hybrid ratios have been realeased in the second “optimal hybridization scenario” for which the fuel cell sizing is adapted by optimization to minimize the kerosene consumption along the whole mission. In that case, hybrogen is burnt during the whole mission at taxi and descent phases but also during climb and cruise: the corresponding optimization results show that heavier but less CO2 emitting aircrafts would be possible.

The last analysis (see Fig. IV-49 & Fig. IV-50) has synthesized the importance of technology improvements especially involving two axis related to specific power and efficiency variations:

- The power density is firstly essential because it will induce sizing variations amplified by the through snowball effects on the whole propulsion chain, thus varying fuel consumption.
- Once a new maximum take-off weight has been estimated by the looped process, the efficiency in turn influences the gas turbine fuel consumption. An increased efficiency downstream of the powertrain will lead to lower power constraints on upstream devices reducing all the more the power demand on both sources (thermal and/or electrical), consequently lowering aircraft fuel burn.

Based on that results, the HASTECS framework is now in an intermediate stage between conventional all-thermal aircrafts and future electrically-powered aircrafts; these studies are still necessary in order to more fully anticipate the possibilities and challenges of a zero-emission aircraft potential.

CONCLUSION

Integrating a hybrid-electric propulsion system into an aircraft brings additional complexity compared to the conventional full thermal powertains. Many interactions are present in the design of an aircraft. Its structure is designed by the propulsion thrust vs drag balance and is also directly influenced by the embedded mass to take off the aircraft: this latter aspect involves snowball effects which are specific in aeronautics as supplementary transported kilos involves an increase of the structure surface consequently with additional penalties on fuel burn and transported kerosen. In order to integrate all phenomena, reduced and specific design models must be implemented in a problem to design the whole aircraft in an optimal way: “this process is called Multidisciplinary Design Optimization (MDO)”. The MDO approach makes easier to understand couplings between components.

Even if the efficiency and specific power of the electrical components are excellent, the hybrid propulsion system (due to its more complex architecture) will inevitably be penalized in terms of embedded weight with respect to a full thermal reference aircraft.

However, it can be noticed that only the energy point of view has been focused in our work. Supplementary potential gains offered by electric powertrains are shortly reminded in the first chapter but are not assessed in the study. Indeed, the electrification of the propulsion system is leading to rethink new aircraft architectures, in particular distributed propulsion. The scalability and dynamic of electrical component is better than thermal components: distributing propulsion permits to blow the entire wing for example, bringing a lift gain which improves stall performance, thus allowing reduced sizing of the wings. Distributed propulsion may also provides a certain degree of safety against engine failure, as the propulsion is much more robust with several actuators. While thermal engine efficiency decreases with altitude contrarily to electric motors, which constitutes another advantage of the electric propulsion. These numerous advances have also led to the introduction of new aircraft concepts: Urban Air Mobility (UAM). These VTOLs are mostly electrically powered and have static flight performance allowing them to land on platforms such as helicopters. The aircraft electrification promises to be increasingly present in the aerial landscape.

The HASTECS project is definitely in line with this innovative dynamic, the goal being to couple several technological studies with the integrated process proposed in that thesis in order to optimize the sizing of the hybrid-eletric propulsion system. The studies resulting from the technological developments of the various work packages make it possible to provide models for an integrated design by optimization. The problem is clearly multidisciplinar because of the number of involved themes: thermal, electromagnetic, power electronics, electrical networks, partial discharges, electric machines.

All the models are presented in chapter II and completed by the appendices at the end of this thesis in order to illustrate the level of precision and complexity of the models integrated in the optimization.

The global sensitivity analysis presented in the chapter III was the first study to emphasize these interactions between components. The sensitivity analysis was based on Sobol indices. An initial global study was carried out, highlighting the first-order impact of power densities and efficiency on aircraft performance. Specific power has a major impact on aircraft performance (weight and fuel consumption), indeed the snowball effect leads to the aircraft resizing. Efficiency also has a huge impact on aircraft fuel consumption, all devices downstream in the powertrain impacting on the sizing of the gas turbine and therefore on its consumption. The sensitivity analysis at component level has highlighted the importance of the sizing constraints, some parameters that would be sensitive from a mathematical point of view are no longer sensitive by taking the actual constraints into account. The study of a set of electromechanical components (propeller + gearbox + electric motor) with and without constraints has highlighted the sensitivities of each parameter with their interations. Without taking account of the actuator constraints, the propeller and its gearbox were not so sensitive to the sub system efficiency, but, taking the thermal and peripheral speed constraints into account, the propeller diameter and the gearbox ratio has become among the most sensitive variables of the electro-propulsion unit. These results have been confirmed by the overall optimization of the propulsion system.

In the chapter IV, several levels of optimizations have been studied. The first level of optimization is at "component level" dealing with the electromechanical actuator which is probably the most sensitive of the integrated design. In the HASTECS project, three complementary technological developments have been performed around the electromechanical actuator: the actuator design, its cooling and the partial discharges constraints in windings. The first optimization study has highlighted the multidisciplinary context of the design of an electromechanical actuator and its sensitivity to cooling performance. The sizing of an electrical component is directly related to its cooling system which is definetly the most sensitive factor. This part of the study has shown that using the thermal capacitances of the actuator greatly helps to relieve thermal constraints which reduces the volume of the actuator.

The optimization of the complete propulsion system makes it possible to take into account all the interaction phenomena between components, in particular between propeller, gearbox and electric motor. The sensitivity analysis performed in the previous chapter has predicted the results obtained by the optimization. The improvement in the power density of the electromechanical actuator is directly linked to the performance of the propeller and its gearbox; a lighter engine will lead to an oversizing of the aero-propulsion components (propeller-gearbox). Fuel economy is possible by improving efficiency in the very high power phases: this improvement is made possible thanks to the oversizing of the propeller diameter. This latter issue is a typical example of "emergence property", rather usual in systemic studies: indeed, the propeller oversizing emerges only through the integrated design coupling all devices in a whole system!

But an aircraft would really save fuel burn when the power sharing between both sources in the hybrid architecture is released. The rest of the study has focused on a complete optimization of the propulsion system sizing, also taking the hybridization ratios as decision variables during the flight mission: an adaptation of the optimization problem formulation has been proposed to reduce its complexity; finally, only the fuel cell stack power has been added as supplementary decision variable. By changing hybridization ratio during the mission, the auxiliary electrical source is more or less used to save fuel used by the turboshafts. The mass of the hydrogen storage becomes more cumbersome in our case and a new constraint is reached related to the maximum weight allowed by the aircraft without changing its wingspan (initial assumption).

The optimal integrated design of a hybrid-electric aircraft has emphasized and partly solved several key locks on the design of the powertrain components. Thermal issue plays a major role in the design since the temperature limits are reached at the critical points of the components (coil head, stator yoke and magnets). This issue is also fundamental for power electronics, but high performance two-phase cooling system (CPLIP) has tackled the problem to offer highly integrated power electronic systems. The study of partial discharges allows to find the optimal compromise on the DC bus value. The higher the voltage value, the more insulation thickness will have to be added. On the other hand, increasing this voltage value also reduces the cable mass and more generally the current flowing through the electrical components, thus their mass. In addition to the mass issue, the powertrain efficiency can be improved thanks mainly to the oversizing of the downstream elements of the chain (propeller, gearbox). At the global aircraft level, the nominal power rating of fuel cells has a clear impact on the reduction of kerosene consumption.

Finally, the optimal hybrid-electric aircraft will tend to be heavier than its predecessors but will consume less fuel. However, such a propulsion system brings with it a complexity of control, design and integration issues. Despite the fact that the aircraft will consume slightly less fuel, the cost at purchase is far from derisory compared to a conventional aircraft. The addition of electrical components, combined with an oversize of the mechanical devices (gearbox, propeller) will also increase the price of the aircraft. These elements make the concept of hybrid electric propulsion less attractive.

Several issues may be of interest for future studies:

- The linear approximation between thrust and mass (MTOW) ratio has allowed us to tackle the snowball effect and the interaction between the powertrain design and the aerodynamic structure. Jowever, the simplification assumption has strong limits in terms of MTOW range. Coupling the electric powertrain design with aerodynamic simplified design seems necessary to explore new concepts of aircraft, typically for hydrogen based aircrafts.
- This latter issue would lead to an increase of the design complexity which was even really high with our optimization problem (remember that several days ~10-15) of computation was necessary for solving the more complex problem in our thesis (with up to date personal computer without parallel computing). A general methodological thinking on the “MDO approach”, splitting the optimization process with several hierarchical levels with imbricated loops (multi level optimization) is clearly necessary beyond our application to hybrid electric design.

- In terms of architecture, the project leader of HASTECS (i.e. Airbus) has proposed to focus on series hybrid chain, being the most critical in terms of technological constraints (with the highest electric power). As shown in J. Thauvin's thesis, other strutures as parallel architectures may be more appropriate in terms of MTOW and should be studied coupled with technological model and optimization.
- However, the main technological breakthrough, certainly of major interest, is the zero emission aircraft powered entirely by fuel cells: it is clearly the main prospect of this thesis.

REFERENCES

[1] "IATA - Healthy Passenger Demand Continues in 2018 with Another Record Load Factor." [Online]. Available: https://www.iata.org/en/pressroom/pr/2019-02-07-01/. [Accessed: 18-Mar-2020].

[2] EUROCONTROL, "Press release Press release."

[3] "Eurocontrol Predicts A Bleak Winter Ahead For European Aviation - Simple Flying." [Online]. Available: https://simpleflying.com/eurocontrol-european-winter-predictions/. [Accessed: 28-Dec-2020].

[4] "Welcome to Clean Sky | Clean Sky." [Online]. Available: https://www.cleansky.eu/. [Accessed: 25-Feb-2021].

[5] AIRBUS, "GMF 2019-2038 Airbus Commercial Aircraft book," 2019. [Online]. Available: http://gmf.airbus.com/. [Accessed: 18-Mar-2020].

[6] European Commission, "European aeronautics: a vision for 2020."

[7] European Commission, "Flightpath 2050 Europe's vision for aviation: Report of the high level group on aviation research," p. 28, 2011, doi: 10.2777/50266.

[8] IATA, "Technology Roadmap to 2050," *International Air Transport Association*, 2013. [Online]. Available: https://www.iata.org/contentassets/8d19e716636a47c184e7221c77563c93/technology20roadmap20to20205020no20foreword.pdf.

[9] R. Thomson *et al.*, "Aircraft Electrical Propulsion – Onwards and Upwards," *Roland Berger*, 2018. [Online]. Available: www.rolandberger.com.

[10] "Would you pledge not to fly for a year? - BBC News." [Online]. Available: https://www.bbc.com/news/av/world-europe-46362159/the-two-swedish-mums-who-want-people-to-give-up-flying-for-a-year. [Accessed: 18-Mar-2020].

[11] "Electric propulsion is finally on the map — Roland Berger." [Online]. Available: https://www.rolandberger.com/fr/Point-of-View/Electric-propulsion-is-finally-on-the-map.html. [Accessed: 18-Mar-2020].

[12] J. Thauvin, "Exploration de l'espace de conception d'un avion régional hybride par optimisation multidisciplinaire.," PhD Thesis, Institut National Polytechnique de Toulouse (Toulouse INP), 2018.

[13] SAFRAN, "SAFRAN AND AVIATION-S ELECTRIC FUTURE - Press Kit Paris Air Show 2019," 2019.

[14] R. C. AKLI, "Conception systémique d'une locomotive hybride autonome. Application à la locomotive hybride de démonstration et d'investigations en énergétique LHyDIE développée par la SNCF," PhD Thesis, Institut National Polytechnique de Toulouse (Toulouse INP), 2008.

[15] TURBOTECH, “Innovative turbines, Turboprops, Turbogenerators & Range-Extenders.” [Online]. Available: https://www.turbotech-aero.com/. [Accessed: 18-Mar-2020].

[16] AIRBUS, “Clean Sky 2 - Helicopters - Airbus.” [Online]. Available: https://www.airbus.com/newsroom/news/en/2016/06/clean-sky-2.html. [Accessed: 18-Mar-2020].

[17] J. R. Welstead, D. Caldwell, R. Condotta, and N. Monroe, “An overview of the layered and extensible aircraft performance system (Leaps) development,” *AIAA Aerosp. Sci. Meet. 2018*, no. 210059, 2018, doi: 10.2514/6.2018-1754.

[18] K. V. Papathakis, P. A. Burkhardt, D. W. Ehmann, and A. M. Sessions, “Safety Considerations for Electric, Hybrid-Electric, and Turbo-Electric Distributed Propulsion Aircraft Testbeds,” 2017, doi: 10.2514/6.2017-5032.

[19] S. Clarke, M. Redifer, K. Papathakis, A. Samuel, and T. Foster, “X-57 Power and Command System Design,” in *IEEE Transportation Electrification Conference and Expo (ITEC)*, 2017, doi: 10.1109/ITEC.2017.7993303.

[20] K. A. Deere *et al.*, “Computational Component Build-up for the X-57 Distributed Electric Propulsion Aircraft,” in *2018 AIAA Aerospace Sciences Meeting*, 2018, doi: https://doi.org/10.2514/6.2018-1275.

[21] J. Murray and J. Lechniak, “The LEAPTech Experiment Approach Results Recommendations,” 2016. .

[22] J. Thauvin, G. Barraud, X. Roboam, B. Sareni, M. Budinger, and D. Leray, “Hybrid propulsion for regional aircraft: A comparative analysis based on energy efficiency,” *2016 Int. Conf. Electr. Syst. Aircraft, Railw. Sh. Propuls. Road Veh. Int. Transp. Electrif. Conf. ESARS-ITEC 2016*, 2016, doi: 10.1109/ESARS-ITEC.2016.7841392.

[23] K. R. Antcliff and F. M. Capristan, “Conceptual design of the parallel electric-gas architecture with synergistic utilization scheme (PEGASUS) concept,” *18th AIAA/ISSMO Multidiscip. Anal. Optim. Conf. 2017*, no. June, pp. 1–15, 2017, doi: 10.2514/6.2017-4001.

[24] N. K. Borer *et al.*, “Design and performance of the NASA SCEPTOR distributed electric propulsion flight demonstrator,” in *16th AIAA Aviation Technology, Integration, and Operations Conference*, 2016, pp. 1–20, doi: 10.2514/6.2016-3920.

[25] J. Hermetz, M. Ridel, and C. Doll, “Distributed electric propulsion for small business aircraft a concept-plane for key-technologies investigations,” in *ICAS 2016*, 2016, p. 11.

[26] E. Dillinger *et al.*, “Handling qualities of ONERA’s small business concept plane with distributed propulsion,” in *ICAS 2018*, 2018, p. 10.

[27] A. Arntz, O. Atinault, D. Destarac, and A. Merlen, “Exergy-based aircraft aeropropulsive performance assessment: CFD application to boundary layer ingestion,” *32nd AIAA Appl. Aerodyn. Conf.*, 2014, doi: 10.2514/6.2014-2573.

[28] J. S. Gray, “Design Optimization of a Boundary Layer Ingestion Propulsor Using a Coupled Aeropropulsive Model,” PhD Thesis, University of Michigan, 2018.

[29] R. H. Jansen, C. Bowman, A. Jankovsky, R. Dyson, and J. Felder, “Overview of NASA electrified aircraft propulsion research for large subsonic transports,” *53rd AIAA/SAE/ASEE Jt. Propuls. Conf. 2017*, pp. 1–20, 2017, doi: 10.2514/6.2017-4701.

[30] D. J. Sadey, J. T. Csank, P. A. Hanlon, and R. H. Jansen, “A generalized power system architecture sizing and analysis framework,” *2018 Jt. Propuls. Conf.*, pp. 1–11, 2018, doi: 10.2514/6.2018-4616.

[31] A. Yildirim, J. S. Gray, C. A. Mader, and J. Martins, “Aeropropulsive Design Optimization of a Boundary Layer Ingestion System,” pp. 1–23, 2019, doi: 10.2514/6.2019-3455.

[32] J. Welstead *et al.*, “Overview of the NASA STARC-ABL (Rev . B) Advanced Concept,” Washington, DC, 2017.

[33] J. L. Felder, H. D. Kim, and G. V. Brown, “Turboelectric distributed propulsion engine cycle analysis for hybrid-wing-body aircraft,” *47th AIAA Aerosp. Sci. Meet. Incl. New Horizons Forum Aerosp. Expo.*, no. January, pp. 1–25, 2009, doi: 10.2514/6.2009-1132.

[34] L. Bruno, “Turboelectric Distributed Propulsion in a Hybrid Wing Body Aircraft,” in *20th International Society for Airbreathing Engines (ISABE 2011)*, 2011, vol. 53, no. 9, pp. 1689–1699, doi: 10.1017/CBO9781107415324.004.

[35] K. P. Duffy and R. H. Jansen, “Turboelectric and Hybrid Electric Aircraft Drive Key,” *2018 AIAA/IEEE Electr. Aircr. Technol. Symp.*, pp. 1–9, 2018.

[36] J. L. Felder, “NASA N3-X with Turboelectric Distributed Propulsion,” *IMechE Disruptive Green Propuls. Technol. Conf.*, p. 18, 2014, doi: 2060/20150002081.

[37] P. Schmollgruber *et al.*, “Multidisciplinary exploration of dragon: An onera hybrid electric distributed propulsion concept,” *AIAA Scitech 2019 Forum*, 2019, doi: 10.2514/6.2019-1585.

[38] P. Schmollgruber *et al.*, “Multidisciplinary Design and performance of the ONERA Hybrid Electric Distributed Propulsion concept (DRAGON),” in *American Institute of Aeronautics and Astronautics (AIAA)*, 2020, doi: 10.2514/6.2020-0501.

[39] “Project 804: The Opportunity - YouTube.” [Online]. Available: https://www.youtube.com/watch?v=mTWLebimFOk. [Accessed: 18-Mar-2020].

[40] “Ampaire Electric EEL^{TM} - YouTube.” [Online]. Available: https://www.youtube.com/watch?v=KIM50ILeK9Q. [Accessed: 18-Mar-2020].

[41] “Daher, Airbus et Safran s’associent pour développer EcoPulse^{TM}, un démonstrateur d’avion à propulsion hybride distribuée - Daher.” [Online]. Available: https://www.daher.com/daher-airbus-et-safran-sassocient-pour-developper-ecopulse-un-demonstrateur-davion-a-propulsion-hybride-distribuee/. [Accessed: 18-Mar-2020].

[42] “VoltAero hybrid-electric flight testing with the Cassio 1 testbed aircraft - YouTube.” [Online]. Available: https://www.youtube.com/watch?v=X5mUGg6DFw4. [Accessed: 18-Mar-2020].

[43] “E-Fan X - Electric flight - Airbus.” [Online]. Available: https://www.airbus.com/innovation/future-technology/electric-flight/e-fan-x.html. [Accessed: 18-Mar-2020].

[44] “Zunum Aero.” [Online]. Available: https://zunum.aero/. [Accessed: 18-Mar-2020].

[45] “Découvrez le nouveau système de propulsion hybride électrique ‘by Safran’ - YouTube.” [Online]. Available: https://www.youtube.com/watch?v=7wfZyZU4Io8. [Accessed: 18-Mar-2020].

[46] E. Joubert, D. Chapuis, D. Esteyne, J.-C. Lambert, O. Siri, and D. Müller-Wiesner, “The E-FAN all electrical aircraft demonstrator and its industrialization.,” in *ICAS 2016*, 2016.

[47] L. Juvé, J. Fosse, E. Joubert, and N. Fouquet, “Airbus group electrical aircraft program, the E-FAN project,” in *52nd AIAA/SAE/ASEE Joint Propulsion Conference, 2016*, 2016, doi: 10.2514/6.2016-4613.

[48] F. Anton, “eAircraft: Hybrid-elektrische Antriebe für Luftfahrzeuge,” 2019. [Online]. Available: https://www.bbaa.de/fileadmin/user_upload/02-preis/02-02-preistraeger/newsletter-2019/02-2019-09/02_Siemens_Anton.pdf. [Accessed: 16-Jan-2021].

[49] “Our Products | magniX.” [Online]. Available: https://magnix.aero/products/#. [Accessed: 19-Mar-2020].

[50] “Magni 500 Specification - Google Drive.” [Online]. Available: https://drive.google.com/file/d/1Lxbs4wx_0a_HOSaR0l0nLdMbOroXPJvu/view. [Accessed: 19-Mar-2020].

[51] “Harbour Air and magniX Announce Successful Flight of World’s First Commercial Electric Airplane – Harbour Air Seaplanes: World’s Largest Seaplane Airline – Since 1982 – Harbour Air.” [Online]. Available: https://www.harbourair.com/harbour-air-and-magnix-announce-successful-flight-of-worlds-first-commercial-electric-airplane/. [Accessed: 19-Mar-2020].

[52] M. Westlake, “Electrifying flight,” *Aerosp. Am.*, vol. 49, no. 9, pp. 8–10, 2011.

[53] “Our stories - Introducing ACCEL –Rolls-Royce.” [Online]. Available: https://www.rolls-royce.com/media/our-stories/innovation/2018/introducing-accel.aspx. [Accessed: 19-Mar-2020].

[54] K. Memmott and E. Jacobson, “YASA 750 Product Sheet,” *Internal Auditor*. [Online]. Available: https://www.yasa.com/wp-content/uploads/2018/01/YASA-750-Product-Sheet.pdf.

[55] “CityAirbus - Vehicle demonstrators - Airbus.” [Online]. Available: https://www.airbus.com/innovation/urban-air-mobility/vehicle-demonstrators/cityairbus.html. [Accessed: 19-Mar-2020].

[56] NASA, “NASA to Develop a Novel Approach for All-Electric Aircraft Using Cryogenic Liquid Hydrogen as Energy Storage - FuelCellsWorks.” [Online]. Available: https://fuelcellsworks.com/news/nasa-to-develop-a-novel-approach-for-all-electric-

aircraft-using-cryogenic-liquid-hydrogen-as-an-energy-storage/. [Accessed: 19-Mar-2020].

[57] “Clean Hydrogen for Europe | Hydrogen.” [Online]. Available: https://hydrogeneurope.eu/clean-hydrogen-europe. [Accessed: 28-Dec-2020].

[58] McKinsey & Company, *Hydrogen-powered aviation*, no. May. 2020.

[59] “Avions Mauboussin obtient une subvention de 800 000 €.” [Online]. Available: https://www.air-cosmos.com/article/avions-mauboussin-obtient-une-subvention-de-800-000-24290. [Accessed: 26-Feb-2021].

[60] “Airbus reveals new zero-emission concept aircraft - Innovation - Airbus.” [Online]. Available: https://www.airbus.com/newsroom/press-releases/en/2020/09/airbus-reveals-new-zeroemission-concept-aircraft.html. [Accessed: 26-Feb-2021].

[61] “Skai revises targets for its liquid-hydrogen, long-range eVTOL.” [Online]. Available: https://newatlas.com/aircraft/alakai-skai-liquid-hydrogen-evtol-update/. [Accessed: 26-Feb-2021].

[62] “Essai nouvelle Toyota Mirai hydrogène : les taxis vont-ils l’adorer ?” [Online]. Available: https://www.automobile-propre.com/essai-nouvelle-toyota-mirai-hydrogene-les-taxis-vont-ils-ladorer/. [Accessed: 26-Feb-2021].

[63] “Hopium Machina : une berline hydrogène française hors normes.” [Online]. Available: https://www.h2-mobile.fr/actus/hopium-machina-berline-hydrogene-francaise-hors-normes/. [Accessed: 26-Feb-2021].

[64] “Le premier yacht à hydrogène dévoilé à Monaco.” [Online]. Available: https://www.h2-mobile.fr/actus/premier-yacht-hydrogene-devoile-monaco/. [Accessed: 26-Feb-2021].

[65] ATR, “ATR 72-600 Datasheet,” 2020. [Online]. Available: http://www.atr-aircraft.com/wp-content/uploads/2020/07/Factsheets_-_ATR_72-600.pdf.

[66] M. Pettes-Duler, X. Roboam, and B. Sareni, “Integrated design process of a hybrid electric propulsion system for future aircraft,” *Electrimacs 2019*, no. May, pp. 1–6, 2019, doi: https://doi.org/10.1007/978-3-030-37161-6_6.

[67] X. Yi, A. Yoon, and K. S. Haran, “Multi-physics optimization for high-frequency air-core permanent-magnet motor of aircraft application,” *2017 IEEE Int. Electr. Mach. Drives Conf. IEMDC 2017*, 2017, doi: 10.1109/IEMDC.2017.8002293.

[68] L. Cheng, F. Zhang, S. Liu, and Z. Zhang, “Configuration method of hybrid energy storage system for high power density in More Electric Aircraft,” *J. Power Sources*, 2020, doi: 10.1016/j.jpowsour.2019.227322.

[69] D. Zhang, J. He, and D. Pan, “A Megawatt-Scale Medium-Voltage High-Efficiency High Power Density ‘SiC+Si’ Hybrid Three-Level ANPC Inverter for Aircraft Hybrid-Electric Propulsion Systems,” *IEEE Trans. Ind. Appl.*, vol. 55, no. 6, pp. 5971–5980, 2019, doi: 10.1109/TIA.2019.2933513.

[70] D. Zhang, J. He, D. Pan, M. Dame, and M. Schutten, “Development of Megawatt-Scale

Medium-Voltage High Efficiency High Power Density Power Converters for Aircraft Hybrid-Electric Propulsion Systems," *2018 AIAA/IEEE Electr. Aircr. Technol. Symp. EATS 2018*, 2018, doi: 10.2514/6.2018-5007.

[71] A. Iwaniuk, W. Wisniowski, and J. Zóltak, "Multi-disciplinary optimisation approach for a light turboprop aircraft-engine integration and improvement," *Aircr. Eng. Aerosp. Technol.*, vol. 88, no. 2, pp. 348–355, Mar. 2016, doi: 10.1108/AEAT-02-2015-0070.

[72] A. Sgueglia and T. M. Young, "Wing-Body with distributed electric ducted fans," PhD Thesis, Institut Supérieur de l'Aéronautique et de l'Espace, 2020.

[73] A. Gazaix *et al.*, "Industrial application of an advanced bi-level mdo formulation to an aircraft engine pylon optimization," in *AIAA Aviation 2019 Forum*, 2019, pp. 1–28, doi: 10.2514/6.2019-3109.

[74] S. Kreuawan, F. Gillon, and P. Brochet, "Optimal design of permanent magnet motor using multidisciplinary design optimization," *Proc. 2008 Int. Conf. Electr. Mach. ICEM'08*, pp. 1–6, 2008, doi: 10.1109/ICELMACH.2008.4800108.

[75] N. Bracikowski *et al.*, "Multi-physics design rules using lumped models for a permanent magnet synchronous machine," *Int. J. Appl. Electromagn. Mech.*, 2018.

[76] D. Temple and M. Collette, "Understanding lifecycle cost trade-offs for naval vessels: minimising production, maintenance, and resistance," *Ships Offshore Struct.*, vol. 12, no. 6, pp. 756–766, Aug. 2017, doi: 10.1080/17445302.2016.1230039.

[77] A. Matine *et al.*, "Optimal sizing of submarine cables from an electro-thermal perspective," *Eur. Wave Tidal Conf.*, 2017.

[78] MIT, "Production of Thrust with a Propeller." [Online]. Available: https://web.mit.edu/16.unified/www/FALL/thermodynamics/notes/node86.html. [Accessed: 18-Mar-2019].

[79] K. R. Antcliff, M. D. Guynn, T. V. Marien, D. P. Wells, S. J. Schneider, and M. T. Tong, "Mission analysis and aircraft sizing of a hybrid-electric regional aircraft," *54th AIAA Aerosp. Sci. Meet.*, no. January, pp. 1–18, 2016, doi: 10.2514/6.2016-1028.

[80] A. J. Eyne3, "Airbus HASTECS deliverable."

[81] M. Cheng, L. Sun, G. Buja, and L. Song, "Advanced electrical machines and machine-based systems for electric and hybrid vehicles," *Energies*, vol. 8, no. 9, pp. 9541–9564, 2015, doi: 10.3390/en8099541.

[82] T. Finken, M. Felden, and K. Hameyer, "Comparison and design of different electrical machine types regarding their applicability in hybrid electrical vehicles," *Proc. 2008 Int. Conf. Electr. Mach. ICEM'08*, pp. 1–5, 2008, doi: 10.1109/ICELMACH.2008.4800044.

[83] S. Touhami, "Analytical Sizing Models to Assess the Performances of High Specific Power Electric Motors for Hybrid Aircraft," PhD Thesis, Institut National Polytechnique de Toulouse (Toulouse INP), 2020.

[84] S. Touhami, A. Zeaiter, M. Fénot, Y. Lefevre, and J. Llibre, "Electro-thermal Models and

Design Approach for High Specific Power Electric Motor for Hybrid Aircraft," in *Aerospace Europe Conference*, 2020.

[85] A. Petrowski, "Clearing procedure as a niching method for genetic algorithms," *Proc. IEEE Conf. Evol. Comput.*, pp. 798–803, 1996, doi: 10.1109/icec.1996.542703.

[86] C. Igel, N. Hansen, and S. Roth, "Covariance Matrix Adaptation for Multi-objective Optimization."

[87] A. Zeaiter, "Thermal modeling and cooling of electric motors application to the propulsion of hybrid aircraft," PhD Thesis, Ecole Nationale Supérieure de Mécanique et d'Aérotechnique (ENSMA), 2020.

[88] F. Accorinti, "Two-phase power electronics cooling solution design in air context answer to the objectives of the hybrid aircraft 2035.," PhD Thesis, Ecole Nationale Supérieure de Mécanique et d'Aérotechnique (ENSMA), 2020.

[89] P. Collin, "Design, taking into account the partial discharges phenomena, of the electrical insulation system (eis) of high power electrical motors for hybrid electric propulsion of future regional aircrafts," PhD Thesis, Institut National Polytechnique de Toulouse (Toulouse INP), 2020.

[90] Eyne3 and J. Allias, "Specification dossier for HASTECS," 2018.

[91] F. Paschen, "Ueber die zum Funkenübergang in Luft, Wasserstoff und Kohlensäure bei verschiedenen Drucken erforderliche Potentialdifferenz," *Ann. Phys.*, vol. 273, no. 5, pp. 69–96, 1889, doi: 10.1002/andp.18892730505.

[92] P. Collin, D. Malec, and Y. Lefevre, "Tool to predict and avoid Partial Discharges in stator slot of rotating motors fed by inverter," in *Aerospace Europe Conference*, 2020.

[93] N. Erroui, "Chaine de conversion forte puissance pour la propulsion aéronautique hybride," PhD Thesis, Insititut National Polytechnique de Toulouse (Toulouse INP), 2019.

[94] N. Erroui, N. Roux, and G. Gateau, "Pré-dimensionnement de Convertisseur de Très Forte Puissance pour une Application à la Propulsion Aéronautique Hybride," in *JCGE 2017*, 2017.

[95] F. Accorinti, V. Ayel, and Y. Bertin, "Steady-state analysis of a Capillary Pumped Loop for Terrestrial Application with methanol and ethanol as working fluids," *Int. J. Therm. Sci.*, vol. 137, no. October 2018, pp. 571–583, 2019, doi: 10.1016/j.ijthermalsci.2018.10.036.

[96] F. Accorinti *et al.*, "High-efficiency cooling system for highly integrated power electronics for hybrid propulsion aircraft," *IEEE Int. Symp. Ind. Electron.*, vol. 2019-June, pp. 870–877, 2019, doi: 10.1109/ISIE.2019.8781086.

[97] M. Tognan, "Preliminary delivery Battery & Fuel Cell metamodels; 'HASTECS M6.1' Technical report."

[98] G. Chastaing, "Indices de Sobol généralisés pour variables dépendantes," PhD Thesis, Institut National Polytechnique de Grenoble (Grenoble INP), 2013.

[99] M. Le Guyadec, L. Gerbaud, E. Vinot, and B. Delinchant, “Sensitivity analysis using Sobol indices for the thermal modelling of an electrical machine for sizing by optimization,” *COMPEL - Int. J. Comput. Math. Electr. Electron. Eng.*, vol. 38, no. 3, pp. 965–976, 2019, doi: 10.1108/COMPEL-09-2018-0360.

[100] I. M. SOBOL, “Sensitivity Estimates for Nonlinear Mathematical Models,” *Math. Mod. Comput. Exp.*, vol. 1, no. 4, pp. 407–414, 1993.

[101] F. Gamboa *et al.*, “Statistical inference for Sobol pick freeze Monte Carlo method,” in *Statistics, Taylor & Francis: STM, Behavioural Science and Public Health Titles*, 2016, p. pp.881-902, doi: 10.1080/02331888.2015.1105803.

[102] M. Grandjacques, B. Delinchant, and O. Adrot, “Pick and Freeze estimation of sensitivity index for static and dynamic models with dependent inputs,” *J. la Société Française Stat.*, vol. 157, no. 2, pp. 65-89–89, 2016.

[103] F. Gamboa, A. Janon, T. Klein, and A. Lagnoux, “Sensitivity analysis for multidimensional and functional outputs,” *Electron. J. Stat.*, vol. 8, no. 1, pp. 575–603, 2014, doi: 10.1214/14-EJS895.

[104] Y. Lefevre, S. El-Aabid, J. F. Llibre, C. Henaux, and S. Touhami, “Performance assessment tool based on loadability concepts,” *Int. J. Appl. Electromagn. Mech.*, vol. 59, no. 2, pp. 687–694, 2019, doi: 10.3233/JAE-171059.

[105] M. Pettes-Duler, B. Sareni, and X. Roboam, “Analyse de sensibilité d’un système de propulsion hybride électrique pour des futurs aéronefs,” in *JCGE*, 2019.

[106] M. Pettes-Duler *et al.*, “Sensitivity analysis of a hybrid-electric aircraft powertrain based on Sobol indices,” in *Aerospace Europe Conference*, 2020.

[107] S. Biser *et al.*, “Design space exploration study and optimization of a distributed turbo-electric propulsion system for a regional passenger aircraft,” *AIAA Propuls. Energy 2020 Forum*, pp. 1–27, 2020, doi: 10.2514/6.2020-3592.

[108] M. Hepperle, “Aspects of Distributed Payload,” *Present. Symp. Elektrisches Flieg. - Stuttgart 2016*, pp. 1–26, 2016.

[109] H. Ounis, B. Sareni, X. Roboam, and A. De Andrade, “Multi-level integrated optimal design for power systems of more electric aircraft,” *Math. Comput. Simul.*, vol. 130, pp. 223–235, 2016, doi: 10.1016/j.matcom.2015.08.016.

[110] “Pulse Width Modulation for Power Converters: Principles and Practice - D. Grahame Holmes, Thomas A. Lipo.” [Online]. Available: https://books.google.fr/books?hl=fr&lr=&id=ckETEAAAQBAJ&oi=fnd&pg=PR13&dq=pulse+width+modulation+for+power+converters+principles+and+practice&ots=-_e-OJhnCV&sig=22tj0ocnVNPyU_086qZFqgFNG28#v=onepage&q=pulse width modulation for power converters principles. [Accessed: 19-Feb-2021].

APPENDIX

CONTENTS

APPENDIX A. ENVIRONMENT MODEL

The input and output of the environment model are summarized in the Table A.1:

Table A-1: Input/output variable used in the model:

INPUT VARIABLES		
$Altitude(t)$	$[\mathrm{m}]$	Flight Altitude
$MACH(t)$	$[-]$	MACH speed
OUTPUT VARIABLES		
$P_{static}\ (t)$	$[\mathrm{Pa}]$	Static Pressure
$P_{dynamic}\ (t)$	$[\mathrm{Pa}]$	Dynamic Pressure
$\rho_{air}(t)$	$[\mathrm{kg/m^3}]$	Air density
$T_{static}\ (t)$	$[\mathrm{K}]$	Static Temperature
$T_{dynamic}\ (t)$	$[\mathrm{K}]$	Dynamic Temperature
$V_{sound}(t)$	$[\mathrm{m/s}]$	Sound speed

The process is illustrated in the Fig. A-1:

Fig. A-1: Process chart of the model.

From AIRBUS side, input data are related to [90]:

- Environmental aircraft data: $Altitude(t)$
- Mach speed along the mission profile: $MACH(t)$

It should be noted that both input data, i.e. flight altitude $Altitude(t)$ and Mach speed over the mission profile were provided by the Airbus company at the beginning of the HASTECS project.

Given these inputs, some examples of surrogate models are proposed to design the hybrid-electric power train of the studied aircraft. Readers will find more detailed models in [12]. An environment model is required to design different devices of the power train (turboshaft, propeller, thermal cooling, etc) over the flight mission. Main environment variables are derived:

Table A-1: Environmental model

$P_{static} = 101325 \times \left(1 - \frac{Altitude}{44331}\right)^{5,256}$	Static pressure $[Pa]$	*(A-1)*
$T_{static} = 288{,}15 - 0{,}0065 \times Altitude + DISA$	Static temperature $[K]$	*(A-2)*
$\rho_{air} = 0{,}0034837 \times \frac{P_{static}}{T_{static}}$	Air density $[kg/m^3]$	*(A-3)*
$P_{dynamic} = P_{static} \times (1 + 0{,}2 \times MACH^2)^{3.5}$	Dynamic pressure $[Pa]$	*(A-4)*
$T_{dynamic} = T_{static} \times (1 + 0{,}2 \times MACH^2)$	Dynamic temperature $[K]$	*(A-5)*
$V_{sound} = \sqrt{401{,}8 \times T_{static}}$	Sound speed $[m/s]$	*(A-6)*

Where $Altitude$ is related to the input flight mission is in meter, $DISA$ is the temperature difference from the International Standard Atmosphere (ISA). ρ_{air} is the air density in kg/m^3. These variables will be used in particular in turboshaft and propeller models. Let us remind that other input requirements related to Altitude, MACH, Thrust and A/C speed (thus Aircraft power) mission profiles have been defined in section I.3.

APPENDIX B. PROPELLER MODEL

This appendix describes the design model for a variable-pitch propeller. The disk actuator theory permits to predict performance according to the propeller geometry. The propeller geometry is defined by the diameter and the rotation speed. The following input/output variables are used:

Table B-1: Input/output variables used in the propeller model.

INPUT VARIABLES **(in bold blue, the decision variable for optimization)**		
$\boldsymbol{\rho_{air}(t)}$	$[\mathrm{kg.\,m^{-3}}]$	Air density
$\boldsymbol{V_{A/C}(t)}$	$[\mathrm{m.\,s^{-1}}]$	A/C Velocity
$\boldsymbol{T_{A/C}\ (t)}$	$[\mathrm{N}]$	A/C Thrust
$\boldsymbol{D_{prop}}$	$[\mathrm{m}]$	**Propeller diameter**
OUTPUT VARIABLES		
$\boldsymbol{P_{shaft}\ (t)}$	$[\mathrm{W}]$	Propeller Shaft Power
$\boldsymbol{\eta_{prop}(t)}$	$[\%]$	Propeller Efficiency
$\boldsymbol{M_{prop}}$	$[\mathrm{kg}]$	Propeller Mass
$\boldsymbol{N_{prop_{max}}}$	$[\mathrm{RPM}]$	Maximum propeller rotation speed
$\boldsymbol{D_{prop_{check}}}$	$[\mathrm{m}]$	Propeller diameter checking law

The propeller model is illustrated in Fig. *B-1*.

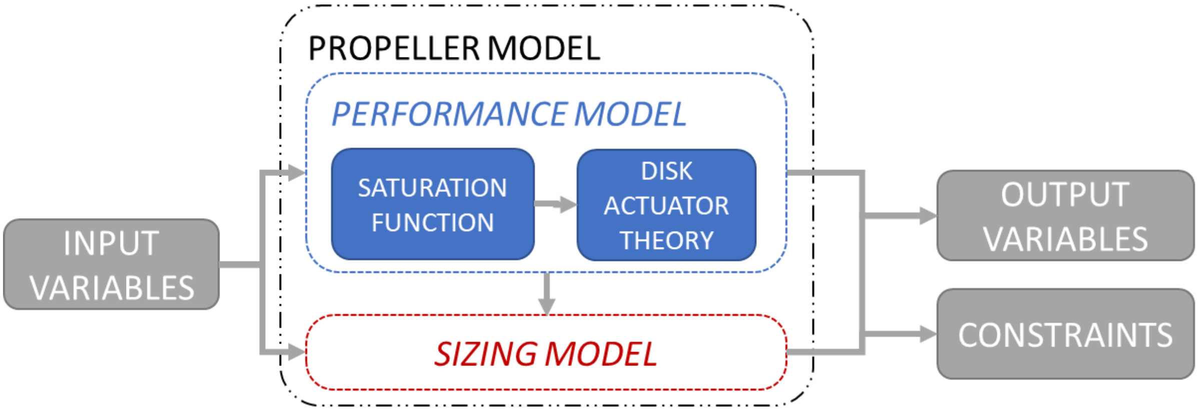

Fig. B-1: Process chart of the propeller model

B.1 Sizing model:

The ATR 72 based sizing point has been considered as a reference:

${D^{ref}}_{prop} = 3{,}93\ m$	Propeller Diameter (m)
${M^{ref}}_{prop} = 185\ \text{kg}$	Propeller mass (kg)
${N^{ref}}_{prop} =\ 1200\ RPM$	Propeller rotational speed (RPM).
${P^{ref}}_{max_{shaft}} = 2{,}4\ MW$	Maximum Propeller shaft power (MW)

A 6-blades variable-pitch propeller is considered. The propeller geometry is sized from two equations. The same tip speed limit is considered as for the ATR 72 propeller [65] used in [12]. The following relationships are based on the similitude principle which sets relationships between ratio of variables (*X/X^{ref}*) divided by reference variables: in our case, reference values are related to the ATR72 case:

Table B-1: Propeller design model

$D_{prop_{check}} = {D^{ref}}_{prop} \times \sqrt{\frac{P_{max_{shaft}}}{{P^{ref}}_{max_{shaft}}}}$	Checking rule for the propeller $[m]$	*(B-1)*
$N_{prop_{max}} = {N^{ref}}_{prop} \times \frac{{D^{ref}}_{prop}}{D_{prop}}$	Rotational speed of the propeller $[RPM]$	*(B-2)*
$M_{prop} = {M^{ref}}_{prop} \times \left(\frac{D_{prop}}{{D^{ref}}_{prop}3}\right)^2$	Propeller mass estimation $[kg]$	*(B-3)*

B.2 Disk Actuator Theory:

The performance model used during simulations (over the mission profile) is based on the Disk Actuator Theory Eq (B-4) which defines shaft power versus thrust and aircraft speed ($V_{A/C}$).

$$P_{shaft} = \frac{1}{2k_{eff}}\left(V_{A/C}.T_{vir} + \sqrt{\left(V_{A/C}.T_{vir}\right)^2 + \frac{2T_{vir}^3}{\rho_{air}A_{prop}}}\right) \qquad (B\text{-}4)$$

The thrust value (T_{vir}) is refined from the real input thrust ($T_{A/C}$) with a saturation function at low speed which is implemented in Eq (*B-9*).

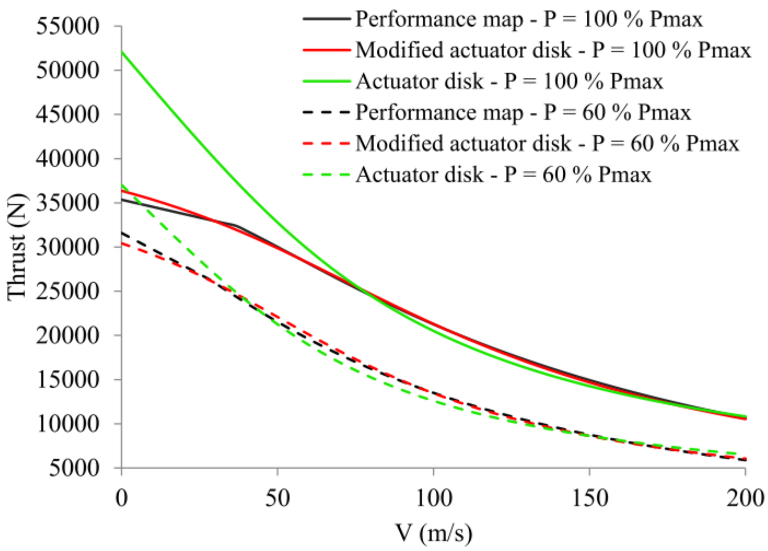

Fig. B-2: Comparison of propeller performance models for a 6-bladed propeller of 3.93 m diameter rotating at maximum tip speed at sea level [12].

In Eq (*B-7*), the maximum thrust T_{max} has been estimated versus the maximum shaft power. The use of the actuator disk theory during low speed phases tends to over-evaluate the propeller thrust (green lines in Fig. B-2). That is why a “virtual” thrust T_{vir}(red lines in Fig. B-2). is redefined in a saturation function Eq (*B-9*) from the real thrust $T_{A/C}$. $T_{A/C}$ comes from the aerodynamic input data set in section I.3.

B.3 Saturation function:

Table B-2: Detailed saturation function.

$kP = \frac{1}{\rho_{air}}$	$0,1 \leq kP \leq 1,5$	Saturation factor $[-]$	*(B-5)*
$k = 1.6 + \frac{\frac{V_{A/C}}{D^{ref}{}_{prop} \times N^{ref}{}_{prop}}}{60}$		Equivalent advance ratio $[-]$	*(B-6)*
$T_{max} = 10^{f(kP)}.P_{max_{shaft}}$		Maximum thrust deliverable by the thrust $[N]$	*(B-7)*
$f(kP) = \alpha_{prop} + \beta_{prop} \times log(kP)^{\gamma}$		Linear regression function of the saturation factor $[-]$	*(B-8)*
$T_{vir} = \left(\frac{2.k.T_{max}}{\pi}\right) \times tan\left(\frac{\pi.T_{A/C}}{2.k.T_{max}}\right)$		Virtual thrust used in the disk actuator theory $[N]$.	*(B-9)*

Where kP is the input value of the linear regression model set in Eq(*B-8*); ρ_{air} is the air density in kg/m^3 varying during the flight mission. $V_{A/C}$ is the aircraft speed in m/s also defined by the mission profile defined in section I.3. An equivalent advance ratio k for the saturation function has been imposed. $f(kP)$ is the linear regression function used by the model where α_{prop}, β_{prop} and γ are constant values. The modified disk actuator theory formula is modelled with a constant value $k_{eff} = 0.9$ and with the propeller disk area: $A_{prop} = \frac{\pi.D_{prop}^2}{4}$.

At the end of the process the efficiency of the propeller is determined by the equation (*B-10*):

$$\eta_{prop} = \frac{T_{A/C} \times V_{A/C}}{P_{shaft}} \tag{B-10}$$

B.4 Constraint:

A constraint on the shaft power has been added in the model in order to ensure that the propeller fulfill the mission Eq*(B-11)*.

$$D_{prop} \geq D_{prop_{check}} \tag{B-11}$$

$D_{prop_{check}}$ is the propeller diameter allowing to face $P_{max_{shaft}}$.
The actual D_{prop} can be set (and possibly oversized) by the optimizer (see Chapter IV) fulfilling the previous equation.

APPENDIX C. GEARBOX MODEL

The required parameters for the gearbox model are the following:

Table C-1: Input/output variables used in the gearbox model.

INPUT VARIABLES **(in bold blue, the 1 decision variable for optimization)**		
$\boldsymbol{R_{gbox}}$	$[-]$	**Gearbox ratio**
$\boldsymbol{P_{prop_{HP}}(t)}$	$[\mathrm{HP}]$	Maximum propeller shaft power
$\boldsymbol{RPM_{\%}\ (t)}$	$[\%]$	Propeller rotation speed in per unit
$\boldsymbol{N_{prop_{max}}}$	$[\mathrm{RPM}]$	Maximum propeller rotation speed
OUTPUT VARIABLES		
$\boldsymbol{M_{gbox}}$	$[\mathrm{kg}]$	Gearbox mass
$\boldsymbol{P_{shaft_{emot}}(t)}$	$[\mathrm{W}]$	E-motor mechanical power
$\boldsymbol{T_{shaft_{emot}}\ (t)}$	$[\mathrm{Nm}]$	E-motor torque
$\boldsymbol{\Omega_{emot}\ (t)}$	$[\mathrm{rad/s}]$	E-motor rotation speed

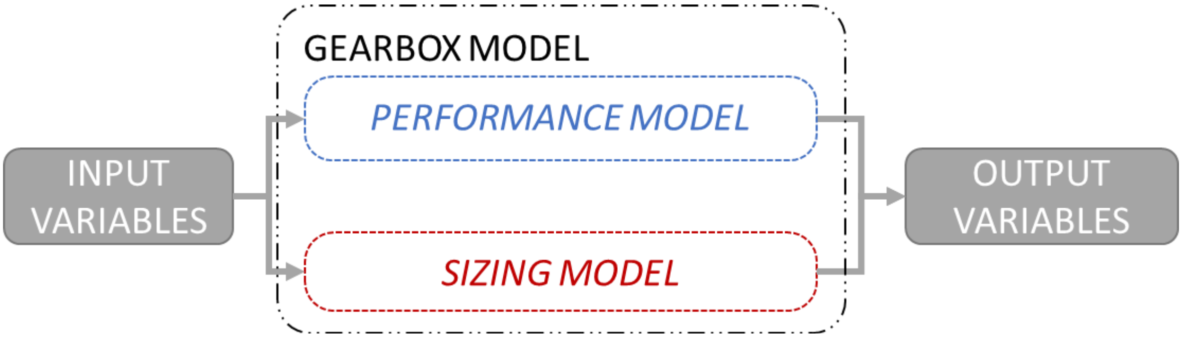

Fig. C-1: Process chart for the gearbox model.

C.1 Sizing model:

To determine the performance of the gearbox and its mass, a rotational speed profile is required. Several studies have been done with the aim of providing the maximum rotational speed during the mission respecting speed limits (cf Chapter I.3.1). The final rotational speed profile is given in Fig. C-2.

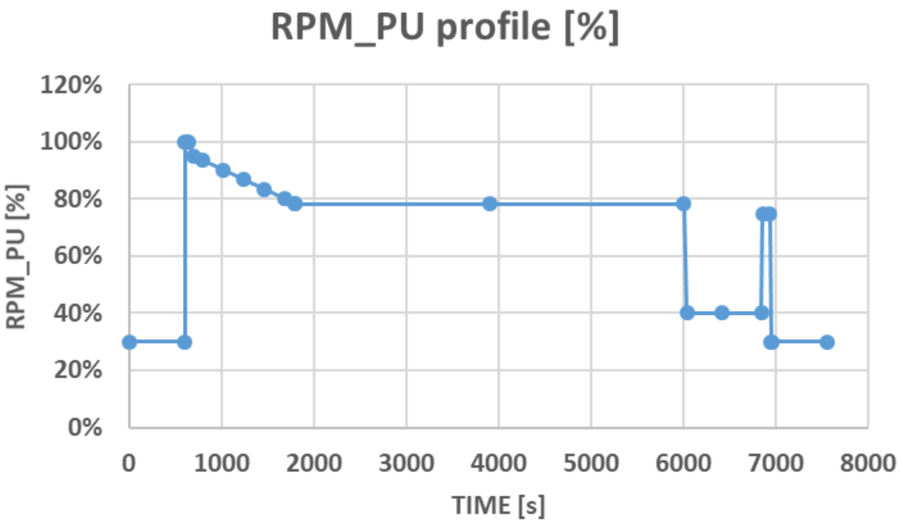

Fig. C-2: Propeller rotation speed profile.

A linear regression model proposed by NASA in [79] is considered for estimating the gearbox mass:

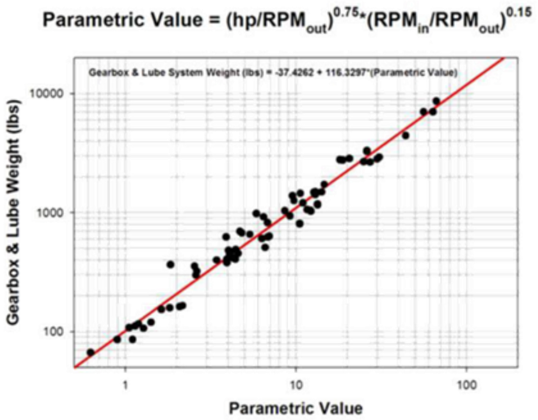

Fig. C-3: Transmission and lubrication system weight correlation from Nasa.

The “parametric value set in the Fig. C-3 is defined by the following equations:

Table C-2: Gearbox mass estimation.

$RPM_{prop}(t) = RPM_{PU}(t) \times RPM_{prop_{max}}$	Propeller rotational speed mission $[RPM]$	*(C-1)*
$Gbox = \left(\max\left(\frac{P_{propHP}(t)}{RPM_{prop}(t)}\right)\right)^{0.75} \times R_{gbox}^{0.15}$	Gearbox parameter (abscissa of the Fig C-3) [-]	*(C-2)*
$M_{Gbox} = 0.45 \times (-37.4 + 116.3 \times Gbox)$	Gearbox mass estimation [kg]	*(C-3)*

Where $P_{prop_{HP}}$ is the maximum propeller shaft power in horsepower [HP], RPM_{prop} the propeller rotational speed in [rpm] and R_{gbox} is the gearbox ratio. A linear function allows estimating the gearbox weight Eq*(C-3)*.

C.2 Performance model:

A constant efficiency value is finally assessed in Eq*(C-4*).

$$\eta_{gbox} = 0.985 \tag{C-4}$$

Thanks to the rotational speed profile, the mechanical power mission (torque $T_{shaft_{emot}}$ and rotational speed Ω_{emot}) can be established:

$$P_{shaft_{emot}}(t) = \frac{P_{prop_{HP}}(t)}{\eta_{gbox}} \times \frac{1000}{1.34} \tag{C-5}$$

$$\Omega_{emot}(t) = N_{prop}(t) \times R_{gbox} \times \frac{\pi}{30} \tag{C-6}$$

$$T_{shaft_{emot}}(t) = \frac{P_{shaft_{emot}}(t)}{\Omega_{emot}(t)} \tag{C-7}$$

APPENDIX D. TURBOSHAFT MODEL

To move an airplane through the air, some kind of propulsion system are used to generate thrust. This figure shows drawings of four different variations of a gas turbine or jet engine. In this study only the turboshaft has been considered.

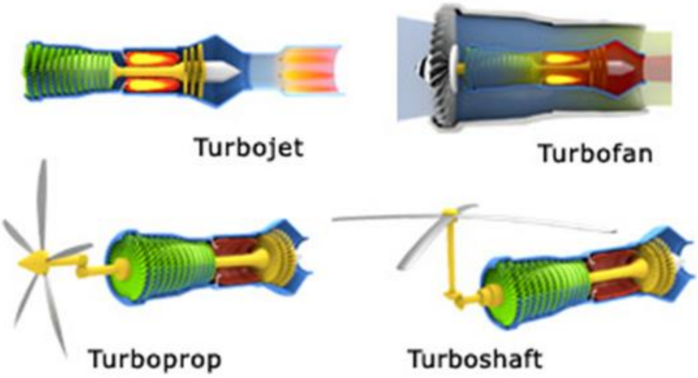

Fig. D-1: Example of gas turbine.

Table D-1: Input/output variables for the turboshaft model.

INPUT VARIABLES		
$P_{dynamic}\ (t)$	[Pa]	Dynamic Pressure
$T_{dynamic}\ (t)$	[K]	Dynamic Temperature
P_{SLS}	[W]	Sea Level Thermal Power
$P_{mech_{GT_{mission}}}(t)$	[W]	Turboshaft power mission
OUTPUT VARIABLES		
M_{fuel}	[kg]	Fuel mass
$M_{turboshaft}$	[kg]	Turboshaft mass

The model is illustrated in Fig. D-2.

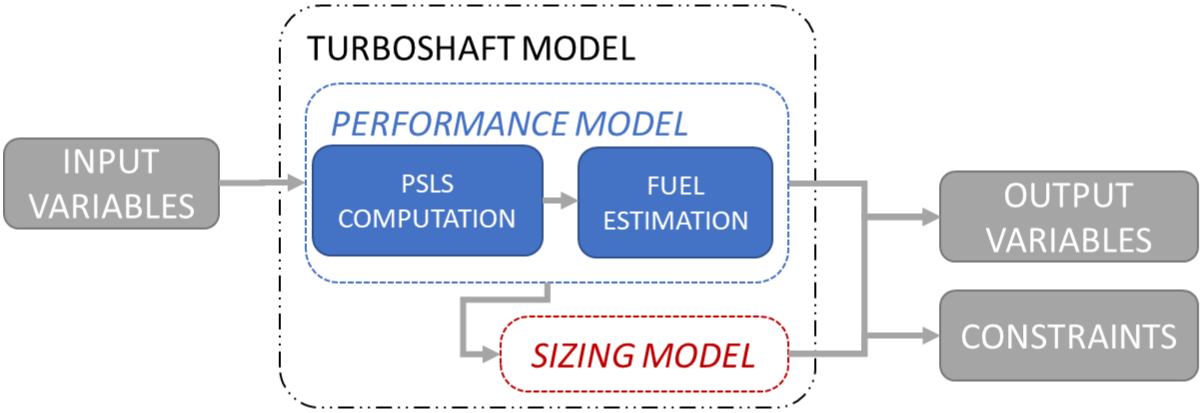

Fig. D-2: Process chart of the turboshaft model.

The turboshaft model is based on response surfaces as mentioned on the data regression of Fig. II-5. Three inputs have been considered: the static power at sea level P_{SLS}, the ratio δ [Pa] between total and static pressures at sea level and the ratio θ [K] between total and static temperatures at sea level previously calculated in Eqs *(A-4)* and *(A-5)*. From these inputs, a one column-vector is derived in Eq*(D-3)* in order to assess the maximum mechanical turboshaft power $P_{max_{shaft_{GT}}}$. α_1 and β_1 are two constant values related to the linear regression.

Table D-2: Turboshaft mechanical power functions.

$\delta = \frac{P_{dynamic}}{101325}$	Pressure ratio $[-]$	*(D-1)*
$\theta = \frac{T_{dynamic}}{288.15}$	Temperature ratio $[-]$	*(D-2)*
$x_C = \begin{bmatrix} log(P_{SLS}) \\ log(\delta) \\ log(\theta) \\ log(P_{SLS})^2 \\ log(\delta)^2 \\ log(\theta)^2 \\ log(P_{SLS}) \times log(\delta) \\ log(P_{SLS}) \times log(\theta) \\ log(\delta) \times log(\theta) \end{bmatrix}$	Regression vector [-]	*(D-3)*
$P_{max_{shaft_{GT}}} = 10^{\alpha_1 + \beta_1 . x_C}$	Maximum mechanical power of the gas turbine $[kW]$	*(D-4)*

The input parameter P_{SLS} is a constant value and it will determine the maximum mechanical turboshaft power during the mission considering altitude and Mach speed. That is why, a convenient P_{SLS} value must be designed ($P_{SLS}\ Computation$ function) in order to suitably supply the hybrid electric propulsion during the whole flight mission, the $P_{max_{shaft_{GT}}}$ has to be higher than the $P_{mission}(t)$. But this process needs an internal loop that is why, another function "$P_{SLS}\ Computation$" is added in this model for determining the right value.

D.1 P_{SLS} computation:

From the Eq*(D-4)*, the process was reversed:

$$log\left(P_{max_{shaft_{GT}}}\right) = \alpha_1 + \beta_1 . x_C \quad (D\text{-}5)$$

Using the Eq*(D-5)*, a second order polynomial function of P_{SLS} has been found:

$$\alpha_{P_{SLS}} \times \log(P_{SLS}^2) + \beta_{P_{SLS}} \times \log(P_{SLS}) + \gamma_{P_{SLS}} = 0 \quad (D\text{-}6)$$

Which the roots are:

$$\log(P_{SLS}) = \min\left(\frac{\left(-\beta_{P_{SLS}} \pm \sqrt{\beta_{P_{SLS}}^{2} - 4\times\alpha_{P_{SLS}}\times\gamma_{P_{SLS}}}\right)}{2\times\alpha_{P_{SLS}}}\right) \qquad \textit{(D-7)}$$

In the equation *(D-6)*, $\alpha_{P_{SLS}}, \beta_{P_{SLS}}, \gamma_{P_{SLS}}$ represent constant values of the 2nd order polynomial function of P_{SLS}. These constant values are determined by three input variables $\delta, \theta, P_{mission}$. For each mission point, a P_{SLS} value is determined and finally the maximum value of this set is chosen.

D.2 Fuel estimation:

Given the vector (x_C) with the right value of P_{SLS}, the maximum Power Specific Fuel Consumption $PSFC_{max}$ is assessed (in $[kg/s/kW]$ as defined in: it corresponds to the turboshaft PSFC when this engine provides its maximum power leading to a minimum consumption. For the real turboshaft fuel consumption, a ratio ($Part_{load}$) is set in Eq*(D-9)* between the required power function (of the environmental data δ and θ° and the maximum mechanical power). Another linear regression is used to estimate the actual PSFC Eq*(D-11)* from which the fuel flow rate is defined given a required power $P_{mission}$ and used in Eq *(D-3).*

Table D-3: Fuel estimation model

$PSFC_{max} = 10^{\alpha_2+\beta_2 . x_C}$	Maximum Specific fuel consumption $[kg/s/kW]$	*(D-8)*
$Part_{load} = \frac{\boldsymbol{P_{mech_{GT_{mission}}}}}{P_{max_{shaft_{GT}}}\times\delta\times\sqrt{\theta}}$	Power ratio $[-]$	*(D-9)*
$y = \begin{bmatrix} log(Part_{load}) \\ log(Part_{load})^2 \\ \dots \\ log(Part_{load})^{10} \end{bmatrix}$	Regression vector $[-]$	*(D-10)*
$PSFC = 10^{\alpha_3+\beta_3 . y} \times \frac{PSFC_{max}}{\theta}$	Specific fuel consumption $[kg/s/kW]$	*(D-11)*
$D_{m_{fuel}}[kg/s] = PSFC \times \frac{\boldsymbol{P_{mech_{GT_{mission}}}}}{1000}$	Mass flow rate [kg/s]	*(D-12)*

In this model, the specific fuel consumption variation is taken into account. The fuel burn can be calculated over the aircraft mission by integrating the $D_{m_{fuel}}$ variable. As displayed in Fig. I-16, the turboshaft consumption is minimum at 100% of the rating power. Contrarily, at low rating, the SFC evolution may be referred to a hyperbolic function. In that way, using secondary energy source in taxi and descent phases and switching off the main thermal source could be interesting in a hybrid electric aircraft. However, an efficient, reliable and fast starting system is mandatory as in modern ground vehicles.

D.3 Sizing model:

Estimating the turboshaft mass is difficult. For that purpose, a typical specific power $P_{SPE} = 9.86\ \mathrm{kW/kg}$ is assessed from experimental data set [12]. Finally, the fuel mass is obtained by the time integral of the mass flow rate.

$$M_{fuel} = \int D_{m_{fuel}}(t)dt \tag{D-13}$$

$$M_{turboshaft} = P_{SLS} \times P_{SPE} \tag{D-14}$$

D.4 Power constraint:

A constraint associated with the shaft power is set in this model in order to ensure that the turboshaft will provide enough power to the propulsion system.

$$P_{max_{shaft_{GT}}} \geq P_{mech_{GT_{mission}}} \tag{D-15}$$

APPENDIX E. CABLE MODEL

Table E-1: Input/output variables for the cable model.

INPUT VARIABLES		
$\boldsymbol{P_{elec_{cable}}(t)}$	$[W]$	Cable electric power
$\boldsymbol{PF\ (t)}$	$[-]$	Power Factor
$\boldsymbol{m}$	$[-]$	Number of phases
$\boldsymbol{V}$	$[V]$	AC/DC voltage (depending on the cable)
OUTPUT VARIABLES		
$\boldsymbol{\eta_{cable}(t)}$	$[\%]$	Cable efficiency
$\boldsymbol{T_{cable}(t)}$	$[°C]$	Cable warming
$\boldsymbol{\Delta V}$	$[V]$	Voltage drop
$\boldsymbol{M_{cable}}$	$[kg]$	Cable mass

The model is illustrated in Fig. E-1.

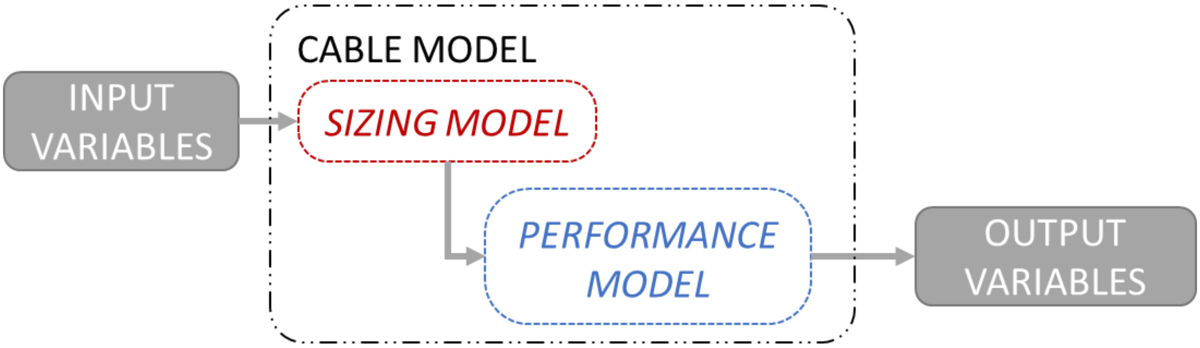

Fig. E-1: Process chart for the cable model.

Several locations have been selected with different ambient temperature assessments. They are listed in the following table:

Table 1: Ambient temperature in each part of the aircraft.

PLACE	T_{amb}
Nacelle	80
Pylon	80
Wing	80
Fuselage	60

Two materials are considered: copper and aluminum.

Table 2: Copper data table

GAUGE	1	0	00	000	0000
K_c $[-]$	11e-4	8,4e-4	6,0e-4	4,3e-4	3,1e-4
M_{lin} $[\mathrm{g/m}]$	470	600	750	950	1200
R_{lin} $[\Omega/\mathrm{m}]$	0,5e-3	0,4e-3	0,31e-3	0,25e-3	0,2e-3
$T_{cable_{max}}$ $[°\mathrm{C}]$	220	220	220	220	220

Table 3: Aluminum data table.

GAUGE	1	0	00	000
K_c $[-]$	20e-4	15e-4	11e-4	8,4e-4
M_{lin} $[\mathrm{g/m}]$	143	181	230	276
R_{lin} $[\Omega/\mathrm{m}]$	0,75e-3	0,60e-3	0,43e-3	0,36e-3
$T_{cable_{max}}$ $[°\mathrm{C}]$	160	160	160	160

The idea is to estimate the cable weight per meter of length for different voltages and locations inside the structure (nacelle, fuselage). The details for this model cannot be provided for confidentiality reasons.

APPENDIX F. ELECTRIC MOTOR MODEL

Table F-1: Input/output variables for the electric motor sizing model.

INPUT VARIABLES (in bold blue, the 10 decision variables for optimization)		
$R_{alesage}$	[m]	**Bore radius of the electric motor**
$R_{Drot_{lm}}$	[%]	**Rotor diameter/rotor length ratio**
$R_{g_{ral}}$	[%]	**Air gap thickness/ bore radius ratio**
$R_{hs_{ral}}$	[%]	**Slot height/ bore radius ratio**
$R_{pm_{ral}}$	[%]	**Magnet thickness/ bore radius ratio**
τ_{magnet}	[%]	Pole pitch (=100%)
τ_{slot}	[%]	Slot pitch (=100% full pitch winding)
k_{carbon}	[−]	Carbon fiber constant for sleeve equation
p	[−]	**Number of pole pairs**
q	[−]	Number of phases
$nepp$	[−]	**Number of slots per pole and per phase**
N_{ce}	[−]	**Number of conductors per slot**
k_{fill}	[−]	Fill factor in the slot
J_a	[T]	Permanent magnet flux density
B_{yoke}	[T]	**Stator yoke flux density**
B_{teeth}	[T]	**Stator teeth flux density**
$B_{yoke_{rotor}}$	[T]	Rotor yoke flux density
V_{uHVDC}	[V]	**Ultra high voltage direct current**
OUTPUT VARIABLES		
M_{motor}	[kg]	Electric motor mass
$PF(t)$	[−]	Power factor mission
$m_a(t)$	[−]	Modulation depth mission
$P_{JDC}(t)$	[W]	DC Joule losses
$P_{Iron}(t)$	[W]	Iron losses
$P_R(t)$	[W]	Friction losses
$P_{Aero}(t)$	[W]	Aerodynamic losses
$h_{XX}, e_{XX}, L_{XX}, R_{XX}, w_{XX}$	[m]	Sizes of the e-motor

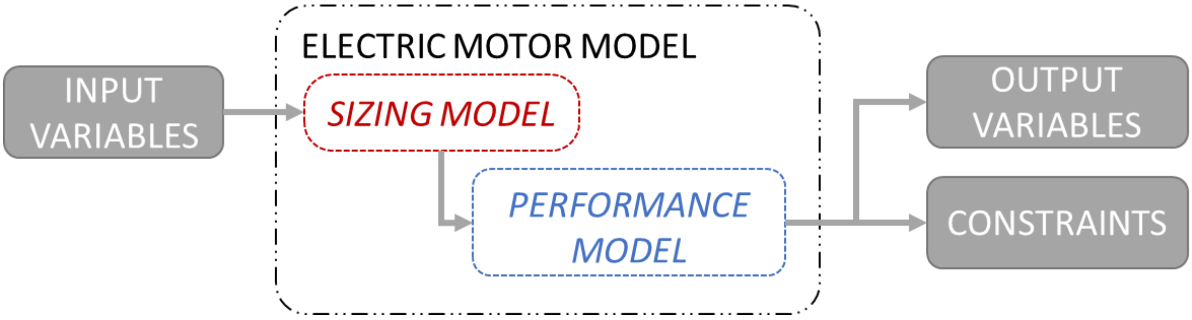

Fig. F-1: Process chart of the electric motor.

More details related to the assumptions of this model can be found in [A5].

F.1 Sizing model.

F.1.1 1rst harmonic air gap flux density

The computation of the air gap flux density is the first step of this model. Most of variables use this parameter. In equation *(F-2)*, the direct calculation is used for determining the air gap flux density [A5].

Table F-2: First harmonic flux density computation process.

$$\gamma_{elec} = \pi \times \frac{\tau_{magnet}}{2} \qquad \textit{(F-1)}$$

$$Bfond_{gap_{rms}} = \frac{R_{pm_{ral}} \times Ja}{log\left(-(1 - R_{pm_{ral}} - R_{g_{ral}})\right)} \qquad \textit{(F-2)}$$

$$B_{gap_{rms}} = Bfond_{gap_{rms}} \times 2\sqrt{2} \times \frac{sin(\gamma_{elec})}{\pi} \qquad \textit{(F-3)}$$

F.1.2 Electric motor geometry.

All sizes of the electric motor are determined from the input variables. The Fig. F-2 represents each variable name on the cross section of an electric machine.

Table F-3: Geometry of the electric permanent magnet synchronous machine.

$L_{motor} = \frac{2 \times R_{alesage}}{R_{Drot_{Lm}}}$	E-motor length [m]	*(F-4)*
$eg_{mag} = R_{alesage} \times R_{g_{ral}}$	Magnetic air gap thickness [m]	*(F-5)*
$e_{magnet} = R_{alesage} \times R_{PM_{ral}}$	Permanent magnet thickness [m]	*(F-6)*
$h_{slot} = R_{hs_{ral}} \times R_{alesage}$	Slot height [m]	*(F-7)*
$N_{enc} = 2p \times q \times nepp$	Number of slot [m]	*(F-8)*
$h_{yoke} = \frac{B_{gap_{rms}}\sqrt{2}}{B_{yoke}} \times \frac{R_{alesage}}{p}$	Stator yoke height [m]	*(F-9)*
$h_{yoke_{rotor}} = \frac{B_{yoke}}{B_{yoke_{rotor}}} \times h_{yoke}$	Rotor yoke height [m]	*(F-10)*
$Ratio_{teeth} = \frac{2}{\pi} \times \frac{B_{gap_{rms}}\sqrt{2}}{B_{yoke}}$	Teeth Ratio [%]	*(F-11)*
$e_{sleeve} = \frac{(R_{alesage} - eg_{mag})}{\left(\frac{1}{k_{carbon} \times \max(\Omega_{emot}(t))}\right)^{-1}}$	Sleeve thickness [m]	*(F-12)*
$e_{gap} = eg_{mag} - e_{sleeve}$	Mechanical air gap thickness [m]	*(F-13)*
$\tau_{teeth+slot} = \frac{2\pi \times R_{alesage}}{N_{enc}}$	Slot + teeth arc [m]	*(F-14)*
$w_{slot} = (1 - Ratio_{teeth}) \times \tau_{teeth+slot}$	Slot arc [m]	*(F-15)*
$w_{teeth} = (Ratio_{teeth}) \times \tau_{teeth+slot}$	Teeth arc [m]	*(F-16)*

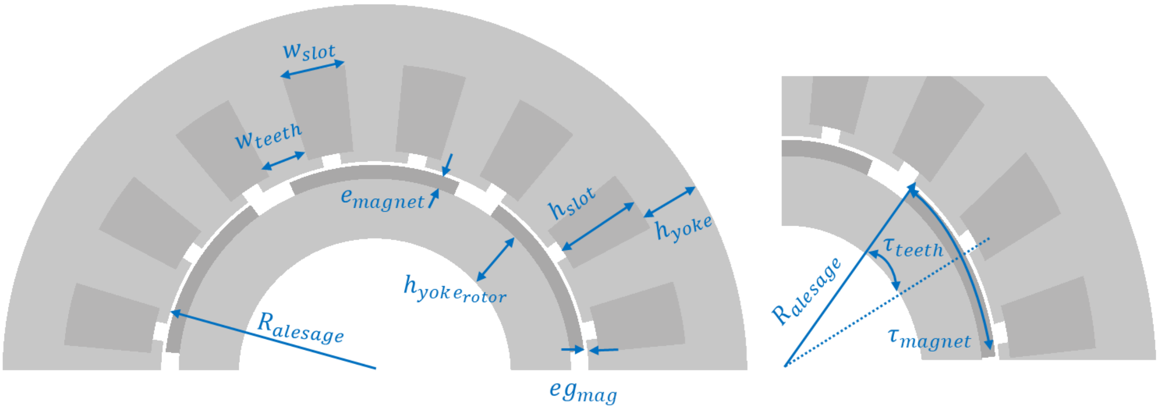

Fig. F-2: Cross section of an electric motor with each variable name.

The slot arc w_{slot} is not sufficient for determining the exact sizes of the slot. That is why the Fig. F-3 describes the geometry of the slot and the process related to the calculation of the slot length in order to find the right value of the slot section.

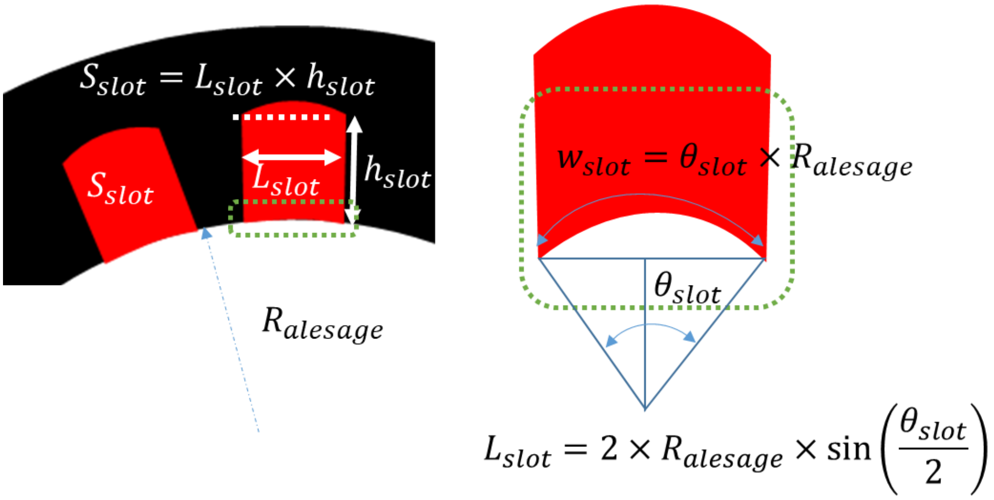

Fig. F-3: Description of the slot length calculation

Table F-4: Slot sizes details.

$\theta_{slot} = \frac{w_{slot}}{R_{alesage}}$	Slot angle [rad]	(F-17)
$L_{slot} = 2 \times R_{alesage} \times \sin\left(\frac{\theta_{slot}}{2}\right)$	Slot length [m]	(F-18)
$S_{slot} = L_{slot} \times h_{slot}$	Slot area [m²]	(F-19)
$S_{CU_{total}} = S_{slot} \times k_{fill}$	Useful copper area [m²]	(F-20)

F.1.3 Centrifugal pressure and peripheral speed.

The centrifugal pressure and the peripheral speed will be uses for the mechanical constraint computations.

Table F-5: Mechanical constraints calculation.

$R_{yoke_{rotor_{OUT}}} = R_{shaft} + h_{yoke_{rotor}}$	*(F-21)*
$R_{mag_{OUT}} = R_{yoke_{rotor_{OUT}}} + e_{magnet}$	*(F-22)*
$R_{sleeve_{OUT}} = R_{mag_{OUT}} + e_{sleeve}$	*(F-23)*
$P_{centrifugal} = \frac{1}{3}\frac{\Omega_{mech_{max}}^2}{e_{sleeve}}\left(\rho_{carbon}.\left(R_{sleeve_{OUT}}^3 - R_{mag_{OUT}}^3\right) + \rho_{PM}.\left(R_{mag_{OUT}}^3 - R_{yoke_{rotor_{OUT}}}^3\right)\right)$	*(F-24)*
$V_{peripheral} = R_{sleeve_{OUT}} \times \Omega_{mech_{max}}$	*(F-25)*

The centrifugal pressure $P_{centrifugal}$ and peripheral speed $V_{peripheral}$ constraints are set in order to design the right carbon sleeve thickness.

F.1.4 Electric motor winding configuration.

The head winding coefficient k_{tb} is determined by the geometry of the electric motor. For the winding layout, several winding factors are taken into account, the global winding factor $k_{windings}$ is the product of these factors for the 1rst harmonic.

Table F-6: Winding factors description.

$k_{tb} = \frac{\left(L_{motor}+\tau_{slot}\times\frac{\pi}{p}\times R_{alesage}+\pi\times\tau_{teeth+slot}\right)}{L_{motor}}$	head winding coefficient [-]	*(F-26)*
$kd1 = \frac{\sin\left(\frac{1}{2}\times nepp\times p\times\frac{\tau_{teeth+slot}}{R_{alesage}}\right)}{nepp\times\sin\left(\frac{1}{2}\times p\times\frac{\tau_{teeth+slot}}{R_{alesage}}\right)}$	twist factor [-]	*(F-27)*
$kr1 = \sin\left(\tau_{slot} \times \frac{\pi}{2}\right)$	shortening factor [-]	*(F-28)*
$ki1 = 1$	distribution factor [-]	*(F-29)*
$k_{windings} = kd1 \times kr1 \times ki1$	global winding factor [-]	*(F-30)*
$k_{lc} = 1$ (1,15 if 2035 target)	AC coefficient losses (2035 target)	*(F-31)*

F.1.5 Electric parameters.

The single-phase equivalent circuit of a permanent magnet synchronous machine is presented in the Fig. F-4.

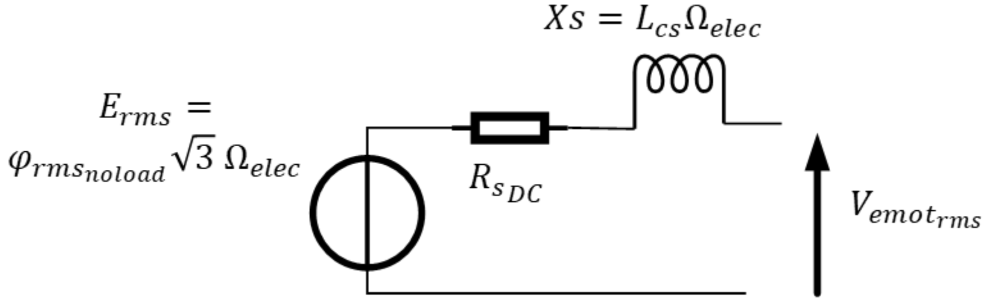

Fig. F-4: Circuit parameters of the PMSM and its electric equivalent circuit.

Table F-7: Circuit parameter equations.

$\varphi_{rms_{noload}} = \frac{N_{ce}\times N_{enc}}{2.q.p} \times 2.k_{windings} \times L_{motor} \times R_{alesage} \times \sqrt{2}.B_{gap_{rms}}$	*(F-32)*
$L_p = \frac{4}{\pi} \times \mu_0 \times k_{windings}^2 \left(\frac{N_{ce}\times N_{enc}}{2.q.p}\right)^2 \times \frac{L_{motor}\times R_{alesage}}{e_{magnet}+eg_{mag}}$	*(F-33)*
$M = -\frac{1}{2}L_p$	*(F-34)*
$L_{cs} = L_p - M$	*(F-35)*
$Rs_{DC} = \frac{\rho_{CU}\times 2\times\frac{N_{ce}\times N_{enc}}{2.q}\times k_{tb}\times L_{motor}\times k_{lc}}{S_{CU_{total}}}$	*(F-36)*

The circuit parameters are the following:

- $\varphi_{rms_{noload}}$ is the RMS value of no load flux in [Wb].
- L_p is the self-inductance of one phase [H].
- M is the mutual inductance of one phase in [H].
- L_{cs} is the cyclic inductance of one phase [H].
- Rs_{DC} is the DC resistance of one phase [Ω].

Once these parameters have been determined, the performance model can be run over the flight mission.

F.2 Sizing constraints.

The maximum peripheral speed is 200 m/s and the maximum centrifugal pressure is $7{,}5 \times 10^8\ Pa$.

Table F-8: Sizing constraints.

$R_{shaft} \geq R_{shaft_{min}}$	Shaft radius constraint	*(F-37)*
$e_{gap} \geq eg_{min}$	Air gap thickness constraint	*(F-38)*
$V_{peripheral} \leq V_{peripheral_{max}}$	Peripheral speed constraint	*(F-39)*
$P_{centrifugal} \leq P_{centrifugal_{max}}$	Centrifugal pressure constraint	*(F-40)*

F.3 Performance model.

F.3.1 Field weakening control

The Maximum Torque Per Ampere strategy has been implemented with capability of field weakening during the flight mission. This strategy is based on the Behn-Eschenburg model presented in Fig. F-4.

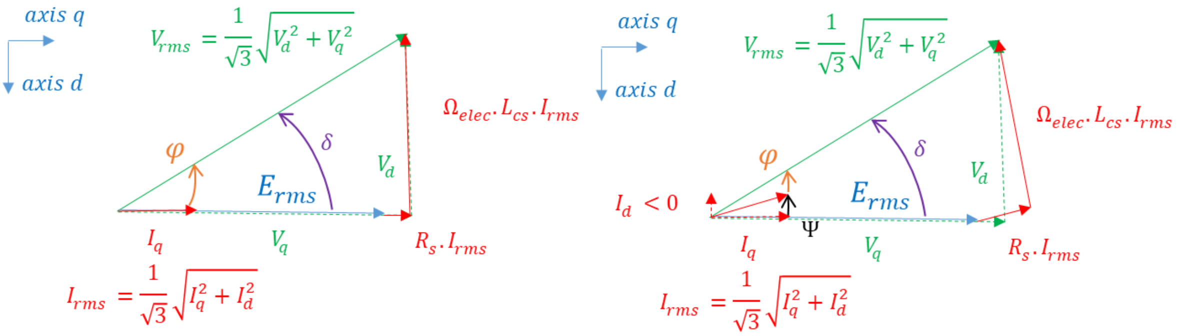

Fig. F-5: Behn-Eschenburg model (left: without field weakening Ψ =0°)(right: with field weakening Ψ >0°) .

The principle of the maximum torque per ampere control is implemented with the angle Ψ equals to 0. Indeed, the choice of " Ψ =0°" represents the optimal angle which allows having the maximum torque with minimal Joule losses. Maintaining a constant torque ("I_q" constant) at a higher speed than the base speed induces a negative current "I_d": this "counter-field current" reduces the air gap flux "Φ_g". This operation in field weakening mode ensures the same power value for a higher speed while remaining at the induced stop-voltage (maximum voltage allowed by the DC bus).

Table F-9: Initialization of the field weakening control.

$Iq_{mission} = \frac{T_{emot}}{p \times \varphi_{rms_{noload}} \times \sqrt{3}}$	Required torque => Iq current	*(F-41)*
$Id_{centre} = \frac{\varphi_{rms_{noload}} \times \sqrt{3}}{L_{cs}}$	Center of the actuator circle	*(F-42)*
$Vdq_{max} = Vond_{max} \times \sqrt{\frac{3}{2}} = \Omega_{elec} \times \Phi_g$	Stop-voltage (max inverter voltage)	*(F-43)*
$R_{mission} = \frac{Vdq_{max}}{L_{cs} \times \Omega_{elec_{mission}}}$	Radius of the actuator circle	*(F-44)*

From a geometrical point of view, the radius of the actuator circle is defined by the maximum available voltage, V_{dqmax}, and the actuator rotational speed over the flight mission, $\Omega_{elec_{mission}}$ (see Table F-9). The intersection between the actuator circle and the current vector defines the operation point (OP1,2 see Fig. F-6a).

When the voltage is not limited (without field-weakening), the circle must contain the operating point (blue circle in Fig. F-6b) and the equivalent condition is the following:

$$R_{mission}^2 \geq Iq_{mission}^2 + Id_{centre}^2$$

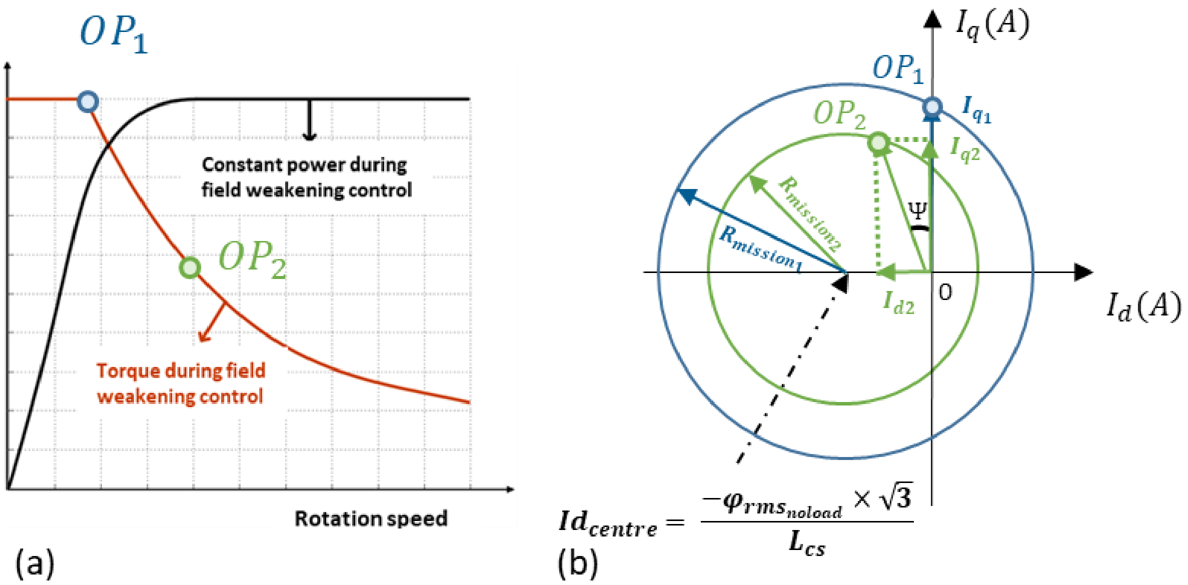

Fig. F-6: Field-weakening operation. (a) Power/torque versus rotational speed plane. (b) Analysis in the d-q plane. Two representations of actuator circles (blue circle: maximum torque per ampere strategy, with I_d = 0, green circle: field-weakening strategy, with increased speed and constant limited voltage).

The inequation becomes an equation when the voltage of the electric actuator reaches the maximum available voltage, V_{dqmax}. In this case, the field-weakening strategy occurs. The operating is then defined by the green circle. During that overspeed operation, the actuator usually operates at constant power, as illustrated in Fig. F-6a. The blue circle shrinks to the green circle (increasing speed) and the current is shifted in phase to reach the operating point (see Fig. F-6b). Both operating points (OP_1 and OP_2) are represented in the torque-speed plan (see Fig. F-6a). The circle characteristic is defined by:

$$R_{mission}^2 = Iq_{mission}^2 + \left(I_{d_{mission}} - Id_{centre}\right)^2$$

This second order is derived in Figure 8 to set the current $I_{d_{mission}}$ in the case of the field-weakening operation:

$$I_{d_{mission}}^2 - 2 \times \frac{-\varphi_{rms_{noload}} \times \sqrt{3}}{L_{cs}} \times I_{d_{mission}} + Iq_{mission}^2 + \left(\frac{-\varphi_{rms_{noload}} \times \sqrt{3}}{L_{cs}}\right)^2 - \left(\frac{Vdq_{max}}{L_{cs} \times \Omega_{elec_{mission}}}\right)^2 = 0$$

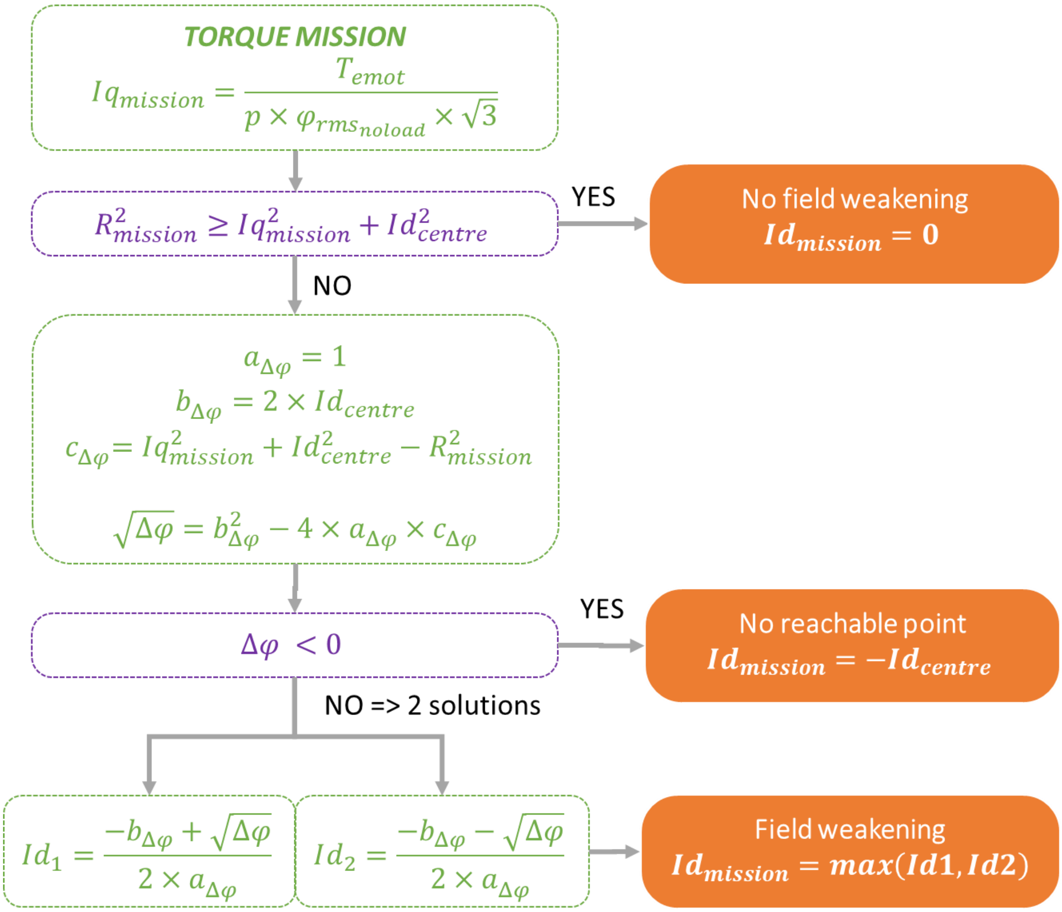

Fig. F-7: Field weakening control description.

Fig. F-7 shows the resolution process of the control strategy. The discriminant is computed to check if there are solutions. Finally, if solutions exist, the least restrictive I_d value is kept. After this calculation process, the electromechanical actuator characteristics can be computed. The currents and voltages are derived from the d, q axis values (see Table F-10).

Table F-10: PMSM electric parameters and flux densities.

$$E_{rms_{mission}} = \varphi\sqrt{3}\,\Omega_{elec_{mission}} \tag{F-45}$$

$$Vd_{mission} = Rs_{DC} \times Id_{mission} - L_{cs} \times \Omega_{elec_{mission}} \times Iq_{mission} \tag{F-46}$$

$$Vq_{mission} = Rs_{DC} \times Iq_{mission} + L_{cs} \times \Omega_{elec_{mission}} \times Id_{mission} + E_{rms_{mission}} \tag{F-47}$$

$$Is_{rms_{mission}} = \frac{1}{\sqrt{3}}\sqrt{Id^2_{mission} + Iq^2_{mission}} \tag{F-48}$$

$$Vs_{rms_{mission}} = \frac{1}{\sqrt{3}}\sqrt{Vd^2_{mission} + Vq^2_{mission}} \tag{F-49}$$

$$\Phi_{g_{noload}} = \varphi_{rms_{noload}} \times \sqrt{3} \tag{F-50}$$

$$\Phi_{g_{field-weakening}} = \sqrt{(Iq_{mission} \times L_{cs})^2 + \left(\Phi_{g_{noload}} + Id_{mission} \times L_{cs}\right)^2} \tag{F-51}$$

$$B_{yoke_{mission}} = B_{yoke_{noload}} \times \frac{\Phi_{g_{field-weakening}}}{\Phi_{g_{noload}}} \tag{F-52}$$

$$B_{teeth_{mission}} = B_{teeth_{noload}} \times \frac{\Phi_{g_{field-weakening}}}{\Phi_{g_{noload}}} \tag{F-53}$$

The electric parameters are the following:

- $E_{rms_{noload}}$ is the RMS value of no load voltage in [V].
- $Vd_{mission}$ and $Vq_{mission}$ are the “d” and “q” axis mission voltages [V].
- $Vs_{rms_{mission}}$ and $Is_{rms_{mission}}$ are the voltage and the current in one phase [V/A].
- $\Phi_{g_{noload}}$and $\Phi_{g_{field-weakening}}$ are the air gap flux density (no load and in load [Wb].
- $B_{yoke_{mission}}$ and $B_{teeth_{mission}}$ are teeth and yoke flux densities during the mission [T].

All inverter parameters can be computed from the Behn-Eschenburg diagram in the Fig. F-5:

Table F-11: Inverter parameters

$ma_{mission} = \frac{Vs_{rms_{mission}}}{\frac{V_{uHVDC}}{2\sqrt{2}}}$	modulation depth [-]	*(F-54)*
$\delta(t) = -atan\left(\frac{V_d(t)}{V_q(t)}\right)$	internal angle [rad]	*(F-55)*
$\Psi(t) = atan\left(\frac{I_d(t)}{I_q(t)}\right)$	field weakening angle [rad]	*(F-56)*
$\varphi(t) = \delta(t) - \Psi(t)$	power factor angle [rad]	*(F-57)*
$PF_{mission} = \cos\big(\varphi(t)\big)$	power factor [-]	*(F-58)*

F.3.2 Losses model

In this study the following losses have been taken into account:

- $P_{JDC_{mission}}$ is the DC Joule losses in the stator windings [W].
- $P_{Iron_{mission}}$ is the Iron losses in the stator yoke [W].
- $P_{R_{mission}}$ is the friction losses in the bearings [W].
- $P_{Agap_{mission}}$ is the windage losses in the air gap [W].
- $P_{Arotor_{mission}}$ is the windage losses in the two rotor surfaces [W].

Table F-12: Electric engine losses description.

$P_{JDC_{mission}} = q \times Rs_{DC} \times Is_{rms_{mission}}^2$	*(F-59)*
$P_{Iron_{mission}} = 2 \times \left(\sum f^{\alpha} B_{yoke}^{\beta} M_{stator_{yoke}} + \sum f^{\alpha} B_{teeth}^{\beta} M_{stator_{teeth}}\right)$	*(F-60)*
$P_{R_{mission}} = 2.C_{froul} \times \Omega\ _{elec_{mission}}$	*(F-61)*
$P_{Agap_{mission}} = k_1 \times C_{f_{air}}.\pi.\rho_{air} \times \Omega^3\ _{elec_{mission}} \times R_{alesage}^4 \times k_{tb} \times L_{motor}$	*(F-62)*
$P_{Arotor_{mission}} = C_{f_r}.\pi.\rho_{air} \times \Omega^3\ _{elec_{mission}} \times R_{alesage}^5$	*(F-63)*

F.4 Performance constraints.

Table F-13: Performance constraints.

$\Delta\varphi \geq 0$	Mission fulfillment (cf Fig. F-7)	*(F-64)*
$\boldsymbol{Demag} \leq 0$ $(Demagnetization\ ok\ ?$ $Yes = 0\ , No = 1)$	Demagnetization constraint [-]	*(F-65)*

The *(F-65)* constraint equation concerns the problem of irreversible demagnetization of the magnet generally caused by its heating and/or by the operation in overspeed (field weakening).

APPENDIX G. ELECTRIC MOTOR COOLING MODEL

Table G-1: Input/output variables for the electric motor cooling model.

	INPUT VARIABLES	
$\boldsymbol{R_{alesage}}$	$[\mathrm{m}]$	Bore radius of the e-motor
$\boldsymbol{h_{XX}, e_{XX}, L_{XX}, R_{XX}, w_{XX}}$	$[\mathrm{m}]$	Sizes of the e-motor
$\boldsymbol{p}$	$[-]$	Number of pole pairs
$\boldsymbol{Nenc}$	$[-]$	Number of slots
$\boldsymbol{k_{fill}}$	$[-]$	Fill factor in the slot
$\boldsymbol{\rho_{fluid}, \rho_{air}}$	$[\mathrm{kg/m^3}]$	Fluid and air density
$\boldsymbol{C_{P_{fluid}}, C_{P_{air}}}$	$[\mathrm{J/(kg.K)}]$	Fluid and air thermal capacity
$\boldsymbol{visd_{fluid}, visd_{air}}$	$[\mathrm{Pa.s}]$	Fluid and air dynamic viscosity
$\boldsymbol{\nu_{air}}$	$[\mathrm{m^2/s}]$	Air kinematic viscosity
$\boldsymbol{\lambda_{fluid}, \lambda_{air}, \lambda_{epoxy}, \lambda_{winding_{channel}}}$	$[\mathrm{W/(m.K)}]$	Fluid, air, epoxy and winding channels thermal conductivity
$\boldsymbol{D_{tube_{total}}}$	$[\mathrm{m}]$	Output diameter of the e-motor cooling system
$\boldsymbol{e_{winding_{channel}}}$	$[\mathrm{m}]$	Winding channel thickness
$\boldsymbol{h_{waterjacket_{housing}}}$	$[\mathrm{m}]$	Water jacket housing thickness
$\boldsymbol{R_{windchannel_{Lslot}}}$	$[\%]$	Ratio between winding channels and slot length
$\boldsymbol{\dot{q}_{stator}, \dot{q}_{rotor}, \dot{q}_{windings}}$	$[\mathrm{m^3/s}]$	Stator, rotor winding channel flow rate
$\boldsymbol{N_{nodes}}$	$[-]$	Number of nodes
$\boldsymbol{P_{JDC_{mission}}, P_{Iron_{mission}}, P_{A_{mission}}, P_{R_{mission}}}$	$[\mathrm{W}]$	DC Joule, Iron, Aerodynamic, Friction losses.
	OUTPUT VARIABLES	
$\boldsymbol{M_{motor+cooling}}$	$[\mathrm{kg}]$	E- motor + cooling mass
$\boldsymbol{P_{SPE_{emotor+cooling}}}$	$[\mathrm{kW/kg}]$	E-motor + cooling specific power
$\boldsymbol{T_{yoke_{stator}}(t)}$	$[°\mathrm{C}]$	Stator yoke temperature
$\boldsymbol{T_{windings}(t)}$	$[°\mathrm{C}]$	Winding temperature
$\boldsymbol{T_{magnet}(t)}$	$[°\mathrm{C}]$	Magnet temperature

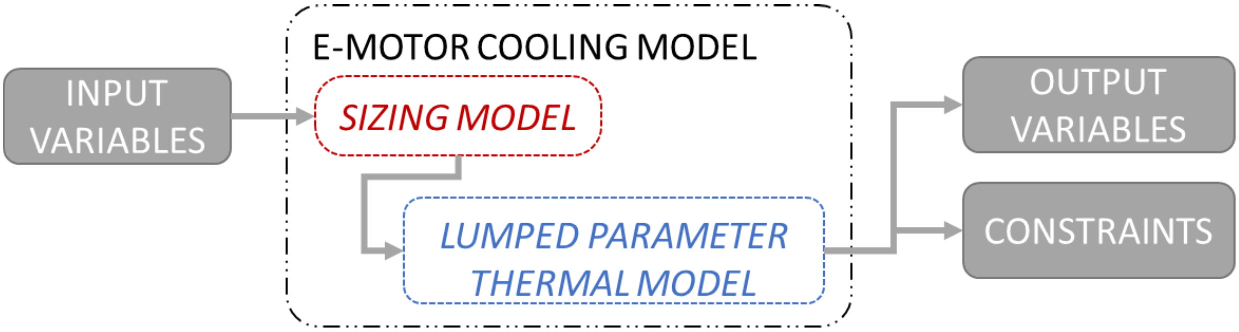

Fig. G-1: Process chart of the electric motor cooling model.

G.1 Sizing model.

Three direct cooling systems studied in [87] have been implemented in the optimization process:

- internal cooling inside the slots of the electric motor (2035 target),
- External cooling outside of the stator through a water jacket,
- and inside the rotor through a shaft cooling system.

G.1.1 Winding channel model for internal cooling (2035 target).

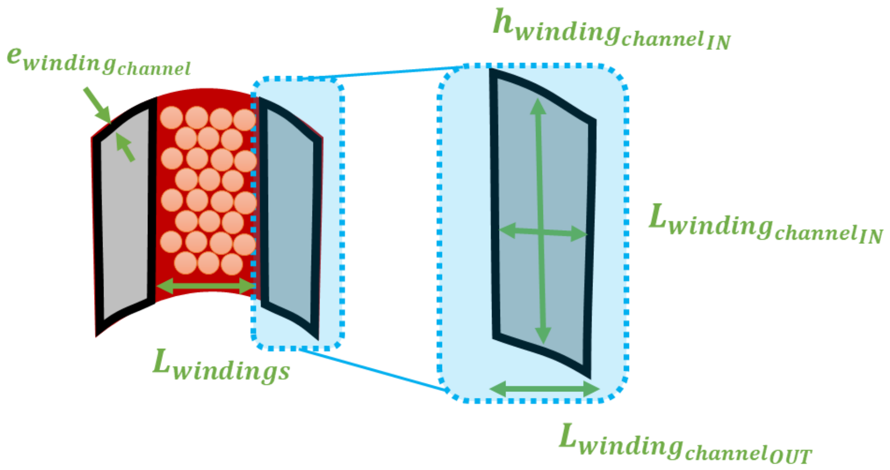

Fig. G-2: Winding channel layout details in the cross section of the slot.

Table G-2: Winding channel sizes.

$$h_{winding_{channel_{IN}}} = h_{slot} - 2.e_{winding_{channel}} \tag{G-1}$$

$$L_{winding_{channel_{OUT}}} = \frac{R_{windchannel_{Lslot}}}{2}.L_{slot} \tag{G-2}$$

$$L_{winding_{channel_{IN}}} = L_{winding_{channel_{OUT}}} - 2.e_{winding_{channel}} \tag{G-3}$$

$$kfill_{winding_{channel}} = \frac{k_{fill}}{1-R_{windchannel_{Lslot}}} \tag{G-4}$$

$$A_{hydro_{winding}} = L_{winding_{channel_{IN}}} \times h_{winding_{channel_{IN}}} \tag{G-5}$$

$$Perim_{hydro_{winding}} = 2 \times \left(L_{winding_{channel_{IN}}} + h_{winding_{channel_{IN}}}\right) \tag{G-6}$$

$$D_{hydro_{winding}} = 4 \times \frac{A_{hydro_{winding}}}{Perim_{hydro_{winding}}} \tag{G-7}$$

$$u_{fluid_{winding}} = \frac{\dot{q}_{winding}}{A_{hydro_{winding}}} \tag{G-8}$$

The channel height $h_{winding_{channel_{IN}}}$ and external/internal length $L_{winding_{channel_{OUT}}}$ & $L_{winding_{channel_{IN}}}$ are determined by the slot height h_{slot}, the slot length L_{slot}, the thickness of the channel $e_{winding_{channel}}$ and the ratio $R_{windchannel_{Lslot}}$. A new fill factor $kfill_{winding_{channel}}$ is computed from the new useful slot area. Hydraulic parameters are computed from the new configuration.

Table G-3: Differences between 2025 and 2035 targets

TARGET	2025	2035
$R_{windchannel_{Lslot}}$	0	25%
$e_{winding_{channel}}$	0	0.1 mm
$\dot{q}_{winding}$	0	5.5e-4 m^3/s

G.1.2 Water Jacket and shaft cooling design (2025 and 2035).

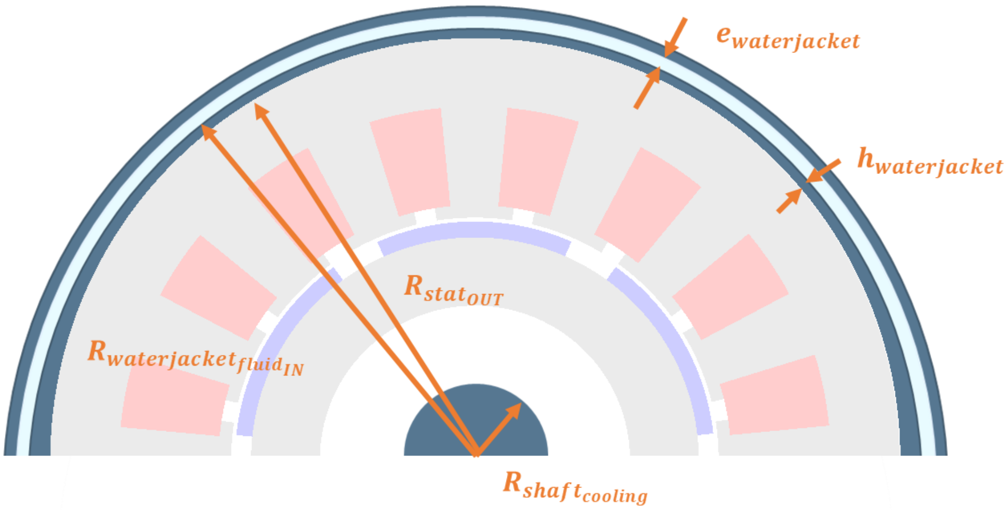

Fig. G-3: Cross section of the electric motor with water jacket and shaft cooling representation.

Table G-4: Water-jacket design equations.

$$R_{waterjacket_{fluid_{IN}}} = R_{stat_{OUT}} + h_{waterjacket_{housing}} \quad \text{(G-10)}$$

$$e_{waterjacket_{fluid}} = 2\% \times R_{waterjacket_{fluid_{IN}}} \quad \text{(G-11)}$$

$$R_{waterjacket_{fluid_{OUT}}} = R_{waterjacket_{fluid_{IN}}} + e_{waterjacket_{fluid}} \quad \text{(G-12)}$$

$$A_{hydro_{stator}} = \pi\left(R^2_{waterjacket_{fluid_{OUT}}} - R^2_{waterjacket_{fluid_{IN}}}\right) \quad \text{(G-13)}$$

$$Perim_{hydro_{stator}} = 2 \times \pi\left(R_{waterjacket_{fluid_{OUT}}} + R_{waterjacket_{fluid_{IN}}}\right) \quad \text{(G-14)}$$

$$D_{hydro_{stator}} = 4 \times \frac{A_{hydro_{stator}}}{Perim_{hydro_{stator}}} \quad \text{(G-15)}$$

$$u_{fluid_{stator}} = \frac{\dot{q}_{stator}}{A_{hydro_{stator}}} \quad \text{(G-16)}$$

Table G-5: Shaft cooling design equations.

$$D_{tube_{rotor}} = 10\% \times R_{shaft_{IN}} \quad \text{(G-17)}$$

$$A_{hydro_{rotor}} = \frac{\pi D^2_{tube_{rotor}}}{4} \quad \text{(G-18)}$$

$$Perim_{hydro_{rotor}} = \pi\left(D_{tube_{rotor}}\right) \quad \text{(G-19)}$$

$$D_{hydro_{rotor}} = 4 \times \frac{A_{hydro_{rotor}}}{Perim_{hydro_{rotor}}} = D_{tube_{rotor}} \quad \text{(G-20)}$$

$$u_{fluid_{rotor}} = \frac{\dot{q}_{rotor}}{A_{hydro_{rotor}}} \quad \text{(G-21)}$$

Table G-6: Heat exchanger tube design equations.

$$A_{hydro_{total}} = \frac{\pi D^2_{tube_{total}}}{4} \quad \text{(G-22)}$$

$$u_{fluid_{total}} = \frac{\dot{q}_{rotor}+\dot{q}_{stator}+\dot{q}_{winding}}{A_{hydro_{total}}} \quad \text{(G-23)}$$

G.1.3 Fluid convection coefficients computation.

Once these systems are designed, Reynolds and Prandtl numbers are computed in order to determine fluid convection coefficients in the cooling system:

Table G-7: Reynolds and Prandtl number used in the fluid convection coefficients computation.

$$Re_{XX} = \frac{\rho_{fluid}\times u_{fluid_{XX}}\times D_{tube_{XX}}}{\lambda_{fluid}} \quad \text{(G-24)}$$

$$Pr = \frac{Cp_{fluid}\times visd_{fluid}}{\lambda_{fluid}} \quad \text{(G-25)}$$

The following process is used for determining each H_{XX} fluid convection coefficients. In the case where the Reynolds number is lower than the critical Reynolds number, the flow is laminar and the Nusselt number is constant. In the other case, a Nusselt equation is computed with a particular one for the heat exchanger.

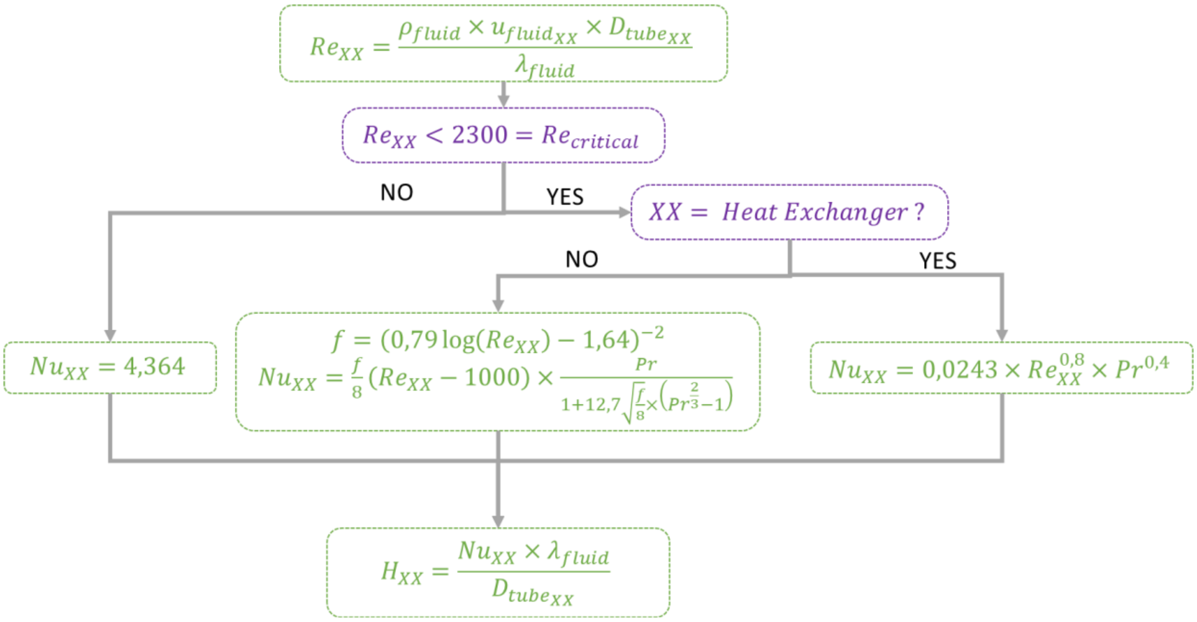

Fig. G-4: Fluid convection coefficient calculation process.

G.1.4 Computation of air convection coefficients.

G.1.4.1 Air gap.

Other processes are used for the air convection coefficients inside the electric motor housing:

Table G-8 : Prandtl and Taylor number in the air gap.

$$Pr_{air} = \frac{Cp_{air} \times visd_{air}}{\lambda_{air}} \qquad \text{(G-26)}$$

$$Ta = \Omega_{emot}^2 \times \left(\frac{L_{total_{emot}}}{2}\right)^3 \times \frac{R_{sleeve_{OUT}}}{\nu_{air}^2} \qquad \text{(G-27)}$$

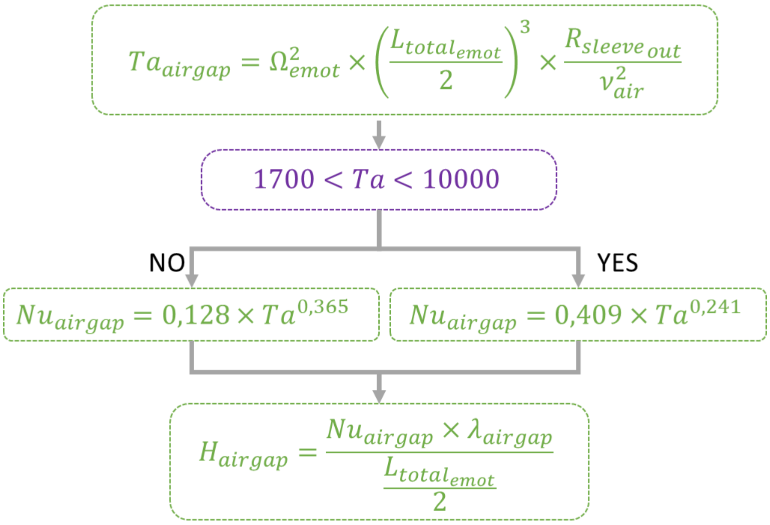

Fig. G-5: Air gap convection coefficient calculation process.

G.1.4.2 End-space frame.

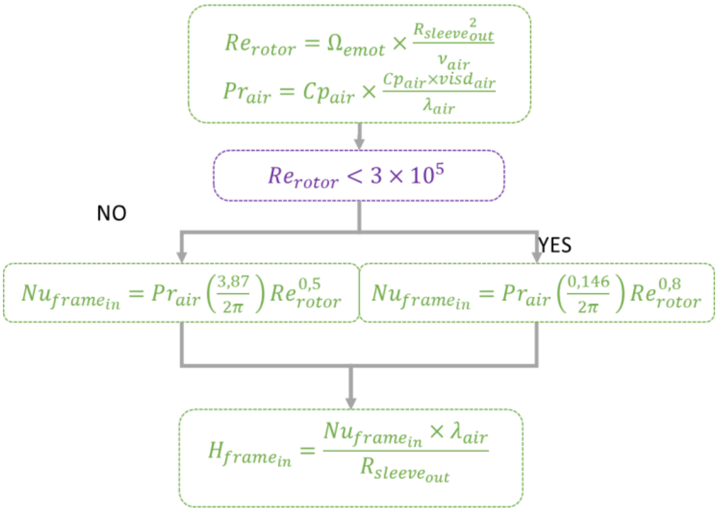

Fig. G-6: End-space frame convection coefficient calculation process

G.1.4.3 End-space rotor.

Table G-9: Prandtl and Nusselt number in the end-space rotor.

$$Re_{rotor} = \Omega_{emot} \times \frac{R_{sleeve}{}_{OUT}^{2}}{\nu_{air}} \quad \text{(G-28)}$$

$$Nu_{rotor} = 0.00823 \times \left(L_{endspace}\right)^{-1/6} \times Re_{rotor}^{0.75} \quad \text{(G-29)}$$

$$H_{end-space_{rotor}} = \frac{Nu_{rotor} \times \lambda_{air}}{R_{sleeve_{OUT}}} \quad \text{(G-30)}$$

G.1.4.4 End-space windings.

Table G-10: Convection coefficient in the end-space windings.

$$H_{end-space_{windings}} = 110 \;\; W/(m^2.K) \quad \text{(G-31)}$$

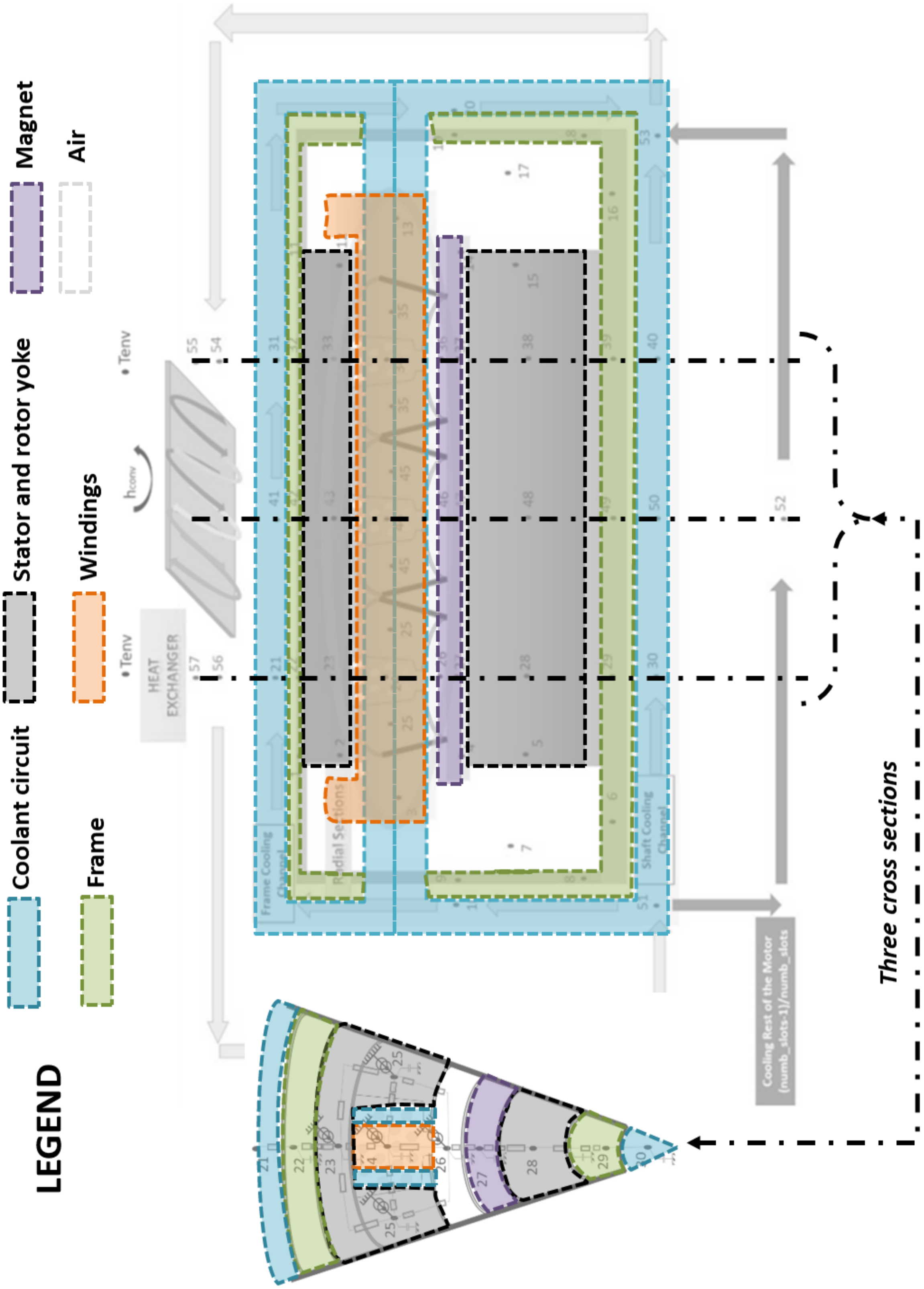

Fig. G-7: Lumped parameter thermal network of the motor and its heat exchanger.

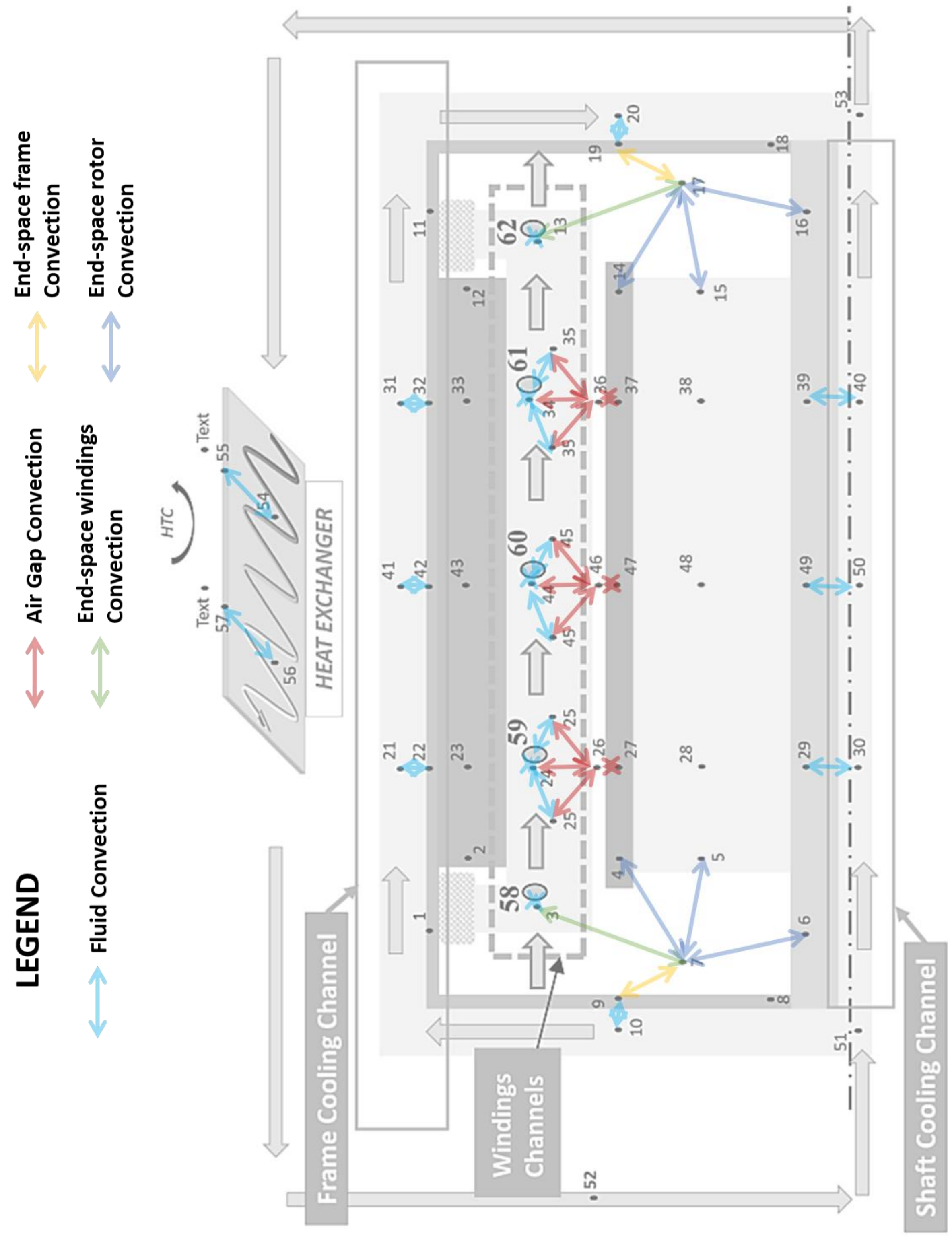

Fig. G-8: Lumped parameter thermal network detailed.

G.2 Lumped parameter thermal model.

The transient model is based on a lumped parameter thermal model Fig. G-7 and Fig. G-8. Solving the system equation in transient regime provides the temperature evolution during the flight mission considering the thermal capacity matrix G of the motor system, with respect to and any variation in input data such as the external temperature and to heat flow profile (motor losses profiles). The thermal balance equation is the following:

$$C.\frac{dT}{dt} = GT + \Psi \qquad (G\text{-}32)$$

Where C and G are [n×n] respectively the matrices representing capacity and conductance effects, and T and Ψ are the vectors [nx1] representing temperatures and heat generation in a system. An implicit Euler method is used to solve Eq.(*G-32*).

Thermal conductance matrix G.

The Table G-11 gives the expressions of the thermal conductances for each heat transfer mode.

Table G-11: Flux and conductance expressions for each heat transfer mode.

Heat transfer mode	Conductance	Heat flow expression
Conduction (axial and ortho-radial)	$G_{axial}^{cond}(i,j) = \lambda.\frac{S_{ij}}{L_{ij}}$	$G_{axial}^{cond}(i,j)(T_j - T_i)$
Conduction (radial)	$G_{radial}^{cond}(i,j) = \frac{2\pi\lambda h}{\ln\left(\frac{r_j}{r_i}\right)}$	$G_{radial}^{cond}(i,j)(T_j - T_i)$
Convection	$G_S^{conv}(i) = HS_i$	$G_S^{conv}(i)(T_f - T_i)$
Fluidic flow	$G^{fluid}(i,j) = \dot{m}C_p$	$G^{fluid}(i,j)(T_j - T_i)$

- S_{ij} is the surface of heat transfer between volumes represented by nodes i and j $[m^2]$
- S_i is the surface exposed to convection heat transfer$[m^2]$
- T_f is the average temperature of the fluid surrounding surface S_i $[°C]$
- r_i, r_j are the radius of nodes i and j $(with\ r_j \geq r_i)$ $[m]$
- $L_{ij}$is the distance between nodes i and j $[m]$
- h is the height of the cylindrical object $[m]$
- H is the heat transfer coefficient $\left[\frac{W}{m^2.K}\right]$
- $\dot{m}$ is the mass flow rate $[kg/s]$
- λ is the thermal conductivity $\left[\frac{W}{m\ \ .K}\right]$
- C_p is the thermal capacitance $\left[\frac{J}{kg.K}\right]$

Once all coefficient calculations are made, the equation (*G-32*) can be calculated in order to find the temperature in each part of the electric motor.

G.3 Constraints.

The thermal constraints are usually the most sensitive with regard to the electrical machine sizing. Three were selected in the optimization process.

Table G-12: Performance constraints.

$T_{stator_{yoke}} \leq T_{stator_{yoke_{max}}}$	Stator yoke temperature constraint [°C]	*(G-35)*
$T_{windings} \leq T_{windings_{max}}$	Winding temperature constraint [°C]	*(G-36)*
$T_{magnet} \leq T_{magnet_{max}}$	Permanent magnet temperature constraint [°C]	*(G-37)*

Different values are chosen for the two (2025 and 2035) targets of the HASTECS project.

Table G-13: Differences between 2025 and 2035 targets.

TARGET	2025	2035
$T_{stator_{yoke_{max}}}$ $[°C]$	180	180
$T_{windings_{max}}$ $[°C]$	180	180
$T_{magnet_{max}}$ $[°C]$	150	150

APPENDIX H. PARTIAL DISCHARGES IN THE SLOT

Table H-1: Input/output variables for the partial discharges model in the slot.

	INPUT VARIABLES	
h_{slot}	$[\mathrm{m}]$	Slot height
L_{slot}	$[\mathrm{m}]$	Slot length
k_{fill}	$[-]$	Fill factor in the slot
N_{ce}	$[-]$	Number of conductors per slot
T_{wind}	$[°\mathrm{C}]$	Maximum winding temperature
ALT_{CRS}	$[\mathrm{m}]$	Cruise altitude
V_{uHVDC}	$[\mathrm{V}]$	Ultra-high voltage direct current
$V_{emot_{rms}}$	$[\mathrm{V}]$	RMS value of the e-motor voltage
t_{rise}	$[\mathrm{s}]$	Switch rising time of the IGBT
	OUTPUT VARIABLES	
e_{liner}	$[\mathrm{m}]$	Liner thickness
$e_{insulation}$	$[\mathrm{m}]$	Insulation thickness
R_{cu}	$[\mathrm{m}]$	Copper radius of one wire
$nb_{turn_{cond}}$	$[-]$	Number of turns per conductor
$k_{remp_{real}}$	$[-]$	Real fill factor in the slot
$Flag_{pos_{windings}}$	$[-]$	Flag for the integration of the windings in the slot (1 = No, 0=Yes)

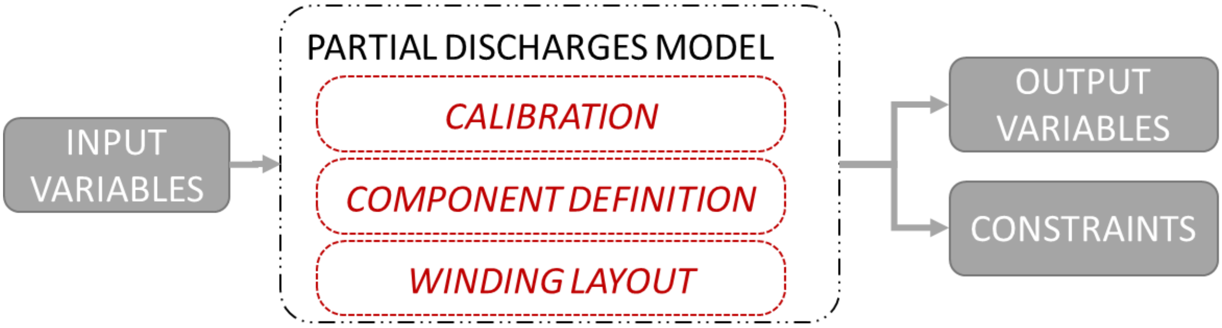

Fig. H-1: Process chart of the partial discharge model in the slot.

H.1 Calibration model.

The partial discharge model are studied in detail in [A8] and simplified (as presented in this Appendix) to face constraints of an optimization base system integration. Basics of partial discharges are based on the physic law of F. Paschen. In 1889, Friedrich Paschen investigated the breakdown of air located between two metallic plane electrodes. In order to take account of environment conditions in this model a calibration considering the temperature and the altitude has been implemented. An abacus permits us to anticipate the reduction of the Partial Discharge Inception Voltage (PDIV) with respect to the ground environmental conditions.

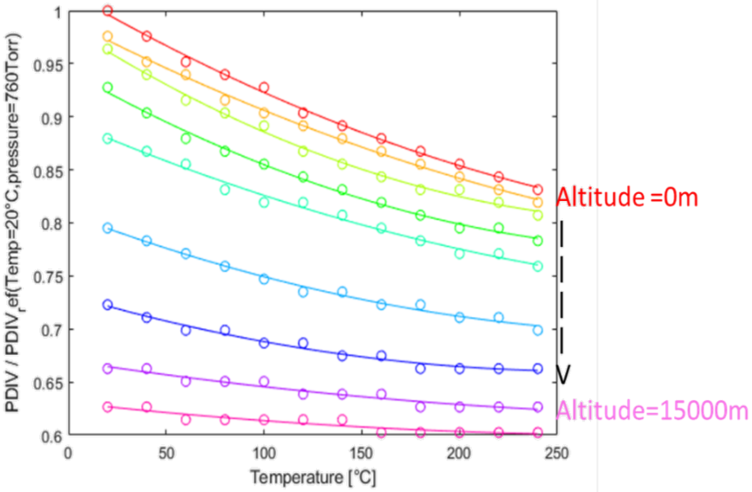

Fig. H-2: PASCHEN abacus: PDIV decrease for a combined variation of temperature and pressure.

The PDIV is maximum at normal temperature and pressure conditions (i.e.: 20 °C, 760 Torr), this maximum value is designated as $PDIV_{ref}$. Using the graph in Fig. H-2, the PDIV level between two enameled round wires in close contact for any point of the mission profile can be evaluated with respect to the actual environment. It is directly derived from $PDIV_{ref}$ obtained with a numerical model. It was assumed that the decrease of the PDIV level with temperature and pressure is the same, considering the turn/slot close contact. A limit winding temperature of $T_{wind_{limit}} = 180°C$ and $ALT_{CRS} = 25\,000\ ft$- (cruise) altitude are used for the $PASCHEN_{abacus}$.

Table H-2: Calibration factor determined by the PASCHEN abacus.

$Factor = PASCHEN_{abacus}(T_{wind_{limit}}, ALT_{CRS})$	Calibration factor [-]	(*H-1*)

H.2 Slot component definition model.

H.2.1 Wire definition model.

The maximum voltage seen by the turns is the one given by power electronics through the equation (*H-2*). An example of 5-level power electronics voltage waveforms is illustrated in the figure Fig. H-3:

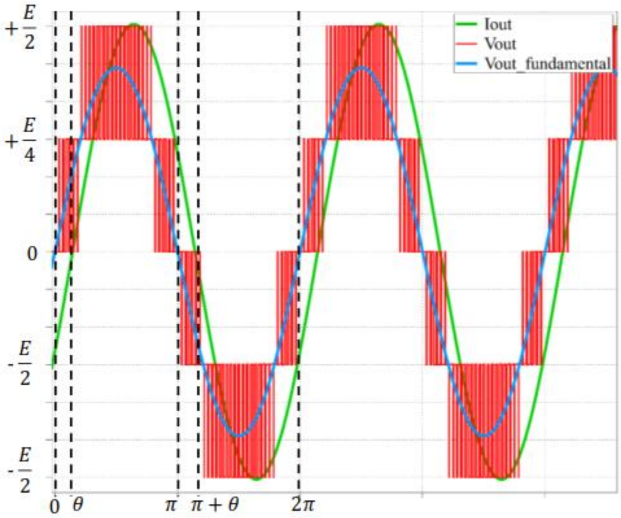

Fig. H-3: 5-level PE voltage and current curves.

The blue line represents the fundamental of the voltage, while the red one is the peak voltage values over two periods. The maximum voltage step (between two successive pulses) value has been taken into consideration for the PDIV value. For a 5-level the voltage step is $\frac{E}{4}$. For a 3-level converter, this step is doubled $\left(\frac{E}{2}\right)$, E being here equivalent with the bus voltage (V_{uHVDC}).

Table H-3: Detailed wire definition model.

$V_{max_{transient}} = \frac{V_{uHVDC}}{nb_{level}-1}$	Max transient voltage seen by the turns [V]	(*H-2*)
$PDIV_{windings_{ref}} = \frac{V_{max_{transient}}}{Factor}$	Related PDIV value for enamel thickness estimation [V]	(*H-3*)

A simple analytical model has been implemented for determining the minimal enamel thickness avoiding partial discharges from the $PDIV_{ref}$ value find previously.

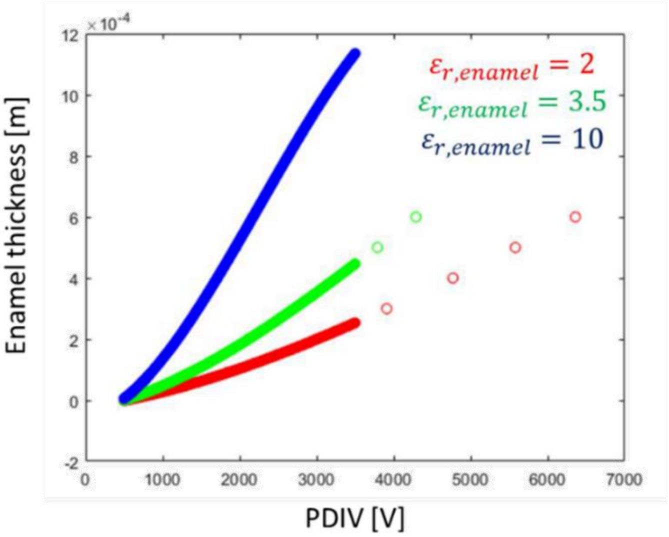

Fig. H-4: Enamel thickness as a function $PDIV_{windings_{ref}}$ *(T=20°C, P = 760 Torr).*

The required enamel thickness e was interpolated versus the PDIV domain using a 3rd order polynomial. The polynomial coefficients depend on the material dielectric constant ($\varepsilon_{r,enamel}$). Thanks to a data sheet, correlations have been highlighted between the copper radius and its enamel thickness, they are illustrated in the next figure Fig. H-5:

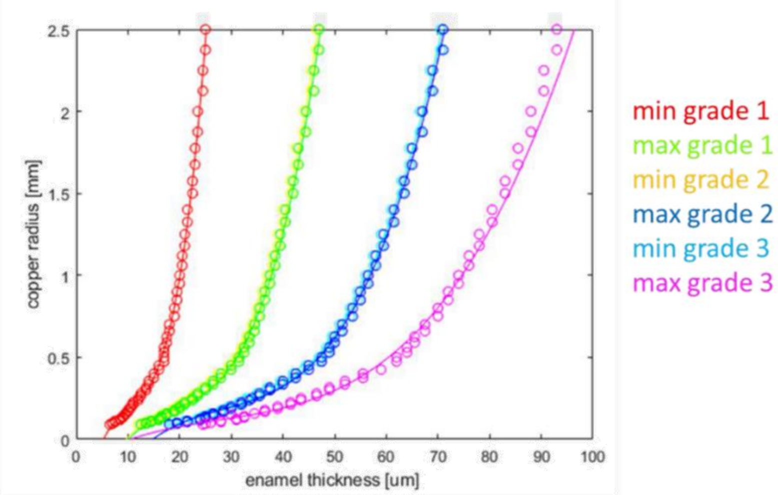

Fig. H-5: Copper radius versus enamel thickness for all grade tolerances (T=20°C, P = 760 Torr).

The Fig. H-5 displays the copper radius as a function of the enamel thickness given by the grade tolerance (min/max), 6 grade tolerances are available. Another 3rd order polynomial has been implemented for each grade tolerance.

H.2.2 Liner definition model.

The maximum voltage seen between the slot and the turn is the maximum voltage of the power electronic supplied electric motor.

Table H-4: Detailed liner definition model.

$V_{max_{steady}} = ma_{max} \times \frac{V_{uHVDC}}{2}$	Max steady voltage seen by the yoke (for a classical PWM without over-modulation) [V]	(*H-4*)
$PDIV_{liner_{ref}} = \frac{V_{max_{steady}}}{Factor}$	Related PDIV value for liner thickness estimation [V]	(*H-5*)

The figure Fig. H-6 gives the slot liner thickness according to the enamel thickness of the windings and the material permittivity.

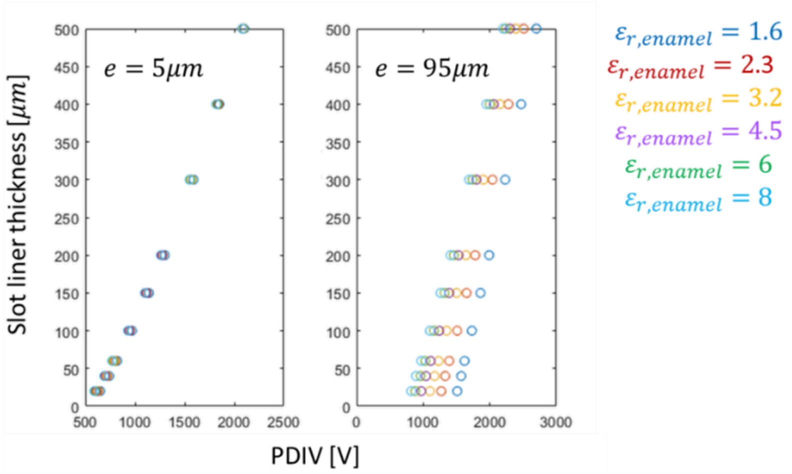

Fig. H-6: Slot liner thickness as a function of $PDIV_{liner_{ref}}$ and enamel thickness (T=20°C, P = 760 Torr).

In that case a 2nd order polynomial has been set considering the enamel thickness and the permittivity of enamel and liner.

H.3 Winding layout model.

Once calculations are done, the slot can be filled by turns and the liner untill reaching the right value of k_{fill}.

Table H-5: Detailed winding layout model.

$nb_{turn_{cond}} = \frac{floor\left(\frac{L_{slot}\times h_{slot}\times k_{fill}}{\pi\times R_{cu}^2}\right)}{Nce} + 1$	Number of turns per conductor [-]	(*H-7*)
$nb_{wires} = nb_{turn_{cond}} \times Nce$	Number of wires [-]	(*H-8*)
$k_{fill_{real}} = \frac{nb_{wires}\times\pi\times R_{cu}^2}{L_{slot}\times h_{slot}}$	Real value of fill factor [-]	(*H-9*)

Two colors are used here symbolizing two different conductors. In this example, three wires per conductor are considered.

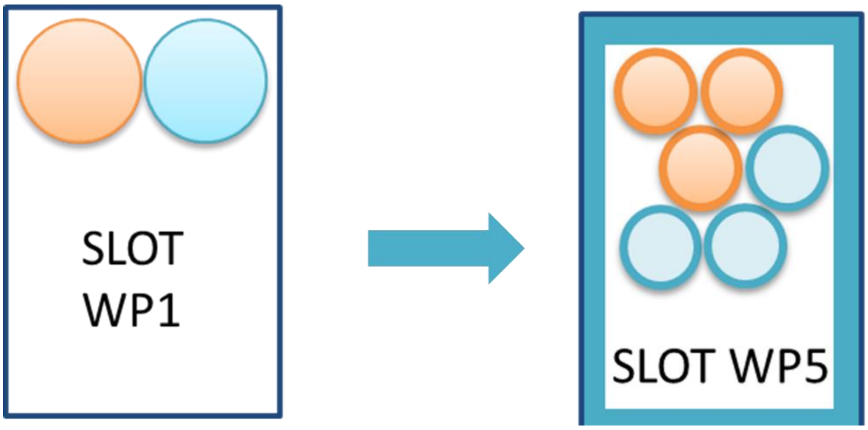

Fig. H-7: Example of winding layout.

The final process is displayed in
Fig. H-8:

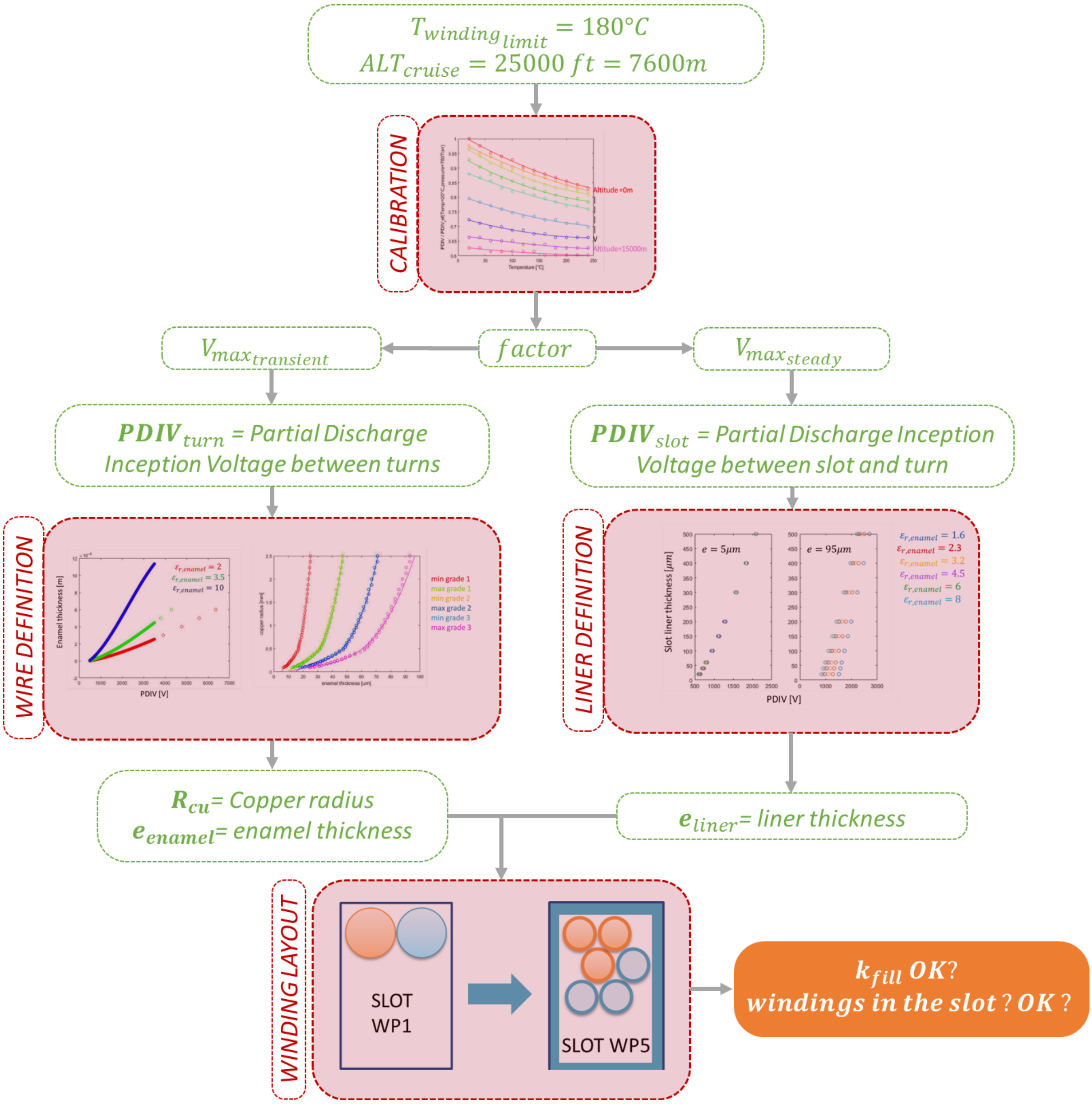

Fig. H-8: WP5 detailed process.

H.4 Constraints.

Two constraints are used in the optimization process:

Table H-6: Constraints.

$k_{fill_{new}} - k_{fill_{ref}} \leq 1\% \times k_{fill_{ref}}$	Fill factor constraint [-]	(H-10)
$\boldsymbol{Flag}_{\boldsymbol{pos}_{\boldsymbol{windings}}} \leq 0$ $(Windings\ in\ the\ slot\ ?\ Yes = 0\ , No = 1)$	Winding layout constraint [-]	(H-11)

The first constraint ensures the proximity with the initial value of fill factor. And the second constraint certifies the integration of the winding in the slot.

APPENDIX I. POWER ELECTRONICS AND ITS COOLING

Table I-1: Input/output variables for the power electronics model.

	INPUT VARIABLES	
$\boldsymbol{ma_{mission}\ (t)}$	$[-]$	Modulation depth over mission
$\boldsymbol{FP_{mission}(t)}$	$[-]$	Power factor over mission
$\boldsymbol{f_{elec_{emot}}(t)}$	$[\mathrm{Hz}]$	Electric frequency
$\boldsymbol{nb_{phase}}$	$[-]$	Number of phases
$\boldsymbol{COM}$	$[-]$	CONTROL of the Power Electronics (PE)
$\boldsymbol{TOPO}$	$[-]$	Topology of the PE
$\boldsymbol{I_{rating}}$	$[\mathrm{A}]$	Current rating of IGBTs
$\boldsymbol{V_{uHVDC}}$	$[\mathrm{V}]$	Ultra-high direct current voltage
$\boldsymbol{P_{elec_{mission}}(t)}$	$[\mathrm{W}]$	Electric power over mission
	OUTPUT VARIABLES	
$\boldsymbol{M_{cooling}}$	$[\mathrm{kg}]$	Cooling mass
$\boldsymbol{M_{inverter}}$	$[\mathrm{kg}]$	Inverter mass
$\boldsymbol{\eta_{inverter}(t)}$	$[\%]$	Inverter efficiency over mission
$\boldsymbol{P_{DC_{cable_{mission}}}(t)}$	$[\mathrm{W}]$	Electric power required at the PE input

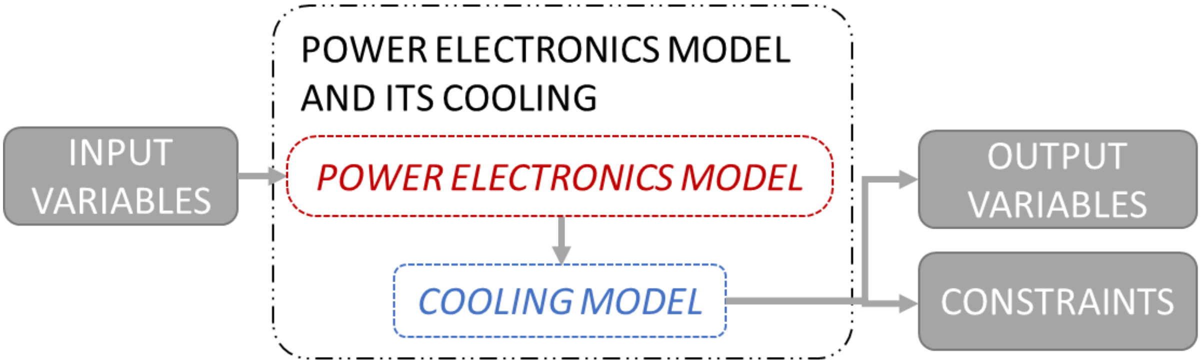

Fig. I-1: Process chart of the models.

I.1 Power Electronics model.

I.1.1 Semiconductor sizing model.

The design of power electronics for the HASTECS project was studied in [A9]. A simplification of this design is proposed here to face the constraints of optimization based system integration. In that context, a voltage based law has been implemented in this model in order to choose the right converter topology with respect to the bus voltage. The process defined in Fig. I-2 is related to the Fig. II-32 in CHAPTER II.

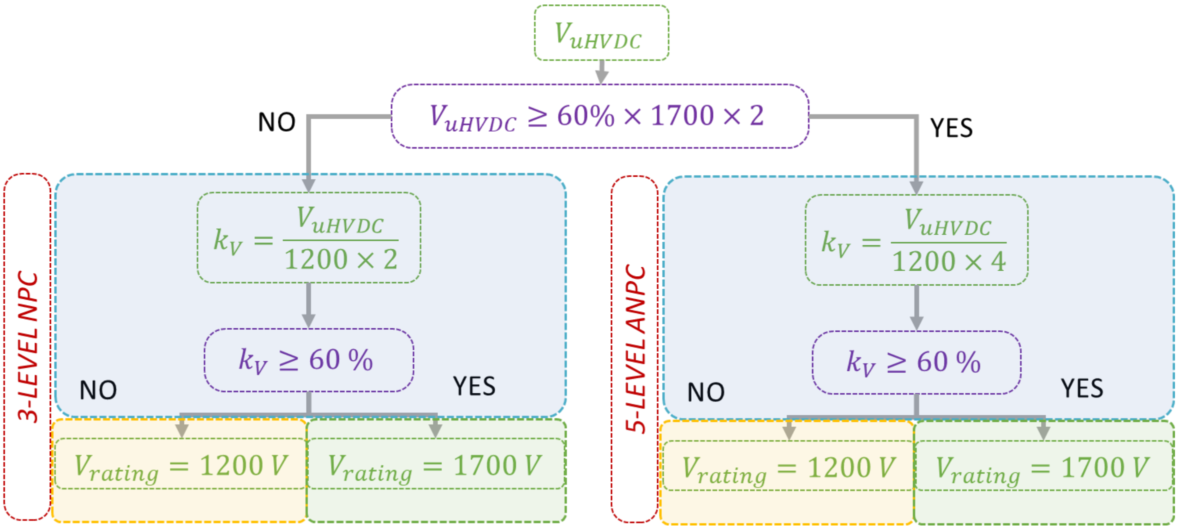

Fig. I-2: Topology and IGBT choice process.

k_V is the IGBT rate of use in voltage; the fixed value of 60% has been assessed by AIRBUS in order to avoid the cosmic radiations. In the previous process, the ultra-high DC voltage V_{uHVDC} firstly determines the topology of the converter: based on the [A9] study, only 3 and 5 multilevel structures have be selected for this system integration. The maximum permissible voltage in this case is given by the higher voltage rating (1700V) and the lower level topology (times 2 because of the 3-level topology).

Once the topology is determined, another rule allows choosing the right IGBT device. Both IGBTs (1200 and 1700V) have the same current rating $I_{rating} = 600\ A$. A certain number of IGBTs are parallelized to fulfill motor current constraints depending on both the voltage and the converter structure. The inverter current and the electric frequency can be determined over the mission profile:

Table I-2: Current and electric frequency computation.

$I_{rms_{mission}} = \frac{\left(P_{elec_{mission}} \times 2\sqrt{2}\right)}{nb_{phases} \times V_{uHVDC} \times ma_{mission} \times FP_{mission}}$	RMS value of the current in the PE [A]	(I-1)
$f_{switch} = 7 \times f_{elec_{emot}}$	Switching electric frequency [Hz]	(I-2)
$nb_{IGBT_{par}} = floor\left(\frac{\max\left(I_{rms_{mission}}\right)}{I_{rating}}\right) + 1$	Number of semiconductor in parallel [-]	(I-3)

To avoid subharmonics and AC joule losses in the electric motor, a minimum ratio of 7 has been set between the switching frequency and the maximum electric motor frequency. According to the topology, this frequency is redefined.

Table I-3: Switching frequency seen by IGBT and definition of the number of semiconductors per phase.

TOPOLOGY	3-LEVEL NPC	5-LEVEL ANPC
Control name	*DPWMMAX*	*PWM*
Number of semiconductors per phase.	$nb_{SC_{pp}} = 6$	$nb_{SC_{pp}} = 12$
Switching frequency seen by IGBTs	$f_{switch_{IGBT}} = f_{switch}$	$f_{switch_{IGBT}} = f_{switch} \times 2$

In the ANPC-topology there is two part: a switcher part and the 3-Level FC part, for the switcher part, 2 IGBT in series are considered. The Fig. II-31shows the 5L-ANPC single phase inverter where there are 4 switches for the switcher part and 4 switches for the other part. Finally, 8 switches for the switcher (4x2) and 4 switches for the 3-level FC equals to 12.

I.1.2 Capacitor sizing model.

The capacitor values can be calculated from the stored energy as shown in the following equations. In both (3 and 5 level) structures, a DC bus capacitor has to be sized. In the 5 level (ANPC) case, an additional flying capacitor must also be sized. In order to choose the most appropriate component from the datasheet, the capacitor current is required:

Table I-4: Capacitor sizing model.

$I_{capa_{rms}} = \sqrt{I_{rms}^2 - I_{avg}^2}$	RMS value of the capacitor current [A]	(*I-4*)
$C_{capa_{DC}} = \frac{I_{capa_{rms}}}{f_{switch_{IGBT}} \times \Delta V_{DC}}$	DC bus capacitor capacity [F]	(*I-5*)
$V_C = \frac{V_{uHVDC}}{2}$	Voltage value for the 5L–ANPC converter topology	(*I-6*)
$C_{capa_{FY}} = \frac{I_{out_{max}}}{\Delta V_{C_{FY}} \times V_C \times f_{emot}}$	Flying capacitor capacity for 5L ANPC converter [F]	(*I-7*)

In this case, we have set certain quality constraints for voltages: $\Delta V_{DC} = 5\%$ and the $\Delta V_{C_{FY}} = 10\%$. The current and the capacity of the capacitor allow choosing a component in the database; its mass is directly extracted from the catalogue.

I.1.3 Loss model.

In order to estimate the efficiency of the power converter, several assumptions have been made:

- The output current is sine
- Steady state is considered

Two kinds of losses are integrated in the model: the conduction and the switching losses.

Table I-5: Conduction and switching losses description.

$P_{cond_{IGBT}} = \frac{1}{T_{mod}} \int V_{ce}(t) \times I_c(t)\, dt$	IGBT conduction losses [W]	(*I-8*)
$P_{cond_{Diode}} = \frac{1}{T_{mod}} \int V_d(t) \times I_d(t)\, dt$	Diode conduction losses [W]	(*I-9*)
$E_X(I \quad) = A_X + B_X \times I \quad + C_X \times I^2$	Energy losses for the X component (X: IGBT/Diode) [J]	(*I-10*)
$P_{sw} = \frac{f_{sw}}{T_{mod}} \int \frac{V_{sw}}{V_{def}}\, E_X(I \quad)\, dt$	Switching losses [W]	(*I-11*)

A_X, B_X, C_X are the 2nd order polynomial coefficients which approximate the curve in the datasheet. $E_{v_{def}}$ is the energy losses of the component, V_{def} and V_{sw} are respectively the half component voltage and the switched voltage of the semiconductor. f_{sw} is the switching frequency and T_{mod} is the modulation period.

I.1.4 Mass and efficiency.

Table I-6: Mass table.

$M_{SC} = nb_{phase} \times nb_{SC_{pp}} \times m_{1device} \times \left(floor\left(\frac{nb_{IGBT_{par}}}{2}\right) + 1 \right)$	SC mass [kg]	(*I-12*)
$M_{PE} = M_{SC} + M_{capa_{DC}} + M_{capa_{FY}}$	PE mass [kg]	(*I-13*)

Where $m_{1device}$ is the mass of one electronic component and nb_{phase} is the number of phases. The DC capacitor mass $M_{capa_{DC}}$ and the flying capacitor mass $M_{capa_{FY}}$ are taken from the database.

Table I-7: Efficiency table.

$\eta_{inverter_{mission}} = \frac{P_{mission}}{P_{sw} + P_{cond} + P_{mission}}$	Efficiency [%]	(*I-14*)

I.2 Cooling model.

The thermal analysis integrates a heat source (losses) as inputs and temperature at different nodes as outputs and is based on thermal resistors depending on the thermal conductivity and chip sizes.

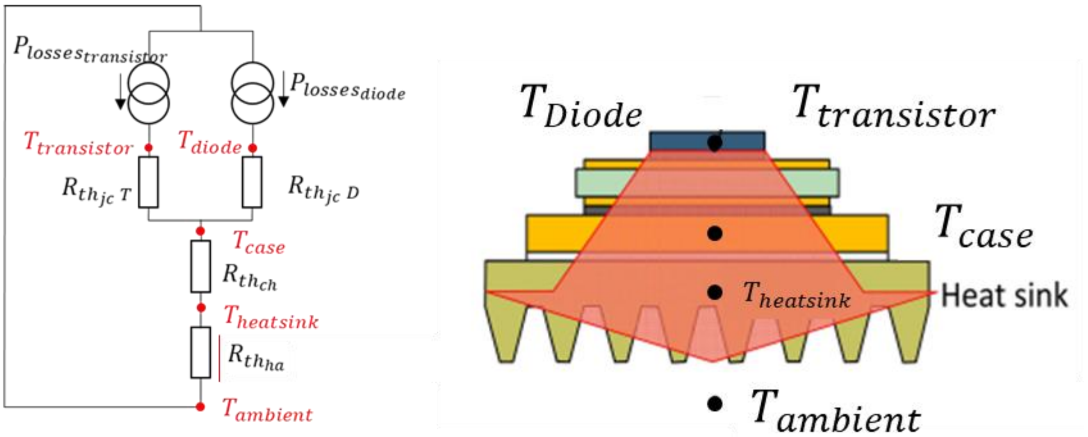

Fig. I-3: Representation the equivalent thermal model of a single module.

Table I-8: Thermal equations related to the Fig. I-3.

$T_{transitor} = P_{losses_{transistor}} \times R_{th_{jc_T}} + T_{case}$	Transistor temperature [°C]	(*I-15*)
$T_{diode} = P_{losses_{diode}} \times R_{th_{jc_D}} + T_{case}$	Diode temperature [°C]	(*I-16*)
$T_{case} = \left(P_{losses_{diode}} + P_{losses_{transistor}}\right) \times R_{th_{ch}} + T_{heatsink}$	Case temperature [°C]	(*I-17*)

Where $R_{th_{jc_T}}, R_{th_{jc_D}}$ are the junction to case thermal resistance (T = Transistor, D = Diode), and $R_{th_{ch}}$ is the case to heatsink thermal resistance. The equation for the heat sink temperature has not been considered because the work package in charge of the cooling system imposes the thermal resistance $R_{th_{ha}}$ in order to set the heat sink temperature to 70°C [A10]. The new equivalent thermal model is detailed in the Fig. I-4:

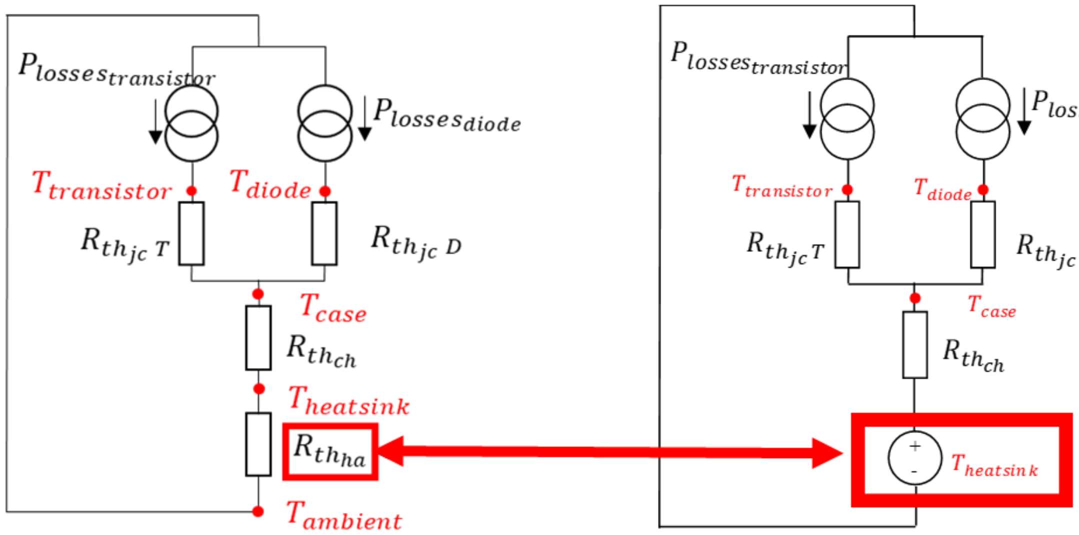

Fig. I-4: New equivalent thermal model for the power electronics.

Based on the detailed study of [A10], the cooling mass estimation has been totally simplified and integrated in the power electronics model. A surrogate model has been built by the work package in charge of the PE cooling system. Two linear curves function of the total losses over the mission $P_{tot_{mission}}$ estimate the cooling system mass.

Table I-9: Cooling system mass linear function.

$P_{tot_{max}} = \max\left(P_{sw_{mission}} + P_{cond_{mission}}\right)$	Total losses [W]	(*I-18*)
$M_{cooling} = a_{cool} \times P_{tot_{max}} + b_{cool}$	Cooling system mass estimation [kg]	(*I-19*)

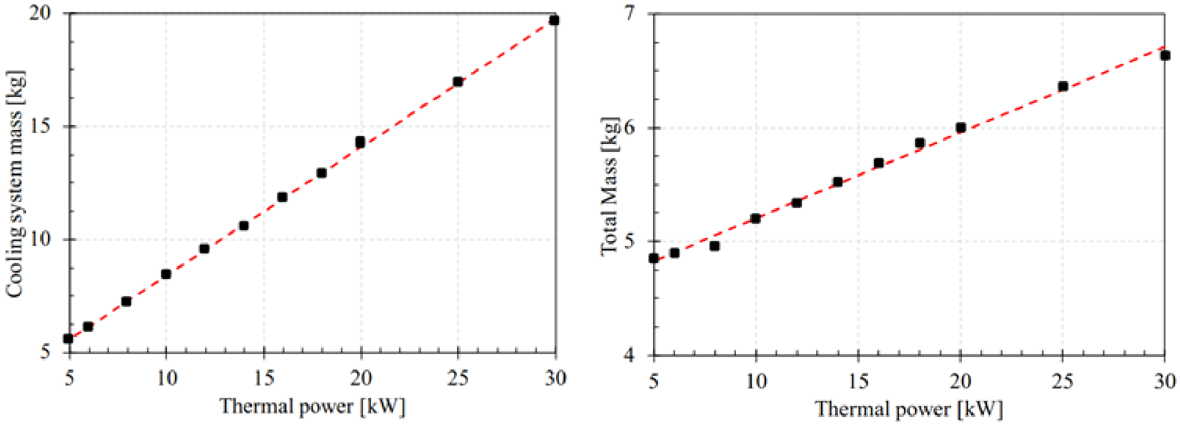

Fig. I-5: Cooling system mass estimation (LEFT: 2025 TARGET and RIGHT: 2035 TARGET).

All parameters are summarized in the Table I-10 below:

Table I-10: Differences between 2025 and 2035 targets

TARGET	2025	2035
$a_{cool}\ [-]$	0.5681	0.0692
$b_{cool}[-]$	2.7323	2.674

In order to integrate the bus bar mass into the total mass for power converter and its cooling, an integration factor $\left(\frac{1}{3}\right)$ has been assessed. Finally, the whole mass can be estimated:

Table I-11: Total inverter mass.

$M_{busbar} = \frac{1}{3} \times \left(M_{PE} + M_{cooling}\right)$	DC bus bar mass estimation [kg]	(*I-20*)
$M_{total_{inverter}} = M_{PE} + M_{cooling} + M_{busbar}$	Total PE mass [kg]	(*I-21*)

APPENDIX J. FUEL CELL SYSTEM AND BATTERY MODEL

Table J-1: Input/output variables for the fuel cell and the battery.

	INPUT VARIABLES	
	MISSION	
$P_{elec_{mission}}$	$[\mathrm{W}]$	Electric source power over mission
$P_{elec_{sizing}}$	$[\mathrm{W}]$	Electric source power sizing point
	FUEL CELL	
$P_{SPE_{stack}}$	$[\mathrm{kW/kg}]$	Stack specific power
$P_{SPE_{aux}}$	$[\mathrm{kW/kg}]$	Auxiliary specific power
$\eta_{FC_{stack}}$	$[\%]$	Stack efficiency
$\eta_{FC_{system}}$	$[\%]$	System efficiency
$comp_{H2_{gaz}}$	$[\%]$	Compression ratio[1] @700 bar compressed H2
$comp_{H2_{liquid}}$	$[\%]$	Compression ratio[1] @20K liquid H2
	BATTERY	
E_{XX}	$[\mathrm{kWh/kg}]$	Cell specific energy of the cell
$C_{rate_{XX}}$	$[\mathrm{h}^{-1}]$	Cell C-rate of the cell
f_{sys}	$[-]$	Integration factor (cell -> system)
	OUTPUT VARIABLES	
$M_{fuel\ cell}$	$[\mathrm{kg}]$	Fuel cell mass
$M_{H2_{storage}}$	$[\mathrm{kg}]$	H2 storage mass
$M_{battery}$	$[\mathrm{kg}]$	Battery mass
$M_{electric_{soruce}}$	$[\mathrm{kg}]$	Electric source mass

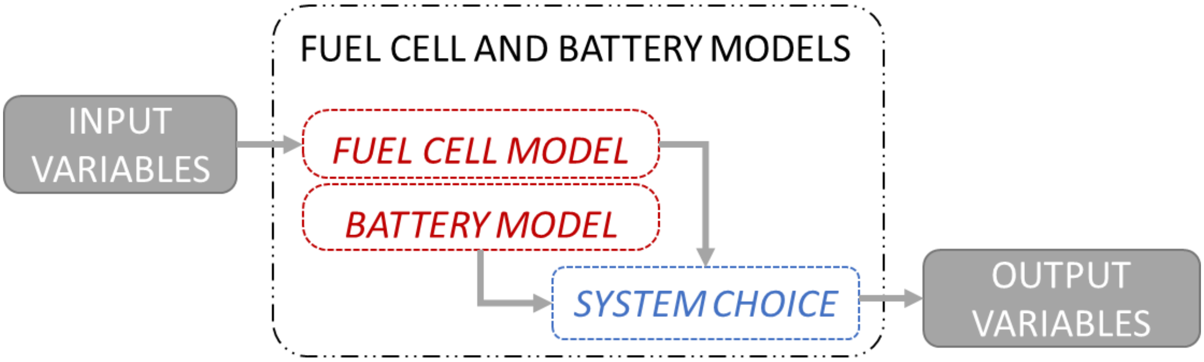

Fig. J-1: Process chart of the electric source model.

---

[1] Set the mass percentage of H2 versus the whole storage

A strongly simplified assessment model is proposed here based on the detailed study of [A11]. The assumptions in terms of specific power, specific energy and c-rate have been presented in chapter II in the Table II-1 and the Table II-2. Once these coefficients are known, the masses of the fuel cell system and of the battery pack system can be evaluated from [A11].

J.1 Fuel cell model.

Table J-2: Fuel cell system mass estimation.

$M_{FC\,stack} = \frac{\max\left(P_{elec_{sizing}}\right)}{P_{spe_{FC_{stack}}}} \times \frac{\eta_{FC_{stack}}}{\eta_{FC_{system}}}$	Fuel cell stack mass $[kg]$	(*J-1*)
$M_{FC\,aux} = \frac{\max\left(P_{elec_{sizing}}\right)}{P_{spe_{FC_{aux}}}} \times \frac{\eta_{FC_{stack}}}{\eta_{FC_{system}}}$	Auxiliary mass $[kg]$	(*J-2*)
$E_{FC_{mission}} = \int^{t} \frac{P_{elec_{mission}}(t)}{\eta_{FC_{system}}(t)} dt$	Hydrogen energy required $[kWh]$	(*J-3*)
$m_{H2_{gaz}} = \frac{\max(E_{FC_{mission}})}{E_{SPE_{H2}} \times comp_{H2_{gaz}}}$	Mass of storage with gaseous hydrogen $[kg]$	(*J-4*)
$m_{H2_{liquid}} = \frac{\max(E_{FC_{mission}})}{E_{SPE_{H2}} \times comp_{H2_{liquid}}}$	Mass of storage with liquid hydrogen $[kg]$	(*J-5*)

An oversizing of the fuel cell is mandatory in order to take account of the power to be supplied to auxiliaries. This oversizing is modeled by the ratio between these two efficiencies in the fuel cell system mass estimation. The following figure (Fig. J-2) represents both efficiency according the net power per unit.

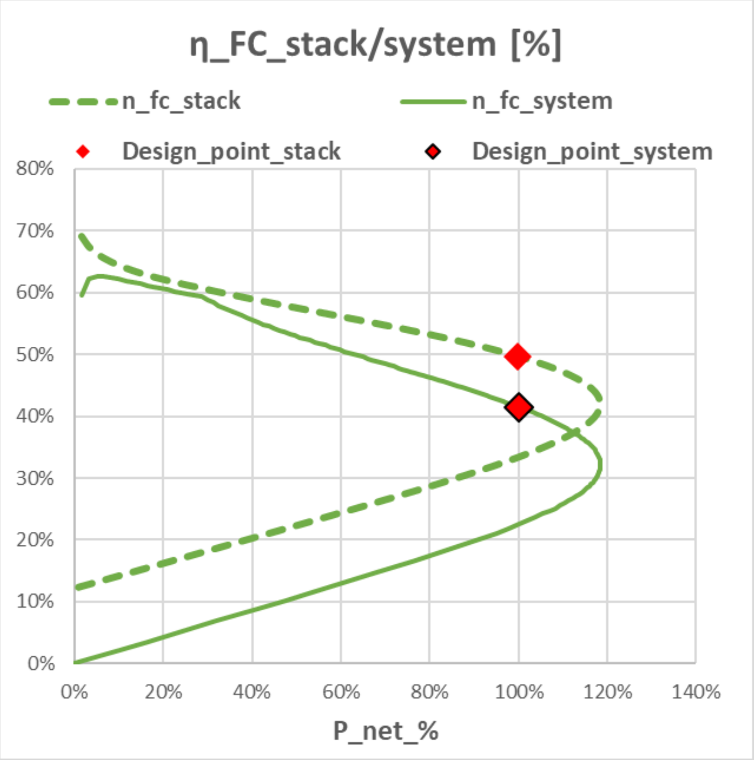

Fig. J-2: Stack/system efficiencies versus the net power to supply per unit.

A linear regression has been implemented for the efficiency estimation during the fuel cell mission. Green points here represent the linear function Fig. J-3.

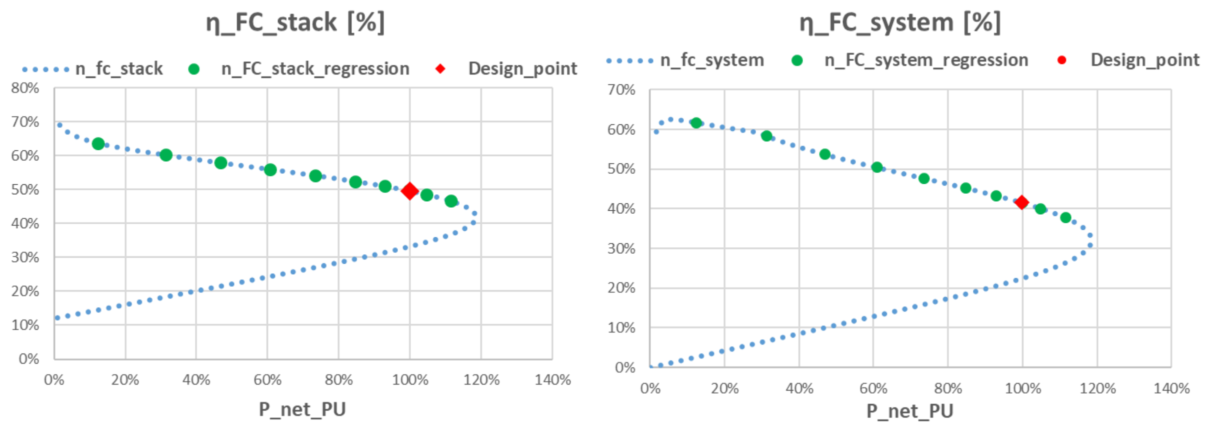

Fig. J-3: Stack and system efficiencies.

Table J-3: Linear function of the fuel cell efficiencies.

$\eta_{FC_{stack}}(t) = \alpha_{FC_{stack}} \times P_{FC_{PU}}(t) + \beta_{FC_{stack}}$	Fuel cell stack efficiency [%]	*(J-6)*
$\eta_{FC_{system}}(t) = \alpha_{FC_{system}} \times P_{FC_{PU}}(t) + \beta_{FC_{system}}$	Fuel cell system efficiency [%]	*(J-7)*

J.2 Battery model.

The mass estimation model for the battery is depending on the technology considered. In this study, three cells have been considered : $LTO - NTO/NMC/LiS$, all parameters are displayed in the Table II-2. Two equations are implemented in this surrogate model: an energy and a power sizing equation:

Table J-4: Mass estimation considering the discharge energy and the C-rate (Power).

$E_{BATT_{mission}} = \int^{t} P_{elec_{mission}}(t)dt$	Energy required $[kWh]$	*(J-8)*
$m_{batt_E} = \frac{\max(E_{BATT_{mission}})}{E_{SPE}}$	Cell mass estimation considering the energy $[kg]$	*(J-9)*
$m_{batt_P} = \frac{\max(P_{elec_{mission}})}{E_{SPE} \times C_{rate}}$	Cell mass estimation considering the power and the C-rate $[kg]$	*(J-10)*
$m_{batt} = \max\left(m_{batt_E}; m_{batt_P}\right) \times f_m$	System mass estimation $[kg]$	*(J-11)*

J.3 Auxiliary electrical power source choice.

To simplify the study, the lightest system between battery and fuel cell will be taken into account in the calculation of the powertrain mass.

APPENDIX K. RECTIFIER AND GENERATOR EFFICIENCY AND WEIGHT ASSESSMENTS

Table K-1: Input/output variables for the rectifier and the e-generator.

	INPUT VARIABLES	
$P_{elec_{GT}mission}$	[W]	Electric power mission for the turboshaft
$P_{SPE_{rectifier}}$	[kW/kg]	Rectifier specific power
$P_{SPE_{rgenerator}}$	[kW/kg]	E-generator specific power
$\eta_{rectifier}$	[%]	Rectifier efficiency
$\eta_{generator}$	[%]	E-generator efficiency
	OUTPUT VARIABLES	
$P_{mech_{GT_{mission}}}$	[W]	Mechanical Power of the turboshaft
$M_{rectifier}$	[kg]	Rectifier mass
$M_{e-generator}$	[kg]	E-generator mass

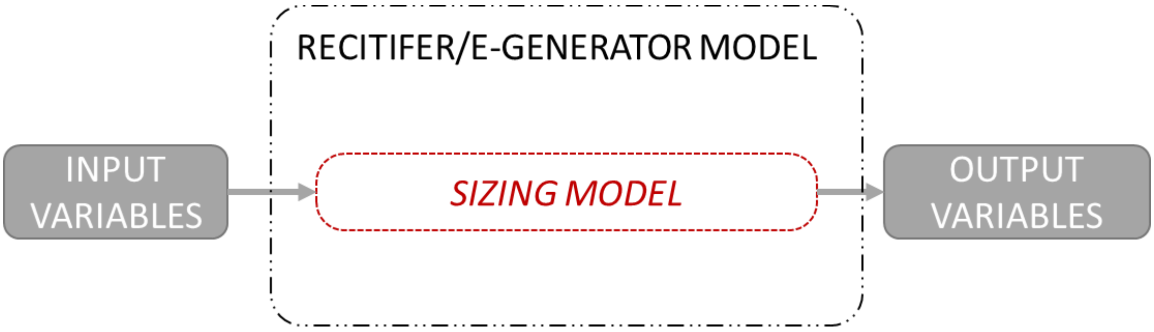

Fig. K-1: Process chart for the rectifier/e-generator model.

K.1 Sizing model.

For these components, simple assessment models have been set simply based on specific power and fixed efficiency. The HASTECS targets are used for assessing the rectifier and electric generator masses.

Table K-2: Assumptions for the electric device fed by the turboshaft.

	2025 TARGET	**2035 TARGET**
Electric generator specific power	5 kW/kg	10 kW/kg
Electric generator efficiency	96%	98.5%
Rectifier specific power	15 kW/kg	25 kW/kg
Rectifier efficiency	98%	99.5%

With these assumptions the mass estimation is simply:

Table K-3: Mass and power estimation for the rectifier and the e-generator.

$m_{rectifier} = P_{elec_{Rectifier}} \times P_{SPE_{rectifier}}$	Rectifier mass $[kg]$	(*K-1*)
$m_{e-generator} = P_{elec_{GT}} \times \frac{P_{SPE_{e-generator}}}{\eta_{rectifier}}$	E-generator mass $[kg]$	(*K-2*)
$P_{mech_{GT_{mission}}} = \frac{P_{elec_{Rectifier}}}{\eta_{rectifier} \times \eta_{e-generator}}$	Mechanical power of the turboshaft	(*K-3*)

APPENDIX L. MULTIDISCIPLINARY DESIGN OPTIMIZATION PROCESS OF A HYBRID ELECTRIC AIRCRAFT PROPULSION SYSTEM

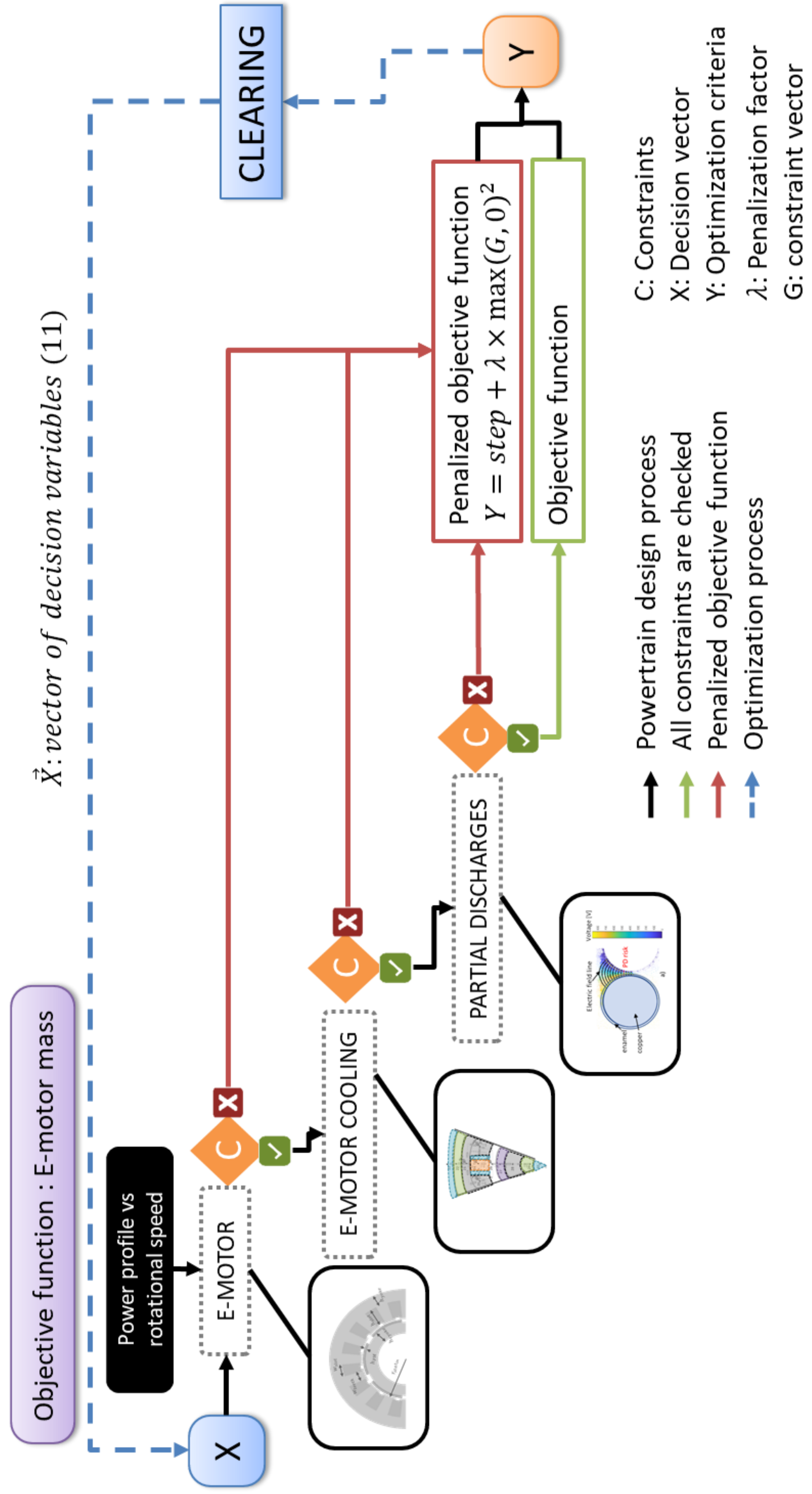

Fig. L-1: Weight optimization process for electric motor.

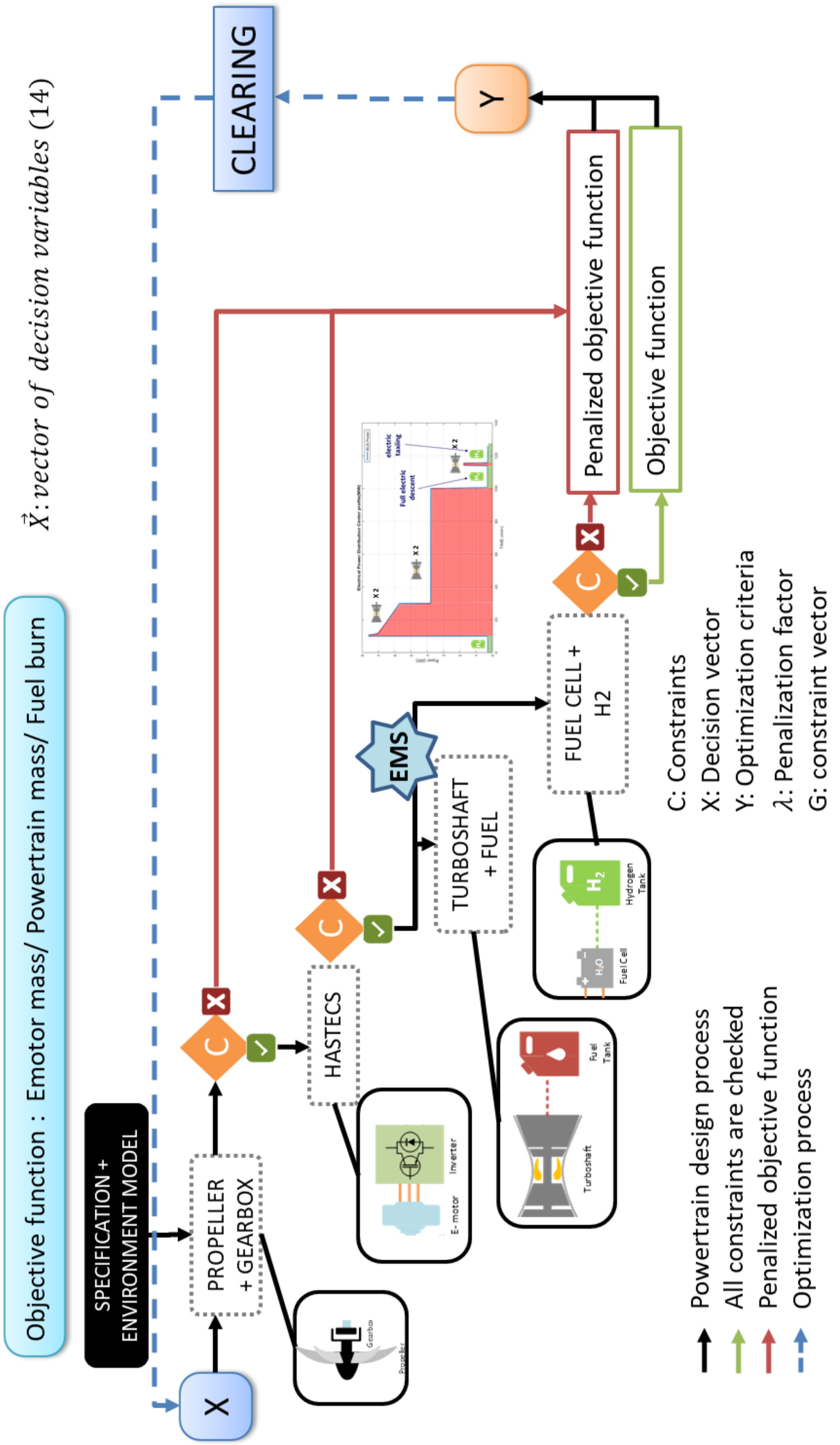

Fig. L-2: Integrated optimal design process of a hybrid electric powertrain.